Impact of fine-scale spatially heterogeneous canopy and soil moisture, and three-dimensional root water uptake on large-scale energy fluxes in vegetated environments

by

Lingli He

A dissertation submitted in partial fulfillment
of the requirements for the degree of
Doctor of Philosophy
(Civil Engineering)
in the University of Michigan
2014

Doctoral Committee:

Associate Professor Valeriy Y. Ivanov, Chair
Associate Professor Gil Bohrer
Professor Nikolaos D. Katopodes
Associate Professor Allison L. Steiner
Professor Steven J. Wright

ACKNOWLEDGEMENTS

CONTENTS

LIST OF FIGURES

LIST OF TABLES

ABSTRACT

The accuracy of transpiration simulation by current land surface models has been limited by several uncertainties, including the representation of canopy-scale heterogeneities of the land surface and sensitivity of transpiration to root-zone soil water content in dry conditions. This work focuses on effects of representing fine-scale (~m) spatially varying soil moisture, vegetation characteristics, radiation environment, as well as three-dimensional root water uptake processes on larger-scale energy fluxes at the plot- (~102 m2) and watershed-scales (~km2).

The study location is a northern temperate mixed forest with spatially heterogeneous canopy, where intermediate disturbance experiment removed canopy of aspen and birch trees. An initial analysis of empirical data on temporal dynamics of soil water content under the canopies with varying degrees of disturbance demonstrates that crown-scale canopy heterogeneity leads to detectable differences in soil water status, attributed predominantly to a decreased root water uptake in areas of thinner canopy. In order to infer larger-scale implications of crown-scale variations in canopy biomass and soil moisture conditions, an ecohydrologic model tRIBS + VEGGIE, the TIN (Triangulated Irregular Networks) based Real-time Integrated Basin Simulator + VEGetation Generator for Interactive Evolution, is used as an integrating tool. It explicitly resolves spatially varying canopy biomass, radiative forcing, and soil moisture. Numerical experimentation shows that root-canopy controls of water uptake exhibit two opposing effects on soil moisture spatial variability: during and shorty after precipitation events they drive increased soil moisture heterogeneity but act to homogenize soil moisture during later

stages of dry-down periods. Further, variations in canopy light environments introduce non-linear effects into large-scale response of transpiration to soil moisture conditions: they result in smaller spatially aggregated transpiration and lower water stress as compared to traditional representations that lump canopy properties.

To alleviate the constraints of commonly used heuristic one-dimensional approach for root water uptake in moisture-limited conditions, a novel formulation based on hydraulic representation of three-dimensional uptake process is designed. When mimicking soil drought at the scale of a single root system, the formulation demonstrates plants' ability to compensate the suppressed root water uptake in water-stressed regions by increasing uptake density in moister regions. Pilot, exploratory experimentation at the plot-scale demonstrates that transpiration and timing of water stress onset are sensitive to different representations of lateral spread. The simulation scenarios with a higher degree of root overlapping tend to exhibit smaller spatial heterogeneity of soil moisture and a later onset of plot-scale water stress. It is argued that detailed, hydraulics-based modeling of small-scale root water uptake can be used to guide improvements in the representation of drought effects in land-surface models.

Chapter 1 : Introduction and scope of the study

1.1 Background and motivation

1.1.1 Modeling resolution and fine-scale spatial heterogeneities

Current land surface models were developed as components of coupled land-atmosphere models to provide a partition of radiation and lower boundary conditions to atmosphere modules. For example, the NOAH-Oregon State University Land Surface Model (NOAH-OSU) (Ek et al., 2003) and the Simplified Simple Biosphere Model (SSiB) (Goward et al., 2002; Xue et al., 1991) were implemented in NCAR's climate models (e.g., WRF and Eta); the Land Ecosystem-Atmosphere Feedback model (LEAF) (Walko et al., 2000) was used as a submodel of Regional Atomspheric Modeling System (RAMS) which was further extended to an Ocean-Land-Atmosphere Model (OLAM) (Medvigy et al., 2008; Walko and Avissar, 2008). The spatial resolution of the land surface in these models is quite coarse and varies over an order of magnitude, for example, grid cells are in the order of ~10 km in regional models and ~100 km in global applications (Bonan et al., 2002; Chen et al., 2003; Dickinson et al., 2006; Hong et al., 2009; Winter et al., 2009; Zeng et al., 2002). These models usually group spatial heterogeneity within grid cells (e.g., soil moisture and vegetation) using a "*big-leaf*" or a "*mosaic*" approach, and treat the land surface as an aggregated patch with spatially uniform properties.

The coarse resolution of grid cells and overly simplified parameterization of the subgrid

land surface heterogeneity may lead to inaccurate predictions of larger-scale water and energy fluxes due to strong nonlinearity of land surface processes (Atchley and Maxwell, 2011; Avissar and Schmidt, 1998; El Maayar and Chen, 2006; Ershadi et al., 2013; Hu et al., 1999; Maxwell et al., 2007; Yates et al., 2003). As an example, Sridhar et al. (2003) investigated the impacts of the aggregation of spatially varying soil and vegetation properties at three different spatial scales (200 m, 2 km, and 20 km) on the simulated domain-scale energy fluxes (e.g., net radiation, latent heat, sensible heat, and ground heat flux). Modeling results based on the 20-km spatial resolution were shown to be 12% less in latent heat, 22% more in sensible heat, and 44% more in ground heat flux than results based on 2-km or 200-m spatial resolutions.

In particular, the aggregation of spatially varying soil moisture in a coarsely resolved grid may obscure the spatial extent of subgrid areas where soil moisture is limiting for plants and thus lead to an inaccurate prediction of grid-scale latent heat flux (Ronda et al., 2002; Sellers et al., 2007). For example, during dry intervals, when averaged soil water content over a large fraction of an area approaches the wilting point and transpiration become moisture-limited, wetter regions that are not stressed may exist because of vegetation variability, topographic shading, or regions of groundwater discharge. Lumping soil moisture over a coarsely resolved grid would theoretically lead to an underestimated grid-scale evapotranspiration. Overall, the impact of aggregating subgrid soil moisture variability on the predicted coarse-scale energy flux may depend on the grid cell size as well as time- and scale-dependent properties of soil moisture fields such as the mean and variance (Crow and Wood, 2002). For example, Crow and Wood (2002) shows that the impact of aggregating spatial heterogeneity of soil moisture from field-scale (~ 1 km^2) to regional-scale ($\sim 10^3$ km^2) on the regional-scale energy flux prediction is directly proportional to the variance of field-scale soil moisture and inversely proportional to the average standard deviation of the point-scale (~ 1 m^2) soil moisture variability in the field.

For a vegetated land surface, the spatial mean and variance of soil moisture can be

2

correlated with the spatial variability of vegetation biomass, as the canopy influences soil water content at very fine spatial scales through the processes of interception of precipitation and transpiration uptake of moisture. The canopy is characterized by a three-dimensional (3-D) structure of spatially varying attributes such as leaf density, leaf area index (LAI), leaf optical properties, tree heights and canopy gaps. The effects of spatially distributed LAI or reflective properties have been well recognized in studies of land surface models (Li and Avissar, 1994; Sellers et al., 1995). The aggregated latent heat simulated by considering sub-grid variable LAI could be either larger or smaller than the domain-scale latent heat simulated with spatially lumped LAI, depending on different vegetation types (El Maayar and Chen, 2006). The 3-D structure of canopies results in complex light regimes leading to different absorption of energy even when crowns have the same exposure to light (Chen et al., 2000; Deutschman et al., 1999; Knyazikhin et al., 1997; Song et al., 2009; Yang and Friedl, 2003). Further, within each crown, the partition of available energy into transpiration and sensible heat flux depends on nonlinear responses of leaf stomata and photosynthesis to moisture and light availability (Law et al., 2001; Pieruschka et al., 2010). Models that did not consider the spatially heterogeneous radiation environment might overestimate latent heat (Knyazikhin et al., 1997; Song et al., 2009).

Recently, a new generation of satellite missions and techniques is poised to provide hydrological data that will be needed for fine-resolution modeling (Clawges et al., 2007; Entekhabi et al., 2010; Lefsky et al., 2002; Vereecken et al., 2010). As a result, it has been argued that land surface models need to better represent the subgrid heterogeneity in finer spatial scales (e.g., finer than 100-1000 m) and adequately address critical water cycle science questions (Green et al., 2006; Wood et al., 2011).

Therefore, one of the main objectives of this PhD research is to explicitly represent fine-scale, spatially varying land surface characteristics to explore the degree to which the spatial

heterogeneity of vegetation and soil moisture is important for determining the domain-scale energy fluxes.

1.1.2 Disturbance of canopy structures and impact on temporal dynamics of soil moisture

As mentioned earlier, canopy structure in particular can profoundly influence soil water in a variety of ways, mainly through rainfall interception, moisture uptake during transpiration, and heterogeneous radiation environment that affects sub-canopy microclimate and evaporative drying of soil (Elliott et al., 1998; James et al., 2003; Leuning et al., 1994; Schrumpf et al., 2011; Vertessy et al., 2001).

Changes to canopy structure due to large-scale clearings or intermediate to small-scale disturbance events may lead to changes in statistical moments of soil moisture, such as the mean and the variance. Previous studies have shown that relatively large-scale clearings (at a scale larger than the size of a single tree crown) lead to a higher level of soil water content due to reduced interception and transpiration rates (Bruijnzeel, 2004; Schrumpf et al., 2011). Conversely, increased radiation levels due to sparser canopy may enhance soil evaporation and promote fast growth of secondary or understory vegetation, both of which can accelerate the depletion of soil moisture (Bhatti et al., 2000; Denslow et al., 1998; Giambelluca, 2002). Similar effects can be expected from changes in crown-scale canopy structure (Bohrer et al 2005), which may also be driven by intermediate disturbances. Common intermediate disturbance events include anthropogenic processes (e.g., selective logging and forest thinning), natural processes (e.g., species shifts due to regional climate change and invasive species, succession and growth), and species-specific pest infestations. Increased correlation between localized leaf area at a single-tree scale and turbulence can drive changes in surface fluxes that may also contribute to changes in soil water content (Bohrer et al., 2009).

A priori, the net outcome of these small-scale, canopy-structure-change driven processes is unclear: soil may become either wetter or drier under the disturbed tree crowns. As such intermediate disturbances usually extend over a very large spatial domain; their implications can

be far reaching: the changed soil water status can further influence vegetation dynamics, groundwater recharge, river flow, and regional climate (Hodnett and Bell, 1986; Rodriguez-Iturbe, 2000; Seneviratne et al., 2010). Understanding soil water dynamics under canopies undergoing a disturbance process is therefore essential for predicting the long term consequences.

Various models of water dynamics in forested environments require continuous, deep-profile soil moisture data for initialization and validation purposes (Bhatti et al., 2000; Koster and Suarez, 2003; Vereecken et al., 2008; Wilson et al., 2003). Soil moisture dynamics in the root zone are of particular interest in modeling studies of land-atmosphere interactions, as dry moisture levels may strongly constrain vegetation transpiration through root water uptake. Soil water content in the root zone or deeper layers is usually inferred through model-based or empirical extrapolations from information on surface soil moisture (within top 5 cm depth or less) provided by remote sensing techniques (Albergel et al., 2008; Bisselink et al., 2011; Calvet and Noilhan, 2000; Fernandez-Galvez et al., 2006; Ragab, 1995; Venkatesh et al., 2011). Monitoring soil water content at depths within and beyond the root zone is therefore necessary for accurate modeling efforts. Despite the need for temporally continuous and deep-profile soil moisture datasets, measurements in temperate forests have been mostly carried out either within shallow soil horizons (Hirano et al., 2003; Martin and Bolstad, 2005; Matamala and Schlesinger, 2000; Schmitt and Glaser, 2011; Schäfer et al., 2002), or at a coarse temporal resolution (Greco and Baldocchi, 1996; Wilson and Baldocchi, 2000). Only a few soil moisture datasets exist for temperate forests at a half-hourly temporal resolution, representing relatively soil profiles (e.g., 1 m deep, Drewitt et al., 2002; 0.61 m deep, Savage et al., 2009).

Consequently, another objective of this PhD research is to understand and evaluate the temporal dynamics of the soil water state in a temperate forest after a disturbance event that altered canopy structures over an area comparable to a size of tower footprint.

1.1.3 Representation of root water uptake process

The accuracy of transpiration simulated by the current generation of land-surface or ecohydrologic models can also be questioned due to the uncertainties in modeling root water uptake, and its sensitivity to plant-available water in the root zone (Desborough, 1997; Feddes et al., 2001; Lai et al., 2000; Zeng et al., 1998).

First of all, in majority of existing models, vegetation transpiration demands are distributed as sink terms in a one dimensional (1-D) Richards' soil-water accounting model according to a vertical profile of root density (Equation (1.1) and (1.2)) (Dickinson et al., 1993; Foley et al., 1996; Gerwitz and Page, 1974). As shown in Figure 1.1, the profile is typically an exponentially decaying function based on observed fine root biomass distribution in the vertical direction (Jackson et al., 1996). Rooting depth is conventionally determined using a 95% threshold of cumulative root biomass (Jackson et al., 1996). To describe water-limited situations, a heuristic "Feddes-type" water stress function is commonly used (Feddes et al., 1976). As shown in Equation (1.2) and Figure 1.2, actual transpiration is constrained by a moisture availability factor β, which is computed as the moisture availability factors at soil layers weighted by the profile of root density (Equation (1.3)and (1.4)) (Ivanov et al., 2008a; Oleson et al., 2004b):

$$\frac{\partial(SM_i)}{\partial t} = \frac{\partial}{\partial z}(K(SM_i) \cdot \frac{\partial}{\partial z}(H_i + z)) - Sink_i \tag{1.1}$$

$$Sink_i = T_{actual,i} = (T_{potential} * r_d) * \frac{\beta_i}{\beta} \tag{1.2}$$

$$\beta_i = \begin{cases} \max[0, \min(1, \frac{SM_i - SM_w}{SM^* - SM_w})], & if \quad T_{soil} > 273.15, \\ 0.01, & if \quad T_{soil} < 273.15. \end{cases} \tag{1.3}$$

$$\beta = \sum_{d=0}^{D_{root}} \beta_i * r_d \tag{1.4}$$

where SM_i is the estimated soil moisture at the i_{th} soil layer in a computational element; H_i is the soil water potential; $Sink_i$ is the sink term at the i_{th} soil layer; $T_{actual,i}$ is the actual transpiration or root water uptake at the i_{th} soil layer; $T_{potential}$ is the potential transpiration of vegetation; r_d is the fractional root biomass at each node with a depth of d [cm] in the subsurface mesh; D_{root} is the root zone depth; SM_i is the estimated soil moisture at the i_{th} node; SM_w [$m^3 m^{-3}$] is the wilting point; SM^* [$m^3 m^{-3}$] is the threshold soil moisture for stomatal closure; T_{soil} is the estimated averaged soil temperature in root zone. The values of SM_w and SM^* are provided in Table 1.
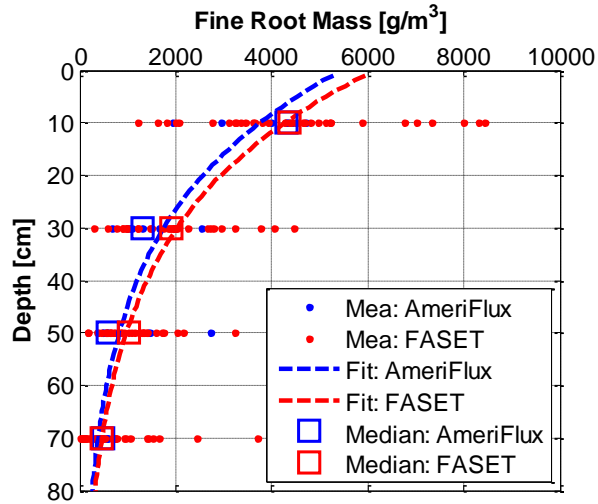
Figure 1.1. The measured fine root biomass at the University of Michigan Biological Station, the median values at each depth, and the fitted exponential lines relating biomass and depth for the AmeriFlux (He et al., 2013): $(Biomass \ [g/m^3] = 5478.8 * exp(-3.8 * z))$ and the FASET: $(Biomass \ [g/m^3] = 6172.2 * exp(-3.7 * z))$ footprints, where z is in [m].
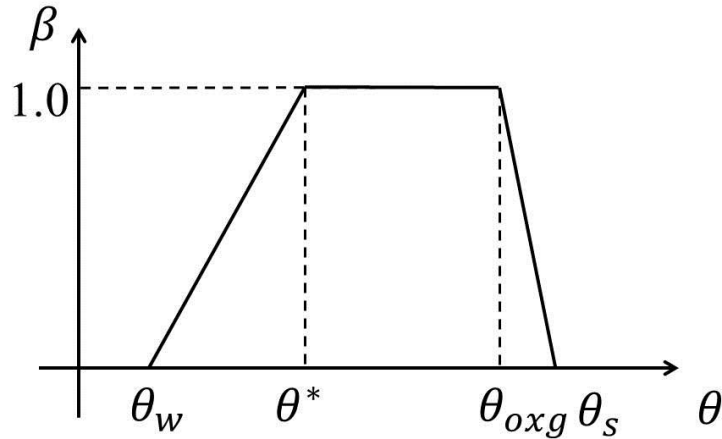
Figure 1.2. The "Feddes-type" water stress function (Feddes et al., 2001): when the soil moisture equals to θ_w (or SM_w, the wilting point) or θ_s (or SM_s, the saturation point), the β is set to zero due to wilting point and oxygen deficit; between θ^* (or SM^*, the water stress critical point) and θ_{oxg} (an oxygen critical point) water uptake is maximal (i.e., 1.0). If β<1, the plant root is water-stressed, and transpiration rate is decreased according to β.

This 1-D approach with the "Feddes-type" parameterization simplifies the actual physical process of three-dimensional root water uptake that takes place at various spatial and temporal scales. At the spatial scale of individual root and a temporal scale of minutes, the water flux is determined by the hydraulic gradient between soil and root xylem and hydraulic properties of the corresponding continuum. At the plant scale and a temporal scale of hours, xylem conductivity may exert a controlling effect on the flow rate at the root collar. At the ecosystem scale and a temporal scale of months or years, individual plants can compete for moisture in overlapping root zones, exerting a particular set of effects on soil moisture variability. These processes are interrelated through 3-D architecture of root systems and their spatio-temporal function (Doussan et al., 1999; Jackson et al., 2000a).

Detailed research on the 3-D root water uptake show that soil water fluxes "streamline" to roots and they are not purely horizontal or vertical (Figure 1.3), illustrating small scale adjustments of soil moisture field to hydraulic gradients due to transpirational pull that would not be captured by one-/two-dimensional approaches (Bruckler et al., 2004; Javaux et al., 2008). Modeling studies demonstrate that if the dimensions of root water uptake were reduced from three- to two- or one- dimensions, the spatial variation of flux density below the rooting zone would decrease, nonlinearly influencing drainage and streamflow (Vrugt et al., 2001a). In order to investigate the role of vegetation on soil moisture spatial variability, root water uptake should be represented in a three-dimensional soil water transfer model, which makes it possible to capture local-scale gradients developing around roots in different conditions of water availability (Doussan et al., 2006).
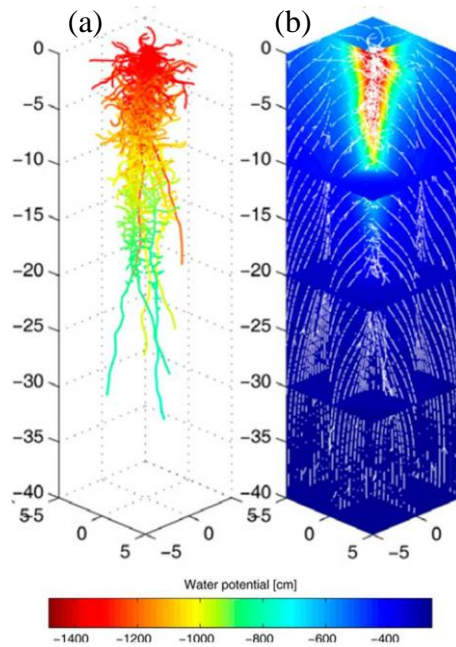
Figure 1.3. A simulated spatial distribution of (a) water potential within a root system and (b) soil water potential in a soil domain contains the root system. The white lines indicate the "streamline" of soil water flow into the root system (Javaux et al. 2008).

Furthermore, plants have been observed to change their root water uptake zones adaptively to meet transpiration demand even when some parts of roots are water stressed. They have the capacity to "compensate" the decreased root water uptake in water-stressed regions by increasing water uptake in moister regions (Garrigues et al., 2006; Guswa, 2005; Lai et al., 2000; Mahfouf et al., 1996; Sharp and Davies, 1985). As the "Feddes-type" water stress approach cannot capture physical processes involving the spatially-distributed and temporally-varying water fluxes from soil to structurally organized root systems (Adar et al., 1995; Draye et al., 2010; Jackson et al., 2000b; Plamboeck et al., 1999), it has been shown to lead to simulations where the soil control on transpiration sets in too early (Feddes et al., 2001).

Moreover, vegetation next to each other may compete for resources through overlapping root zones (Biondini, 2001; Caylor et al., 2006; Chakraborty and Li, 2009; Manoli et al., 2014). These complex processes may introduce spatially heterogeneous soil moisture and be extremely

important in an accurate prediction of energy fluxes on land surface. The current land surface schemes might have different spatial resolution (from a few meter to a few kilometers), but the overlapped root zone are usually not considered. A conceptual sketch comparing the root zone representation in the traditional scheme and a scheme with overlapped root zone is shown in Figure 1.4.
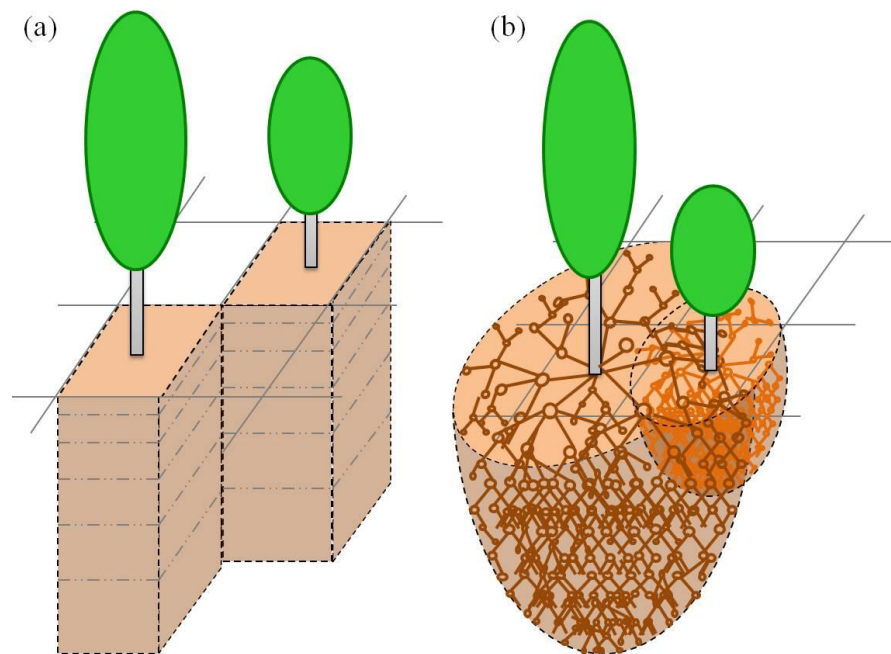
Figure 1.4. A conceptual sketch of root zone representations in: (a) commonly used one-dimensional approach that confines the root water uptake zones of trees within the dimension of the grid cell where the stem locates; (b) a three-dimensional approach that considers root water uptake zones that proportional to tree size and also the overlapped root zones.

The last objective of this PhD study, is to examine the hydrological significance of representing the 3-D microscopic root water uptake in a larger-scale application, and to explain the difference in domain-scale energy fluxes (if any) from this approach and that from the traditional 1-D "Feddes-type" approach.

1.2 Scope of doctoral research

1.2.1 Goals

In summary, the main goals of this doctoral research are to:

- Resolve fine-scale spatial heterogeneities associated with the vegetation transpiration and root water uptake process in land surface or ecohydrologic models, specifically the canopy biomass, radiative environment, soil moisture, and 3-D root architectures.

- Contribute to a better understanding of the nonlinear coupling modes between fine-scale soil moisture, canopy biomass or structure, and root water uptake processes, and their effects on the large-scale energy fluxes.

1.2.2 Dissertation outline

Chapter 2 examines the temporal dynamics of soil water content in a temperate forest located near the University of Michigan Biological Station. This forest consists of tree plots with canopy structures of varying degrees of heterogeneity that were induced by the species-specific, crown-scale disturbance of the canopy structure. To provide observational evidence of changes in hydrological dynamics, measurements of soil moisture were collected at four plots within the study site. Two of the plots represent undisturbed control sites; two other plots are located in the area with disturbed canopy crowns. The differences among these plots were explained through quantitative examination of physical processes, such as interception, evapotranspiration, and root water uptake. The analysis presented in the chapter gives insights on the impacts of crown-scale canopy structure on soil moisture in this temperate forest, and also provided a dataset for the following modeling efforts in Chapter 3 and Chapter 4.

Chapter 3 addresses the explicit representation of crown-scale spatially varying canopy

biomass, soil moisture, and radiative forcing in an ecohydrologic model tRIBS + VEGGIE. It examines how the simulated land surface dynamics can be affected when crown-scale variations are explicitly accounted for. Several simulation cases involving tree-scale variations in initial soil moisture, leaf area, and radiative forcing were designed. A *lumped* case representing the commonly used spatially-lumped representation was also simulated to infer the effects of coarse-scale aggregation. This chapter demonstrates the coupling mode between spatial canopy and soil moisture variations is sensitive to the wetness conditions. However, as the root water uptake processes in this chapter are still parameterized with the one-dimensional "Feddess-type" approach, it generates unreal water-constrained transpiration as compared to the empirical observation at the study site. This discrepancy between the numerical results and the observation has served as a motivation to further improve the modeled dynamics by representing the 3-D microscopic root water uptake (Chapter 4).

Chapter 4 investigates the effects of a hydraulic formulation of upscaling 3-D fine-scale root water uptake processes on plot-scale ($\sim 10^2$ m^2) energy fluxes. A microscopic root water uptake approach based on the "Couvreur" approach is incorporated into a 3-D Richard's equation solver PFLOTRAN. This chapter demonstrates the plant's capability to meet potential transpiration even if the shallow soil layers are dry by decreasing/increasing the fractional root water uptake at shallower/deeper layers. It attributes the differences of the plot-scale transpiration from the 3-D approach from that based on the traditional 1-D approach (e.g., the "Feddes-type" or soil water bucket concept). This chapter examines and explains the sensitivity of plot-scale water stress and spatial heterogeneity of soil moisture to different representations of 3-D root architectures and hydraulic strategy of trees (e.g., lateral spread, rooting depth, and hydraulic conductivity in root systems).

Chapter 5 summarizes key findings, discusses effects of assumptions, and proposes

directions for future research.

Chapter 2 : Temporal dynamics of soil moisture after crown-scale intermediate disturbance

of canopy

2.1 Introduction

In forested environments, canopy structure can profoundly influence soil water in a variety of ways, mainly through rainfall interception, moisture uptake for transpiration, and heterogeneous radiation environment that affects sub-canopy microclimate and evaporative drying of soil (Section 1.1.2). Widespread mortality of tree species (e.g., aspen and birch) is anticipated in the coming decades for temperate forests in the upper Great Lakes Region (Cole et al., 2002; Schier and Smith, 1979; Snetsinger and Ventura, 1990). This successional change may lead to significant, large-scale transient changes of tree-scale canopy structure. To simulate the anticipated large-scale succession process in the Upper Great Lakes area, an intermediate disturbance was prescribed at an experimental site at a northern temperate mixed forest near the University of Michigan Biological Station (UMBS) in year 2008 (Forest Accelerated Succession Experiment, FASET). Stems of all canopy-dominant, early successional aspen and birch trees near a flux tower were girdled. As a result of girdling, the treated canopy became patchy and more open as aspen and birch senesced, the gap fraction of canopy increased from year 2009 to 2011 (Hardiman et al., 2013). The resulting transient modes of spatially heterogeneous canopy may lead to changes in statistical moments (e.g., variance and co-variance) of spatially distributed transpiration and soil moisture. The effects of such changes on a larger-scale

hydrological cycle are currently poorly understood or projected.

The main objectives of this chapter are: (1) to understand and evaluate the change in magnitude and temporal dynamics of soil water under forest canopy undergoing a prescribed intermediate disturbance that simulates an accelerated succession process, as compared to an undisturbed canopy; (2) to explain the differences (if any) in soil water content and dynamics as influenced by the canopy change through a quantitative examination of physical processes, such as interception and evapotranspiration; and (3) to examine soil water dynamics at depths, and to describe a deep-profile soil moisture dataset available for modeling studies in a temperate forest.

2.2 Methods

2.2.1 Details of the studied forest

The studied temperate forest is located near the UMBS (Figure 2.1a, b) in Northern Michigan, U.S.A. (45.56° N, 84.71° W). This location is characterized by a northern hardwood forest, which represents a transitional zone between mid-latitude hardwood and boreal forests. The area is a gently sloping outwash plain at an elevation of ~300 m that varies over a range of ~20 m (Pressley et al., 2005). Soil texture is dominated by well-drained spodosols and contains 92% sand, 7% silt, and 1% clay. The soils tend to exhibit an ortstein layer at 50 cm, which is a cemented layer by amorphous metal and organic materials (Hall, 1986). Well drilling records for a location in the immediate vicinity of the AmeriFlux tower (~50 m distance) show that the water table depth is around 20 m (Tony Sutterley, personal communication, 2012/10). The mean annual rainfall is 817 mm, the average annual temperature is 5.5 °C, and the annual temperature cycle exhibits well-pronounced seasonality (Curtis et al., 2005).

Currently, the forest is dominated by aspen (*Populus grandidentata*) and birch (*Betula paprifera*), with understory of pine (*Pinus strobes, Pinus resinous*), red oak (*Quercus rubra*), and

maple (*Acer rubrum, Acer sacchrum*) (Bovard et al., 2005). Around the study location, aspen and oak contribute 69% of the above-ground biomass, and canopy reaches peak LAI of ~4.0 during summer periods (Curtis et al., 2005). The understory fern (*P. Aquilinum*) contributes an additional LAI of ~0.5 and shows similar phenological timing relative to the canopy-dominant tree species (Curtis et al., 2005). The thickness of surface leaf litter layer varies with moisture conditions. Generally, it is between a few millimeters to one centimeter, and could reach around two centimeters during extremely dry periods. The species composition at the UMBS forest is typical of nearly half of the forested area in the Upper Great Lakes region (Cleland et al., 2001; Frelich and Reich, 1995; Schier and Smith, 1979). As the UMBS forest was heavily logged in the late 19th century and further disturbed by fire until the early and mid 20th century, the individual overstory stands are 30 to 90 years old with an average age of 85 years (Gough et al., 2007b). This average age is older than that of other aspen-dominated, early successional forest stands in the upper Great Lakes region, where aspens are ~50 years old and in early-successional stages (USDA Forest Service, 2001). The UMBS area, therefore, provides an ideal setting for studying emerging ecosystem properties before the occurrence of widespread aspen mortality anticipated in the coming decades for the Great Lakes Region as part of the natural succession process from early to mid-successional stages (Sakai et al., 1985; Wright, 1964).
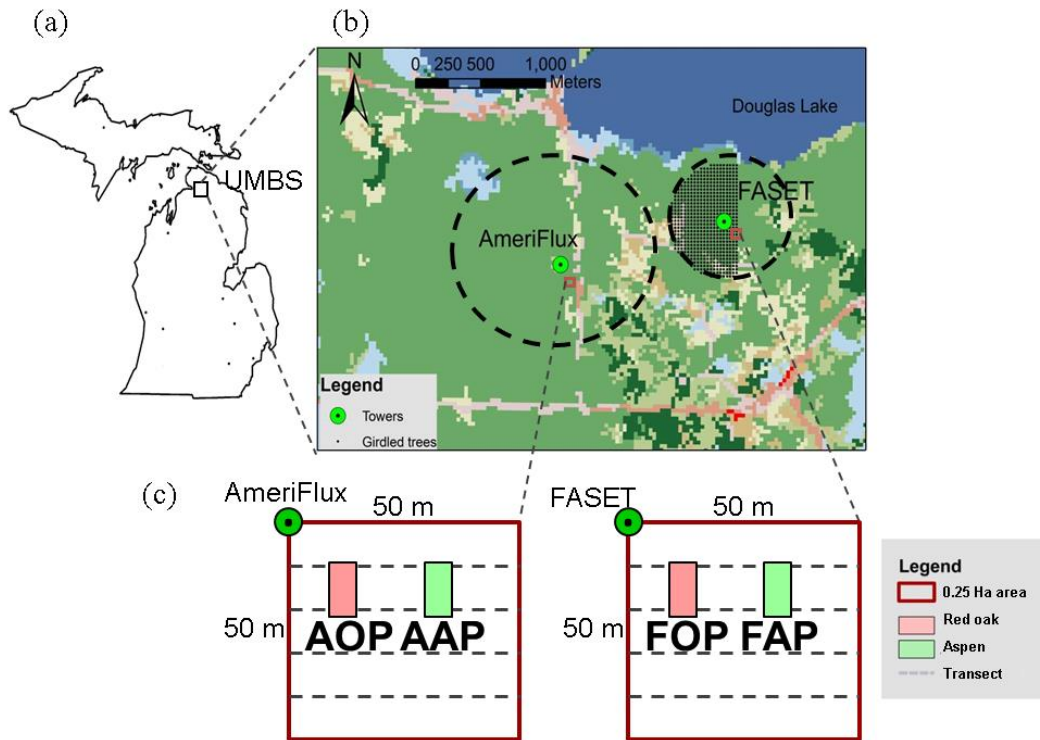
Figure 2.1. The locations of (a) the UMBS (the University of Michigan Biological Station); (b) the AmeriFlux and the FASET towers (filled circles), the AmeriFlux and the FASET sites (dashed circles), the forest area with girdled aspens (black dotted area), and the AmeriFlux and FASET 0.25 Ha areas (red boxes); and (c) the locations of soil plots inside the 0.25 Ha areas, where permanent soil moisture instruments over the 5-300 cm depth were deployed (AAP, AOP, FAP, and FOP), and six transects for the spatial soil moisture measurements (gray lines, including the top and the bottom transect lines that coincide with the red box outline).

19

2.2.2 AmeriFlux and FASET eddy-covariance sites

There are two flux towers near the UMBS. The UMBS AmeriFlux tower (AmeriFlux code: US-UMB) has been monitoring the meteorological conditions and net ecosystem CO_2 exchange since 1998 (Gough et al., 2007b; Gough et al., 2008; Schmid et al., 2000). The forest area within a radial distance of ~800 m from the AmeriFlux tower is hereafter referred to as the "AmeriFlux site".

The FASET eddy-flux tower (AmeriFlux code: US-UMd) was deployed in May of 2007. To accelerate the ongoing large-scale ecological succession experimentally, stems of all birch and aspen trees over 35 Ha around the FASET tower were girdled during Spring of 2008 (Nave et al., 2011). The girdling procedure affected ~7,000 trees. The girdling operation slowly kills trees, while preventing them from sprouting new shoots. From 2008 through 2009, the LAI reduction of girdled trees due to the loss of leaves was 29%. Later successional species however proliferated and, as a result, the total canopy LAI of species over the 35 Ha area is unchanged (Nave et al., 2011). Canopy of the girdled area is nonetheless patchier and exhibits a structure that has higher rugosity, i.e., it is more heterogeneous both vertically and horizontally (Hardiman et al., 2011), as compared to the control AmeriFlux site. The forest area within a radial distance of ~500 m from the FASET tower is hereafter referred to as the "FASET site".

Fine root biomass measurements were conducted in the AmeriFlux and FASET sites before 2006 (i.e., a pre-treatment period; the data are available at the UMBS ftp site: ftp://198.108.200.52). On average, 95% of the fine root biomass is concentrated within the top 80 cm of the soil column. This soil region is therefore defined here as the "root zone". The fine root biomass decays exponentially with depth (Figure 1.1). The fine root biomass of girdled trees is expected to decrease significantly within two years of the girdling operation (Edwards and Rosstodd, 1979).

2.2.3 Soil moisture measurements

Since April 2009, this study initiated continuous soil moisture and temperature measurements in four soil plots. Each site (AmeriFlux or FASET) contains two soil plots ~20 m apart under either aspen- or oak-dominated canopies. These plots are code named as FOP and FAP for FASET-oak plot and FASET-aspen plot, and AOP and AAP for AmeriFlux-oak plot and AmeriFlux-aspen plot (Figure 2.1c). Oak trees in both sites were not treated and therefore serve as the control species. The FAP plot exhibited the smallest LAI among the four plots because the girdled aspen dominates its canopy cover.

In each of the plots, a soil pit with a dimension of 1.5 m × 1.5 m × 3.0 m was dug in April 2009. Soil moisture/temperature probes (Hydra probe SDI-12, Stevens Water Monitoring Systems, Inc., Portland, U.S.A.) were permanently deployed at the depths of 5, 15, 30, 60, 100, 200, and 300 cm to monitor water content and temperature. Measurements were carried out at 10-min resolution. Three successive values were averaged and recorded; the produced soil moisture dataset therefore has a 30-min temporal resolution. For the first four depths, sensors were replicated on the opposite wall (~1.5 m apart) of each soil pit. After the sensor installation, soil pits were filled back with the original soil material, compacted to the nearly original bulk density, and re-covered with the leaf litter that was removed before digging of the pits.

Additionally, spatial soil moisture measurements were conducted in two 50 m x 50 m (0.25 Ha) areas (one in each site) at approximately monthly intervals during the 2010 and 2011 growing seasons (Section 2.2.5). These areas are referred to as the "AmeriFlux 0.25 Ha area" and the "FASET 0.25 Ha area" and contained the oak- and aspen-dominated plots in each site (Figure 2.1b, c). The spatial soil moisture data were collected in each 0.25 Ha area at 2-m intervals along six marked transects, using a "MiniTrase" system (Soil Moisture Equipment Corp., Santa Barbara, U.S.A.) with 40-cm long waveguides. The MiniTrase system was calibrated using

procedures described by Stangl et al. (2009) (Appendix 6.1, **Error! Reference source not found.**), gravimetric samples were collected to validate this calibration.

Figure 2.2. The setup of measurements at UMBS: the measurement of (a) soil moisture at multiple depths, and (b) under-canopy precipitation.

2.2.4 Soil moisture data preprocessing

Over a certain time period after the sensor deployment, the monitored soil system may not be representative of the actual field moisture conditions because of the persisting effect of disturbance caused by the sensor installation. The termination of such a period is difficult to assess without relevant reference data. Qualitatively, it can be associated with a large flux of water through the disturbed soil column that would "re-set" the system and contribute to compacting the soil to its original bulk density. In this study, the soil system was assumed to resume its natural state after a significant precipitation event of ~67 mm on August 15, 2009; the infiltrated volume of this rainfall was so large that water percolated through the entire 300 cm column within a few days. Data preceding this rain event were excluded from the following analyses.

During some of the dry interstorm periods, the soil moisture sensors (Hydra sensors)

recorded values only slightly larger than zero (~0.001[$m^3 \, m^{-3}$]). Since, theoretically, soil moisture cannot drop below the residual soil water content during the natural drying process, data obtained with these sensors were assumed to contain a systematic error. The value of the error was estimated through a "cross-calibration" procedure. The spatial mean moisture contents over the 0-40 cm depth range obtained during periodical spatial observations (Section 2.2.3) were used for the cross-calibration; they were compared with the averaged soil moisture over the same depth range derived from the pit measurements. Corresponding to each sampling date of the spatial measurements, 0-40 cm soil moisture profile in soil plots was derived through a linear interpolation of daily-averaged moisture contents observed at 5, 10, 30, and 60 cm depths with the Hydra sensors (the top 5 cm layer was assumed to have vertically uniform water content). The profiles were integrated over the 0-40 cm depth range and values at the AOP and AAP plots or the FOP and FAP plots were averaged and subsequently compared to the spatial mean of soil moisture obtained with the MiniTrase sensor over the corresponding 0.25 Ha areas (in the AmeriFlux or FASET sites). The values inferred from the plot profiles are smaller than the mean values from spatial measurements with the differences spanning a range of 0.02 to 0.05 [$m^3 \, m^{-3}$] (Figure 2.3). The median value of 0.03 [$m^3 \, m^{-3}$] was estimated as the systematic error. All soil moisture data recorded with the Hydra sensors were subsequently corrected by adding this estimate of systematic bias.

In order to eliminate sensor noise caused by a random error ($\pm$ 0.001 [$m^3 \, m^{-3}$]), the half-hourly soil moisture data were processed with a moving averaging window. The size of the moving averaging window is 10 hours, with 5-hour lead and lag periods. This 10-hour size was determined experimentally, a smaller size (e.g., 8 hours) was not able to smooth out all the "spikes" in the time series that caused by random errors. Since data for all plots went through the same procedure and this study mainly focuses on time- and depth-integrated metrics, the averaging procedure cannot appreciably affect the results of comparison among plots/sites.

Furthermore, replicated soil moisture observations at each depth of the top four locations were averaged. Infrequent spurious readings and data from periodically malfunctioned sensors were excluded from the analysis.
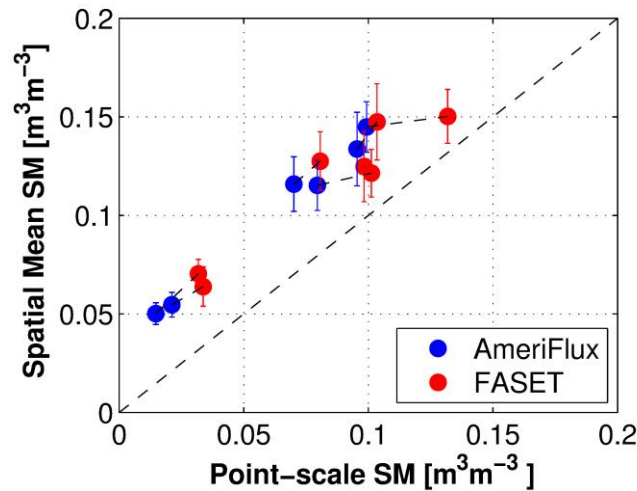
Figure 2.3. A comparison between the spatial mean soil moisture measured over the depth range of 0-40 cm along six sampling transects in the 0.25 Ha areas ("Spatial Mean SM", y-axis), and the derived 0-40 cm soil moisture inferred from the data from the four 5-300 cm soil columns for the same sampling dates corresponding ("Point-scale SM", x-axis). Observations during the 2010 and 2011 growing seasons were used. The error bars represent the spatial standard deviations of each daily set of measurements at each 0.25 Ha area. The black dashed lines connect the data points that correspond to measurements in each of the two 0.25 Ha areas on the same day.

2.2.5 Growing season identification

The soil water content varies mostly during growing seasons through strong interaction with vegetation and tends to stay constant during winters, due to snow cover and negligible root activities (Section 2.3.4). Therefore, this study has mainly focused on analyzing water dynamics in growing seasons, specifically during the years of 2009, 2010, and 2011. The growing seasons in the UMBS forest were identified using a criterion proposed by Schmid et al. (2003), i.e., as the time intervals during which the surface soil temperature was above 13 °C. We defined the timing

of the growing seasons in each year using soil temperature measurements at the 5 cm depth: Julian days 124-272 (148 days in total) in 2009, Julian days 121-281 (160 days) in 2010, and Julian days 132-273 (141 days) in 2011.

2.2.6 Above-canopy and understory precipitation measurements

Above-canopy precipitation was measured with tipping rain gauges installed near the top of the AmeriFlux (at 46 m; TE-525M, Texas Electronics, Inc., Dallas, U.S.A.) and the FASET (at 32 m; TB4, Hydrological Services Pty. Ltd., Warwick Farm, Australia) towers, and have been in operation since 1999 and June of 2010, respectively. Another precipitation data source is a weighing rain gauge (Rainfall Transmitter series 5915-6, Belfort Instrument Co., Baltimore, U.S.A.) located in an open field near the UMBS and has been in operation since 1979 (45.56° N, 84.68°W, NADP/NTN Monitoring Location MI09, data are available from: http://nadp.sws.uiuc.edu/); it is referred to hereafter as the "Reference Precipitation" as it is believed to be a more accurate data source because the data were collected and controlled by the UMBS staff on a daily basis. We found that the tipping gauges at the AmeriFlux and the FASET towers tend to underestimate the rainfall rate relative to the Reference Precipitation by ~15% and ~5%, respectively during the growing seasons of 2010-2011.

By August 2010, four optical precipitation sensors (Model 5.4103.20.041, Thies Clima GmbH., Göttingen, Germany) were deployed in the forest understory at 40 cm above ground at the locations of soil plots. The sensors were designed to continuously measure net precipitation reaching the ground. They had been calibrated in laboratory conditions, and the calibration procedures followed the methodology of Blanquies et al. (2003) (Appendix 6.2).

2.2.7 Quantification of canopy effects on interception, infiltration, evapotranspiration, and soil water storage

Since canopy structure and biomass can affect the subsurface soil water state through interception of rainfall, possible interception differences among the four plots were examined by comparing the measured understory net precipitation. Cumulative net precipitation measured at each plot was calculated starting on August 4, 2010 (i.e., the date of complete deployment of all under-canopy rainfall sensors) through the end of 2010 growing season and over the entire 2011growing season.

The monitored net rainfall data at the four plots may not truthfully represent the spatial mean condition of throughfall over a larger area. This is due to the small sampling area of optical sensor and local effects of canopy structure. In order to address the spatial variability of net precipitation in the understory and thus the representativeness of optical precipitation sensors, spatial throughfall rates were measured for six rainfall events during July-August of 2011. The cumulative rain-event depths varied from 2.5 mm to 9.6 mm. Twenty improvised rain gauges were constructed using empty containers and placed at random locations under dense or thin crowns before each forecasted rain event. The utilized containers were made of 1-liter plastic bottles topped with polypropylene funnels of 100 mm diameter. The bottles were attached to wooden dowels and raised 0.5 m above the ground to avoid "splash in" by rain drops hitting the ground. The volumes of rain water collected in the bottles were measured immediately after each rainfall event to prevent evaporative losses. Measurements were carried out in the AmeriFlux site only, no spatial throughfall measurements were conducted in the FASET site. The spatial mean throughfall at multiple locations at the AmeriFlux site was computed and compared with data obtained with optical rain sensors (as averaged values for the AOP and AAP plots). The comparison was carried for each of the six rain events when the spatial throughfall measurements

were conducted.

As another point-scale proxy of net precipitation, the amount of infiltrated water from the throughfall during a rainstorm period was approximated as an increase of soil water storage in the 0-300 cm column (ΔSWS_{0-300}). The magnitudes of ΔSWS_{0-300} associated with rain events were derived as the difference of soil water storage in the 0-300 cm layer (SWS_{0-300}) immediately after and before each rainfall event. The underlying assumptions are that during rainstorm periods transpiration, surface runoff, and drainage below the 300 cm depth were negligible. Specifically during rain hours, transpiration from vegetation and soil evaporation can be safely neglected due to small radiation input and humidity that is near saturation level. Surface runoff can be assumed negligible at all times; during 13 years of continuous observations at the flux station, surface runoff was never observed. Presumably, this is due to a high percentage of sand and high hydraulic conductivity of the soil (Kolb et al., 2002) that permit full infiltration even for largest events; in conditions of flat topography, episodic infiltration excess runoff is also retained locally by the surface leaf layer. Drainage below the depth of 300 cm can be also considered small because soil moisture contents at the 300 cm depth were generally very low (0.04-0.08 [$m^3\ m^{-3}$]) and exhibited little temporal fluctuation during growing seasons, thereby indicating that most of infiltrated water during these periods remained in shallow soil layers. An analysis of possible drainage rates was performed to support this assumption quantitatively (Appendix 6.3). The values of SWS_{0-300} were calculated by integrating the linearly interpolated vertical soil moisture profiles within the column, which were based on measurements at seven monitored depths. The top 5 cm soil was assumed to have a vertically uniform water content equal to moisture measured at the 5 cm depth. Because of this assumption, the calculated ΔSWS_{0-300} may not represent the true infiltrated water amount for light drizzles during which only a thin soil layer (< 5 cm) was wetted. The values of ΔSWS_{0-300} were therefore

calculated only for rain events with depths higher than a threshold value of 2 mm.

During interstorm periods, the soil moisture state is strongly affected by transpiration rate that is positively correlated to the amount of canopy biomass. Surface moisture also depends on soil evaporation rate, which is affected by shortwave radiative flux transmitted through the canopy. The amount of evapotranspiration during interstorm periods can be approximately quantified as the decrease of water storage over the 0-80 cm root zone, assuming that soil water percolation rate at the bottom of the root zone is negligible. Consequently, it was assumed that when soil moisture at the 80 cm depth was smaller than a threshold value of 0.08 [m^3 m^{-3}], the root zone bottom was dry and the percolation rate was small as compared to plant uptake and evaporative loss. Using this criterion, five relatively long interstorm periods for the 2009, 2010, and 2011 growing seasons were selected, during which light drizzles could have occurred but the magnitudes were small (less than 3 [$mm\ day^{-1}$], with an exception of the rain event of ~10 [$mm\ day^{-1}$] on July 8, 2010). For each interstorm period, the decreased root zone soil water storage at the four plots was estimated. The estimates were denoted as $-\Delta SWS_{0-80}$, i.e., as the negative differences of the root zone soil water storage at the end and start of the chosen periods. The cumulative values of $-\Delta SWS_{0-80}$ for each selected interstorm period were compared among the four plots.

2.2.8 Quantification of soil moisture dynamics at different depths

Temporal dynamics

Temporal characteristics of soil moisture dynamics vary with depths. The variation of water content at each depth was quantified through the Temporal Standard Deviation (*Tstd*); *Tstd* for each of the three growing seasons were averaged to represent the overall variability.

Root zone wetness distribution

As a convenient measure of wetness condition of any layer between the soil surface and a given depth d (in cm) located within the root zone, a Root-zone Relative Soil Wetness factor ($RRSW_d$) was introduced. It was calculated as:

$$RRSW_d = \overline{\theta}_{0-d} / \overline{\theta}_{0-80}, \quad 0 < d < 80 \quad cm. \tag{2.1}$$

where $\overline{\theta}_{0-d}$ is the mean water content in the soil layer between the surface and depth d estimated over the entire monitoring period, and $\overline{\theta}_{0-80}$ is the mean soil water content in the root zone.

Soil water uptake profile

The vertical profile of plant water uptake may or may not coincide with the root distribution, depending on water availability at different depths (Adar et al., 1995; Li et al., 2002; Plamboeck et al., 1999; Sharp and Davies, 1985). As the four plots in this study showed different relative soil wetness conditions with depth (see results Section 2.3.5), the need was to examine whether the root water uptake profiles among the plots would remain identical. Therefore, the relative magnitudes of soil water extracted by vegetation were examined for different soil layers within the root zone. Specifically, the root zone below the 10 cm depth was divided into seven 10-cm thick layers; moisture taken up by roots in each layer during rainless interstorm periods was quantified as a temporal decrease of soil water storage in that layer. The underlying assumption was that percolation flux could be assumed negligible, which is reasonable for dry soil, a definition that relied on the threshold soil water content of 0.08 [m^3 m^{-3}]. The top 10 cm layer was excluded from the analysis because the decrease of soil water storage near the surface can be strongly influenced by soil evaporation.

Rainless interstorm periods corresponding to relatively dry root zone conditions (i.e., the depth-averaged moisture content smaller than 0.08 [m^3 m^{-3}]) were selected within the 2009, 2010,

and 2011 growing seasons. Fifteen interstorm periods were chosen in total, with durations varying from 3 to 6 days. For each period, a fraction of water decrease in a 10-cm soil layer centered at d cm (ΔSWS_d) relative to the total water loss in the partial (i.e., the 10-80 cm interval only) root zone (ΔSWS_{10-80}) was calculated as:

$$PPW_d = \Delta SWS_d / \Delta SWS_{10-80} \tag{2.2}$$

The estimates of PPW_d for the selected interstorm periods were averaged, and the corresponding standard deviations were also calculated.

2.3 Results and discussions

2.3.1 Net precipitation differences

Canopy differences at the four plots resulted in different net precipitation volumes reaching the ground (Figure 2.4). The cumulative net precipitation at the FAP plot was 11%, 19% smaller (for growing seasons of 2010 and 2011, respectively) than at the FASET tower top, and 17%, 25% smaller (2010, 2011, respectively) than the cumulative Reference Precipitation. Cumulative net precipitation totals for the AAP, AOP, and FOP plots were ~31% smaller than cumulative precipitation at the FASET tower (above the canopy) for the 2010 vegetation season, indicating higher interception rates than in FAP. Overall, the value of 31% of intercepted precipitation in the undisturbed canopy plots signifies a very high fraction. Nonetheless, this value is still within a reasonable range, as similarly high interception magnitudes for dense forested environments have been previously reported (e.g., 32% of total rainfall by Schrumpf et al. (2011)). Cumulative net precipitation totals for the AAP, AOP, and FOP plots were similar to each other for the 2010 and 2011 growing seasons. An exception to this observation occurred during several rain events between June 20 and 24, 2011, which resulted in 102 mm of total

rainfall. During these five days, the difference of cumulative net precipitation between FOP and

AOP was as high as 19 mm, representing 72% of the total difference between the two sites for

the entire 2011 vegetation season.
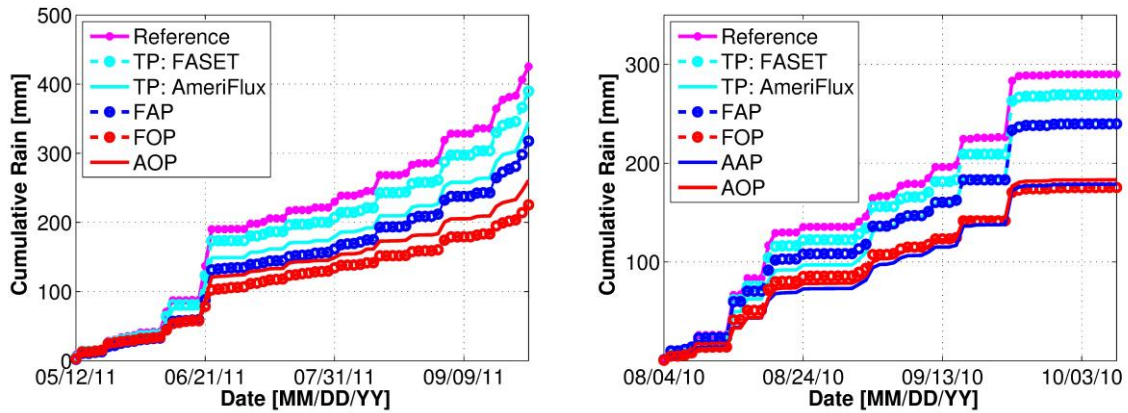
Figure 2.4. Cumulative precipitation for the second half of the growing season of 2010 (from August 4, 2010 through October 8, 2010; left panel) and complete growing season of 2011 (from May 12, 2011 through September 30, 2011 at two-day resolution; right panel) measured with the weighting rain gauge at the UMBS ("Reference"), the tipping rain gauges located at the two flux towers ("TP: FASET", "TP: AmeriFlux"), and the optical sensors at the four under-canopy plots ("FAP", "FOP", "AAP", and "AOP"). Data in AAP were not collected through 2011 due to technical difficulties.

For the six rain events when the spatial values of net precipitation were measured, the

mean collected throughfall was larger than net precipitation monitored with the under-canopy

optical sensors in the AOP or AAP plots. The differences ranged between 6% and 29%. Net

precipitation recorded with the under-canopy sensors at the AOP and AAP plots might therefore

be somewhat lower than the actual net precipitation in the AmeriFlux site. The mean throughfall

was smaller than the above-canopy precipitation measured at the AmeriFlux or the FASET

towers by 22% or 18%.

The monitored under-canopy net precipitation during the 2010 and 2011 growing seasons

agreed well with the ΔSWS_{0-300} estimated for the four plots. As an illustrative example, Figure

2.5 shows a comparison between net precipitation and computed ΔSWS_{0-300} for rainfall events

between August 4 and October 8, 2010. The plot under the girdled aspens, FAP, consistently exhibited the largest ΔSWS_{0-300} (on average, 14.4 mm per rain event), as compared to the estimates for the AAP, AOP, and FOP plots, with average values of 9.9 mm, 10.4 mm, and 10.2 mm per rain event, respectively.

2.3.2 Evapotranspiration differences

For all five long drying periods, the FAP plot had the lowest cumulative $-\Delta SWS_{0-80}$ among the four plots (Figure 2.6a, b, c, e, f), with the daily averaged rates of 1.95, 2.01, 1.60, 1.41, and 1.20 [$mm\ day^{-1}$] (Table 2). This implies that the FAP plot had the smallest evapotranspiration rate among the four monitoring plots. This is expected since girdled aspens at the FAP plot had a lower LAI that should lead to smaller transpiration rates, as compared to the other plots. Although the soil surface layer at the FAP plot received higher shortwave radiation flux, enhanced soil evaporation rates did not completely offset the decreased transpiration rates.
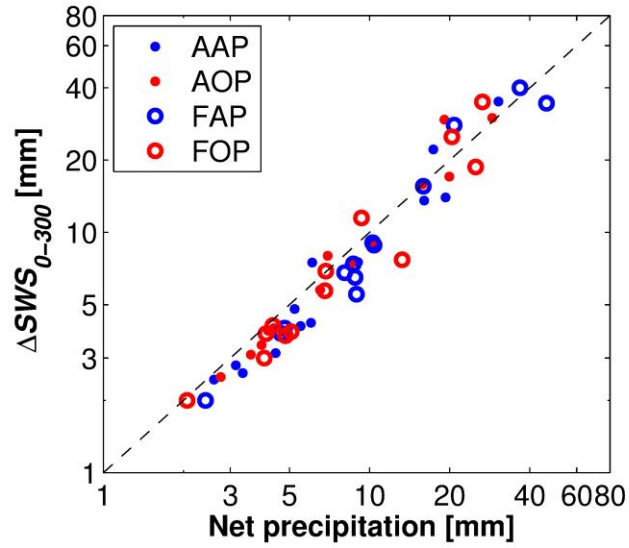
Figure 2.5. A comparison of net precipitation recorded with under-canopy rain sensors ("Net Precipitation") and the estimated values of the change in soil water storage over soil column during interstorm periods, ΔSWS_{0-300}. The estimates are based on the measured soil moisture profiles at the four plots for rainfall depths larger than 2 mm during the period of August 4 through October 8, 2010. The axes use logarithmic scale. The dashed black line indicates the 1:1 correspondence expected by a mass-balance approach.
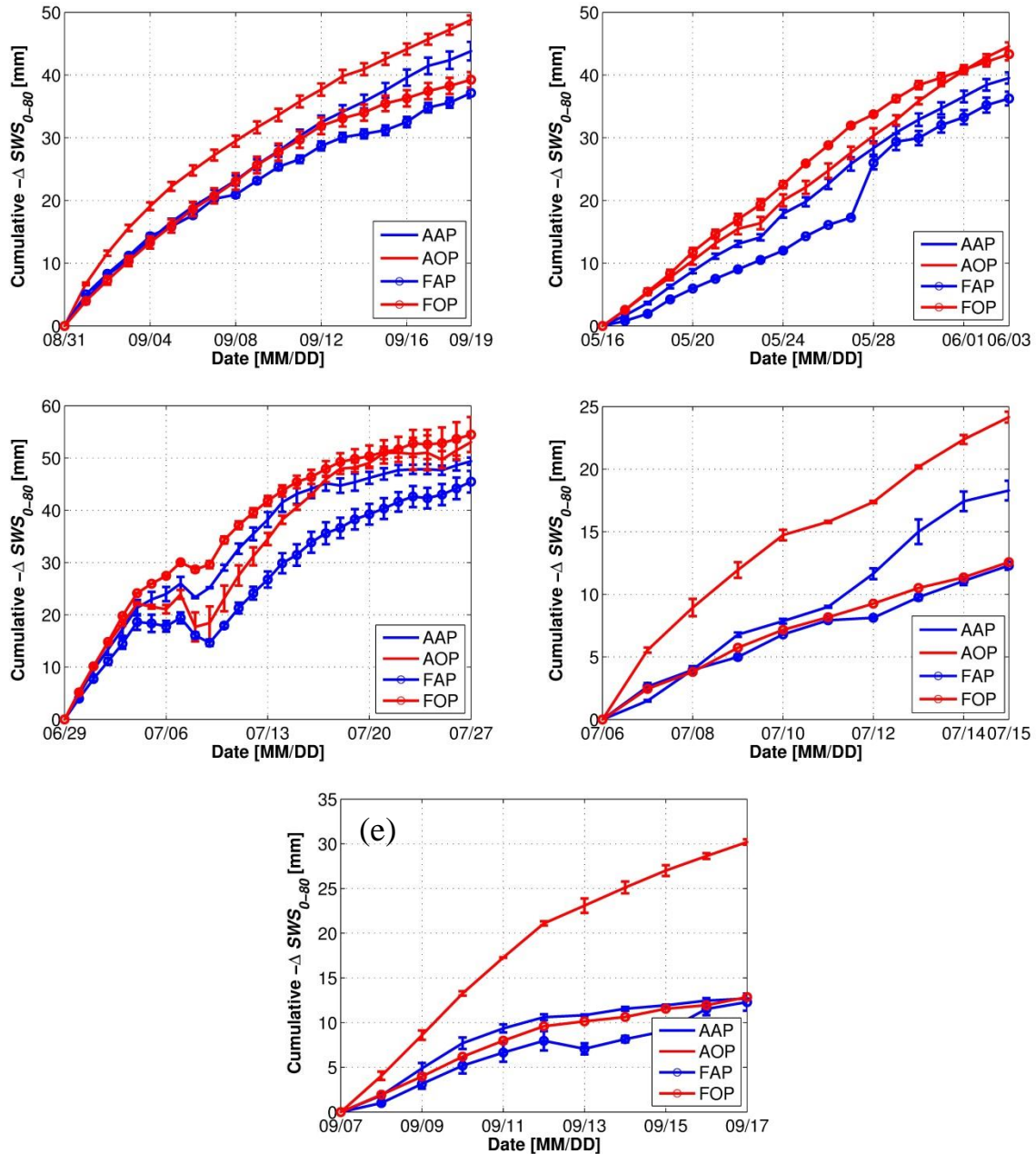
Figure 2.6. Cumulative decreases of 0-80 cm soil water storage ($-\Delta SWS_{0-80}$) in the four under-canopy plots during five interstorm periods: (a) August 31 through September 19, 2009; (b) May 16 through June 3, 2010; (c) June 29 through July 27, 2010; (d) July 6 through July 15, 2011; and (e) September 7 through September 17, 2011. The error bars indicate a range of calculated cumulative $-\Delta SWS_{0-80}$ by using data from sets of duplicated sensors (two sets at each site). The error bars for the FOP plot in (d) and (e) are not shown because one of the duplicated sensors at 15 cm depth malfunctioned.

2.3.3 Soil water storage dynamics

The FAP plot exhibited the wettest 0-300 cm soil column among the four plots throughout the entire analysis period (Figure 2.7). The largest discrepancy of SWS_{0-300} among the plots occurred between the AAP and the FAP plots. This discrepancy fluctuated with an overall increasing trend during the 2010 and 2011 vegetation seasons. Specifically, at the beginning of each growing season, SWS_{0-300} at FAP was larger than that at AAP by 63.0 mm or 65.3 mm; at the end of the growing season, it was 91.7 mm or 91.0 mm higher (2010 or 2011, respectively). The maximum discrepancy during the growing season was 120.1 mm or 134.7 mm (2010 or 2011, respectively). We measured a persistent difference of soil moisture content at 15 cm and 30 cm depths between the two plots. For example, when the 2010 growing season started, soil moisture at the 15 cm depth at AAP was lower than that at FAP by about 0.02 [$m^3\ m^{-3}$]; during this growing season the maximum difference reached 0.06 [$m^3\ m^{-3}$]. At the end of the 2010 growing season, as the shallower soil layers were replenished by precipitation, the difference of soil moisture content at the 15 cm depth between the two plots again reached about 0.02 [$m^3\ m^{-3}$]. This magnitude is far above the sensor error threshold (Section 2.2.4).

The fact that the differences in SWS_{0-300} among the plots persisted over the winter periods is either because 1) soil was not fully replenished to field capacity during the fall or snowmelt periods; or 2) the soil properties (e.g., the field capacity) at the four plots are different. Since the AOP and FOP plots, i.e., the control plots in the two sites, exhibited similar magnitudes and temporal dynamics of SWS_{0-300}, this suggests that a substantial difference of soil properties between the two sites is unlikely.

The inference that the soil state is wetter at the girdled plot is further supported by a comparison of mean spatial soil moisture (in the 0.25 Ha areas) within the two sites. The mean

value of 0-40 cm soil moisture observation at the FASET site was generally higher than that in the AmeriFlux site (Figure 2.3). This difference further indicates that the effect of increased incoming solar radiation at the forest floor did not offset the impact of reduced interception and transpiration on soil water moisture level.

2.3.4 Soil moisture temporal variability at depths

During winter periods after fall precipitation and a flush of "excess" water from shallow soil to deeper layers, soil moisture remained nearly constant at each depth mainly due to the presence of snow cover and dormant vegetation. During summer periods, soil moisture was more variable than during winter due to more frequent rain events and strong root water uptake. Significant dry-down periods could be observed during growing seasons. Soil moisture at 60 cm depth was relatively dry as compared to the locations above and below it, possibly because of the presence of ortstein layer near the 50 cm depth (Hall, 1986). Soil moisture below 100 cm was low and showed little temporal variation. Soil moisture at the 300 cm depth was extremely low and sometimes dropped to moisture contents near the residual point ($\sim$0.03 [$m^3\ m^{-3}$]) or below the detection limit of the sensors. The low soil moisture contents below the identified "average" rooting depth of 80 cm may be explained by deep extraction of moisture by oak (and other tree species) roots: deep extension of oak root systems is well known and fine roots at 1-5 m depths have been observed (Breda et al., 1995).

The temporal standard deviation of soil moisture averaged over the three growing seasons changes with depth and is within a range of 0.01 to 0.04 [$m^3\ m^{-3}$] (Figure 2.8). Beyond the 100 cm depth, the standard deviation of soil moisture at all four plots is very small (< 0.02 [$m^3\ m^{-3}$]). The decreased variability with depth is a combined result of dampened maximum moisture contents of infiltration fronts propagating through the soil column as well as reduced root water uptake.

Soil moisture at the 5 cm depth at the FAP plot exhibited the greatest temporal variation among the four plots. The larger variability of surface water content at this plot is likely associated with more intensive drying and wetting cycles as compared to the other plots. Specifically, the surface layer at the FAP plot was exposed to higher levels of radiation due to sparser canopy and thus larger soil evaporation rates have likely occurred; during rain hours, the plot also received less interception and thus larger net rainfall than the other plots.
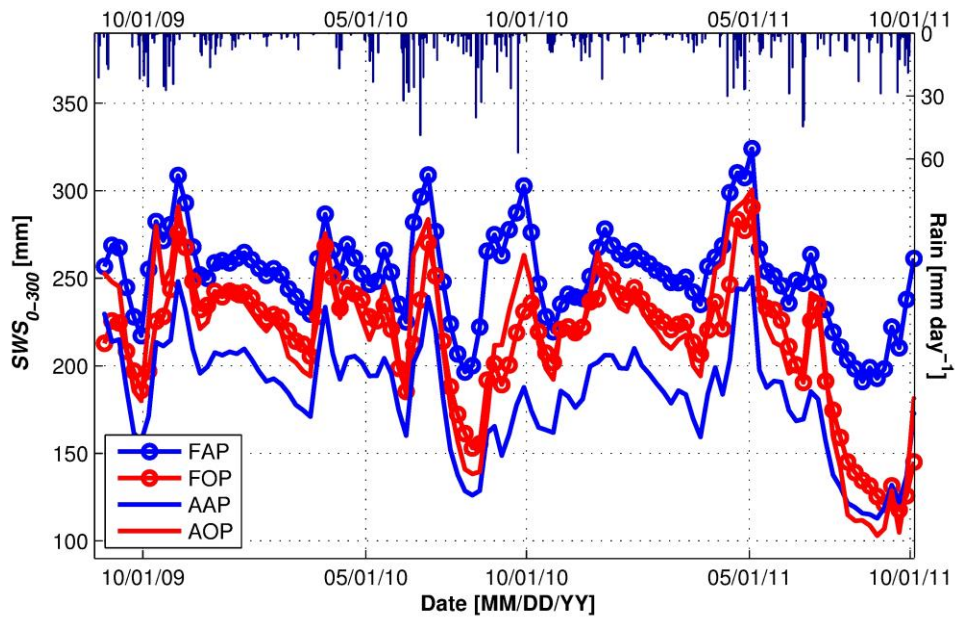
Figure 2.7. The time series of the 0-300 cm soil water storage (SWS_{0-300} $SWS_{0\text{-}300cm}$) at the four plots over the period of August 16, 2009 through October 1, 2011, resolved at the weekly time step. Blue bars at the plot top are the daily series of Reference Precipitation.
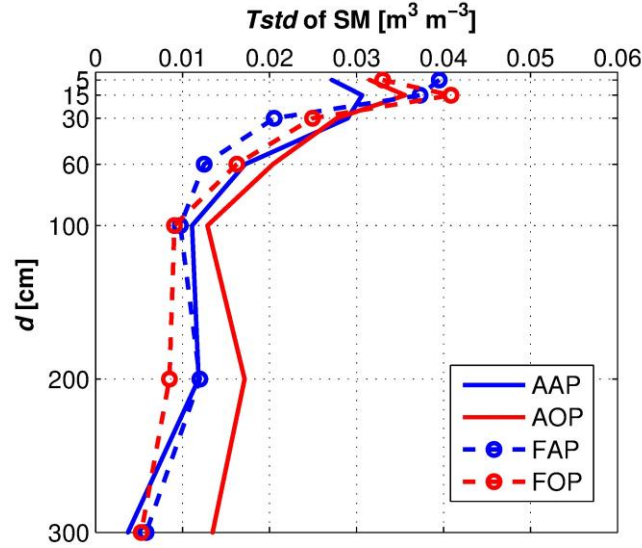
Figure 2.8. The mean seasonal temporal standard deviations (average over the 2009, 2010, and 2011 growing seasons), *Tstd,* of soil moisture at each observational depth (*d*) for the four under-canopy plots.

2.3.5 Root-zone wetness distribution

The estimates of Root-zone Relative Soil Wetness factor ($RRSW_d$) for soil layers at different depths are shown in Figure 2.9. The control plots (AOP and FOP) exhibited nearly uniform relative soil moisture distributions over the root zone, while the aspen plots (FAP and AAP) showed more heterogeneous profiles. In particular, FAP exhibited relatively wetter soil at shallow depths, and AAP showed relatively drier shallow layers and wetter deeper layers. Since the plots exhibit such differences, this might serve as an incentive for modeling efforts to consider statistical distributions of initialization soil moisture profile according to canopy-structure-specific conditions and account for the effects of increased vertical gradients under highly heterogeneous canopies with high rugosity (Hardman et al. 2011).
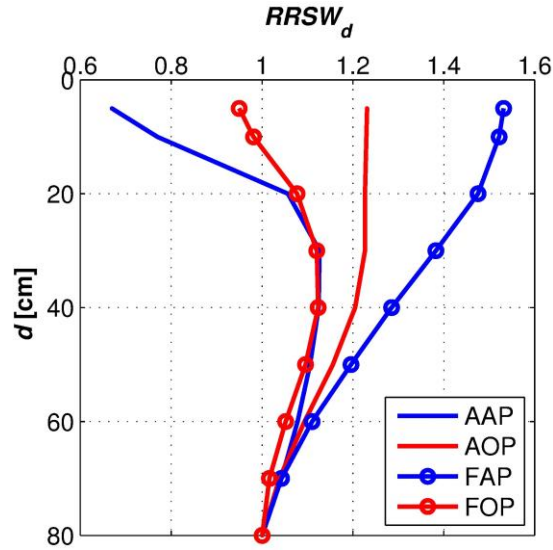
Figure 2.9. The Root-zone Relative Soil Wetness factor ($RRSW_d$) for 0-d cm soil layers in the root zone at the four plots.

2.3.6 Soil water uptake profiles

The averaged fractions of water withdrawal from each 10-cm layer within the 10-80 cm zone during the fifteen identified interstorm periods are shown in Figure 2.10; the standard deviations of PPW_d are shown as error bars for each depth. The obtained vertical profile for each plot is related to the root density profile in terms of its decay with depth; however, it does not assume an exponential form. At the FAP plot, 52% of water uptake in the root zone occurred in the top 10-30 cm layer. This value is higher than the fractions computed for other plots, which were approximately equal to 42%. The resulting implication that undisturbed trees extracted fractionally more water from deeper layers is consistent with the observed occurrence of very dry conditions in shallow soil layer at the monitored plots. As suggested by experimental studies (Doussan et al., 2006), root systems are capable of adjusting uptake zones to satisfy potential transpiration rate, i.e., when some roots are located in water-limited layers. On the other hand, the weakening root systems of girdled trees could not supply similar (as compared to the

undisturbed trees) amounts of soil water for transpiration, which reduced the overall role of the adjusting process in water loss at the disturbed plot. Concurrently, forest floor at the FAP plot received higher radiation and, expectedly, should have responded with higher fluxes of soil evaporation. This would have emphasized the relative role of shallow soil layers in water loss from the top 80 cm soil layer at the disturbed plot.
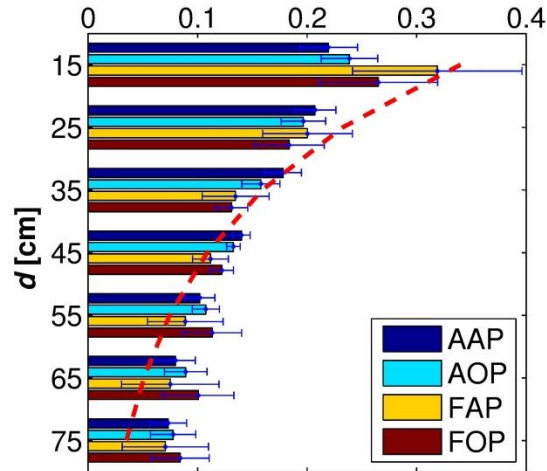
Figure 2.10. The colored bars represent fractions of water extracted from each 10-cm soil layer centered at a depth of d cm with respect to the water extracted from the partial root zone (PPW_d) at the four under-canopy plots. The error bars indicate the standard deviation of the PPW_d for fifteen interstorm periods. The red dashed line indicates a fractional root density profile in the 10 to 80 cm root zone.

2.3.7 Effects of heterogeneous canopy on variability of soil moisture

The spatial variability (as the spatial standard deviation) at the FASET site was larger than that at the AmeriFlux site (Figure 2.11). Additionally, the FASET site was generally wetter than the AmeriFlux footprint. At both sites, the spatial variability increased with the mean spatial soil moisture. The mean spatial soil moisture at two spatial scales (footprint-scale and the meter-scale in nested plots) was highly correlated with point-scale soil moisture. An linear relationships can be inferred between the spatial mean soil moisture and the point-scale soil moisture (Figure 2.3). This indicates that point-scale soil moisture can be used to infer spatial mean soil moisture without large errors in this particular forest environment.
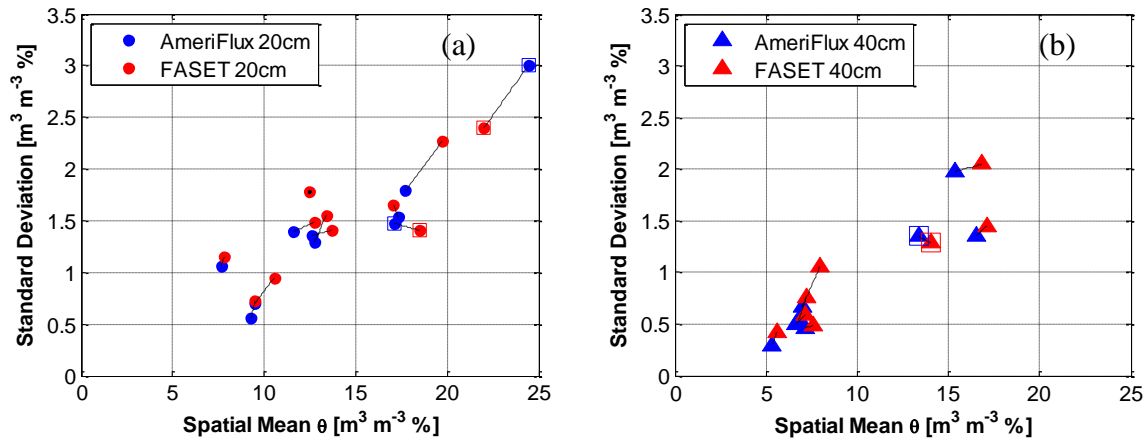
Figure 2.11. A relationship between the mean soil moisture and spatial standard deviation for soil depth of (a) 0~20 cm and (b) 0~40 cm in the plots located in footprints of the AmeriFlux and FASET towers. The dashed lines indicate the pairs of measurements at two footprints were conducted at the same time. Circles or triangles with a square outer boundary indicate measurements outside growing seasons.

2.4 Summary

Half-hourly, 3-m deep soil moisture measurements and throughfall data were collected under oak and aspen trees at an undisturbed control site and experimental site, where all early successional aspen and birch trees were girdled. The experiment represented a controlled

large-scale treatment that simulated a wide-spread, species-specific intermediate disturbance of a forest environment. Moisture storage in the 0-300 cm soil layer under disturbed aspens was higher than that under other undisturbed trees. While the plots under aspen trees (one in the disturbed site and the other in the control site) exhibited large differences in soil moisture, the plots under oak trees at both sites showed similar magnitudes of 0-300 cm soil water storage. This observation rejects the factor of substantial variation of soil properties between the two sites as a possible explanation of the indicated differences in soil water storage between the two aspen plots. It also indicates that the effects of the treatment are expressed at very small spatial scales, i.e., the effects are significant just under the girdled trees but not under neighboring un-girdled trees. This emphasizes the importance of representing disturbance processes at a high resolution and the difficulty of providing a site-level mean effect for intermediate disturbance processes that selectively affect individual trees, even when a large area is impacted.

The larger soil water storage under the girdled aspens was argued to be due to higher net precipitation and lower evapotranspiration. Specifically, the wetter state implies that the effects of decreased aspen canopy biomass (i.e., decreased interception and evapotranspiration) dominated the overall trend of soil water dynamics, despite the presumably enhanced interception and transpiration by understory species as well as increased soil evaporation.

Among the four plots, the plot under the girdled aspen exhibited the most significant temporal fluctuations of surface soil moisture. As argued, this is because the soil surface was exposed to higher shortwave radiation during interstorm periods and larger net precipitation during precipitation intervals. The disturbed plot also exhibited the highest vertical gradient of soil moisture distribution in the root zone, with a relatively wetter shallow soil layer. The root water uptake at the undisturbed aspen and oak plots appeared to have taken place at deeper layers, as compared to the girdled aspen plot where the soil moisture loss occurred predominantly from shallower layers. The latter effect is likely due to weakened root system and enhanced soil

evaporation at the disturbed plot.

A qualitative inference that follows from this chapter is that transient removal of major canopy species is likely to increase forest soil wetness and decrease its evapotranspiration; this can potentially lead to a higher recharge of groundwater systems. Depending on whether the rate of aspen mortality in the Great Lakes region will be high and the corresponding successional process will be co-occurring in space over large areas, the inference can have a regional implication.

The better understanding of the physical mechanisms controlling the fine-scale soil moisture and the datasets collected in this chapter provided insights and observational support for modeling studies described in Chapter 3 and Chapter 4.

Chapter 3 : Effects of fine-scale soil moisture and canopy heterogeneity on energy and water fluxes

3.1 Introduction

Vital land-surface characteristics such as soil moisture and canopy biomass exhibit a high degree of heterogeneity at different scales, resulting in spatially varying energy and water exchanges between the land-surface and the atmosphere (Anderson et al., 2003; Brunsell and Gillies, 2003; Raupach and Finnigan, 1995; Ryu and Famiglietti, 2006; Salmun and Molod, 2006). The current generation of land surface models considers spatial heterogeneity at a scale of a few kilometers and lumps characteristics of finer scales using the *"big-leaf"* or *"patch-mosaic"* schemes that represent surface cover as aggregated patches with uniform properties (Avissar and Pielke, 1989; Koster and Suarez, 1992; Sellers et al., 1996; Seth et al., 1994; Sridhar et al., 2003; Walko et al., 2000). However, the coarse grid/patch resolutions and simplified parameterizations of subgrid-scale heterogeneity may result in errors of the modeled mean water and energy fluxes due to the strong nonlinearity and fine-scale heterogeneity of land surface processes (Atchley and Maxwell, 2011; Avissar and Schmidt, 1998; Brunsell et al., 2011; El Maayar and Chen, 2006; Hu et al., 1999; Maxwell et al., 2007; Rowe, 1993; Sellers et al., 2007; Wood et al., 2011; Yates et al., 2003).

The main objective of this chapter is to explore the degree to which the spatial structure of vegetation characteristics is important for determining the magnitude and spatial variation of

soil moisture and evapotranspiration. It was hypothesized that fine-scale heterogeneous canopy interacts with spatially variable soil moisture and regulates domain-scale transpiration. The study addresses this hypothesis by (1) explicitly representing spatially varying vegetation biomass and soil moisture at a tree scale in a numerical model and; (2) examining the differences in the estimates of spatially integrated energy and water fluxes obtained with fine-scale representations vs. a commonly used spatially-lumped representation; and (3) presenting an approach to consider tree-scale heterogeneity of radiation and assessing its role in estimating domain-scale transpiration.

3.2 Observational data

3.2.1 Vegetation and root zone

The study location is the temperate mixed forest near the UMBS (details are in Section 2.2.1). The forest has a mean overall stand density of 1,012 [*stems ha^{-1}*], while the stand density for trees with the diameter at breast height (DBH) larger than 20 cm is 281 [*stems ha^{-1}*] (Garrity et al., 2012b). Field data collected at the UMBS forest (Gough et al., 2007a; Gough et al., 2008) shows the fine root biomass decays exponentially with depth and that 95% of the biomass is concentrated within the top 80 cm of the soil (Section 2.2.2). Yearly growing season start and end dates were determined following the methods of Schmid et al. (2003) (Section 2.2.5).

3.2.2 Meteorological data and energy fluxes

Meteorological variables and energy fluxes in the UMBS forest have been monitored at the AmeriFlux eddy-covariance tower since 1999 (Section 2.2.2), including wind speed, wind direction, frictional velocity, air and soil temperature, atmospheric pressure, water vapor pressure, downwelling and upwelling shortwave and longwave radiation, net radiation, photosynthetic

active radiation, latent, sensible, and ground heat fluxes. Meteorological data processing and analysis follows that used by Nave et al. (2011). Specifically, the latent heat was obtained by eddy covariance measurements of water vapor concentrations using closed-path infrared gas analyzers (LI-6262 and LI-7000, LI-COR Inc., Nebraska, U.S.A.). Precipitation is recorded with a Belfort weighing rain gauge (Section 2.2.6).

3.2.3 Soil moisture

Soils are dominated by well-drained spodosols (Section 2.2.1); and the soil properties were observed to be fairly uniform over the study site. Two well drilling records for a location in the immediate vicinity of the AmeriFlux tower show that the water table is at a depth of 20 m during middle of a growing season. Soil moisture data has been collected in two soil pits near the AmeriFlux tower with a half-hourly resolution since April 2009 (Section 2.2.3). Soil moisture probes were deployed at each of the following depths: 5, 15, 30, 60, 100, 200, and 300 cm. As further evidence of a deep water table, the observed volumetric moisture contents at 300 cm were smaller than 0.08 [$m^3\ m^{-3}$] or near the residual content (~0.04 [$m^3\ m^{-3}$]) over most of the period of observation.

Soil moisture has also been sampled within a 0.25 Ha area near the AmeriFlux tower along six 50-m long transects at 2-m intervals (He et al., 2012). These measurements represent averaged moisture contents over the top 20 cm layers. Data was collected at roughly monthly intervals during the 2010 growing season.

3.3 Model and simulation configuration

3.3.1 tRIBS + VEGGIE overview

The tRIBS + VEGGIE model is a spatially distributed, high-resolution, ecohydrological

model that represents the essential water and energy processes over a basin and links them to plant life regulatory processes (Ivanov et al., 2008a; Ivanov et al., 2008b). The model operates with the concept of Plant Functional Type (PFT), which allows combining of species with similar characteristics into the same groups. It is assumed that vegetated surfaces are composed of multiple PFTs that may differ in life form (e.g., tree, shrub, and grass), vegetation physiology (e.g., leaf optical and photosynthetic properties), and structural attributes (e.g., height, leaf dimension, or root profile). A single computation element may contain one PFT or multiple PFTs (e.g., patches of deciduous tree and evergreen tree). The model represents the spatio-temporal variability of key variables at fine scales (5 to 100 m), and resolves hydrologic processes at a high temporal resolution ranging from minutes to hours. Because of the model's flexibility and the capability of simulating detailed hydrologic processes, it has been applied to watersheds in various hydrological or vegetation settings (Flores et al., 2009; Ivanov et al., 2008b; Ivanov et al., 2010).

The processes represented in the tRIBS+VEGGIE model include (Figure 3.1):

1) **Interception**: Throughfall, drainage, storage, and evaporation depend on tree type and biomass.

2) **Transpiration and evaporation**: Two "big-leaves" (sunlit and shaded) represent a vegetation layer. Evapotranspiration flux is a sum of soil and canopy evaporation and transpiration. Explicit moisture distribution in the root zone is used to constrain transpiration and soil evaporation fluxes using a "Feddes-type" moisture availability factor.

3) **Surface energy balance**: Shortwave and longwave radiation are specified or computed using meteorological conditions, geographic location, time of year, and site aspect and slope. Canopy and understory latent and sensible, and ground heat fluxes.

4) **Infiltration**: Finite-element Richards' infiltration model with gravity-dominated lateral transfer is simulated in sloped and anisotropic soil. The root biomass distribution specifies fractional distribution of moisture sinks.

5) **Snow hydrology**: Full energy balance of snowpack (Rinehart et al., 2008).

6) **Groundwater**: The Boussinesq-type model under the Dupuit-Forchheimer approximation.

7) **Runoff**: Saturation and infiltration excess perched subsurface storm-flow, and groundwater.

8) **Overland/channel flow**: Dynamic wave of the Saint-Venant equations (Kim et al., 2011).

R   – precipitation
S_{atm} – shortwave radiation
μ   – direct beam type
Λ   – waveband interval
λE / H – latent/sensible heat
G   – ground heat
Q_{in} – subsurface influx
Q_{out} – subsurface outflux
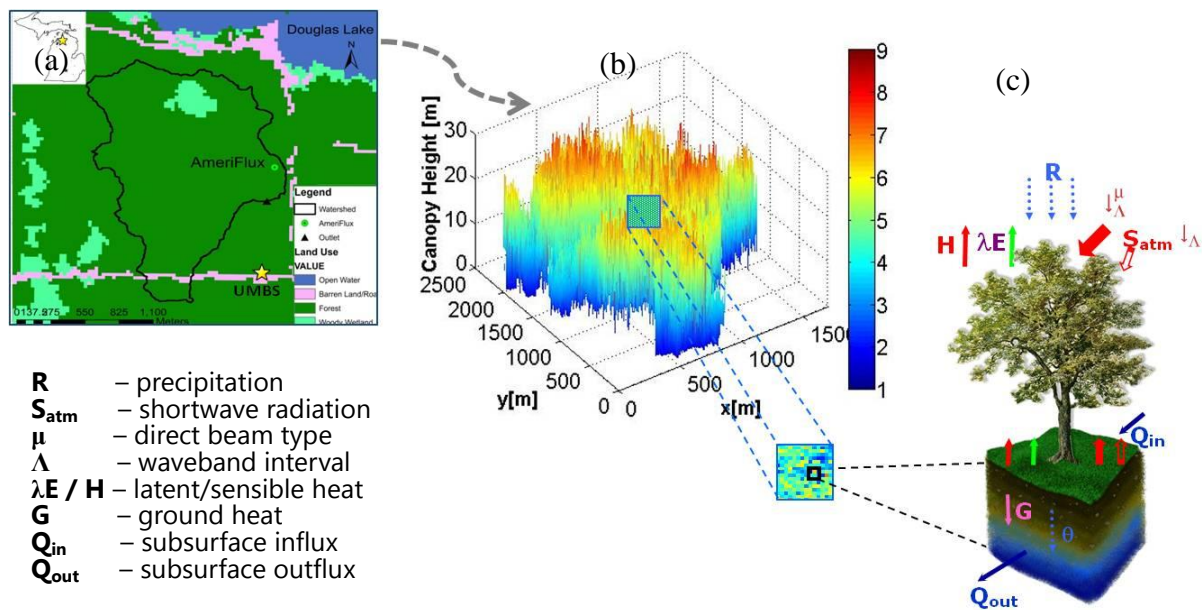
Figure 3.1. A schematic illustration of modeled processes in the tRIBS+VEGGIE model: (a) the simulation domain (He et al., 2011a; He et al., 2011b); (b) a fine-resolution canopy height dataset as modeling input; (c) energy and water transfer processes simulated within a grid cell.

In the original formulation of tRIBS+VEGGIE, spatial variations of shortwave radiation incident on a unit surface of vegetated area are introduced only in the presence of topography; this irradiance will be referred to as "above-canopy" radiation hereafter. The process of radiative transfer within the canopy (i.e., radiation absorption, reflection, and transmission) is simulated

with the two-stream approximation of Dickinson (1983) and Sellers (1985), which has been used in numerous studies (Bonan, 1996; Oleson et al., 2004b; Sellers et al., 1996). The absorbed radiation is partitioned to sunlit and shaded leaves, with separate treatment of stomatal conductance and assimilation rates but a single prognostic temperature (Ivanov et al., 2008a).

Heat fluxes are computed using the resistance analogy (Ivanov et al., 2008a). The resistances to heat transfer have the dimensions of inverse of velocity and are parameterized according to surface roughness characteristics (e.g., canopy structure and leaf dimensions), wind speed, and conditions of atmospheric stability (Ivanov et al., 2008a). Latent heat flux is estimated (Ivanov et al., 2010) with a formulation that couples models of photosynthesis (Farquhar et al., 1980) and stomatal aperture (Leuning, 1995). As an improvement to the original tRIBS + VEGGIE formulation, a new module simulating heat storage in plant biomass was developed and used in this study (Appendix 6.4).

The representation of vegetated surface is based on the concept of Plant Functional Type (PFT). A single computational element may contain a fraction of bare soil and multiple fractions of PFTs. The fractional areas of bare soil and vegetated patches in elements are used to weigh their relative contributions to the element-scale energy fluxes. Within a vegetation fraction, the actual transpiration rate could be constrained by the availability of root zone soil water. To quantify the departure of the actual flux from the climate-controlled potential value, a "Feddes-type" soil moisture availability factor (Bonan, 1996; Feddes et al., 1976) is used (Section 1.1.3).

3.3.2 Representation of simulation domain

Digital elevation model (DEM) and canopy height elevations for a 40 km^2 area including the UMBS forest site were obtained at a 1-m spatial resolution in a lidar campaign (Garrity et al., 2012b). These lidar datasets were subsequently resampled to 5 m $\times$ 5 m resolution using

ArcGIS (ArcGIS version 9.3.1, Redlands, California: Environmental Systems Research Institute, 2009). This resolution approximately corresponds to the scale of a mature tree crown.

Using the resampled 5 m $\times$ 5 m DEM grid, a watershed domain with an area of 2.12 km^2 (Figure 3.2) incorporating the location of the AmeriFlux tower was delineated. The total number of grid elements was 85,017. The simulation domain was confined to such a relatively small size due to the high computational costs associated with the large number of elements.

Figure 3.2. The location of the UMBS at Northern Michigan (blue box), the AmeriFlux tower (yellow star), and the delineated domain (white line).

A subsurface mesh with 25 nodes resolving the soil profile in the vertical direction to a depth of 1.88 m was used in each computational element. The mesh had a higher resolution near the surface and exhibited a coarser resolution at greater depths. For the initialization of spatially distributed soil moisture, several scenarios were constructed (Section 4.2.2).

The soil hydraulic parameters of van Genuchten (1980) were inferred with an inverse

estimation methodology of Hou and Rubin (2005). The time series of soil moisture monitored at multiple depths in one of the soil pits over the period of 3/11/2010-3/16/2010 was used. The derived parameter values are provided in Table 1.

Within each computational grid cell, energy and water dynamics were solved independently from the rest of the simulation domain. Spatial dependencies among grid cells were introduced through locally modified boundary conditions by considering subsurface moisture transfers and spatial effects of radiative forcing (i.e., shading or exposure, Section 3.4.3). These dependencies affected local dynamics via the coupled energy-water interactions.

3.3.3 Vegetation representation

Vegetation fractions (Section 3.4.1) were assigned to be equal to one in all of the elements of the simulation domain, and each computational element was assumed to contain a single canopy layer. At the resolution of 5 m x 5 m, this resulted in a stand density of 400 [*stems ha^-1*], which is a reasonable magnitude for this forest environment.

Spatial variations of canopy height and biomass among individual elements were explicitly represented using the lidar dataset of canopy heights resampled to 5 m x 5 m resolution. The mean and standard deviation of the height over the simulation domain were 12.9 m and 6.55 m. Several scenarios were constructed to test the effects of spatial variability of biomass. These scenarios are detailed in Section 4.2.1 and only general characteristics common to all of the scenarios are discussed here.

Canopy biomass characteristics were measured using a ground-based Portable Canopy Lidar (PCL) system for the 0.25 Ha area (Section 3.2.3) at a 1 m x 1m spatial resolution during the 2008 growing season (Hardiman et al., 2011). Within the 0.25 Ha area, vegetation area index (VAI) was calculated in each 1 m x 1 m grid cell as the ratio between the number of laser signal returns due to reflection from the crown surface and the sum of canopy and sky hits. The

PCL-measured VAI was converted to LAI by assuming that the mean VAI corresponds with the mean LAI and that VAI and LAI scale linearly (Hardiman et al., 2011). The obtained spatial dataset of LAI was resampled to a 5-m resolution. The resampled grid was characterized by the mean of 4.2 [m^2 m^{-2}], the standard deviation of 1.23 [m^2 m^{-2}], and the autocorrelation length of 1.16 m. These spatial statistics of canopy were further assumed to be representative for the entire watershed domain.

An exponentially decaying root profile with the maximum depth of 80 cm (He et al., 2012) was assigned to each of the elements. The profile was used to infer the distribution of relative density of moisture uptake (Ivanov et al., 2008a), which was also assumed to be identical for all computational elements.

3.3.4 Model forcing and evaluation data

The simulation time period corresponds to a representative subset of the 2010 growing season, starting on 06/07/2010 and ending on 8/23/2010. In total, there were 1990 simulation hours. For the same period, the hourly time series of meteorological variables from the monitoring network near/at the AmeriFlux tower provided model input, and measurements of energy and water fluxes and soil moisture provided data for evaluation of the model. Specifically, data collected with the Belfort weighing gauge were used as precipitation forcing. Wind speed, air temperature, atmospheric pressure, and water vapor pressure data measured at the AmeriFlux tower were used as other meteorological inputs. Further, the tRIBS+VEGGIE model requires four input shortwave radiation components: visible (VIS) direct, near infrared (NIR) direct, VIS diffuse, and NIR diffuse radiation. To partition the global solar radiation measured at the AmeriFlux tower at a height of 46 m into these components, their fractions were estimated with a sub-routine of an hourly weather generator AWE-GEN (Advanced Weather GENerator) detailed in Fatichi et al. (2011).

Observations of latent, sensible, and ground heat fluxes, as well as net radiation, outgoing shortwave radiation, and monitored soil moisture were used to evaluate the model performance. The measured ground heat flux at the 5 cm depth was corrected for the soil heat storage according to the calorimetric method of Fuchs and Tanner (1968), using soil temperature measured at a 2.5 cm depth. It should be noted that there was a slight imbalance in the energy closure: the sum of daily latent heat, sensible heat, and ground heat was smaller than the net radiation by about 12%. This could be explained by heterogeneity in soil heat flux that is not captured by our sensors, and by lateral advection of sensible heat and water vapor away from the flux tower.

3.4 Simulation design

3.4.1 The *lumped* case

In the spatially *lumped* simulation case, the domain was represented as a single 2 km^2 grid cell. The single vegetation layer was assigned the domain-scale mean canopy height of 12.9 m and mean LAI of 4.2 [m^2 m^{-2}]. It should be noted that in this *lumped* representation of the canopy, the numerical scheme partitions the canopy into sunlit and shaded fractions; however only a single canopy prognostic temperature is computed (Ivanov et al., 2008a). The soil moisture in the subsurface mesh nodes was initialized according to a soil moisture profile derived from the observation data (Section 3.3.3 and Section 3.4.2).

3.4.2 Spatial distribution scenarios

By using permutations of three LAI scenarios and three soil moisture scenarios, nine simulation cases were carried out in total and referred to hereafter by their hyphenated names. All nine simulation cases were first carried out using "above-canopy" radiation (Section 3.3.1),

i.e., without taking into account the local effects of crown light exposure and shading. These cases are referred to as the "*UNFRM*" simulation set. In the case when irradiance is modified according to local effects of crown light exposure/shading (Section 3.4.3), simulations are denoted as the "*HETER*". All of the simulation cases use the same parameter set provided in Table 1.

Leaf Area Index

Three scenarios of LAI spatial variability were constructed: "*UnfmLAI*", "*RgrsLAI*" (Figure 3.3a), and "*StatLAI*" (Figure 3.3b). Specifically, the *UnfmLAI* scenario was constructed using a spatially uniform value of LAI and canopy height as in the *lumped* representation; however, this scenario will include topographic information and allow permutations with spatially variable soil moisture. In the *RgrsLAI* scenario, the spatially-varying LAI was derived using canopy heights and an allometric equation relating biophysical properties of vegetation (Bohrer et al., 2007):

$$LAI_i = \max(0.1, (H_i - \overline{H})/\delta_H \times \delta_{LAI} + \overline{LAI}) ,$$
(3.1)

where LAI_i is the calculated LAI for an *i-th* element; H_i is the canopy height estimated for an *i-th* element (Section 3.3.3); $\overline{H}$, δ_{H}, $\overline{LAI}$, δ_{LAI} are the domain-scale mean canopy height, the spatial standard deviation of canopy height, the mean LAI, and the spatial standard deviation of LAI, respectively; and *max* is the maximum function operator. The result is a spatial field of LAI values that are perfectly correlated with the lidar-observed field of tree heights, and vary with the observed standard deviation of LAI.

For the *StatLAI* scenario, the LAI spatial distribution was generated with a virtual canopy generator *V-CaGe* (Bohrer et al., 2007), using the same LAI spatial mean and standard deviation as those used in the *RgrsLAI* scenario; the assumed spatial autocorrelation length of LAI was set equal to 1.16 m. Note that the *StatLAI* and *RgrsLAI* scenarios have the same spatial distributions

of canopy height but different distributions of LAI. While the *RgrsLAI* scenario has a unique relationship between canopy height and LAI, the two are "decoupled" in the *StatLAI* scenario.
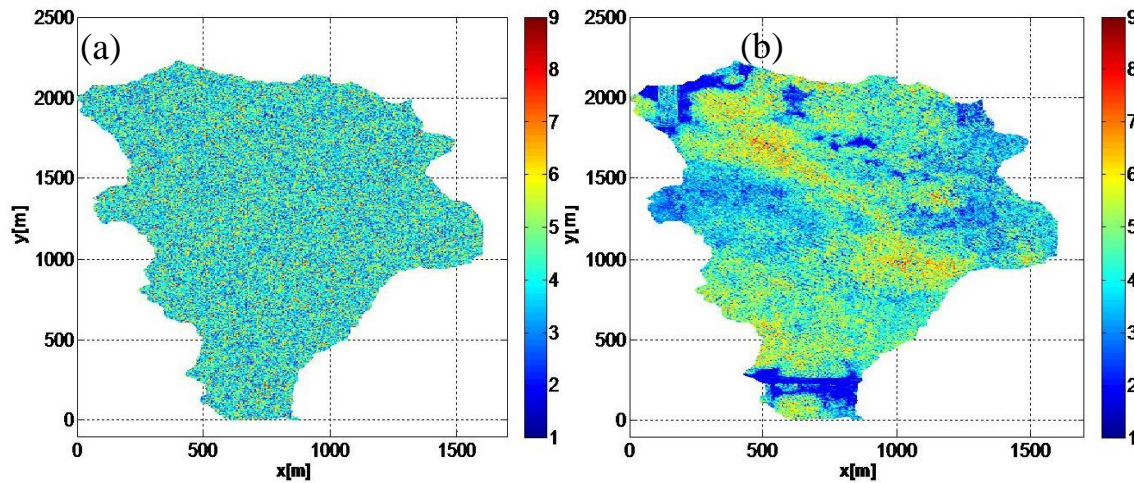
Figure 3.3. Generated scenarios for the spatial distributed LAI over the simulated domain: (a) the *RgrsLAI* scenario and (b) the *StatLAI* scenario. The color bar illustrates the value of LAI.

Initial soil moisture

Monthly spatial datasets of average moisture over the soil depths of the top 20 cm collected within the 0.25 Ha area (Section 3.2.3, measured in 2-m resolution) were resampled to grids at 5 m x 5 m resolution. The resampled grids were used to estimate the following statistics: a maximum spatial standard deviation of 0.025 [$m^3\ m^{-3}$] and an average autocorrelation length of 0.94 m. The statistics were obtained as a result of analysis of all resampled grids.

The observed moisture profile on the first day of the simulation period, i.e., 06/07/2010, was used as a reference in designing the spatial soil moisture scenarios. It was estimated by averaging observations at each monitoring depth at the two soil pits in the vicinity of the AmeriFlux tower. In order to map the observed profile to the subsurface computational mesh, the measured values were linearly interpolated to the depths of the mesh nodes. Soil moisture over the top 5 cm layer was assumed to be uniform and equal to the observed value at the 5 cm depth.

Three spatial scenarios of soil moisture initializations were generated: "*UnfmSM*",

"*RgrsSM*" (Figure 3.4a), and "*StatSM*" distributions (Figure 3.4b). For each scenario, the spatial distribution of moisture in the surface mesh node was first determined. Specifically, in the *UnfmSM* scenario, it was set uniformly to $\overline{SM_0}$ =0.135 [$m^3\ m^{-3}$] in all computational elements. In the *RgrsSM* scenario, surface soil moisture was assumed to be positively correlated to canopy height using a formulation analogous to Equation 3.1, in which $\overline{LAI}$ and δ_{LAI} were substituted with the spatially mean surface soil moisture $\overline{SM_0}$ [$m^3\ m^{-3}$] and the maximum observed standard deviation of spatial surface soil moisture δ_{SM} = 0.025 [$m^3\ m^{-3}$]. Note that, in real situations, tall trees are most likely to be associated with low soil moisture due to higher interception loss and larger amount of transpiration (as shown later in Section 3.5.2). The *RgrsSM* scenario, which has a positive relationship between canopy height and initial soil moisture, was intentionally developed to demonstrate the transformation process of the spatial distribution of soil moisture (Section 3.5.2). In the *StatSM* scenario, surface water content was generated with *V-CaGe* using the same values of domain-scale mean and standard deviation as in the *RgrsSM* scenario. The spatial autocorrelation length of soil moisture was set to 0.94 m.

Soil water contents in the subsurface mesh of each element were obtained by scaling the reference soil moisture profile. If the surface soil moisture was SM_0, soil moisture in a mesh node at a depth of *d* cm was calculated as follows:

$$SM_d = \max(0.04, SM_{d,ref} \times (SM_0 / \overline{SM_0}))\,, \tag{3.2}$$

where $SM_{d,ref}$ is the soil water content at depth *d* in the reference soil moisture profile.
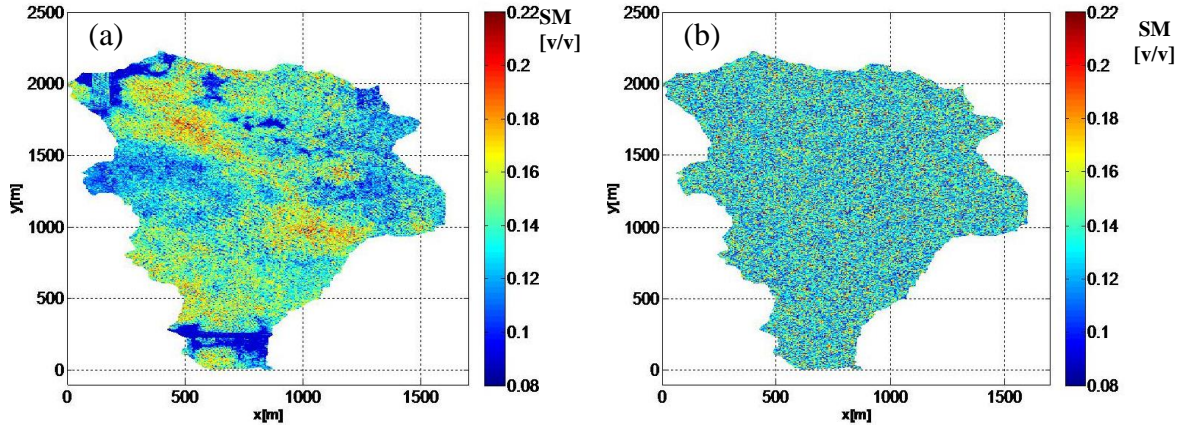
Figure 3.4. Scenarios of initialized spatially heterogeneous soil moisture: (a) *RgrsSM*, and (b) *StatSM*. The *RgrsSM* scenario is regressed from the spatially distributed *RgrsLAI*. The *StatSM* scenario is generated by the virtual generator V-CaGe. The spatial mean soil moisture is 0.1345 [v/v] and the standard deviation of soil moisture over the domain is 0.025 [v/v]. All the SM statistical properties were derived from the measured soil moisture datasets.

3.4.3 Crown effects on local radiative forcing

In a natural forest system, individual tree crowns of different height exhibit spatial variations in shortwave energy absorbed by canopy surfaces. For example, a shorter tree may receive relatively less radiation because it could be in a shade of taller surrounding trees. On the contrary, a tall tree may protrude through neighboring trees and receive higher radiation at an exposed side. As a conceptual analogy, forest canopy can be considered as a "topographic surface" and tree crowns could be either located in shaded regions, or exposed to the direct Sun's radiation. The apparent key difference with actual terrain topography is that canopy is not a solid medium; it is transparent to some fraction of radiation. The extent of the effects of shading or exposure on a given tree depends on its properties, such as height, canopy structure, and biomass density, as well as properties of crowns of surrounding trees.

To mechanistically introduce such tree-scale effects on radiative forcing, previous research used ray tracing techniques (Brunner, 1998; Govaerts and Verstraete, 1998; Kobayashi and Iwabuchi, 2008; Rowe, 1993). However, computational demands of such a method make it

prohibitive in applications with a large number of trees. This study has attempted to reproduce such tree-scale effects in a simplified, computationally efficient way. Specific details of the developed solution are provided in Appendix 6.5. Note that the domain-scale average of the spatially-variable, tree-scale radiative forcing was equal to the measured shortwave radiative flux incident on a unit horizontal surface. This ensured that no artificial radiative energy sources or sinks were generated.

3.5 Results

3.5.1 Model confirmation

The simulated energy fluxes from the *lumped* simulation case were evaluated against the measurements. The average diurnal cycles of the measured and simulated energy components are shown in Figure 3.6. As the measured energy components at the UMBS site were not balanced (Section 3.3.4) and particularly latent heat might be underestimated (Su et al., 2004), the model was parameterized in such a way that the simulated latent heat intentionally exceeded the observed values, and the other modeled energy components matched the measurements. The root mean square error (RMSE) of the hourly measured and simulated net radiation, outgoing shortwave, sensible heat, latent heat, and ground heat fluxes during rainless day-time periods (6am - 8pm) are 17.4, 4.8, 37.8, 96.3, and 14.1 [$W\ m^{-2}$], respectively. We excluded the observational data during rain hours or night time in the calculation of RMSE because i) eddy-covariance measurements are less reliable during such time periods, and ii) most significant energy exchange occurs during day-time hours. Note that the model was confirmed by using the *lumped* case rather than cases with scenarios of spatial heterogeneity, due to practical considerations of the iterative calibration process and computational time.
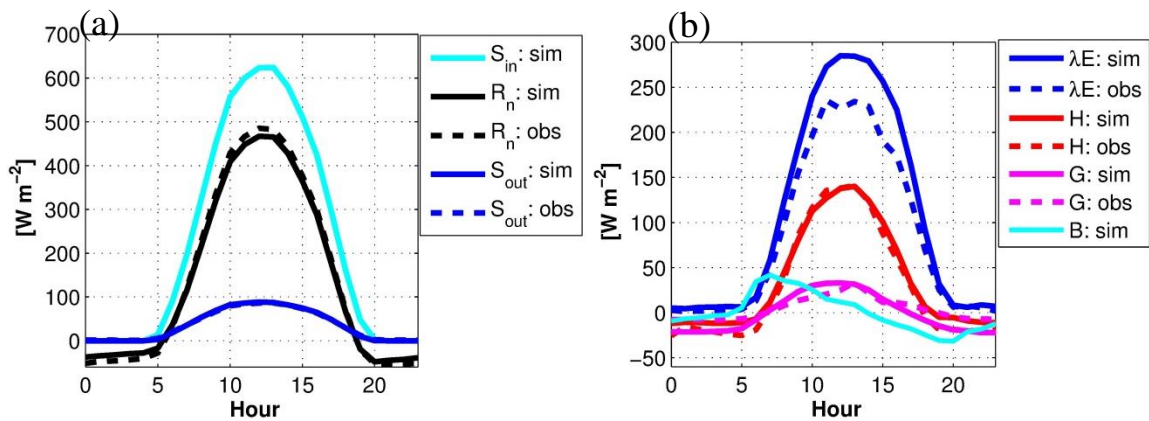
Figure 3.5. Average diurnal cycles of the observed ("obs") and simulated ("sim", from the *lumped* simulation case) energy components over the period of 06/07/2010 to 8/23/2010: (a) incoming shortwave radiation (S_{in}), net radiation (R_n), and outgoing shortwave radiation (S_{out}); (b) latent heat (λE), sensible heat (H), ground heat (G), and biomass storage (B) fluxes.

Simulated soil moisture was evaluated against observations at the monitoring depths. The simulated values are quite consistent with the measured water content to a depth of 30 cm (Figure 3.6). At the depths of 60 cm and 100 cm, the simulated soil moisture is slightly higher than the measured data. The difference with observations can be due to several reasons including a larger water uptake by deeper roots during interstorm periods. Also, the measured data exhibit a more rapid water flux through the soil column to deeper layers after precipitation events, resulting in earlier peaks of moisture content than what is generated with a model (e.g., a few days after August 15, 2010). The rapid percolation flux may be explained by the existence of macrospores, flow instabilities, or preferential flow paths near sensors. However, these phenomena could not be precisely quantified and were not considered in the model.
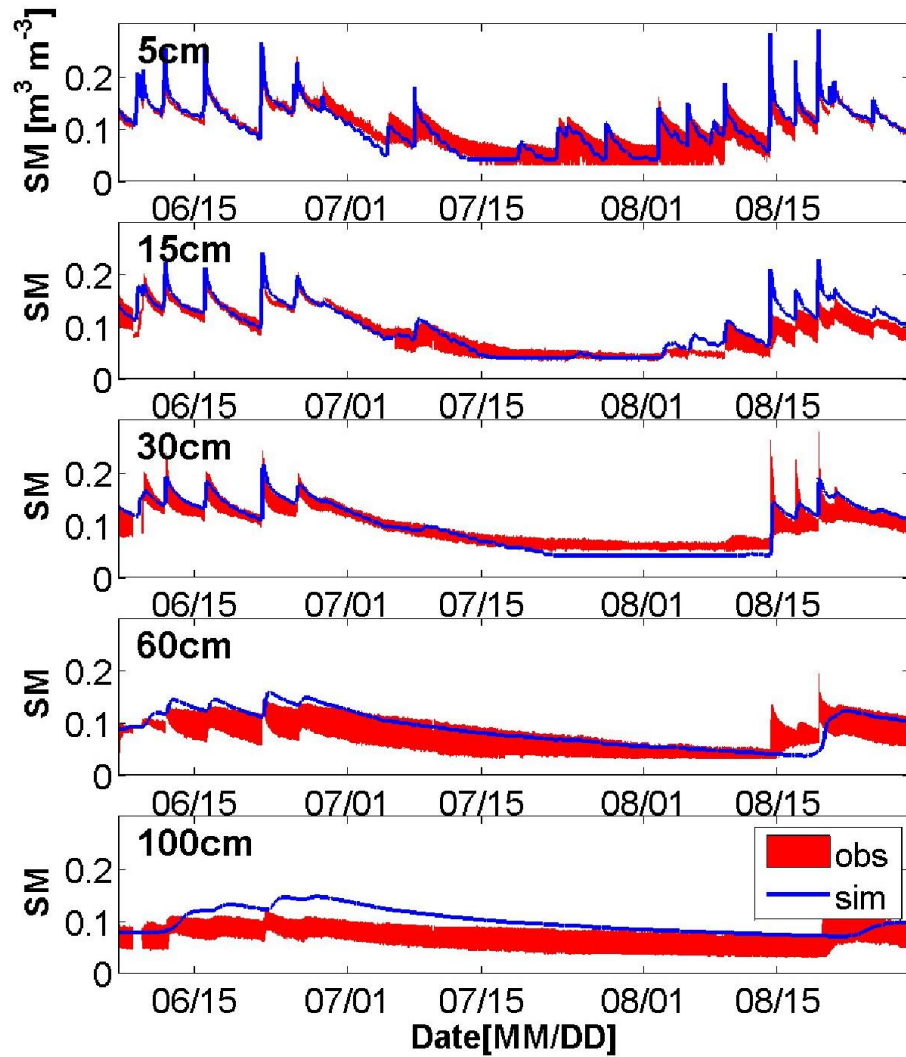
Figure 3.6. The observed ("obs", red region) and the simulated ("sim", blue lines, from the *lumped* simulation case) volumetric soil moisture (SM) at the depths of 5, 15, 30, 60, and 100 cm. The observed soil moisture at each depth is shown as a range that was determined based on maximum and minimum water contents measured by either four (at 5-60 cm) or two (at 100 cm) sensors in two soil pits near the AmeriFlux tower.

3.5.2 Simulation cases with spatially uniform radiative forcing (*UNFRM*)

Spatially averaged energy and water fluxes

With spatially uniform incoming radiation, the simulated hourly time series of domain-scale averaged transpiration rate (Figure 3.7a) and root zone soil moisture are nearly identical for all nine permutations of LAI and initial soil moisture and are similar to that of the *lumped* simulation case. The *UnfmLAI-UnfmSM* case exhibits only ~1% less of absorbed shortwave radiation, and ~1% less of net rain reaching the surface, as compared to the *lumped* case, because of minor effects of relatively flat topography. The differences are ~2.7% and ~1.3% larger latent and sensible heat fluxes from vegetation and ~4% less biomass storage, as compared to the *lumped* case.

The time series of domain-scale averaged Feddes-type soil moisture availability factor from the nine simulation cases and the *lumped* case are similar; their time series are shown in Figure 3.7b. When this heuristic factor is smaller than one, soil moisture is limiting and transpiration is "water-stressed"; otherwise transpiration is at the potential magnitude. As seen in Figure 3.7b, the domain has sufficient soil water at the beginning of the simulated time period ("water-ample" period, hours 0-804), and experiences prolonged soil water stress over the period of hours 805-1772 ("water-stressed" period); the soil moisture becomes sufficient again over the time period of hours 1773-1990 ("water-ample" period).
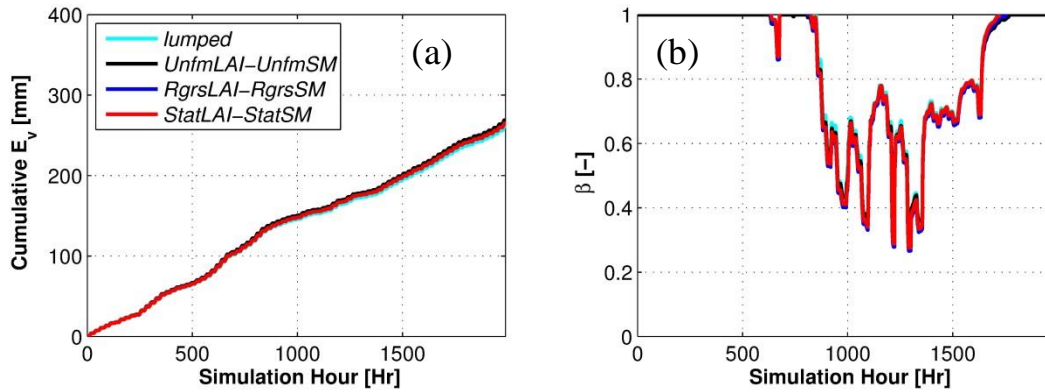
Figure 3.7. The times series of the domain-averaged cumulative transpiration (E_v) and soil moisture availability factor (β) for the *lumped*, *UnfmLAI-UnfmSM*, *RgrsLAI-RgrsSM*, and *StatLAI-StatSM* simulation cases corresponding to *UNFRM* radiative forcing. Domain-averaged results from all nine permutation cases are nearly identical; the results from only three of the nine cases are shown as an example.

Relationships between LAI, transpiration, and soil moisture

The effects of spatially variable canopy biomass on the spatial states and fluxes of the forest system are studied by examining the results from simulation cases using all three LAI scenarios and a single scenario of moisture initialization (specifically, the *UnfmSM* scenario). Three characteristic simulation hours were identified: hour 588, 1332, and 1884. These hours respectively represent the state of the system during a water-ample period, a water-stressed, and another consequent water-ample period; the latter, in consequence of a rainfall event (Section 3.5.2). For each of the three hours, scatter plots among different variables are shown in Figure 3.8.

For the *RgrsLAI-UnfmSM* simulation case (Figure 3.8a), the plotted relationships change with time. At hour 588, transpiration rate is positively related to LAI and net radiation. Soil moisture is negatively correlated with LAI, as locations with higher canopy biomass have extracted more soil water for transpiration and therefore the soil has dried relatively quicker. At hour 1332, transpiration is "insensitive" to net radiation and slightly negatively correlated with

LAI. Transpiration is simulated as limited by the root zone soil water availability with a domain-average β of 0.39. Locations with higher LAI now exhibit higher water stress due to a more rapid prior water depletion, i.e., stress has built up due to memory of the soil water reservoir. The higher water stress at this hour leads to a relatively lower transpiration rate. By hour 1884, the soil water reservoir has been replenished by several rain events and transpiration is now again positively related to net radiation.

For the *StatLAI-UnfmSM* simulation case (Figure 3.8b), the relationships among the same variables exhibit a noisier pattern as compared to the *RgrsLAI-UnfmSM* case. This is because the former simulation case includes a "decoupled" relationship between the spatial distribution of canopy biomass and canopy height, i.e., elements with the same LAI may have different crown heights. This leads to different aerodynamic resistances above and within canopy, boundary layer and stomatal resistances and thus varying transpiration rates and soil moisture.

The simulation results of the *UnfmLAI-UnfmSM* case are shown as red dots in Figure 3.8a, for a relative comparison. In the *UnfmLAI-UnfmSM* case, all elements have a LAI of 4.2 [m^2 m^{-2}], but some of them experience terrain effects of incoming shortwave, which results in a non-zero variability of net radiation, transpiration rates, and soil moisture.
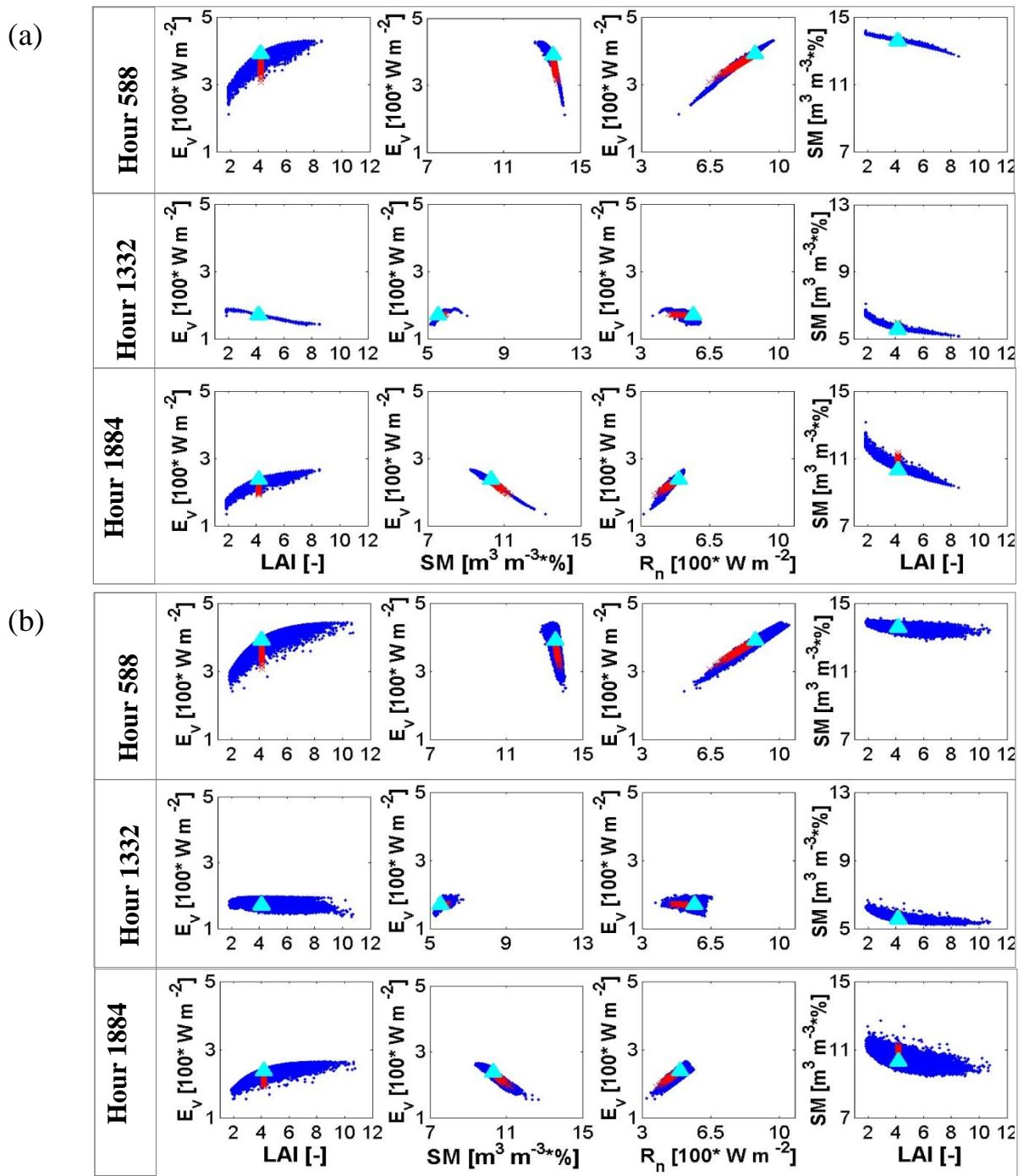
Figure 3.8. Relationships among spatially distributed LAI, transpiration (Ev), net radiation (Rn), root zone soil moisture (SM) at hour 588, 1332, and 1884 for: (a) the RgrsLAI-UnfmSM (blue points), (b) the StatLAI-UnfmSM (blue points) simulation cases. The red dots correspond to the UnfmLAI-UnfmSM case and the cyan triangle shows the uniform result from the "lumped" case.

Initialization effect on spatial dynamics of soil water

The effect of moisture initialization is studied by examining the simulated dynamics of spatial variability of soil water. The results from the three simulation cases used a specific distribution of initial soil moisture (*UnfmSM*, *RgrsSM*, and *StatSM*) but the same canopy scenario (the *RgrsLAI* scenario). In all cases, the imposed spatial initialization of soil moisture undergoes a substantial transformation, but for all scenarios the final distribution becomes inversely related to the spatial distribution of LAI. Figure 3.10 illustrates this graphically. As seen, the *RgrsSM* initialization (positively correlated with LAI) and the *StatSM* initialization (random) are transformed by a wetting phase at hour 228 that tends to wipe out the spatial heterogeneity of the root zone soil moisture. About ten days later (hour 468), the spatial distributions of root zone soil moisture in both simulation cases evolve to a spatial pattern that is negatively related to spatial variability of LAI.

For the purpose of examining the temporal dynamics of the transformation of spatial soil moisture as showed in Section 3.5.2, instantaneous spatial distributions of soil moisture are quantified with empirically estimated Shannon Information Entropy (Shannon and Weaver, 1964):

$$\widetilde{\theta}_i = (\theta_i - \theta_{\min})/(\theta_{\max} - \theta_{\min}), \tag{3.3}$$

$$H(\widetilde{\theta}) = -\sum_{k=1}^{50} p_k(\widetilde{\theta})\ln(p_k(\widetilde{\theta})), \tag{3.4}$$

where θ_i [$m^3\ m^{-3}$] is the volumetric root zone soil moisture in an *i-th* element; $\theta_{\min}$ [$m^3\ m^{-3}$] and $\theta_{\max}$ [$m^3\ m^{-3}$] are minimum and maximum root zone moisture contents that were simulated in all simulation cases (0.05 [$m^3\ m^{-3}$] and 0.22 [$m^3\ m^{-3}$], respectively); $\widetilde{\theta}_i$ [-] is the element-scale effective root zone saturation (varies between 0 and 1); $p_k(\widetilde{\theta})$ [-] is an empirical representation

of the Probability Distribution Function (PDF) for the spatially distributed effective root zone saturation ($\tilde{\theta}$), k is the number of bins (k = 1, 2, … 50), where the chosen bin size is 0.02 [-]; and $H(\tilde{q})$ [-] is the empirical Shannon Information Entropy of $\tilde{\theta}$. The magnitude of $H(\tilde{\theta})$ is concerned with the shape of PDF: generally a PDF with a narrower base results in a smaller magnitude of $H(\tilde{\theta})$. The Entropy value was calculated at 12pm of each day of the simulation.

The calculated time series of $H(\tilde{\theta})$ for the three simulation cases converge at approximately hour 468 (Figure 3.9). At this time, the PDFs of root zone soil moisture for all simulation cases become nearly identical. After the convergence at hour 468, the time series of $H(\tilde{\theta})$ have a somewhat decreasing trend from hour ~600 to hour ~1380. During this time period, soil in the root zone becomes progressively drier due to evapotranspiration and a lack of precipitation. As minimum moisture is physically bounded by the residual value, the PDF becomes progressively "narrower" (i.e., with a smaller spatial variance), which explains the overall decreasing trend of $H(\tilde{\theta})$.

This transformation of spatial distribution of soil moisture is a combined result of i) wetting process due to precipitation (uniform in space above canopy), and ii) drying process that depends on spatial variation of LAI magnitude. When precipitation occurs, it diminishes the relative differences among drier and wetter locations (Figure 3.10b, e). During post-storm period, the spatial variability of transpiration rate is mainly determined by the spatial pattern of LAI, such that the drying of root zone soil leads to an "inverse-LAI" distribution of soil wetness (Figure 3.10c, f).
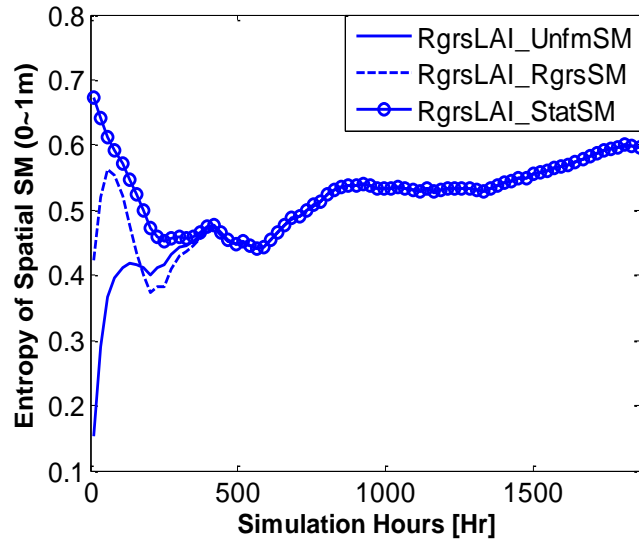
Figure 3.9. The time series of Shannon Information Entropy for the spatial root zone soil moisture content over the domain simulated by cases with *UnfmSM*, or *RgrsSM*, and *StatSM* scenarios.
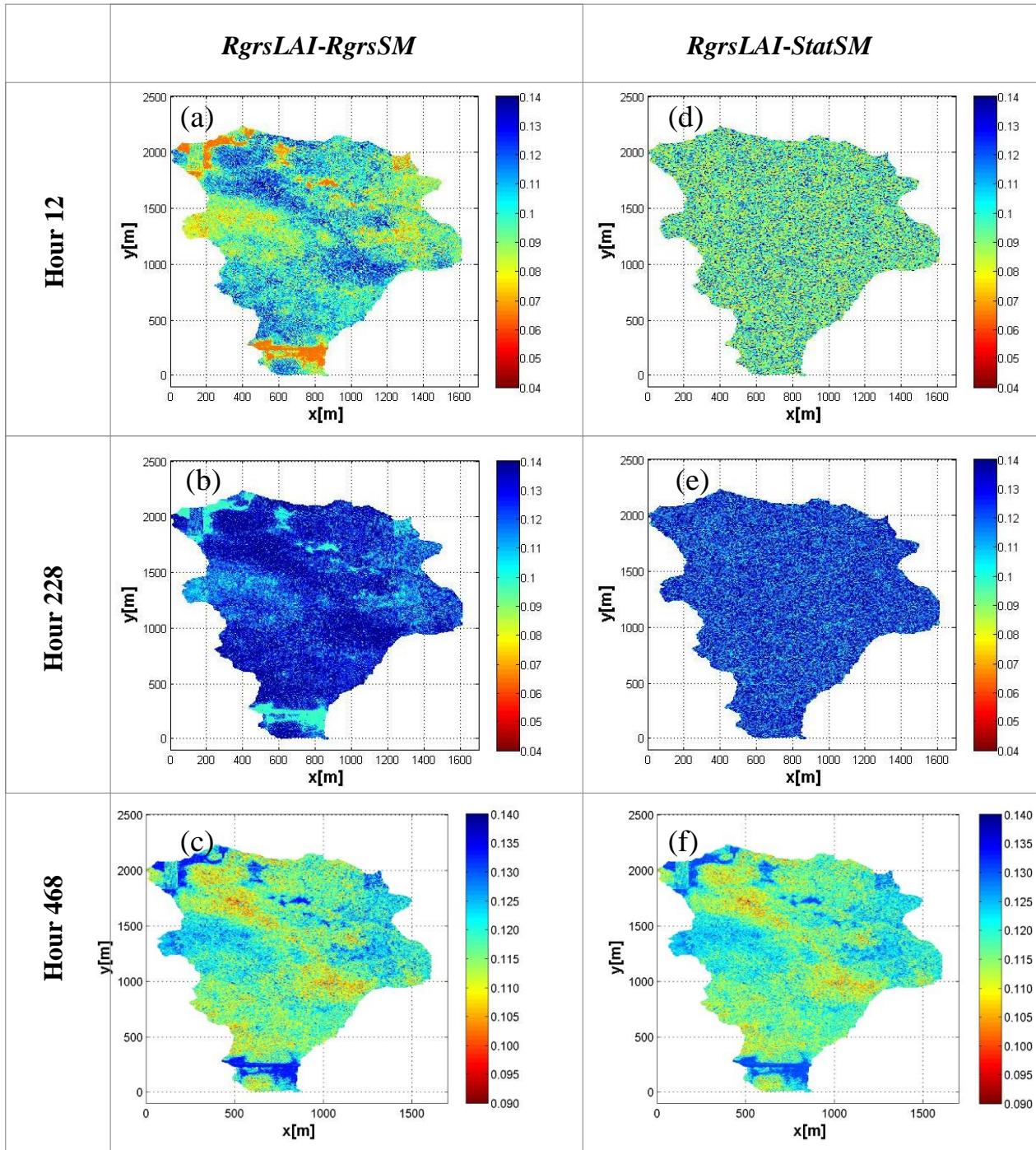
Figure 3.10. The spatial distribution of volumetric root zone soil moisture at hour 0, 228, and 468 for the *RgrsLAI-RgrsSM* case (a, b, c), and the *RgrsLAI-StatSM* simulation case (d, e, f).

3.5.3 Comparison of *UNFRM* and *HETER* simulation cases

Individual tall or short trees

Tall trees behave differently in the *HETER* case and in the *UNFRM* case. For a 19-m tall tree (with surrounding trees shorter than 19 m), it is exposed to more radiation and therefore transpires more in the *HETER* case than in the *UNFRM* case for most of the time (Figure 3.11a, b). As a result, the soil water is generally depleted to a lower level for the 19-m tree in the *HETER* case than in the *UNFMR* case. During severe water-stressed periods, although the 19-m tree in the *HETER* case has a larger radiation input, its transpiration is constrained to a lower level in the *HETER* case than in the *UNFMR* case. These time periods are shown as blue points below the 1:1 relationship line in Figure 3.11b.
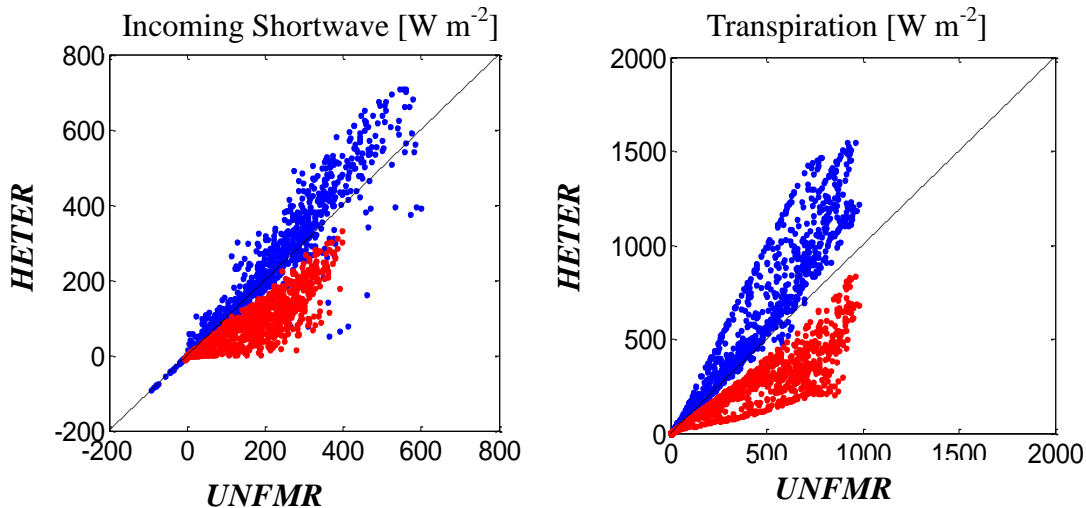
Figure 3.11. A comparison of simulated hourly incoming shortwave and hourly transpiration for a 19-m tall tree (blue points) and a 5-m short tree (red points) in the *HETER* case (y-axis) and in the *UNFMR* case (x-axis).

Short trees also behave differently in the *HETER* case and in the *UNFMR* case. For a 5-m short tree (with surrounding trees taller than 5 m), it is shaded and therefore receives less amount of input radiations and transpires less in *HETER* scenario than in the *UNFMR* scenario (red

points in Figure 3.11). No water stress is observed for this short tree in the *HETER* scenario during the whole simulation period. On contrast, in the *UNFMR* case, all tall trees and short trees experience similar water stress condition, with β smaller than one from simulation hour 693 to hour 1689.

Domain scale

In the *HETER* simulation case, nearly half of tree crowns within the domain are exposed to higher than average levels of daily incoming shortwave radiation and the other half are at least partially shaded and experience lower radiation levels than average. Trees in these two groups will be referred to as "exposed trees" and "shaded trees", respectively. The average radiation levels are uniformly prescribed to all crowns in the *UNFRM* case. For the following paragraphs, magnitudes of canopy irradiance and transpiration will be referred as daily average values over periods of 6am to 8pm.
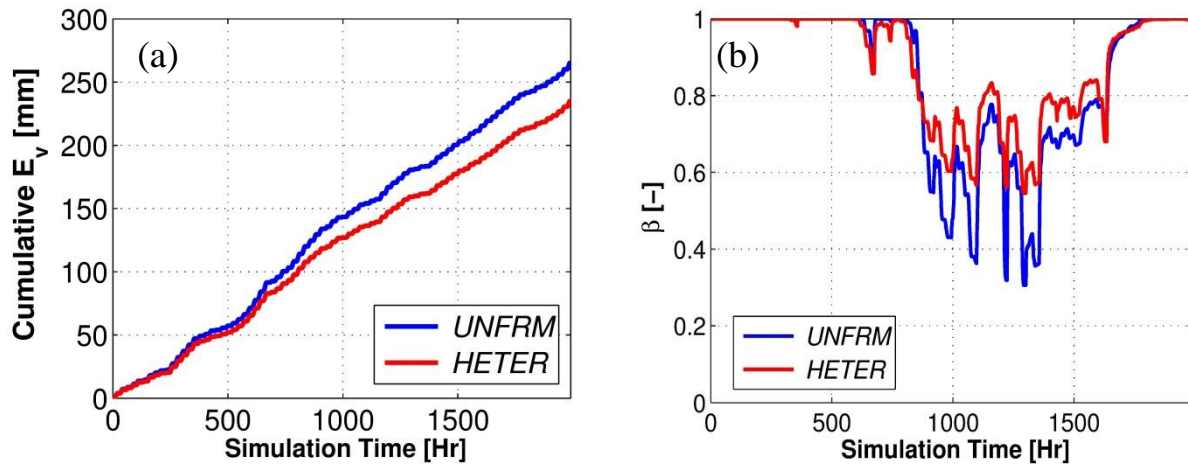
Figure 3.12. The time series of cumulative transpiration (E_v) and soil moisture availability factor (β) for the *UNFRM* and the *HETER* simulation cases.

The domain-scale averaged net radiation for the *HETER* and the *UNFRM* cases are nearly identical (not shown), however, the differences in transpiration flux and water stress conditions are more pronounced. The cumulative domain-averaged transpiration for the *HETER* case is ~9% smaller than that for the *UNFRM* case (Figure 3.12a). The diurnal cycles of latent heat in *HETER* case seems to better match measurements than the *UNFRM* case, in terms of the mean values, standard deviations, and 95% percentiles (Figure 3.13). As argued later, the smaller amount of the domain-scale latent heat in the *HETER* case (as compared to the *UNFMR* case) is mostly due to smaller transpiration during the simulated water-stress period between hour 610 and 1808. During other periods corresponding to non-limiting conditions of soil moisture, the domain-scale transpiration for the two cases is nearly identical (not shown). While resulting in smaller total transpiration, the *HETER* case also exhibits a lower level of water stress at the domain scale during the water-stressed period (Figure 3.12b).
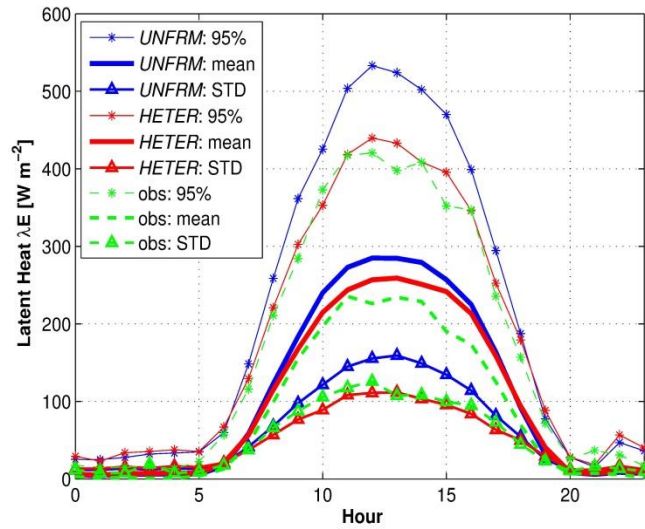
Figure 3.13. Diurnal cycles of the simulated latent heat in *UNFRM* or *HETER* cases and observed latent heat ("obs") over the considered period: 95% percentile ("95%"), mean values ("mean"), and standard deviations ("STD"). Note that the data error of the observed latent heat can be as high as ~20%, given the energy imbalance in empirical data.

During the *water-ample* periods in the *HETER* case, the irradiance of exposed trees is on average 118.9 [$W\,m^{-2}$] higher than that in the *UNFRM* case. Their transpiration flux is also 36.1 [$W\,m^{-2}$] higher. Over the same period, the irradiance of shaded trees is 118.8 [$W\,m^{-2}$] lower than that in the *UNFRM* case, which leads to their 36.2 [$W\,m^{-2}$] lower transpiration. As a result, the increased transpiration by exposed trees and the decreased transpiration by shaded trees in the two simulation scenarios lead to nearly the same domain-scale transpiration in the *HETER* and *UNFRM* cases during periods when conditions are not moisture-limiting. In order to further elucidate the above effect, several off-line simulations were carried out and they are discussed later.

During the water-stressed period simulated in the *HETER* case (i.e., hour 610 through 1808), transpiration of exposed trees is on average 9.7 [$W\,m^{-2}$] higher than that in the *UNFRM* case. Over the same period, transpiration of shaded trees is 39.4 [$W\,m^{-2}$] lower than that in the *UNFRM* case. This implies that the increased latent heat from exposed trees does not entirely

offset the decreased transpiration from shaded trees. This imbalance is due to a disproportional level of water stress simulated for exposed trees that have exploited soil reservoir more rapidly. To gain a better insight on the occurring dynamics, off-line simulations were carried out and are presented later. The argument is further generalized by defining a "transpiration response efficiency" calculated as the absolute magnitude change in transpiration normalized by the absolute change in shortwave irradiance. As can be inferred from Figure 3.14a, when the spatial radiative forcing changes from the *UNFRM* case to the *HETER* case, the "transpiration response efficiency" of exposed trees is lower than that of shaded trees.
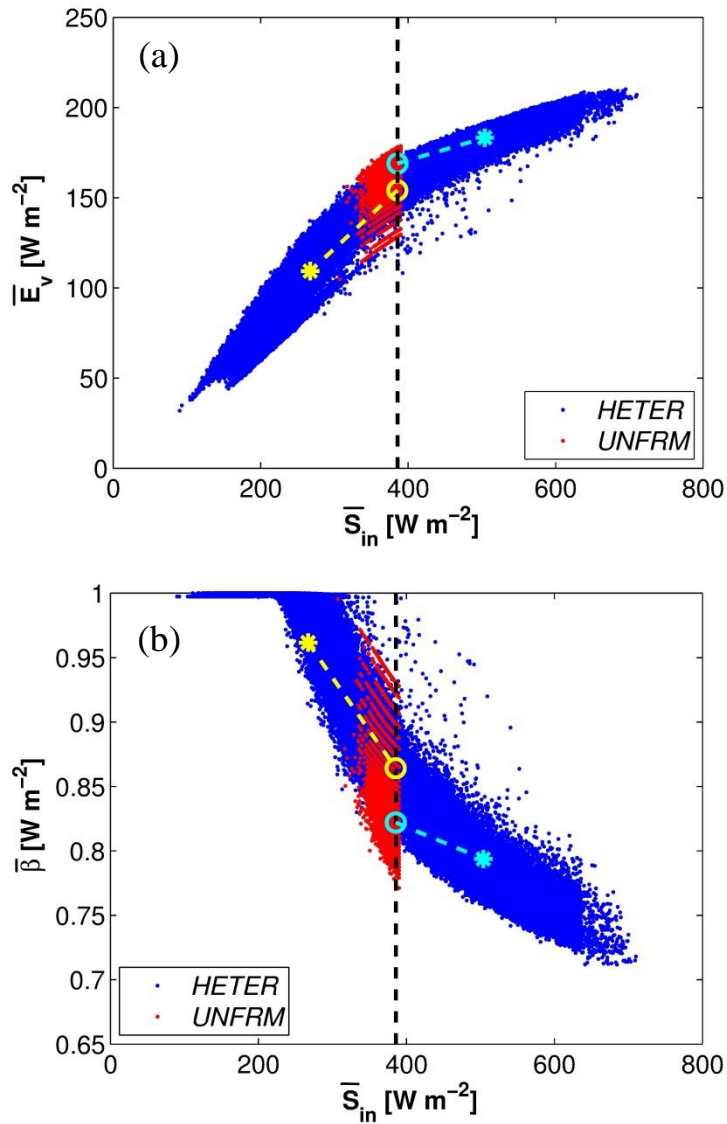
Figure 3.14. The relationships between the simulated element-scale daily shortwave irradiance ($\overline{S}_{in}$) and (a) transpiration ($\overline{E}_v$) or (b) root zone soil moisture availability factor ($\overline{\beta}$). Each point represents results for a given computational element. The black dashed line ($\overline{S}_{in} = 386 \ [W \, m^{-2}]$) indicates the domain-scale average radiation for the *HETER* and *UNFRM* cases. The coordinates of yellow (cyan) star represent the average values of $\overline{S}_{in}$, $\overline{E}_v$, and $\overline{\beta}$ for shaded (exposed) trees in the *HETER* case. The coordinates of yellow (cyan) open circle represent the average values of $\overline{S}_{in}$, $\overline{E}_v$, and $\overline{\beta}$ for shaded (exposed) trees in the *UNFRM* case. The scatter of points for the *UNFRM* case is due to local effects of topographic slope and aspect.

The somewhat counterintuitive result of a smaller domain-scale water stress in the *HETER* case as compared to the *UNFRM* case is confirmed by Figure 3.14b. The daily moisture availability factor $\bar{\beta}$ of exposed trees decreases by 0.029 (3.5%) from the *UNFRM* case to the *HETER* case; the same metric for shaded trees increases by 0.098 (11.4%). The overall implication is that the absolute change of β for exposed trees is smaller than that for shaded trees. By definition, the magnitude of $\bar{\beta}$ depends on two factors (Bonan, 1996; Feddes et al., 1976): the amount of soil water and root density. The change of $\bar{\beta}$ is therefore expected to be smaller in elements where the change of soil moisture is less and uptake depth becomes associated with smaller root densities. As the radiation condition changes from *UNFRM* to the *HETER* case, the total increased water uptake by exposed trees is smaller than a decrease by shaded trees. Further, exposed trees in the *HETER* case tend to take up moisture from deeper   soil layers than shaded trees, and these locations exhibit a lower strength of the sink due to exponentially decaying root profile (Section 3.3.3). The overall result is the change of $\bar{\beta}$ for exposed trees is relatively smaller than that for short trees.

Note that although the *HETER* simulation case considers tree-scale heterogeneity of radiation, it still assumes spatially uniform vegetation parameters and rooting depths for different species composing the forest. The effects of these assumptions are discussed in Section 3.6.

Off-line simulations to illustrate domain-scale differences between the *HETER* and *UNFMR* cases

The presented off-line simulations examine the energy partition by trees of different exposure under various situations and are intended to help in understanding the domain-scale differences in transpiration of the two simulation scenarios. Eight locations with different canopy biomasses are selected from the simulation domain: LAI is equal to 2.0, 2.7, 3.3, 4.4, 5.3, 6.6, 7.4, and 8.2 [$m^2\ m^{-2}$]. The surface energy budget of each element is simulated with a *lumped*

approach using synthetic time series of rainfall and shortwave radiation.

Five time series of shortwave radiative forcing are generated, obtained as the products of the observed time series and the following fractions: 0.2, 0.6, 1.0, 1.4, and 1.8. The series are respectively denoted as "*0.2S*", "*0.6S*", "*1.0S*", "*1.4S*", and "*1.8S*". These time series are assumed to represent changing conditions from highly shaded, shaded, not shaded or exposed (i.e., the same irradiance as in the *UNFRM* case), exposed, and highly exposed situations, thereby mimicking local-scale effects of the *HETER* simulation case.

In the first set of simulations, rainfall input is designed in such a way, so as to ensure water-ample condition for all simulation hours. Specifically, synthetic rainfall at a rate of 10 [*mm hr^{-1}*] is imposed every night, from 11pm to 3am; for all other hours, the observed rainfall time series are used.

As shown in Figure 3.15a, the relationship obtained from simulations between the mean daily transpiration ($\overline{E}_v$) and the mean daily shortwave radiation ($\overline{S}_{in}$) is essentially linear. Further, for all LAI magnitudes, the derivative $d\overline{E}_v / d\overline{S}_{in}$ is nearly constant and does not depend on actual $\overline{S}_{in}$ or LAI. This implies that during water-ample periods, when radiative forcing changes from the *UNFRM* case (i.e., all canopies are forced with the same radiation) to the *HETER* case (i.e., the mean daily shortwave radiation is higher or lower than *1.0S*), linear changes of transpiration are expected: a unit increase of $\overline{S}_{in}$ causes the same magnitude of transpiration change as a unit decrease of $\overline{S}_{in}$. As long as the domain-averaged irradiance in the *HETER* case is the same as in the *UNFRM* case, the changes in the domain-averaged $\overline{E}_v$ are close to zero. As stated in Section 3.5.3, the total input of shortwave energy into the system for the *HETER* and *UNFRM* cases is nearly the same. Based on Figure 3.15a, a total increase of $\overline{E}_v$ due to the surplus of energy received by exposed trees is thus offset by a decrease of $\overline{E}_v$ due to a decrease of energy received by shaded trees.

In a second set of simulations, the actual rainfall series is used. Explanatory insights on the dynamics of energy fluxes under the actually simulated water conditions, including possible water-stressed periods, are sought. The results of the off-line simulation are shown in Figure 3.15b. As shortwave irradiance changes from *1.0S* to *1.4S*, and to *1.8S*, the slope between $\overline{E}_v$ and $\overline{S}_{in}$ changes, contrary to the relationship for water-ample conditions. This is due to water limitation that exposed trees increasingly experience with growing energy input. Conversely, for short shaded trees (e.g., LAI = 2.0 [$m^2\ m^{-2}$]), as input shortwave energy changes from *1.0S* to *0.6S*, to *0.2S*, the slope between $\overline{E}_v$ and $\overline{S}_{in}$ remains nearly constant and is equal to the slope corresponding to water-ample conditions. This signifies favorable soil moisture conditions for any input of shortwave radiation. Overall, the slope of the relationship between $\overline{E}_v$ and $\overline{S}_{in}$ levels off as conditions of shading are changed to exposure (Figure 3.15b), implying a growing effect of soil moisture limitation on transpiration. Correspondingly, when the domain forcing changes from the *UNFRM* case to the *HETER* case, the enhanced transpiration flux due to exposed trees is smaller than the total reduced flux due to shaded trees. This is mostly because exposed trees become highly water-stressed.
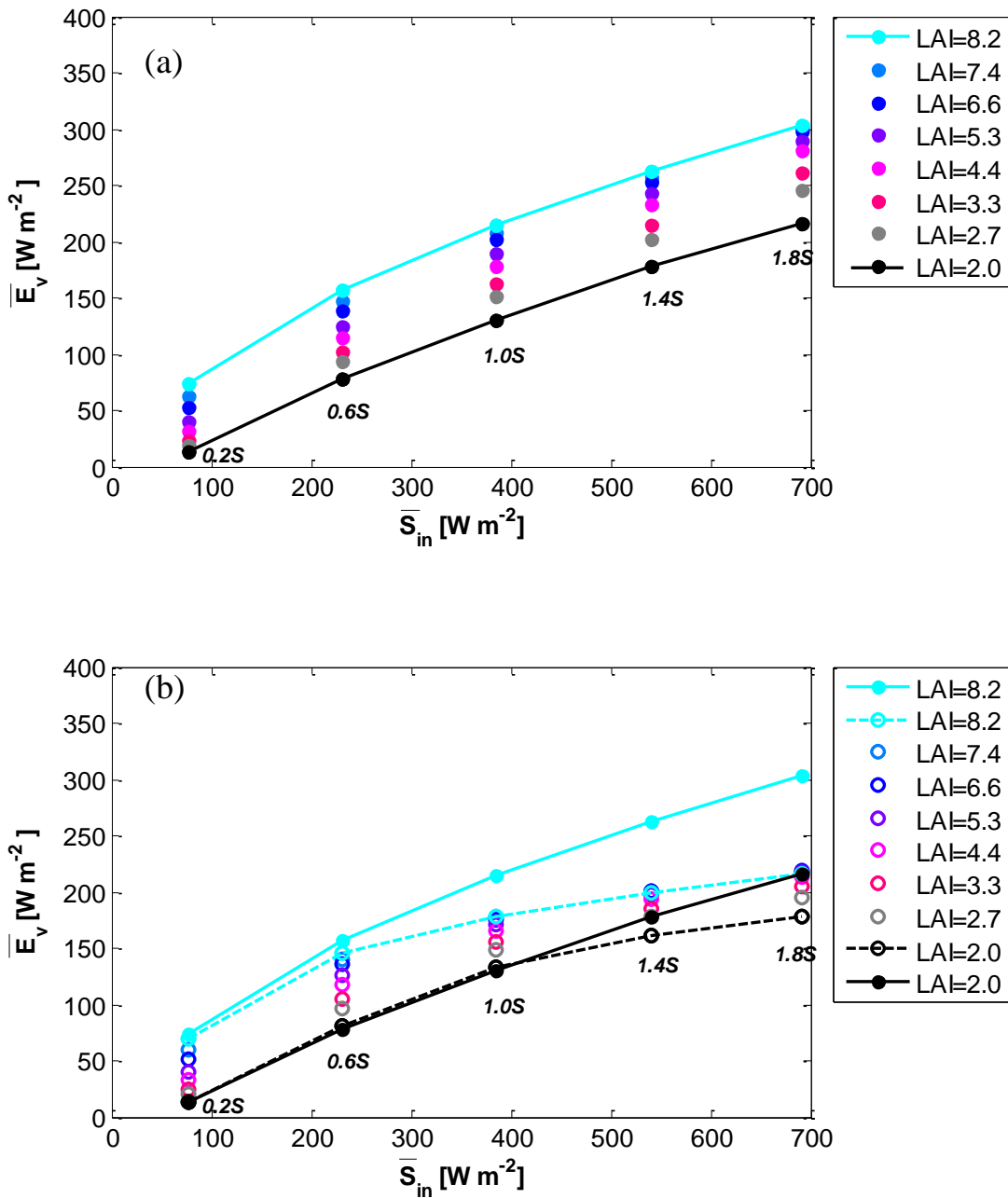
Figure 3.15. The relationships between the simulated mean daily transpiration $\overline{E}_v$ and shortwave irradiance ($\overline{S}_{in}$) for eight elements with LAI of 2.0, 2.7, 3.3, 4.4, 5.3, 6.6, 7.4, and 8.2 [$m^2\ m^{-2}$] selected within the simulation domain: (a) water-ample condition (filled circles), in which water stress was artificially eliminated, and (b) actually simulated water condition (open circles). The imposed shortwave irradiance was obtained as a product of a given fraction (from 0.2 to 1.8) and the original observed series (i.e., the notation *0.2S*, *0.6S*, *1.0S*, *1.4S*, and *1.8S*). The solid lines indicate the slope of the $\overline{E}_v$ - $\overline{S}_{in}$ relationship under water-ample conditions. The dashed lines illustrate the $\overline{E}_v$ - $\overline{S}_{in}$ relationships for two elements (LAI = 2.0 and 8.2 [$m^2\ m^{-2}$]) for an actually

simulated water condition (i.e., including a water-stress period). The mean daily fluxes are used and computed as averages over the 6am - 8pm period.

3.6 Discussion

This study examines ecohydrologic effects of representing spatial vegetation characteristics on temporal and spatial variations of energy fluxes and their coupling with soil moisture. Emphasis is placed on inter-relationships between soil moisture, LAI, radiative forcing, and domain-scale transpiration.

3.6.1 Modes of coupling between canopy and soil moisture variations

For the studied temperate forest, fine-scale root-canopy interactions exhibit controls on domain-scale soil moisture spatial variability. Specifically, vegetation drives soil moisture heterogeneity that tends to approach a pattern of variation inversely related to the spatial distribution of LAI.

Despite the significant differences among the soil moisture simulation scenarios, the impact of moisture initialization is negligible after ~20 days. While the result is not unexpected, it is indicative of the possibly predominant role of canopy heterogeneity in the spatial variations of root soil moisture in such forested systems during periods when water conditions are non-limiting. A concomitant inference then is that variability of moisture over a depth range comparable to the root zone can be dominated by variations in canopy biomass. This is not an apparent conclusion as growing season hydro-climate (i.e., large spatial scale forcing) can theoretically exhibit modes that would destroy any patterns of variability imposed by biotic (and/or abiotic) factors (i.e., local scale).

It is important to note that the role of topography is not pronounced in any of the simulation results due to the relatively flat domain surface. In areas of complex terrain, the study

inferences are subject to local (e.g., terrain slope and aspect) or nonlocal (e.g., upslope contributing area) controlling factors (Ali et al., 2010; Grayson et al., 1997). They are likely to have an important impact on spatial variations of soil moisture but that discussion is beyond the scope of this study.

3.6.2 Spatial variability of canopy vs. lumped representation

The implications of explicit representation of spatial variability of canopy biomass on the domain-scale energy fluxes differ depending on soil wetness conditions. During periods when the soil in a forest system is relatively wet, the domain-scale fluxes are nearly identical to fluxes simulated with the *lumped* representation. This is because higher transpiration from canopies of larger LAI is balanced by reduced fluxes from trees with smaller LAI. The effect of a particular type of LAI spatial variability is insignificant.

During dry periods, the implications of spatial canopy variations may become more pronounced and ultimately play a role in determining the domain-scale fluxes. Specifically, while the cases with a uniform shortwave radiation input do not exhibit appreciable differences when compared to the *lumped* case, the spatially varying canopy irradiance and LAI results in transpiration flux that is smaller and corresponds to a lower water stress, as compared to the results of the lumped representation. As argued, this is because exposed trees experience higher radiation load and deplete soil moisture more rapidly; consequently, their transpiration is limited by availability of soil water during dry periods. In combination with light-limited transpiration of shaded trees, the domain-scale flux becomes lower than that simulated with the *lumped* case.

It is believed that the demonstrated non-linearity of response to dry episodes or, more specifically, the asymmetry of dynamics at locations of different exposure, meaningfully represents ecohydrologic variations at the landscape scale. An indirect but plausible support to the statement is recent empirical evidence from tropical forests that demonstrated that exposed

trees with larger evapotranspirative demands are more vulnerable to water stress (Phillips et al., 2010). The conjecture is that in coarse-scale land surface models, with a grid cell size in the order of kilometers to dozens of kilometers, the representation of area-averaged dynamics could be particularly vulnerable to inconsistencies during dry conditions. It is possible, that this effect which reduces the overall spatial extent of soil-moisture stress is, in part, driving an increased water use efficiency in structurally diverse forests, a phenomenon that was recently discovered in our forest site (Hardiman et al., 2011; Hardiman et al., 2012).

Note that the LAI over the domain in cases of spatial heterogeneity has a normal distribution (Section 3.4.2). When the tree-scale radiation heterogeneity is not considered, the domain-scale latent heat with the distributed LAI is nearly identical to the *lumped* case. As indicated by previous studies, the deviation between cases of spatial heterogeneity and the *lumped* case might be more evident when the spatial LAI has a more skewed distribution (Li and Avissar, 1994). However, even with the normal distribution of spatial LAI, this study shows that large differences in latent heat can occur with the nonlinearity introduced by the tree-scale heterogeneous radiation and water stress (Section 3.5.3). The fact that the *HETER* case has a smaller latent heat than the *UNFRM* case suggests the same direction of sensitivity as in other studies (Knyazikhin et al., 1997; Song et al., 2009) but for different reasons. Instead of focusing on representing realistic spectral reflection and transmission within crowns, this study emphasizes on the nonlinearity caused by the water-constrained transpiration processes of exposed trees in dry conditions.

3.6.3 Key assumptions

The simulated cases are subject to a number of assumptions and the associated uncertainties. Note that the emphasis here was on linking the effects of two gross structural characteristics (i.e., LAI and height) to consequences of vegetation function. Specifically, tree-scale effects on

81

radiative forcing (i.e., "shading" or "exposure" effects) were considered by generating "effective input shortwave radiation" above individual canopies. Those were achieved by modifying the two-stream radiative transfer approximation for a semi-infinite homogeneous canopy layer. Although more sophisticated modeling techniques existed for accurate three-dimensional radiative forcing on tree scale (such as ray tracing techniques), their expensive computational demands usually prohibit them to be used in ecosystem-scale simulations. Although not exact, the modified approach in this study nonetheless explicitly considers the crown properties (height and biomass) of neighboring trees and permits qualitatively correct effects of exposure and shading related to the actual lidar-derived spatial variation of canopy, resulting in nearly identical radiation absorption as compared to the *lumped* case.

This study does not represent species-specific differences in optical properties or leaf stomatal regulation that can be very important for simulating accurate transpiration rate (Pataki and Oren, 2003). Previous studies have demonstrated that ignoring species-specific parameterization in the transpiration process (e.g., spectral reflectance and transmission, leaf stomatal conductance) may lead to an over-estimated domain-scale transpiration by up to 50% during dry periods (Oltchev et al., 2002). Consequently, the *HETER* simulation case serves as a 'virtual' experiment that relaxes only one of the assumptions traditionally made in coarse-scale modeling: spatially uniform radiation forcing. It offers insights of sensitivity highly relevant for the development of modeling approaches. A "realistic" representation of the forest would ideally consider all other important spatial heterogeneities, i.e., species-specific rooting depth, stomatal controls, root architecture, and hydraulic strategies. But this would require collection of appropriate data and further research on appropriate parameterizations.

In particular, root water uptake is a key process controlling the magnitude of transpiration and the accuracy of its representation has been generally limited by a number of uncertainties

stemming from the difficulties of obtaining relevant observations. This chapter involves two major simplifications that are also characteristic of other land surface models applied at crown-scale resolution. Firstly, the root water uptake region of an individual tree is confined to a single grid cell of $5 \times 5 \times 2$ m^3 dimension. Trees, in reality, may have very extensive root systems, e.g., surface roots of a 5-year-old pine [*P.pinaster*] extend beyond a 5-m radius (Danjon et al., 1999), and more mature root systems can extend to over 20 m (Stone and Kalisz, 1991). Different species in a mixed forest uptake water from different vertical depth intervals in the soil profile (Meissner et al., 2012). Consequently, the modeling assumption is likely to exaggerate the simulated spatial variability of moisture. That is, under larger trees, the subsurface is modeled drier than in reality, because all uptake is forced to originate within the top 80 cm in a single grid cell, and under short trees it is modeled wetter, because the existence of roots from neighboring trees is not accounted for. The exact implications are addressed in Chapter 4.

Secondly, in approximating the effects of water limitation on potential transpiration, the model uses the Feddes-type water stress function. This commonly used heuristic function is based on species-specific, hard-to-define parameters and is likely too sensitive to moisture conditions (Desborough, 1997). It has been shown to lead to simulations where soil control on transpiration would set in too early, as compared to observations (Feddes et al., 2001). This has inspired further research to capture the 3-D spatio-temporal process of root water uptake more adequately (Doussan et al., 2006; Javaux et al., 2008; Schneider et al., 2010), which are introduced in 0.

3.7 Summary

The coupling mode between spatial canopy and soil moisture variations is sensitive to the wetness conditions. The non-linear relationships between radiation heterogeneity and soil moisture and leaf area heterogeneity are important in determining the total spatially-aggregated

transpiration. However, fine-scale heterogeneity in leaf area and soil moisture and their interactions without radiation heterogeneity do not generate a non-linear feedback that affect the total mean transpiration over a large area. The *lumped* representation generates consistent domain-scale energy fluxes during wet periods, but may predict larger spatially-aggregated transpiration and severer water stress than actual during dry periods. Specifically, non-linear responses of water and energy dynamics to the moisture-limiting situation were demonstrated at locations with different canopy biomass and light conditions.

Furthermore, the study presented here incorporated two major simplifications about root water uptake that were addressed in Chapter 4. Specifically, (1) the root water uptake of individual trees was confined to grid cells where tree stems are located, and (2) the heuristic, "Feddes-type" water stress function was used to constrain the transpiration in dry conditions.

Chapter 4 : Upscaling microscopic root water uptake to ecosystem-scale

4.1 Introduction

The accuracy of current land surface or ecohydrological models can be limited by uncertainties in modeling transpiration, and its sensitivity to root zone wetness, especially in dry conditions (Desborough, 1997; Feddes et al., 2001; Lai et al., 2000; Zeng et al., 1998). Most land surface models use the 1-D Richards' equation with a sink term to describe the transient water flow and soil water uptake (Dickinson et al., 1993; Foley et al., 1996). For water-limited situations, the commonly used "Feddes-type" water stress approach may lead to simulations where the soil control on transpiration sets in too early as compared to observations (Feddes et al., 2001). Previous research effort at the UMBS also shows that, the ecohydrological model using this heuristic water stress function indicates severe water-stressed transpiration when soil at the shallow depth becomes dry (see Chapter 3). Empirical observation at this study site however suggests little control on transpiration by soil wetness near the surface. This is likely because the traditional approach cannot mimic the fact that plants uptake water in a 3-D fashion, and may have the capability to meet potential transpiration demand by dynamically compensating decreased water uptake in dry regions through increased uptake from other relatively wetter regions.

In this chapter, the 3-D root water uptake process of individual trees is simulated and scaled to a plot size (~10^2 m^2). The main objectives are (1) to gain mechanistic insights about the sensitivity of plot-scale transpiration and water stress to the representation of 3-D root water

uptake and tree-scale architecture strategies (i.e., lateral spread and rooting depth); (2) to explain the difference (if any) in the simulated plot-scale transpiration from the traditional 1-D approach (e.g., the "Feddes-type" water stress function and a soil water bucket model) and the 3-D approach.

4.2 Constrained transpiration by the "Fedess-type" water stress function at UMBS

Soil moisture monitoring at the UMBS site shows frequent dry periods with volumetric soil moisture contents dropping to 4% ~ 8% [$m^3 m^{-3}$] within the top 40-cm layer, where 60 ~ 80% of fine roots are located (Figure 1.1). As the soil water availability factor β by the "Feddes-type" water stress function is very sensitive to the soil dryness at shallow depths (Equation (1.4)), any land surface model with the "Feddes-type" approach applied for the conditions of the UMBS site would exhibit a decline of transpiration because of the frequent dry soil conditions near the top. This is no exception for simulations with the tRIBS+VEGGIE model. As described in Chapter 3, a "*big-leaf*" simulation case with the "Feddes-type" formulation was run for the 2010 vegetation season. As shown in Figure 4.1a, latent heat becomes water-constrained when there are large transpiration demands and when the top soil layers are dry. However, analysis of the observation datasets at the AmeriFlux shows that, even when shallow soil layers were dry, latent heat might still be sustained by the plants (Figure 4.1b). The implication is that, trees might have the capability to dynamically adjust the fractional root water uptake at the shallow or deep depths according to the spatial distribution of soil water potential.
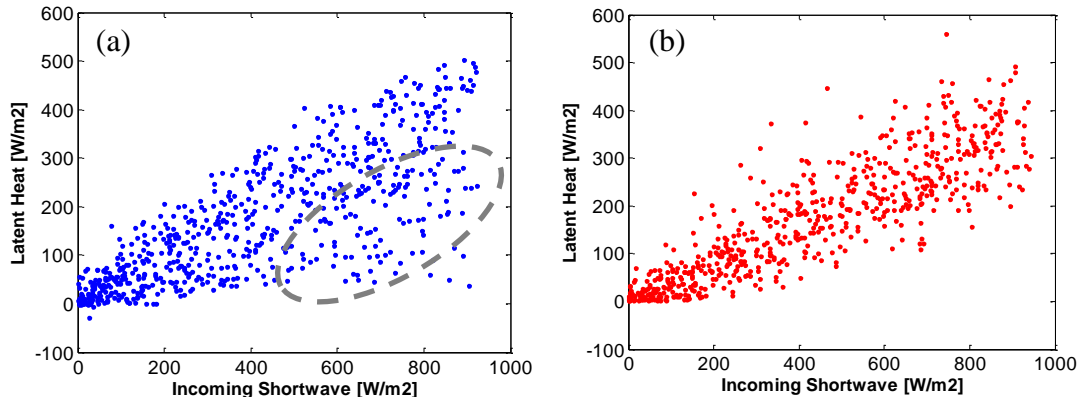
Figure 4.1. A relationship between hourly incoming shortwave and latent heat from simulation (a) and measurements (b). The shown data points for (a) and (b) are from day-time period (6 AM to 8 PM) when the "Feddes-type" water stress function is smaller than one in the "*big-leaf*" simulation case (Chapter 3). The grey dash circle in (a) denotes the simulated water-constrained latent heat by the low water content in shallow layers.

4.3 Review of models for 3-D root water uptake

4.3.1 Modeling the "compensation" effect

The phenomenon that, plants might be able to change their root water uptake zones adaptively to meet transpiration demand even when some parts of roots are water stressed, is referred as the "compensation" effect. To simulate the compensation effect, two categories of methods have been developed.

One approach is to empirically compensate the decreased water uptake in one part of the root zone (due to low soil water content) by an increased uptake in other locations of soil profile (Li et al., 2001; Simunek and Hopmans, 2009; Teuling et al., 2006). For example, a dimensionless root water adaptability factor was suggested by Simunek and Hopmans (2009). If the ratio of the actual transpiration (determined by the "Feddes-type" approach) to the potential transpiration is larger than a defined root adaptability factor, the reduced water uptake in the stressed parts of the root is expected to be fully compensated by water uptake from other

less-stressed parts. This kind of approach still ignores the actual three dimensional physical mechanisms that take place, and lacks the capability to incorporate plant hydraulic process in stem xylem, which can exert further control through stomatal closure (more details are discussed in Section 5.3).

Another approach is to model the physical mechanisms of root water uptake in a microscopic fashion (Amenu and Kumar, 2008; Doussan et al., 2006; Javaux et al., 2008). The water flow within plants starts as a radial flux from soil to root nodes and root segments, and propagates along the xylem tubes of root systems axially. Various simplifications of the process have been employed, depending on the purpose of a study. For example, water potential was assumed to be constant within the root system in the study by Theseira et al. (2003), or root system was constructed as a network of parallel pipes consisting of xylem tubes in the study by Amenu and Kumar (2008).

4.3.2 Review of root architecture models

Root architectural models have been developed to explicitly describe the deployment (i.e., the spatial locations) of root nodes and segments (Diggle, 1988; Dunbabin et al., 2013; Jourdan and Rey, 1997; Lynch et al., 1997; Pages et al., 1989). The construction of 3-D root architecture usually requires parameters such as primary growth rate, inter-lateral length, branching angle, and geotropism (Collet et al., 2006; Dunbabin et al., 2013; Pages et al., 2004; Vercambre et al., 2003). Such root system characterizations may be obtained from measuring a subsample of roots in field.

One of the most popular models is the RootTyp model developed by Pages et al. (2004). In this model, root systems are generated as root segments that are interconnected in a designated order. Different orders of segments are assigned with different growth parameters, and the overall size of the root system (i.e., lateral spread, or rooting depth) depends on the age of growth. The model tracks each root segment by recording its positions, properties, and other segments that are connected to it. The deployment and development of a new order or branch is a result of random processes of root emission, axial and radial growth, sequential branching, reiteration, transition, decay, and abscission. Figure 4.2 shows a comparison of an observed root system and a root system simulated by the model RootTyp (Pages et al., 2004).
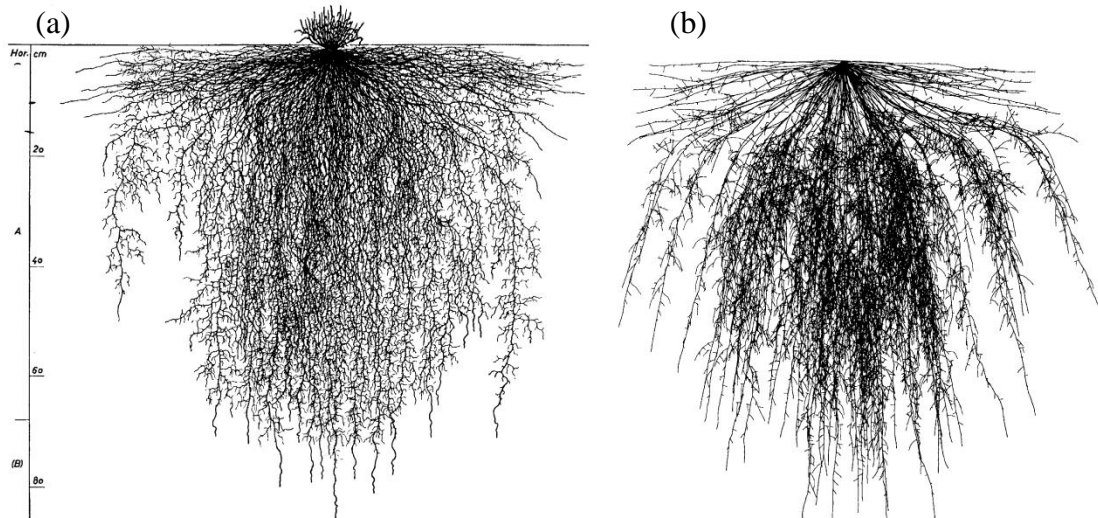
Figure 4.2. A comparison of (a) an observed root system by Kutschera (1960) and (b) a simulated root system by the RootTyp model, for a centralized secondary root system for a ryegrass [*Lolium multiflorum*].

Godin et al. (1999) developed a multi-scale tree graph approach to describe root architectures (MTG's). The root system is a directed graph with a set of vertices, which are connected by binary edges. According to this concept, an AMAPmod software was developed (Godin et al., 1999). Studies using the AMAPmod software generated a dataset containing recommended parameters for root architectures of various species (Danjon et al., 2008; Danjon et al., 1999; Di Iorio et al., 2005; Godin and Guedon, 2001; Khuder et al., 2007; Nicoll et al., 2006; Tamasi et al., 2005).

Another type of models may treat root systems as self-similar entities by using the repetitive nature of the root structure. For example, Prusinkiewiez et al. (2000) generated a root structure based on a "L-system" pattern (Lindenma, 1968). Wilderotter et al. (2003) simulated the root growth and root structure with a cellular automaton method.

While constructing a root system, one should keep in mind that actual root architecture can evolve over a long term according to the surrounding soil characteristics and resources states, for

example, soil or rock barriers, and local dry or moisture spots. This adaptive mechanism of root systems may benefit the plant by increasing the overall magnitude of total root water and nutrient uptake (Garre et al., 2011).

4.3.3 Microscopic water transfer process

With generated root architectures, the microscopic water uptake approach simulates radial and axial water fluxes based on water potential gradient between soil and root surface and within the root system. The axial (J_{ax} [$mm\ s^{-1}$]) and radial fluxes (J_{rad} [$mm\ s^{-1}$]) for a root segment are described as (Doussan et al., 2006; Schneider et al., 2010):

$$J_{ax} = \frac{1}{R_{ax}}(\Delta\varphi_{root} + \Delta z), \tag{4.1}$$

$$J_{rad} = \frac{1}{R_r}\left(\varphi_{root} - \varphi_{soil}(r_o)\right), \tag{4.2}$$

where R_{ax} [$mm^{-1}\ s$] is the axial root resistance; R_r [s] is the intrinsic radial root resistance; φ_{root} [mm] is the root xylem water potential; z is the elevation potential; $\varphi_{soil}(r_o)$ [mm] is the soil water potential at the root surface with a diameter of r_o [mm]; Δ is the potential gradient (of φ_{root} or z [mm]) between two connecting root nodes or segments.
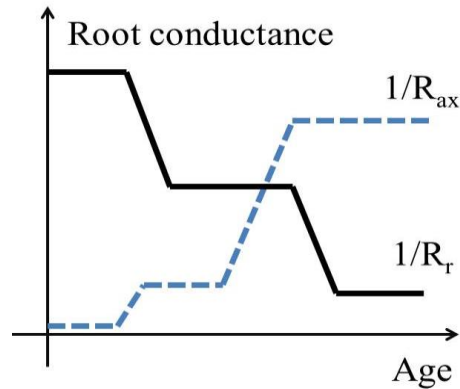
Figure 4.3. The varied plant root axial and radial hydraulic conductivity with root tissue age (Doussan et al., 2006).

Root hydraulic properties (R_{ax} and R_r) may vary with the root age (Doussan et al., 2006; Doussan et al., 1999; Fiscus, 1972; Schymanski et al., 2008; Zwieniecki and Boersma, 1997), as shown in Figure 4.3. The conductance of water flux from soil to root might be further influenced by the soil water content, as proposed by Amenu and Kumar (2008).

4.3.4 Three-dimensional root water uptake coupled with three-dimensional soil water flow

Doussan et al. (2006) made the first attempt to fully couple the 3-D root water uptake with a 3-D soil water flow model by solving a system of linear equations that described the root water transfer process in the root and soil systems (Figure 4.4). The plant boundary conditions are the spatial distribution of soil water potential in grids, and a flux or a fixed water potential at the root collar. The microscopic root systems provide sink terms for the 3-D Richards' equation, then the transient soil water content is solved. At each time step, the model generates a three-dimensional distribution of water content in the soil, a distribution of xylem water potential within the root system, and a total water uptake by the roots. The model's performance was assessed by comparing the simulation outputs with experimental measurements of young plants in

homogeneous soil slabs. The experiments measured the spatial and temporal changes of root water content by using quantitative imaging techniques such as light transmission and X-ray. Both experimental and modeling results revealed that there existed an "extraction front", i.e., the root mainly took up water in a spatial zone between the soil top and the depth of the "extraction front". As the top soil layers became drier and drier, the extraction front propagated deeper with time. The water extraction front also denoted that, at times, some parts of the roots (e.g., the deeper layer) did not uptake water even though the water was readily available. Nevertheless, the modeling results supported the concept of "hydraulic redistribution" observed in the field, i.e., water was extracted from deep and moist soil layers by roots and was transported via the root xylems to shallow zones where soil water potential was much lower. The hydraulic redistribution effect was inherently considered as the direction of radial flow between soil and root was determined by the gradient of water potential, it could be oriented either towards the roots (as root water uptake) or towards the soil (as hydraulic redistribution). This model is referred to as "Doussan model" hereafter.

Based on the work of Doussan et al. (2006), Javaux et al. (2008) examined the sensitivities of the model to parameters such as soil hydraulic conductivity, root radial conductivity, and axial conductivity. For example, highly conductive soil promoted root water uptake due to enhanced lateral and vertical soil water fluxes but at the same time decreased the spatial variability in soil water content. For the radial conductivity, large values increased the amount of water extracted by the root. For the axial conductivity, as long as it was high enough to conduct all of the extracted water, a further increase did not lead to a different water uptake or soil moisture patterns. In all of the explored test scenarios, the aggregated vertical profile of root water uptake was different from the profile of root density, especially when conditions lead to water stress. In

order to compare the differences in the vertical profiles of root water uptake with that from the traditional "Feddes-type" approach, an "effective one-dimensional water stress factor (or soil water availability factor)" was calculated by normalizing the uptake fraction at depths by the fractional root density. The estimated effective water stress function indicated a different relationship between soil water potential and the soil water availability factor as compared to the traditional monotonic function from the "Feddes-type" approach (Figure 4.5).
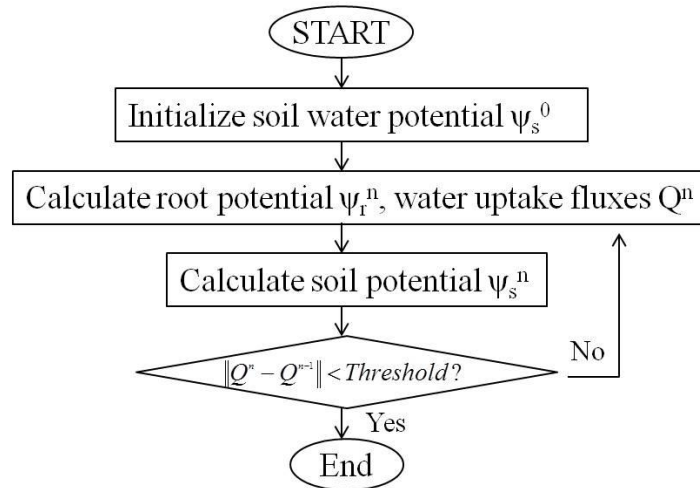
Figure 4.4. An iterative computational scheme coupling a three-dimensional microscopic root water uptake model with a three-dimensional soil water transfer process, according to Doussan et al. (2006).
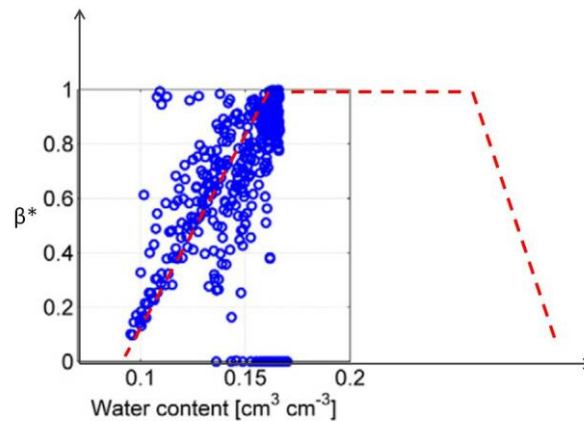
Figure 4.5. A comparison of the effective one-dimensional water stress function (blue open circles) simulated by the microscopic approach by Javaux et al. (2008), and the traditional "Feddes-type" water stress function (red dashed line).

Schneider et al. (2010) further advanced the microscopic root water uptake modeling scheme by accounting for a local drop of soil hydraulic conductivity immediately around the root surface in the bulk soil. In his "aRoot" model, a variety of root architectures were constructed, which had a similar vertical profile of root length density. Despite the similar vertical profile of fractional root length density, the varied root architectures resulted in a wide range of vertical profile of root water uptake. The differences among these uptake profiles became larger with the simulation time. It was also shown that root architectures might have different "critical values" in soil moisture to trigger water stress. As shown in Figure 4.6, the water stress was associated with a decreased flux at the root collar, and the used 50 root architectures showed different critical soil water content (towards the dry end) to have a decreased transpiration flux, mostly because of the differences of the spatially-distributed and temporally-varying sink terms of root nodes. On the contrary, the traditional "Feddes-type" approach (red line) would constrain transpiration using a single critical value SM^* in the entire domain, as shown in Equation (1.3). Therefore, the "Feddes-type" approach did not capture that fact that, root water uptake behavior may vary greatly, even when the soil domains have a similar vertical profile of root biomass distribution.
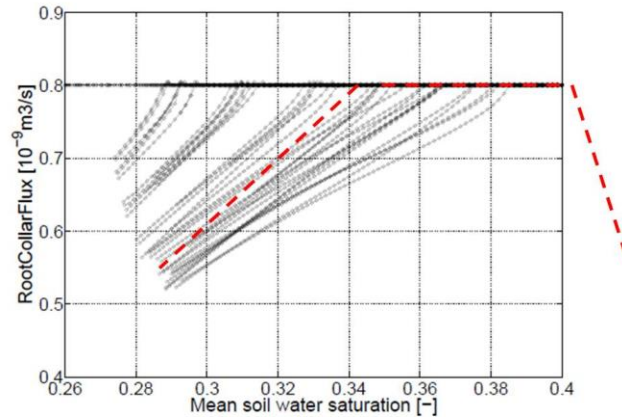
Figure 4.6. The varied water-constrained collar fluxes (black lines) for 50 varied individual root architectures with a similar vertical profile of root density (Schneider et al., 2010). The x-axis is the domain-averaged soil water condition during the simulated time period. The red line indicates a traditional time-invariant "Feddes-type" approach for the water-constrained root collar flux.

4.3.5 The "Couvreur" approach

Despite the progress in microscopic root water uptake modeling, most of the models so far have been limited to "stand-alone" plants. That is likely because solving the linear system of equations that describe the physical mechanisms of water flow from soil to root nodes and within root nodes usually involves expensive computational resources even for a single root system. To solve the computational challenge, Couvreur et al. (2012) proposed a computationally efficient model that implicitly considers the root system hydraulic architecture for simulating distributed root water uptake and plant water stress in a 3-D soil water flow models. The "Couvreur" approach generates several macroscopic parameters for a root system and the soil grid cells it occupies by considering a root architecture, its hydraulic properties, and the soil grid geometry. By using the macroscopic parameters, the computational time of this model was shorter by a factor of 28 to 214 as compared to root water uptake models that implicitly solve the 3-D microscopic process. This has provided a conceptual scheme making it possible to upscale the

microscopic root water uptake process of individual trees to a larger scale (more details are in Section 4.5).

4.4 Study site and observation data

The study site UMBS was described in Section 2.2.1 and Section 3.2. Meteorological variables and energy fluxes in the UMBS forest were detailed in Section 2.2.2 and 3.2.2.

4.4.1 Spatial soil moisture

Soil moisture was measured over a 50 m $\times$ 50 m area near the AmeriFlux tower (Figure 4.8a, b), with a spatial scale of 2 m $\times$ 10 m. The measurements occurred almost monthly in vegetation seasons from year 2009 to 2011, and soil water content was sampled over two integrating depths: 20 cm and 40 cm. Two types of hand-held soil moisture sensors were used: Hydrosense CD-620 (20 cm, Campbell Scientific., Logan, UT, USA) and MiniTrase kit (40 cm, Soil Moisture Corp., Santa Barbara, CA, USA).

4.4.2 Tree-scale observations: stem location, DBH, and leaf water state

Tree-scale measurements of stem locations, DBH, and leaf water potential were conducted at the UMBS site. Specifically, locations of individual tree stems and their DBH were measured in a 50 m $\times$ 50 m plot during the vegetation season of 2011, the area had a stem density of 748 [*stems ha^-1*]. Leaf water potential of oak species was measured during vegetation seasons of 2011 and 2012 (Caple, 2012; Thomsen et al., 2013). Values of leaf water potential at the heights of 2 m or 5 m were measured at different times of the day: predawn, mid-day, and late-day (Caple, 2012; Thomsen et al., 2013). On a specific day in the 2011 vegetation season (6/26/2011), the leaf water potential of a tall oak tree was measured at 5 different heights ranging from 6 m to 20 m, at 6 AM, 9 AM, 1 PM, 5 PM, and 9 PM (Figure 4.7).
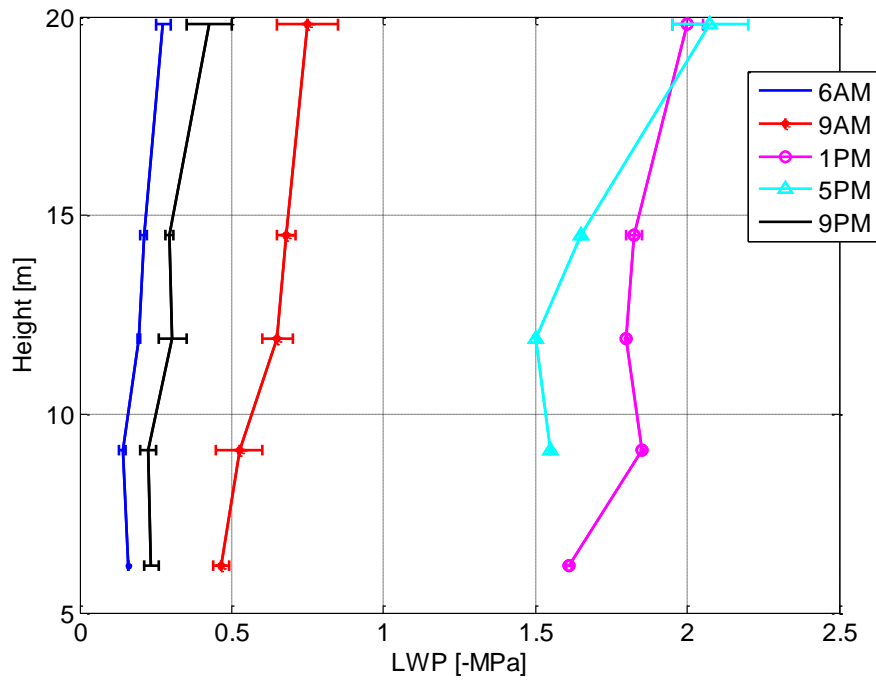
Figure 4.7. Values of leaf water potential measured on an oak at five heights (6, 9, 12, 14, and 20 m) at 6 AM, 9 AM, 1 PM, 5 PM, or 9 PM on 6/26/2011 at UMBS.

Water potential at the root collar was subsequently estimated, which was used for model confirmation (Section 4.7.1). Specifically, using measured values of leaf water potential at multiple heights of the oak tree (e.g., 5 heights ranging from 5 m to 20 m), its gradient along the stem was estimated to be 0.01 [$MPa\ m^{-1}$] for time periods when there was little sap flow (e.g., pre-dawn), and in a range of 0.01 to 0.05 [$MPa\ m^{-1}$] for hours when there sap flow was driven by transpiration (e.g., mid-day or late-day). With the estimated gradient of leaf water potential along the stem and its values at the 2-m and 5-m heights of oak trees, the water potential at the root collar was estimated to be in a range of -2 to 0 [MPa] for any time of the day.
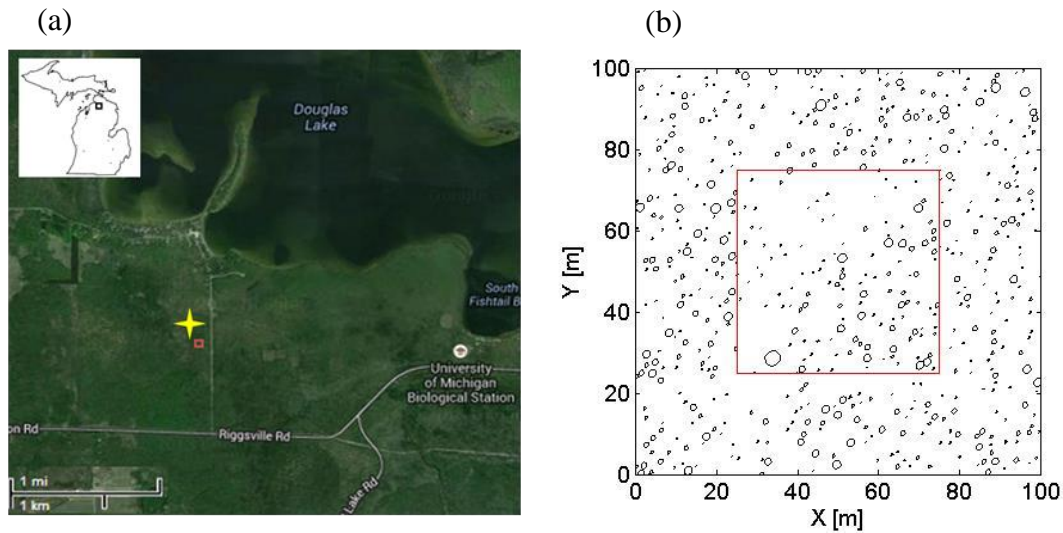
Figure 4.8. The UMBS site (a): location in Northern Michigan (black box in the contour map of Michigan in the upper left corner), the AmeriFlux tower (yellow star), the 50 m × 50 m plot (red box), where the locations and DBHs of individual trees were measured. The 100 m × 100 m plot used in simulations (b): locations of tree stem (center of black circles), the centered 50 m × 50 m area (red box) where the locations of trees and their DBH are parameterized according to the *in-situ* measurement. In (b), the size of each tree is denoted by the diameter of the black circle, for the convenience of visualization, the shown magnitude of the diameter is four times larger than the actual DBH value.

4.5 Simulation configuration and methods

4.5.1 Simulation domain

A simulation domain of 100 m $\times$ 100 m was constructed (Figure 4.8b). In the centered 50 m $\times$ 50 m area, the locations and DBH of tree stems were set up as measured at the 50 m $\times$ 50 m plot at the UMBS (Section 4.4.2). For the simulation domain outside the centered 50 m $\times$ 50 m area, the locations of stem were randomly distributed in a fashion that it has the same stem density and probability distribution frequency of DBH as in the centered 50 m $\times$ 50 m area. Stems located within 1.5 meter from each other were assumed to be from a multi-trunk tree, i.e., a tree with multiple stems that share the same root system. In that case, an effective *DBH* was calculated to represent the overall size of the multi-trunk tree by using the DBH of the corresponding stems:

$$DBH = \sqrt{\sum_{i=1}^{N} DBH_i^{2}} \quad , \tag{4.3}$$

where *N* is the total number of stems in a multi-trunk tree (*i* =1, …, *N*), and DBH_i is the DBH of each individual stem. After this procedure, there are 574 stems in the simulation domain, which is a drop of 23% from the number of 748 before the procedure.

Simulations were conducted for a subset of a representative growing season, starting on 06/07/2010 and ending on 8/23/2010 (in total, 1990 simulation hours). Soil grid cells are in a size of 5 m (X-dimension) $\times$ 5 m (Y-dimension) $\times$ 0.05 m (Z-dimension). The numerical scheme consists of several models: the RootTyp model for root architecture, the "Couvreur" approach for fine-scale root water uptake process, the PFLOTRAN model for 3-D soil water transfer process, and the tRIBS+VEGGIE model for meteorological boundary conditions (Figure 4.9).

4.5.2 Root architecture based on RootTyp

For each individual tree in the simulation domain, root hydraulic architecture was determined by using root networks generated by the RootTyp model (Pages et al., 2004). The RootTyp model considers root development processes (such as root emission, axial and radial growth, sequential branching, reiteration, transition, decay, and abscission) and plant-specific properties (such as inter-lateral length, branching angle, and geotropism). Using the RootTyp model, this study generated root networks for oak, whose root system is characterized as the "primary root system" (Figure 4.10). A "primary root system" is composed of a primary root and of lateral roots that may develop from the primary root as first order, second order, etc (Cannon, 1949). Other species with different root architectures do exist at the UMBS, but are not considered in this study. For example, aspen has the "secondary root system", which might have more than one primary roots (Cannon, 1949). Five root networks for oak were generated based on parameters and information of oak root system from Collet et al. (2006). Overall they have a vertical profile of fractional root length consistent with the observation (Figure 4.11). The five root networks would be referred to as the "study root networks" hereafter.

Each tree was assigned to have one of the five study root networks in a random fashion; the root network was further adjusted according to the size of the tree. Specifically, a value of "lateral spread" was used, which is defined as the horizontal distance between the stem base location and the location of the furthest root node. The lateral spread was determined using an allometric relationship with canopy volume (more details are in Section 4.6.1). According to the uncertainty of the allometric relationships, several scenarios of lateral spread were constructed (Section 4.6.1). Due to the difficulty of generating a reasonable root architecture with a large lateral spread, the root network of individual trees was scaled horizontally (i.e., in X- and Y-dimension) to achieve a root architecture that has the desired lateral spread. In a specific

simulation scenario (Section 4.6.1), the root network was also scaled vertically, along the

Z-dimension to obtain different rooting depth.
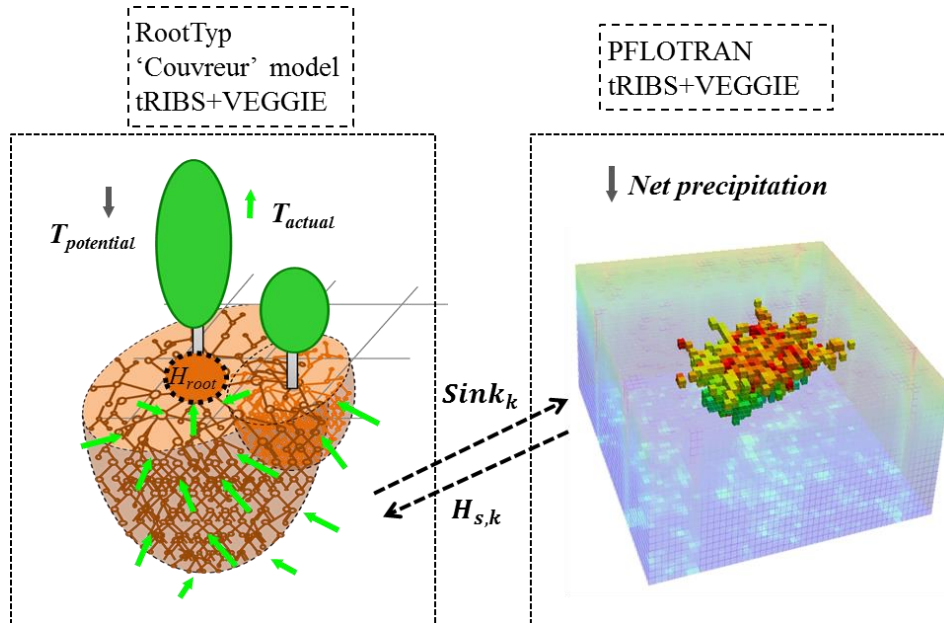
Figure 4.9. A conceptual sketch of the coupled models for simulating plot-scale transpiration: multiple 3-D root architectures were generated by using the RootTyp model (left panel); the sink terms in the k-th grid cell, $Sink_k$, were simulated using the "Couvreur" approach (left panel); the sink terms $Sink_k$ were used by a 3-D soil-water accounting model PFLOTRAN to update the 3-D distribution of soil water potential $H_{s,k}$ in the soil domain (right panel). Boundary conditions such as tree-scale potential transpiration $T_{potential}$ and net precipitation were derived based on the tRIBS+VEGGIE model.

Figure 4.10. Two primary root systems generated by the RootTyp model, which were used to represent the root architectures of the oak species.
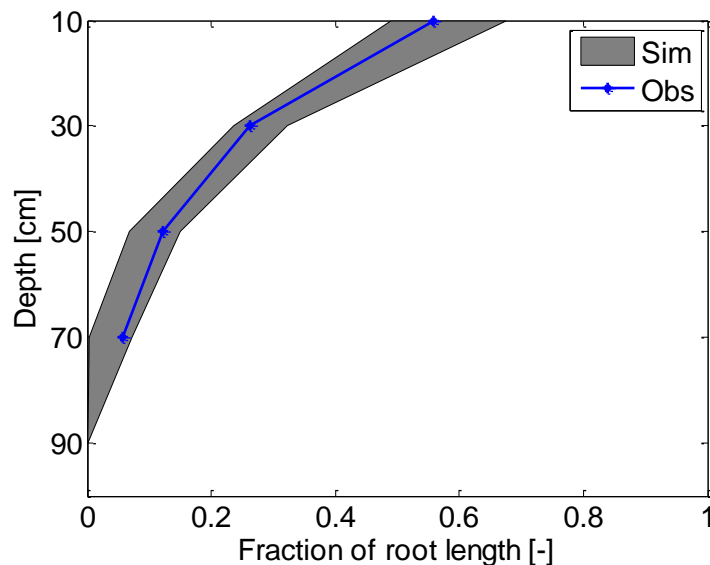
Figure 4.11. The fractional distribution of root length density in each 20-cm soil layer over the top 80-cm depth, derived from the five generated root networks (shown as a range, 'Sim') and observation ('Obs'). The observation data points were derived from the median values of fine root biomass density measured at UMBS, with an assumption that the conversion factor between the root length and root biomass is constant with depth.

4.5.3 Root water uptake based on the "Couvreur" approach

Magnitudes of root water uptake by each individual tree in soil grid elements were derived

by the using the "Couvreur" approach (Couvreur et al., 2012). This "Couvreur" approach implicitly considers the 3-D root water uptake process (i.e., radial water flux from soil to root, and axial water flow between root segments), and the spatial distribution of soil water potential in soil elements which a root system occupies. The analytical solution used to generate sink terms for each soil element $Sink_k$ is shown in Equation (4.4) to (4.7):

$$Sink_{k,p} = T_{actual,p} SUF_{k,p} + K_{comp,p}(H_{s,k} - \sum_{j=1}^{M} H_{s,j} SUF_{j,p}) SUF_{k,p}$$ (4.4)

$$H_{collar,p} = \sum_{j=1}^{M} H_{s,j} SSF_{j,p} - T_{actual,p} / K_{comp,p}$$ (4.5)

$$T_{actual,p} = \begin{cases} K_{comp}(\sum_{j=1}^{M} H_{s,j} SSF_j - H_{threshold}), & if \; |H_{collar}| > |H_{threshold}| \\ T_{potential,p}, & if \; |H_{collar}| < |H_{threshold}| \end{cases}$$ (4.6)

$$Sink_k = \sum_{p=1}^{N} Sink_{k,p}$$ (4.7)

where $Sink_{k,p}$ is the generated sink term for a root system p ($p=1, \ldots. N$) in soil grid cell k; $T_{actual,p}$ is the actual transpiration; $H_{s,k}$ is the soil water potential in soil grid cell k; M is the total number of soil elements the root system p occupies; $H_{collar,p}$ is water potential at the root collar; $H_{threshold}$ is the threshold of water potential at the root collar for stomatal closure in leaves, which is set to be -2.5 [MPa]; $T_{potential,p}$ is a potential transpiration for an individual tree (Section 4.5.5); $Sink_k$ is the total sink term for the soil element (i.e., in overlapped root zones) where exist roots from multiple trees; $SUF_{k,p}$ is the fractional root water uptake of root system p in the soil grid cell k when the soil water potential is spatially uniform; $K_{comp,p}$ is a

"compensatory conductivity" for root system p. Note that if $H_{collar,p}$ reaches the threshold value

of $H_{threshold}$, the actual transpiration $T_{actual,p}$ is constrained accordingly.

The values of SUF_k and K_{comp} were pre-determined for each root system by using

simulation results of the Doussan model that explicitly considers the 3-D root water uptake

process (Section 4.3.4). Specifically, for each root system, two simulations were conducted using

the Doussan model with a spatially uniform or heterogeneous distribution of soil water potential.

When the soil water potential is spatially uniform, the second term of the right hand side in

Equation (4.4) becomes zero, and the values of SUF_k were derived by using the simulated

$Sink_k$ and T_{actual} from the Doussan model. The magnitude of SUF depends on a specific root

architecture (e.g., root network and size) and root hydraulic properties (e.g., radial and axial

hydraulic properties), and is independent of the distribution of soil water potential or

transpiration rate. For the value of K_{comp}, it was derived by fitting Equation (4.4) with the

simulated $Sink_k$ and spatial distribution of $H_{s,k}$ from the Doussan model with the spatially

heterogeneous distribution of soil water potential. The K_{comp} parameter adjusts how strong the

compensatory root water uptake is in soil elements when the spatial soil water potential is not

uniform. The value of K_{comp} depends on root axial and radial resistances to water flow in root

segments of a root architecture. Note that all root architectures used the same set of root

hydraulic properties and radius for roots from order 0 to 4 (Table 3). A sensitivity test of K_{comp}

to different sets of hydraulic properties was presented in Appendix 6.7. The values of K_{comp} are

positively correlated with the lateral spread of root systems (Figure 4.12), and are not sensitive to

the rooting depth of the root networks (Figure 4.13).
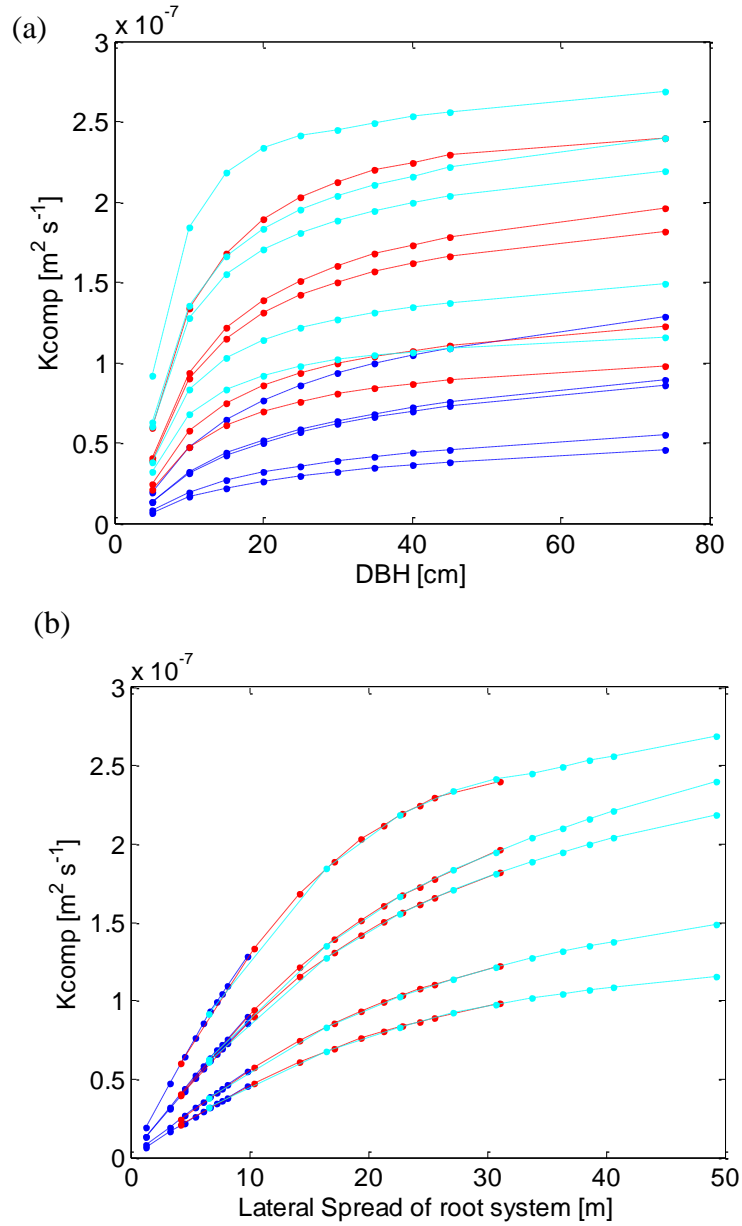
Figure 4.12. A relationship between K_{comp} and (a) DBH or (b) lateral spread of representative root systems derived from the five study root networks. The root systems shown in the figure have DBHs of 5, 10, 15, 20, 25, 30, 35, 40, 45, and 74 cm, respectively. Different colors indicate scenarios of lateral spread (Section 4.6.1): small (blue), benchmark (red), and large (cyan).
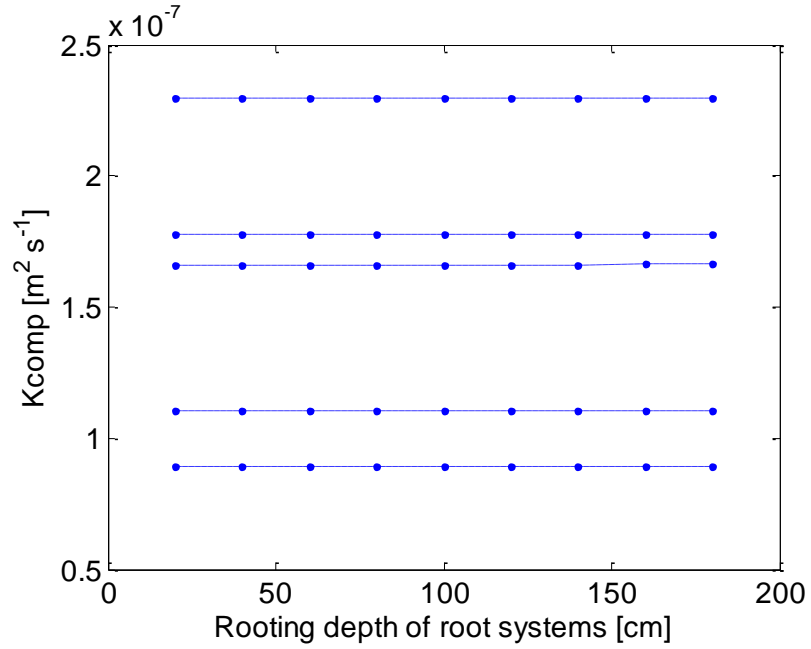
Figure 4.13. A relationship between K_{comp} and rooting depth of root systems derived from the five study root networks. The root systems shown in the figure have a DBH of 40 cm, a lateral spread of 25 m (as in the benchmark scenario of lateral spread), and rooting depths of 20, 40, 60, 80, 100, 120, 140, 160, and 180 cm, respectively.

For the convenience of description in a later section (Section 4.7.3), a soil grid cell "Uptake Fraction (*UF*)" was defined, calculated for each soil grid cell as its sink term divided by the plot-aggregated sink term (i.e., total transpiration, Equation (4.8)). The *UF* consists of two terms. The first term indicates the fractional root water uptake in a soil grid cell, if the soil domain has spatially uniform soil water potential; the second term accounts for the compensatory adjustment of root water uptake when there is a spatial variation of the soil water potential in the plot. The first and second terms are hereafter referred to as $UF1_k$ and $UF2_k$, respectively:

$$UF_k = \frac{Sink_k}{\sum_{q=1}^{Q} Sink_q} = \frac{\sum_{p=1}^{N}(T_{actual,p}SUF_{k,p})}{\sum_{q=1}^{Q} Sink_q} + \frac{\sum_{p=1}^{N}(K_{comp,p}(H_{s,k} - \sum_{j=1}^{M} H_{s,j}SUF_{j,p})SUF_{k,p})}{\sum_{q=1}^{Q} Sink_q} \quad (4.8)$$

$$UF_k = UF1_k + UF2_k \quad (4.9)$$

where UF_k is the Uptake Fraction of a soil grid cell *k*; *q* indicates all the soil grid cells in the simulation domain (*q* = 1, …, *Q*). The sign of the compensatory term $UF2_k$ of a soil grid cell depends largely on its relative soil water potential ($H_{s,k}$) as compared with the soil water potential in other soil grids ($H_{s,j}$).

4.5.4 Three-dimensional soil water accounting based on PFLOTRAN

The spatial distribution of soil water potential was updated at every time step by solving the 3-D Richards' Equation using the PFLOTRAN model (Equation (4.10)). The PFLOTRAN model is a computationally efficient multiphase flow and multi-component reactive transport model (Hammond et al., 2007; Mills et al., 2007). The model is composed of a flow module PFLOW and a transport module PTRAN; it solves flow and reactive transport through variably

saturated porous media. The model can run in a parallel mode, if needed. The code has been

successfully used to solve for contaminant migration (Hammond et al., 2008) and impacts of

CO_2 sequestration on hydrologic basins (Lu and Lichtner, 2007; Person et al., 2010). The

objected-oriented approach of PFLOTRAN is shown in Figure 4.14. Soil properties are

parameterized as shown in Table 1.

The PFLOTRAN model is coupled with the "Couvreur" approach through communications

of sink terms and spatial distribution of soil water potential in soil elements at each time step. At

the beginning of each time step, the root water uptake model provides a sink term for each

computational grid cell in the PFLOTRAN domain. The sink term is capped not to exceed the

maximum available soil water storage in the soil grid cell. The distribution of soil water potential

is updated (Equation (4.10)). At the end of each time step, the PFLOTRAN domain feedbacks to

the root water uptake model with updated spatial distribution of soil water potential (Figure 4.9).

$$\frac{\partial(SM_k)}{\partial t} = \nabla \cdot (K(H_k) \cdot \nabla(H_k + z)) - Sink_k \tag{4.10}$$

where SM_k is the value of soil moisture at a soil grid cell k, $K(H_k)$ is the hydraulic

conductivity, H_k is the soil water potential, z is the vertical elevation of a soil grid cell.
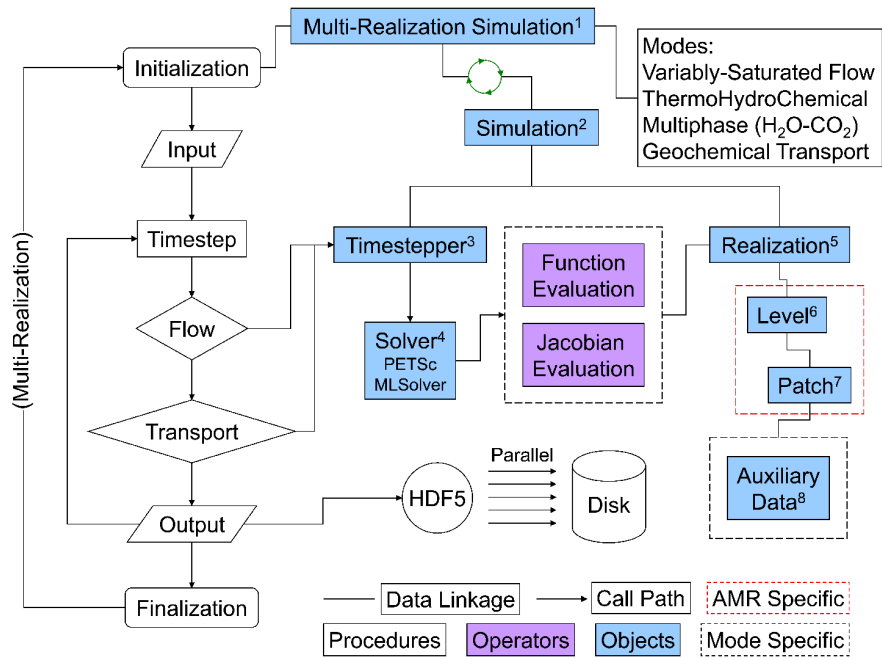
Figure 4.14. A flowchart illustrating procedures, operators, and objects of the PFLOTRAN model (Hammond et al., 2008). It is based on an efficient PETSs solver (Portable Extensible Toolkit for Scientific computation).

Note that, by considering overlapped zones of root systems (Section 4.5.3), the simulated soil water content in those root zones would be influenced by the collective uptake of multiple trees.

4.5.5 Boundary conditions from tRIBS + VEGGIE

Boundary conditions for the "Couvreur" approach or the PFLOTRAN model such as the time series of potential transpiration and net precipitation were generated by using the tRIBS + VEGGIE model. The tRIBS + VEGGIE model is a spatially distributed, high-resolution, ecohydrological model that represents the essential water and energy processes over a basin and links them to plant life regulatory processes (Ivanov et al., 2008a; Ivanov et al., 2008b). The processes represented include interception, evapotranspiration, surface energy balance, infiltration, snow hydrology, groundwater, runoff, and overland or channel flow (He et al., 2014;

Ivanov et al., 2008a; Ivanov et al., 2008b). The lumped *"big-leaf"* simulation scheme was used, where the plot was represented as a single grid cell (as described in Chapter 3). Using ecosystem-scale meteorological variables and the vegetation condition at the UMBS (Section 3.3.4), the time series of net precipitation was generated. For the domain-scale potential transpiration (i.e., representing the potential root water uptake within the simulation domain), rainfall input was designed in such a way, so as to ensure water-ample condition for all simulation hours. Specifically, synthetic rainfall at a rate of 10 [*mm hr^{-1}*] was imposed every night, from 11pm to 3am; for all other hours, the observed rainfall time series were used. Based on this domain-scale potential root water uptake, each tree was assigned with a specific tree-scale potential root water uptake value according to its canopy biomass and the fraction of its root system within the 100 m × 100 m plot:

$$T_{potential,p} = T_{potential,domain} * A_{domain} * \frac{F_{root,p} * V_p}{\sum_{p=1}^{N} F_{root,p} * V_p} * \frac{1}{3600}$$

(4.11)

where $T_{potential,p}$ [*kg s^{-1}*] is the potential root water uptake for a root system *p* in the simulation domain (*p* = 1, …, *N*); $T_{potential,domain}$ [*mm hr^{-1}*] is the potential root water uptake of the simulation domain; A_{domain} is the area of the plot (i.e., 100 *m^2*); $F_{root,p}$ is the fraction the root biomass within the simulation domain of root system *p*; V_p is the volume of the canopy biomass, which was calculated as described in Section 4.6.1.

4.6 Simulation design

4.6.1 Cases with 3-D root water uptake based on root architectures

<u>Scenarios of lateral spread</u>

Three scenarios of lateral spread were determined for each tree in the simulation domain according to allometric relationships in literature relating root lateral spread to canopy size (Casper et al., 2003). Specifically, a regression line between root lateral spread and canopy volume for humid vegetation systems was determined (Equation (4.12)) based on a study by Casper et al. (2003). A scenario of lateral spread inferred from this regression line is referred to hereafter as "benchmark scenario". To represent the uncertainty of this regression line, a 95% confidence interval was estimated. According to the low and high bounds of the 95% confidence interval (Equation (4.13) and (4.14)), two additional scenarios of lateral spread were generated. They are referred to hereafter as "small scenario" and "large scenario", respectively. The canopy volume used in the regression lines was calculated by assuming that the crown has an ellipsoidal shape (Equation (4.15)). The height of actual crown layer was assumed to be three fifths of the tree height (Equation (4.16)) (Canham, 2005). The height and canopy diameter of a tree were derived from their allometric relationships with DBH at UMBS (Equation (4.17) and (4.18)) (Garrity et al., 2012a). The relationship between DBH and the lateral spread for different scenarios is shown in Figure 4.15.

The procedure of scaling the root networks to attain root systems of the desired lateral spread resulted in root systems with different total root length density. A root system of a larger size tends a smaller total root length density (Figure 4.16), and the generated root system might involve some artificial areas where there are fewer root segments than in the actual situation. To examine the possible effect of the root systems generated from this "scaling procedure" on the

simulation results, another simulation case with a "synthetic potential fractional root water uptake" was generated (Section 4.6.2).

$$\log_{10}(L) = 0.298 + 0.406 * \log_{10}(V) \tag{4.12}$$

$$\log_{10}(L) = -0.202 + 0.406 * \log_{10}(V) \tag{4.13}$$

$$\log_{10}(L) = 0.488 + 0.406 * \log_{10}(V) \tag{4.14}$$

$$V = \pi * H' * W^2 / 6 \tag{4.15}$$

$$H' = 0.6 * H \tag{4.16}$$

$$H = 9.97 * \ln(DBH) - 12.61 \tag{4.17}$$

$$W = 2.67 * \ln(DBH) - 1.90 \tag{4.18}$$

where L [m] is the lateral spread, V [m^3] is the canopy volume, H' [m] or W [m] are the height or width of a canopy volume, H [m] is the tree height, DBH is in unit of [cm].

Root systems in the small scenario of lateral spread have a relatively smaller size and therefore a smaller soil water reservoir they can explore. As an example, a tree with a DBH of 7.2 cm in the small scenario has a lateral spread of 2.3 m and can access a soil region of ~13 m^3 for root water uptake, versus ~ 137 m^3 in the benchmark scenario with a lateral spread of 7.4 m.
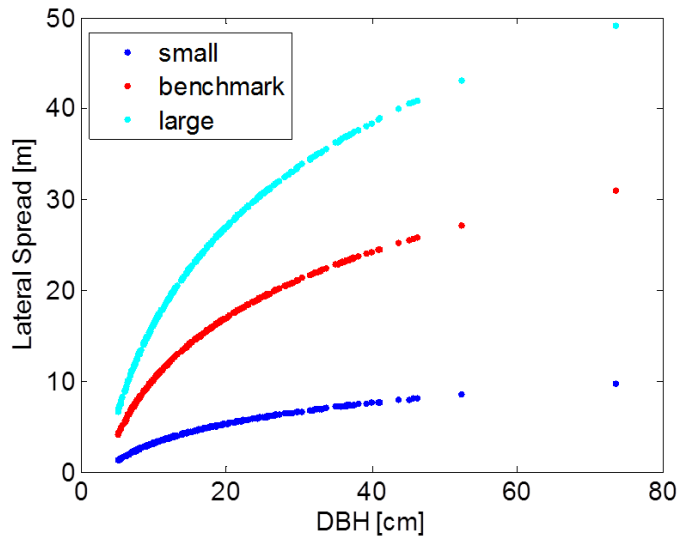
Figure 4.15. The relationship between DBH and lateral spread of trees in scenarios of small, benchmark, and large lateral spread.
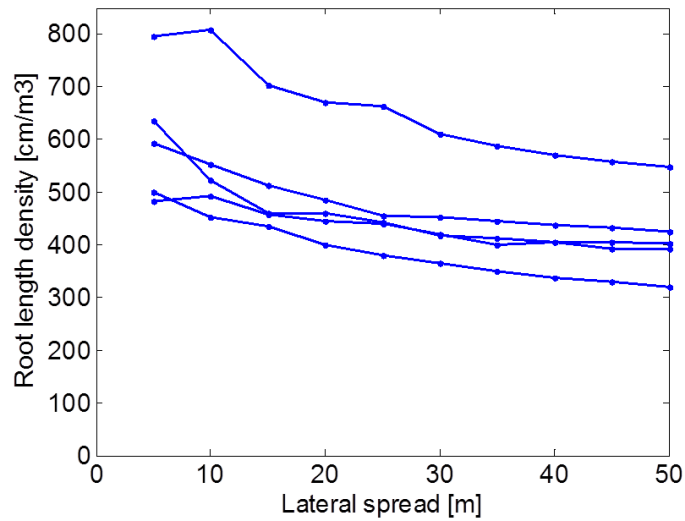
Figure 4.16. Root length density (y-axis) of the five basic root network topology scaled to have a certain lateral spread (x-axis). The root length density of a root system was calculated as the total root length of biomass divided by the total soil volume of grid cells that contain its root segments.

Scenarios of rooting depths

Two scenarios of rooting depth were generated for each tree in the simulation domain. One scenario assumes that each root system has a rooting depth of ~ 80 cm as indicated by the observation at UMBS (Section 4.4.1). This scenario is referred to hereafter as the "spatially uniform rooting depth". The other scenario reflects an observation that rooting depth is usually positively correlated with the tree size (Schenk and Jackson, 2002). Specifically, the rooting depth of individual trees was linearly interpolated in the range of 20 cm and 180 cm according to their values of DBH. For example, the rooting depth of the smallest-size tree was set to be 20 cm; the rooting depth of the largest-size tree was set to be 180 cm. This scenario is referred to hereafter as the "spatially varying rooting depth". Note that, the simulation domain in this study was set up to have a 2-m depth to avoid additional computational expense, while in natural ecosystems, oaks have been observed to have a rooting depth as deep as 5 m (Breda et al., 1995). This scenario is therefore only an approximate representation of real conditions and rooting strategies by trees in this forest. Nevertheless, it explicitly approaches the observation that small-sized trees tend to occupy shallower depth and large-sized trees explore water storage over deeper layer. Therefore, this scenario can provide insightful inferences about the sensitivity of plot-scale transpiration or water stress to different representations of rooting depth.

Simulations were conducted by using various permutations of scenarios of lateral spread and rooting depths, and they are referred to as "3-D simulation cases".

4.6.2 Case with fractional potential root water uptake

A simulation case with a synthetic fractional potential root water uptake in soil grid cells for each root system was generated, by using an approach by Vrugt et al. (2001b). A shape factor describing the 3-D spatial distribution of potential root water uptake was generated, and

normalized to derive the fractional root water uptake in soil grid cells (Equation (4.20)). This function is based on the observation that root length density decays exponentially with distance from the location of a stem (Dwyer et al., 1988; Heinen, 2014; Raats, 1974), and an assumption that strength of root water uptake is correlated with root length density:

$$f'(x,y,z) = (1-x/X_m)(1-y/Y_m)(1-z/Z_m)e^{-[(p_x/X_m)|x^*-x|+(p_y/Y_m)|y^*-y|+(p_z/Z_m)|z^*-z|]} \qquad (4.19)$$

$$f(x,y,z) = \frac{f'(x,y,z)}{\int_{-Xm}^{Xm}\int_{-Ym}^{Ym}\int_{0}^{Zm} f'(x,y,z)} \qquad (4.20)$$

where $f'(x,y,z)$ [-] is the shape factor for potential root water uptake of a soil grid cell centered at (x, y, z); $f(x,y,z)$ [-] is the normalized fractional potential root water uptake; X_m, Y_m, and Z_m [m] are the maximum distances of root location in the x, y, and z direction; x^*, y^*, and z^* [m] are empirical parameters adjusting the asymmetry of fractional root water uptake in horizontal direction or in vertical direction, x^*, y^* were set to be zero assuming that fractional root water uptake is radially symmetric to the stem location on the horizontal plane, and z^* was set to 0.05 m, assuming that the maximum fractional root water uptake in the vertical direction is near the top and at a depth of 5 cm; p_x, p_y, and p_z [-] are empirical factors, they were set to be 5, 5, and 1, so that the 3-D distribution of fractional potential root water uptake is consistent with the 3-D distribution of the root length density (Figure 4.17). The latter was estimated with the five study root networks generated by the RootTyp model (Section 4.5.2). Each root system in this scenario was assumed to be of a cylinder shape, with a radius equals to the lateral spread and a rooting depth of 80 cm (Figure 4.18). The simulation case is referred to as the "synthetic simulation case" hereafter.
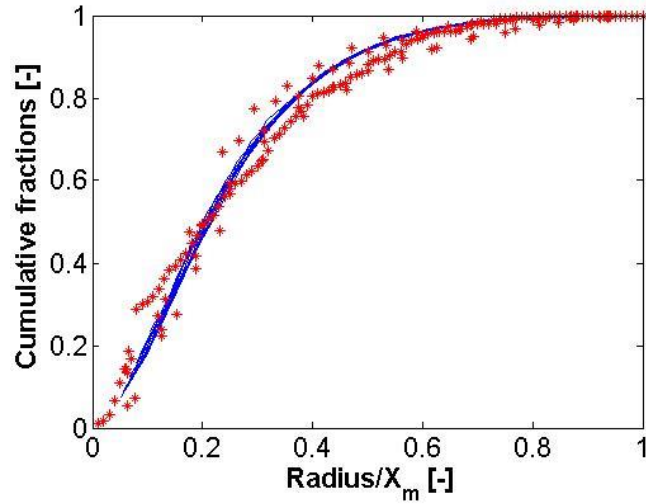
Figure 4.17. The cumulative fractional root length derived from the five study root networks (red stars) within a cylinder space of a certain radius (the cylinder space is centered at the stem location); or the cumulative synthetic fractional root water uptake calculated from Equation (4.20) for synthetic root systems within a cylinder space of a certain radius (blue lines), the synthetic root systems shown in the figure are with a lateral spread of 5, 10, 15, 20, 25, 30, 35, 40, 45, and 50 m, respectively. In the X-axis, X_m is the lateral spread of the root system.
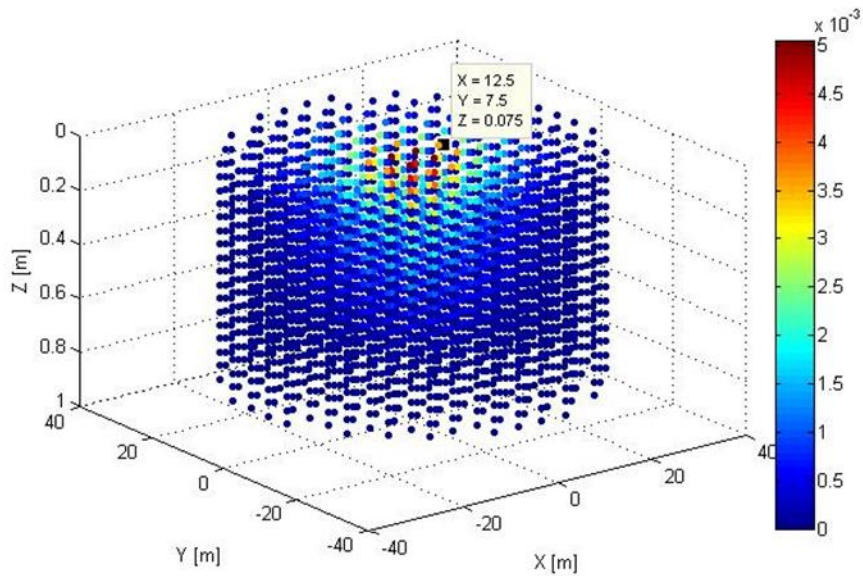
Figure 4.18. An example of the 3-D potential fractional root water uptake for a root with a lateral spread of 20 m and a rooting depth of 80 cm.

This approach eliminates possible "artificial sparse spots" of root water uptake in soil grid cells that may be introduced in the process of scaling root networks (Section 4.5.2). This approach was then adapted into the scheme of "Couvreur" approach by replacing SUF with f, both of which indicate the potential fractional root water uptake at soil elements when there is no water stress. However, as this approach does not generate 3-D networks for root architectures, there is no way to generate K_{comp} as in the "Couvreur" approach. Thus the same values of K_{comp} for individual trees as in the "Couvreur" approach were used.

4.6.3 Cases with 1-D "Feddes-type" approach

Three simulation cases with the 1-D "Feddes-type" approach for root water uptake were generated. Two of them are based on the concept of soil water bucket model (Robock et al., 1995). The simulation domain was represented as a single grid cell with two different depths: 80 cm and 2 m. These two simulation cases are hereafter referred to as "80-cm bucket" or "2-m bucket", respectively. Different depths in these two simulation cases have an implication that the available water storage for root water uptake is different: the water reservoir is either constrained to the top 80 cm, or the top 2 m. In either simulation case, the soil water content was determined by input (e.g., net precipitation) and output (e.g., transpiration or water uptake, and drainage) mass fluxes in the soil grid cell. When the soil grid cell became dry, a "Feddes-type" soil moisture availability factor β was generated to constrain the actual transpiration:

$$T_{actual} = \beta * T_{potential} \tag{4.21}$$

$$\beta = \max[\,0, \min(1, \frac{SM - SM_w}{SM^* - SM_w})] \tag{4.22}$$

where SM [$m^3\ m^{-3}$] is the estimated soil moisture in the soil grid, SM_w [$m^3\ m^{-3}$] is the wilting point (Table 1); SM^* [$m^3\ m^{-3}$] is the threshold soil moisture for stomatal closure.

A third simulation case was designed by using the tRIBS+VEGGIE model. In this case, a finely resolved subsurface mesh was used, with 25 nodes resolving the soil profile in the vertical direction. The mesh has a higher resolution near the surface and exhibits a coarser resolution at greater depths (He et al., 2014; Ivanov et al., 2008a). For this simulation case, a slightly different "Feddes-type" soil moisture availability factor β was calculated using the information at each depth, details were described in Section 1.1.3 and Equation (1.3) and Equation (1.4). This simulation case is referred to as "1-D finely resolved" hereafter.

The simulation cases with 1-D representation of root water uptake process have the same plot-scale potential transpiration and net precipitation, as in the simulation cases of 3-D root water uptake process.

4.7 Results and Analysis

4.7.1 Model confirmation

The results of a 3-D simulation case with the benchmark scenario of lateral spread and spatially uniform rooting depth were compared with the observations, specifically the spatial variations of soil moisture and leaf water potential at root collar. In the simulation, the variations of soil water content within the top 20 cm (or 40 cm) depth were in a range of 0.2% to 2.1% [m^3 m^{-3}] (or 0.3% to 2.2% [m^3 m^{-3}]) (Figure 4.19). This is qualitatively consistent with the range of variations observed in the measurement of spatial soil moisture in the 50 m $\times$ 50 m plot during vegetation seasons (Section 4.4.1). The measurement of the top 20-cm (or 40-cm) soil moisture showed variations ranging from 0.5% to 2.0% [m^3 m^{-3}] (or 0.2 % to 2% [m^3 m^{-3}]). Note that the measurement has a relatively coarser temporal frequency (~monthly) and a slightly different spatial resolution (2 m $\times$ 10 m) as compared to the simulation domain (5 m $\times$ 5 m).

Simulated water potential at the root collar is shown to be within the range of -2 to 0 [MPa],

which is qualitatively consistent with observations (Figure 4.20). Trees of a larger size tend to have a relatively higher negative water potential at the root collar due to the larger transpiration demand.
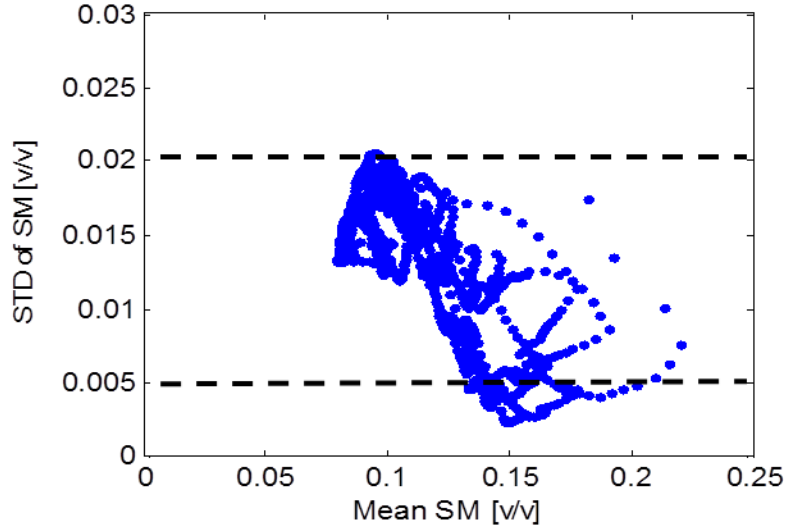
Figure 4.19. The simulated hourly spatially mean (x-axis) and standard deviation (STD, y-axis) of the top 20-cm soil moisture within the simulation domain (blue dots), and the range of the spatial STD of the top 20-cm soil moisture derived from the observation (black dash lines). The simulation results or observation range for top 40-cm soil moisture are not shown.
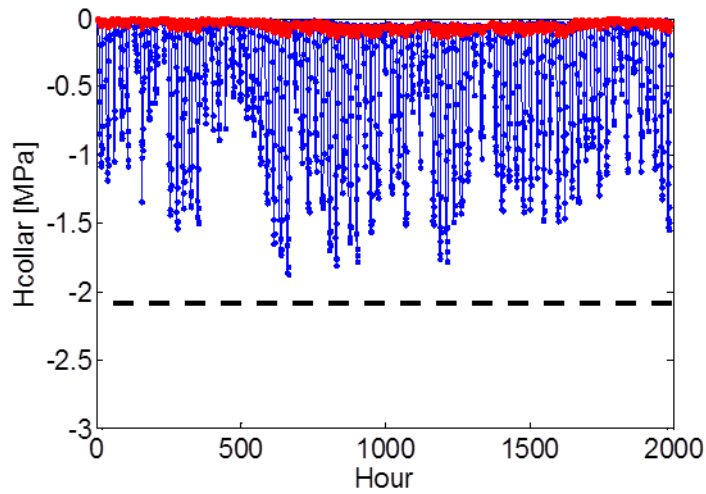
Figure 4.20. The simulated time series of water potential at the root collar for a small tree of a 5-cm DBH (red line), or a large tree of 74-cm DBH (blue line), and the estimated range of water potentials at the root collar by observation datasets (black dash line).

4.7.2 Compensation effect in 3-D root water uptake process

The generated plot-scale transpiration from the 1-D or 3-D simulation cases was compared. As shown in Figure 4.21, while the 1-D finely-resolved simulation case exhibits constrained actual transpiration, the 3-D simulation case shows actual transpiration with similar magnitude as the potential transpiration.

The difference of the cumulative actual transpiration between the two simulation cases mainly occurs between hour 800 and 1750, when the transpiration in the 1-D finely-resolved simulation case is constrained by the "Feddes-type" water stress factor β. When the shallow soil layer with a large amount of root biomass is dry, e.g., the top 20-cm soil layer that contains over 50% of the root biomass approaches the wilting point (~4% to 5% $[m^3 \ m^{-3}]$), the water stress factor is smaller than 1. The fractional root water uptake at deeper layers cannot be larger than its fractional root biomass in the root zone even when it is relatively wet (e.g., above 8% $[m^3 \ m^{-3}]$) (Figure 4.11). For example, the soil layer of 60–80 cm has a fractional root biomass of 6%; as a result, the maximum fractional water uptake from this layer is 6%.
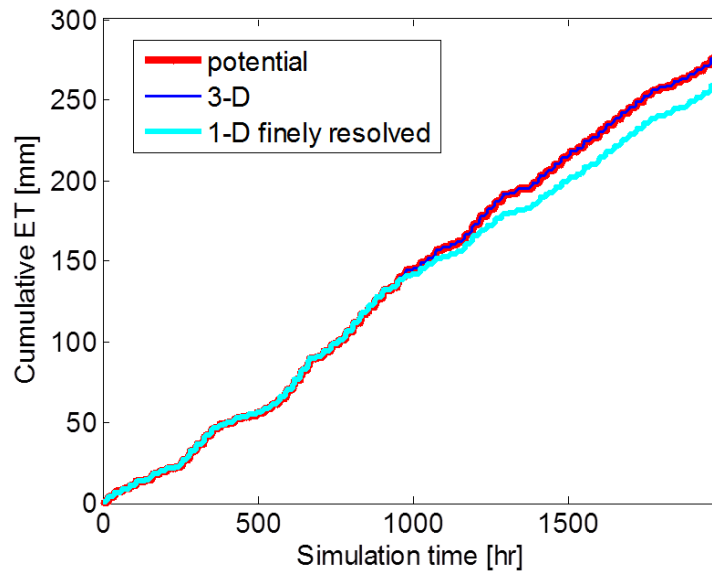
Figure 4.21. The cumulative plot-scale potential transpiration ("potential", red line), the simulated transpiration from the 3-D simulation case ("3-D", blue line), and simulated transpiration from the -D finely resolved simulation case ("1-D finely resolved", cyan line). The 3-D simulation case shown here used scenarios of the benchmark lateral spread and spatially uniform rooting depth.

The 3-D simulation case, on the contrary, demonstrates dynamic changes of the fractional root water uptake across soil layers in accordance with the overall soil wetness condition (Figure 4.22). For example, during hours when soil layers at depths are wet (e.g., the soil water content within the root zone is above 8% [m^3 m^{-3}]), more than 70% of the total water uptake of a root system takes place from the first 40-cm soil layer (Figure 4.22a). During hours when shallow soil layers become dry (e.g., the soil water content within the top 20 cm is below 8% [m^3 m^{-3}]), the simulated amount of root water uptake from the 40-80 cm soil layer could reach as much as 65% of the total potential transpiration of an individual tree, while the fractional water uptake from shallower layers (e.g., top 40 cm) decreases to ~35% (Figure 4.22b). In summary, in relatively dry conditions, the 3-D simulation case demonstrates the capacity of a root system to compensate

the decreased root water uptake in the water-stressed regions by increasing water uptake in relatively moister regions, generating a plot-scale actual transpiration equal to the potential transpiration.
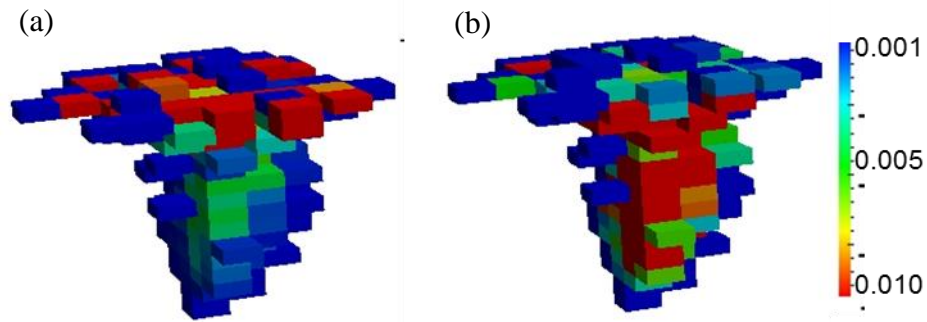
Figure 4.22. The fractional root water uptake at soil grid cells for a root system with a DBH of 40 cm in benchmark scenario of lateral spread at (a) hour 542 when the soil layers at depths were wet, and at (b) hour 1692 when shallow soil layers were dry and deep soil layers were relatively wetter.

4.7.3 Sensitivity of plot-scale water stress to root architecture: lateral spread and rooting depth

Lateral spread

Simulation cases using different scenarios of lateral spread were compared, in terms of plot-scale water stress, strength of the "compensation effect", and spatial variation of soil moisture.

As shown in Figure 4.23, the simulation cases with the small scenario of lateral spread generate water-stressed transpiration; the cumulative plot-scale transpiration at the end of the simulation is smaller than the potential value by ~14 mm or ~10 mm, for the 3-D simulation case or the synthetic simulation case. The water-stressed transpiration occurs when some trees reach the threshold water potential at the root collar (Figure 4.24).

The value of the water potential at the root collar depends on the soil water content in soil grid cells, transpiration demand, and the property of the root system such as K_{comp} (Equation (4.5)). For any simulation hour, with a given soil water potential condition and transpiration demand of any root system, a threshold $\tilde{K}_{comp}$ can be estimated (Equation (4.23)). Given a specific uptake rate, if K_{comp} of a root system is smaller than the calculated $\tilde{K}_{comp}$, then water potential at the root collar would reach the threshold value, leading to a water-constrained transpiration rate.

$$\tilde{K}_{comp,p} = T_{potential,p} / (\sum_{j=1}^{M} H_{s,j} SSF_{j,p} - H_{threshold})$$ (4.23)

To examine the role of K_{comp} in determining the water stress, values of $\tilde{K}_{comp}$ for root systems were estimated for each simulation hour in all simulation cases with different scenarios

of lateral spread. As shown in Figure 4.25, for all trees at any simulation hour, the value of $\tilde{K}_{comp}$ is positively proportional to the potential transpiration. As an example, for the tree of 74-cm DBH (Figure 4.25f), at hours when transpiration demands are higher than 0.020 [$kg\ s^{-1}$], the value of K_{comp} has to be larger than 8×10^{-8} [$m^2\ s^{-1}$] to avoid water-constrained transpiration. As shown in the Figure 4.12a, in the benchmark and large scenarios of lateral spread (red and cyan lines), the values of the K_{comp} of the root systems with the 74-cm DBH are all above 8×10^{-8} [$m^2\ s^{-1}$]; therefore the tree in those two scenarios of lateral spread is not water stressed and has the actual transpiration equals to the potential value. On the contrary, in the small scenario of lateral spread, the value of K_{comp} could be smaller than 8×10^{-8} [$m^2\ s^{-1}$], depending on which root network is assigned to this tree of 74-cm DBH. As the same, trees of other size in the small scenario of lateral spread have relatively smaller values of K_{comp} as compared with benchmark or large scenarios of lateral spread, the smaller values of K_{comp} in the former simulation case result in occasional water-stressed transpiration (Equation (4.5) and (4.6)).
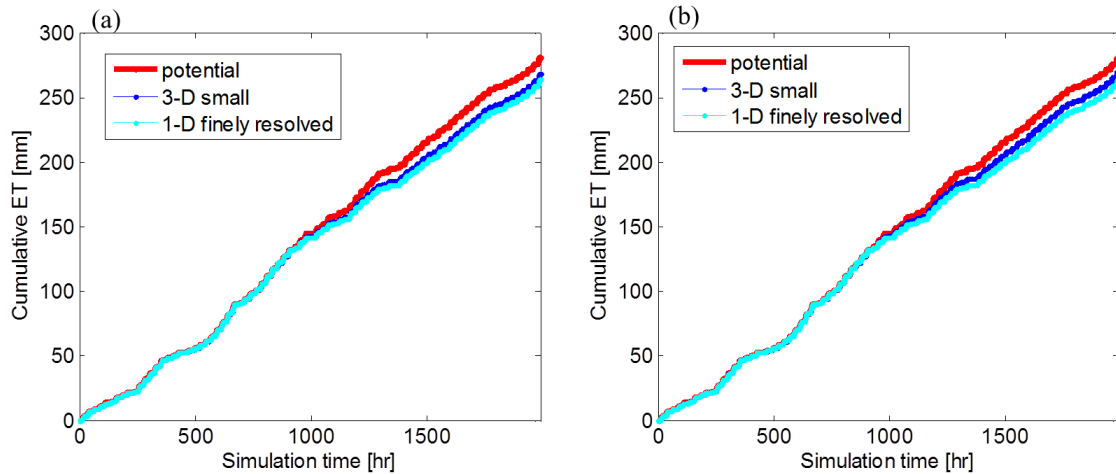
Figure 4.23. The cumulative plot-scale transpiration generated by using (a) the spatially scaled root networks or (b) the synthetic fractional potential root water uptake, from the small scenario of lateral spread ("3-D small", blue lines), or transpiration generated by the 1-D finely resolved simulation case ("1-D finely resolved", cyan lines), as compared to potential transpiration ("potential", red lines). The cumulative transpiration by those two 3-D approaches in (a) and (b) is smaller than the potential by 14 and 10 [mm], respectively.
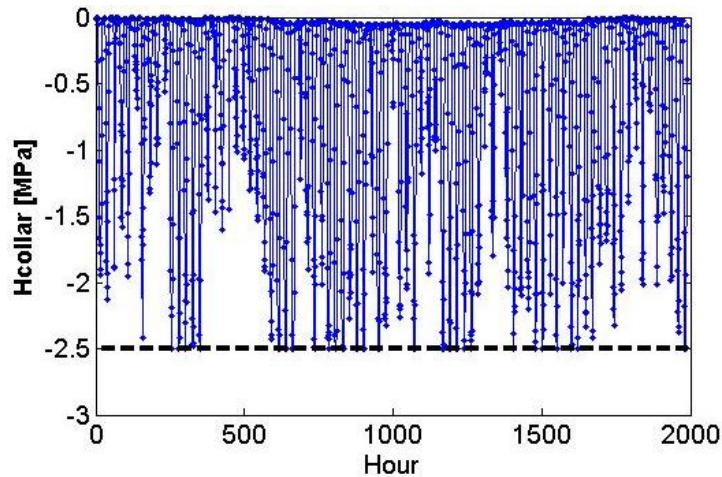
Figure 4.24. The time series of water potential at root collar (y-axis) for a tree of DBH equals to 74 cm in the small scenario of lateral spread. The water potential at root collar reached the threshold value of -2.5 *MPa* occasionally, when the boundary condition changed from flux (i.e., potential transpiration) to a fixed water potential at the root collar.
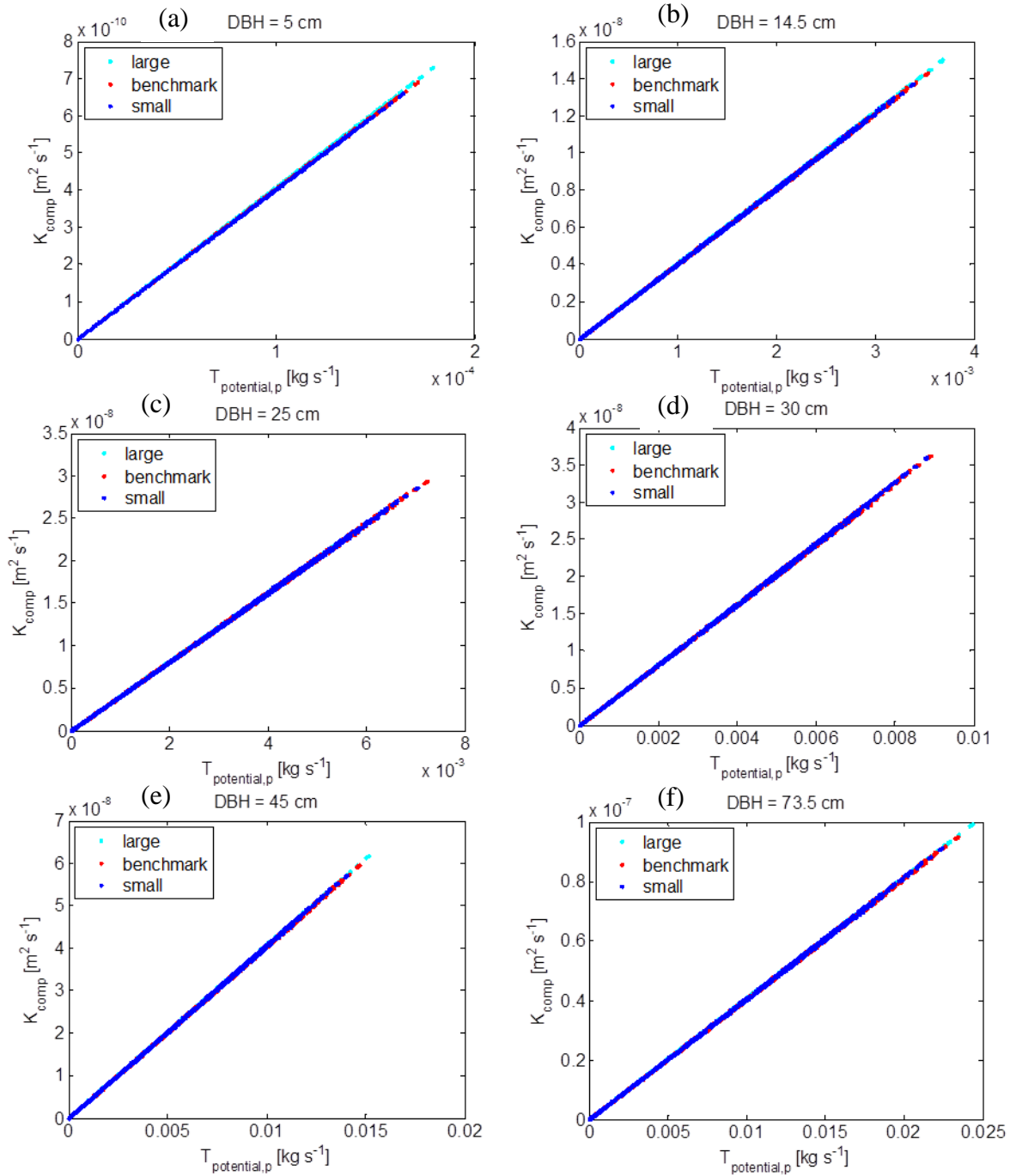
Figure 4.25. A relationship between the $\tilde{K}_{comp}$ (y-axis) and the potential transpiration of root system p ($T_{potential,p}$, x-axis) for each simulation hour, in the small (blue dots), benchmark (red dots), and large (cyan dots) scenarios of lateral spread. The shown root systems were derived for trees with a DBH of (a) 5 m, (b) 15 m, (c) 25 m, (d) 30 m, (e) 45 m, and (f) 74 m.

The above simulation cases show similarities in the "compensation effect" within the simulation domain. As shown in Figure 4.26, in all scenarios, the compensatory term $UF2_k$ of soil grid cells (defined in Section 4.5.3) tends to be negative (positive) in relatively dry (wet) soil grid cells. This means that the root systems decrease (or increase) their root water uptake fractions from these relatively dry (or wet) regions due to the spatially varying hydraulic gradients, as compared to that if the soil water potential is spatially uniform. In the scenario of the benchmark and large lateral spread, the domain-aggregated $UF2_k$ of the positive sign equals to the total sum of the negative $UF2_k$ in all simulation hours, indicating the increased amount of root water uptake by root system in the wetter region is entirely compensated by the decreased root water uptake in drier regions. As mentioned in Section 4.5.3, the sign of the compensatory uptake fraction of a soil grid cell depends on its soil water potential as compared to that in other soil grid (H_s). As shown in the Equation (4.24), a threshold value of soil water potential $\tilde{H}_{s,k}$ can be estimated for each grid cell, such that if the actual soil water potential is below this threshold, the compensatory water uptake would be negative.

$$\tilde{H}_{s,k} = \frac{\sum_{p=1}^{N}(K_{comp,p} SUF_{k,p}(\sum_{j=1}^{M} H_{s,j} SUF_{j,p}))}{\sum_{p=1}^{N} K_{comp,p} SUF_{k,p}}$$ (4.24)

Additionally, these scenarios demonstrate different strengths of the "compensation effect" (Figure 4.27). As an example, at hour 1650, the total sum of the compensatory uptake fraction $UF2_k$ that has a positive sign in the domain for the scenarios of small, benchmark, or large lateral spread is 0.0053, 0.0121, and 0.3915 [-], respectively. The simulation case of the large lateral spread demonstrates the strongest "compensation effect", which is due to the fact that this

scenario exhibits root systems with the largest values of K_{comp} as compared to other scenarios.
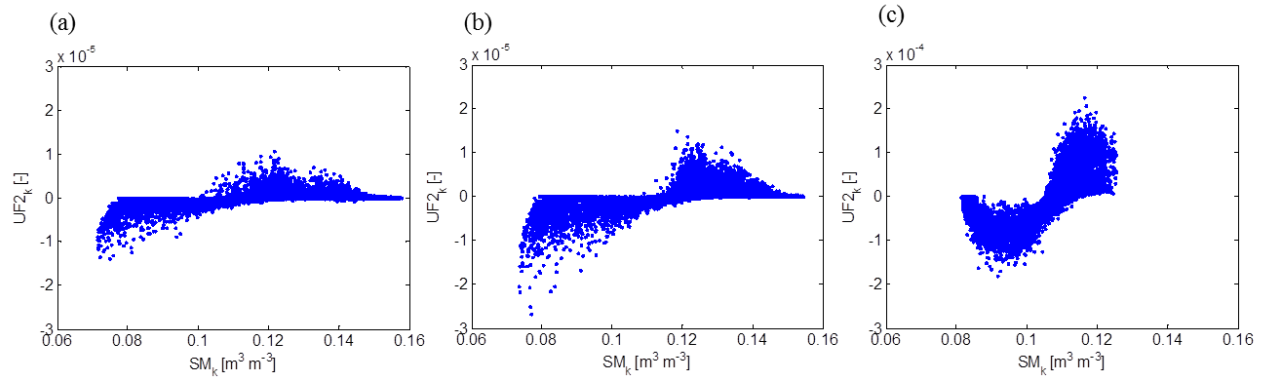
Figure 4.26. The relationship between the compensatory term $UF2_k$ (y-axis) and soil moisture SM_k for soil grid cells that contain roots, in scenario of (a) small lateral spread, (b) benchmark lateral spread, and (c) large lateral spread, for simulation hour 1692. The definition of $UF2_k$ was described in Section 4.5.3.
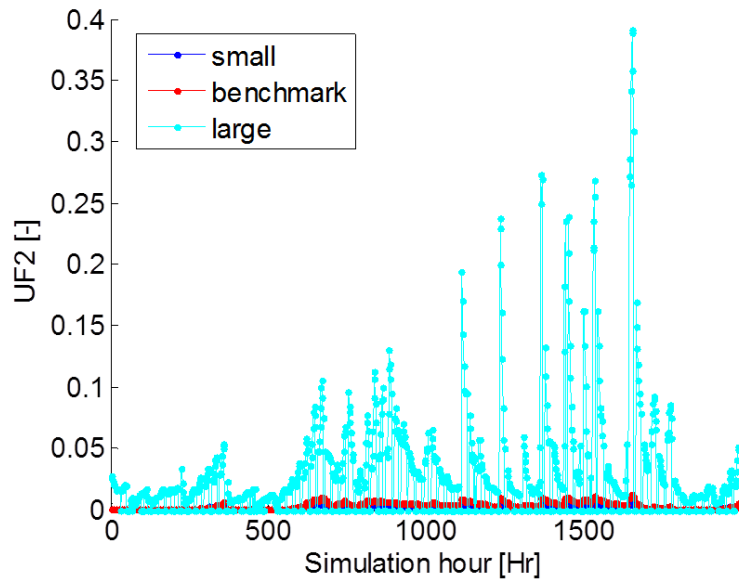
Figure 4.27. The time series of domain-aggregated $UF2_k$ [-] that has positive sign for simulation case with small (blue), benchmark (red), and large (cyan) lateral spread.

The simulation case with the small scenario of lateral spread has the largest amount of spatial variations of soil moisture as compared with other scenarios (Figure 4.28b, d). This is not surprising as the root systems in the small spread scenario are confined to small soil volumes, creating localized dry spots. At the same time, the simulation case with small scenario of lateral spread has the largest amount of soil water content for hour ~800 to hour ~1600 (Figure 4.28a, c), this is because the total root water uptake of root systems in this scenario is less than that in other scenarios due to the water-constrained transpiration (Figure 4.23). An interesting implication is that, although the small scenario of lateral spread exhibits the largest soil water storage in the domain as compared to the other scenarios, the trees are more likely to be water-stressed due to the spatial heterogeneity of soil water potential and the existence of local dry spots. In other words, the small scenario of lateral spread results in a less efficient water use.

The synthetic simulation cases show slightly smaller spatial variations of soil moisture in the root zone than the 3-D simulation cases (Figure 4.29 and Figure 4.30). For example, for a simulation hour 1692, the standard deviation of spatial soil moisture within the root zone of these two sets of simulation cases is 1.7% versus 1.9% (the small scenario of lateral spread), 0.7% versus 1.1% (the benchmark scenario of lateral spread), and 0.2% versus 0.2% (the large scenario of lateral spread). Those two sets of simulation case have similar drainage out of the root zone (Figure 4.31). Considering the small amount of differences between those two sets of simulation, it is safe to conclude that the scaling procedure of root network (into root system with different lateral spread) did not introduce significant "artificial" spatial heterogeneity of root water uptake as described in Section 4.5.2.
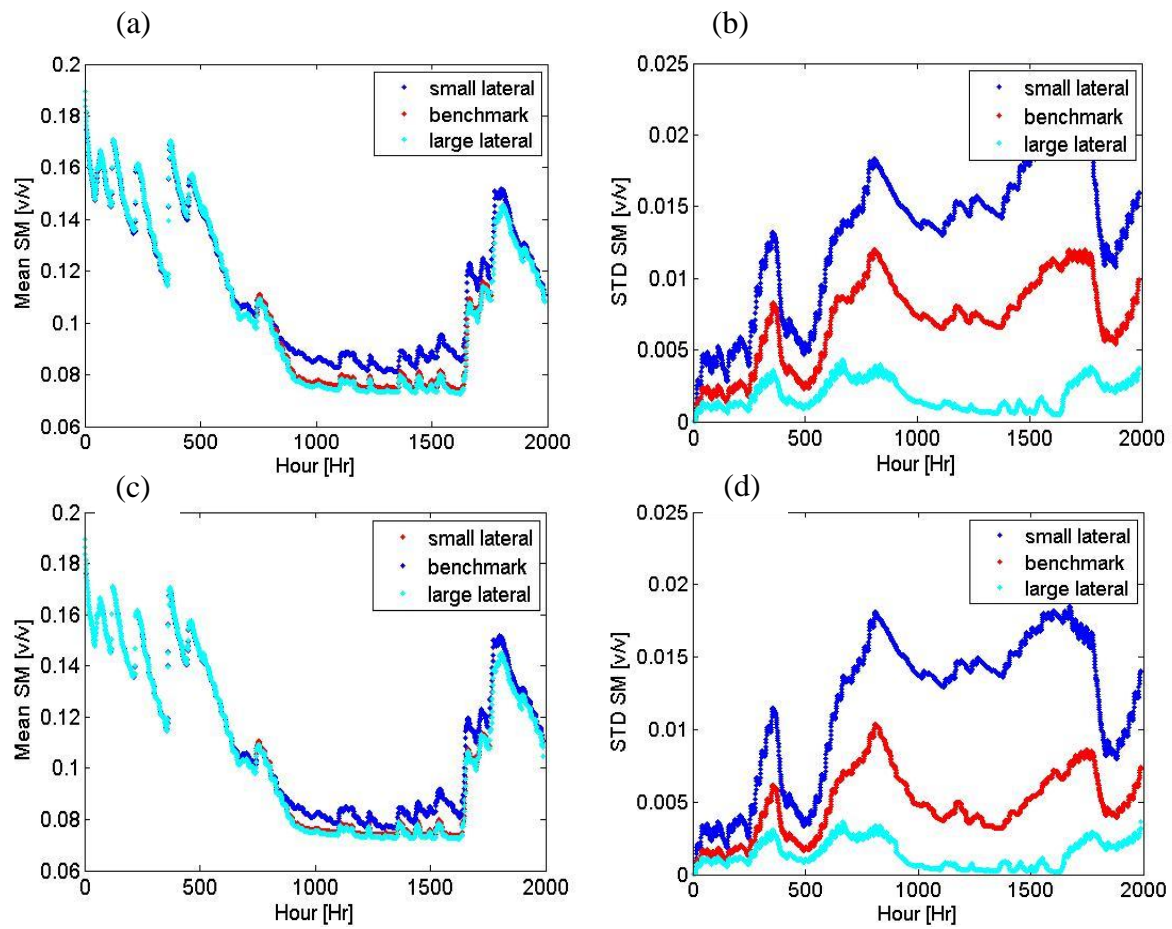
Figure 4.28. The time series of (a, c) spatial mean and (b, d) standard deviation of soil moisture $[m^3\ m^{-3}]$ within the root zone (top 80 cm), for simulation with (a, b) scaled root network or (c, d) synthetic potential root water uptake fractions. The scenarios of lateral spread are small, benchmark, and large.
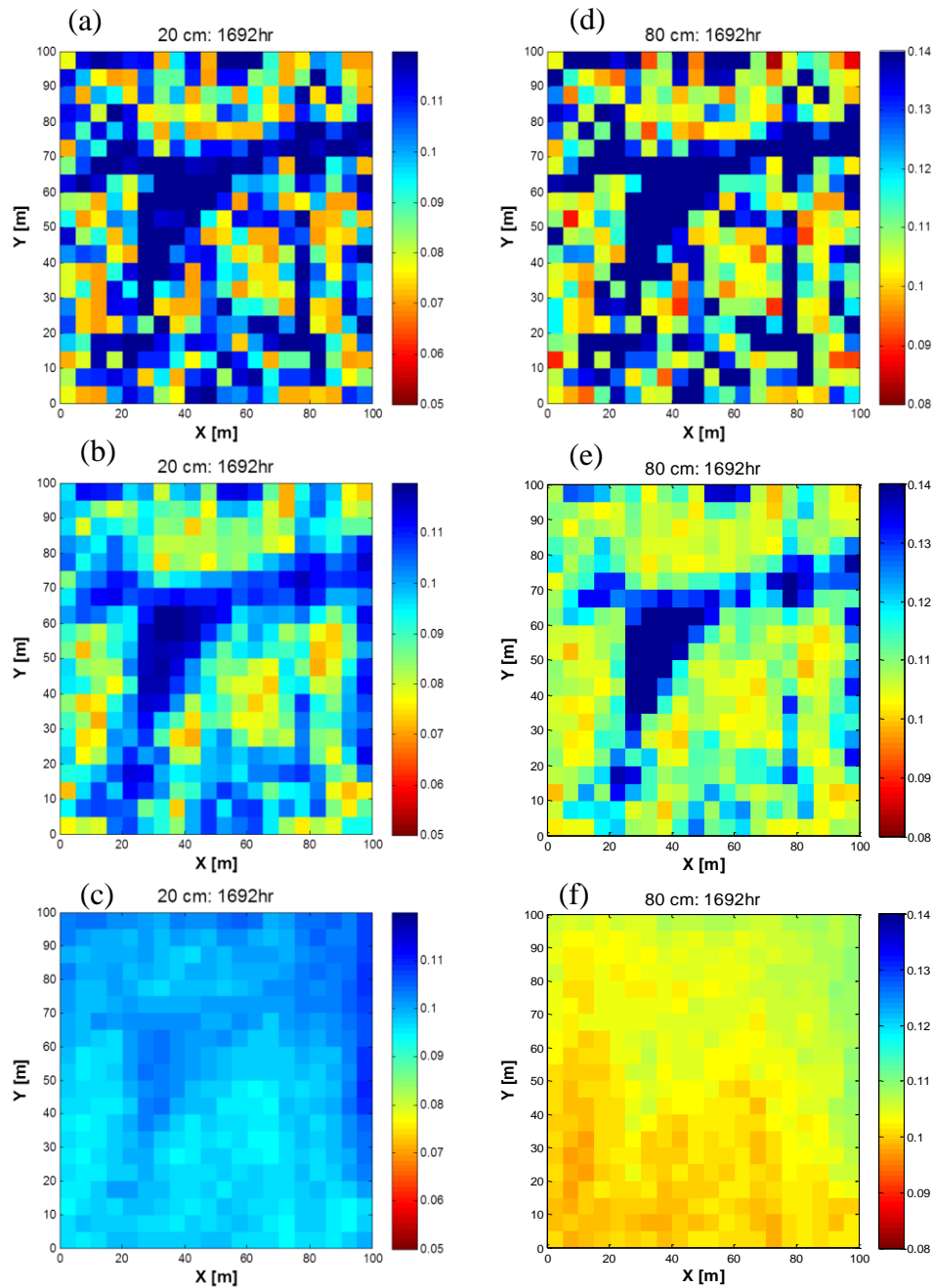
Figure 4.29. The spatial distribution of soil moisture [m^3 m^{-3}] within (a, b, c) the top 20 cm or (d, e, f) the top 80 cm at a simulation hour (hour 1692). The simulation cases with the scaled root network and scenarios of (a, d) small lateral spread, (b, e) benchmark lateral spread, and (c, f) large lateral spread. All simulation cases shown here used the scenario of spatially uniform rooting depth. The spatial distribution of the top 20-cm soil moisture in these three scenarios showed a similar mean value of 12% or 11% [m^3 m^{-3}], and a standard deviation of 1.1%, 0.6%, and 0.5%, respectively.
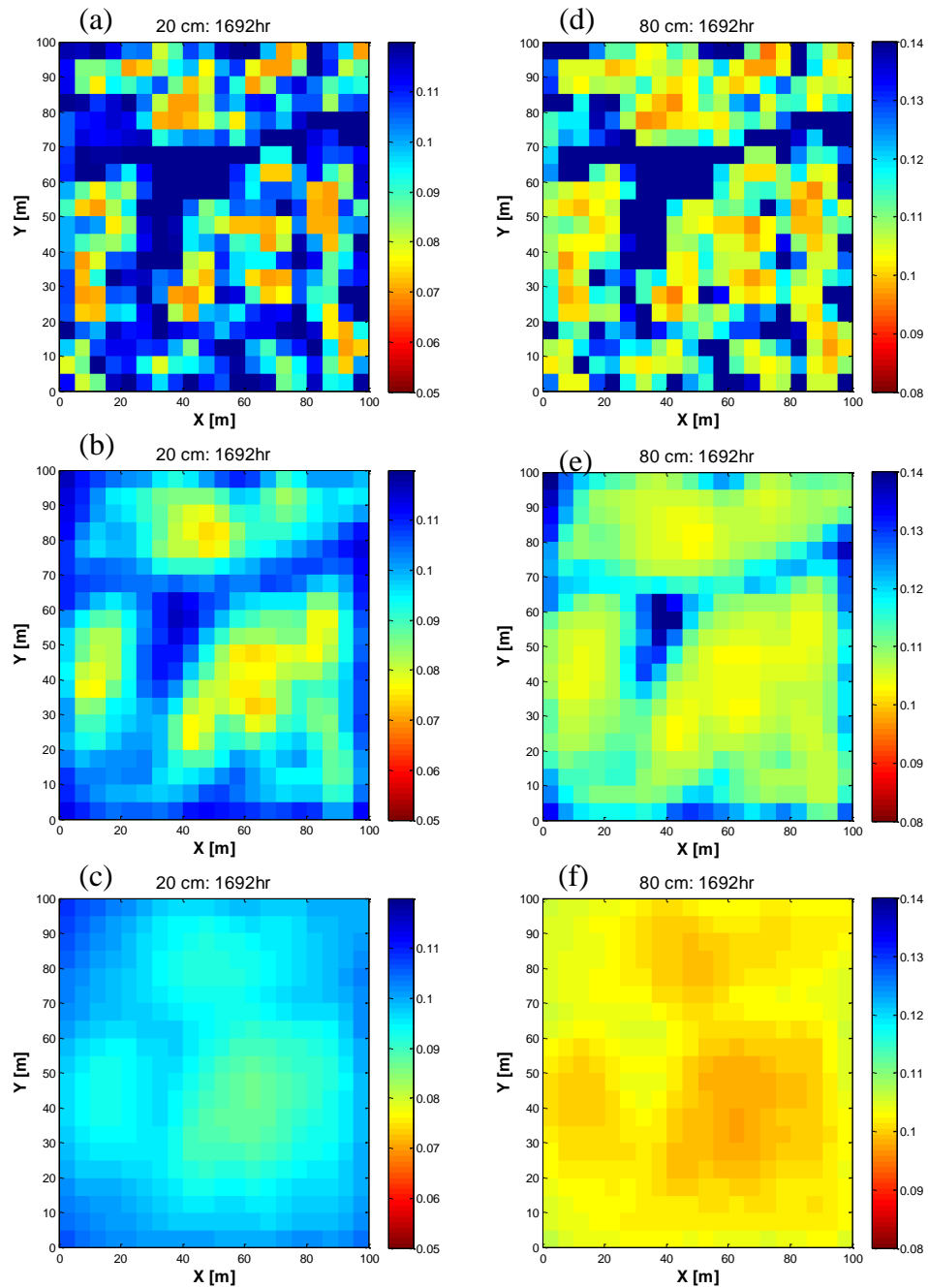
Figure 4.30. The spatial distribution of soil moisture [$m^3\ m^{-3}$] with (a, b, c) the top 20 cm or (d, e, f) the top 80 cm at a simulation hour (hour 1692). The simulation cases with the synthetic fractional potential root water uptake and scenarios of (a, d) small lateral spread, (b, e) benchmark lateral spread, and (c, f) large lateral spread. All simulation cases shown here used the scenario of spatially uniform rooting depth. The spatial distribution of the top 20-cm soil moisture in these three scenarios showed a similar mean value of ~11% or 10% [$m^3\ m^{-3}$], and a standard deviation of 0.9%, 0.5%, and 0.2%, respectively.
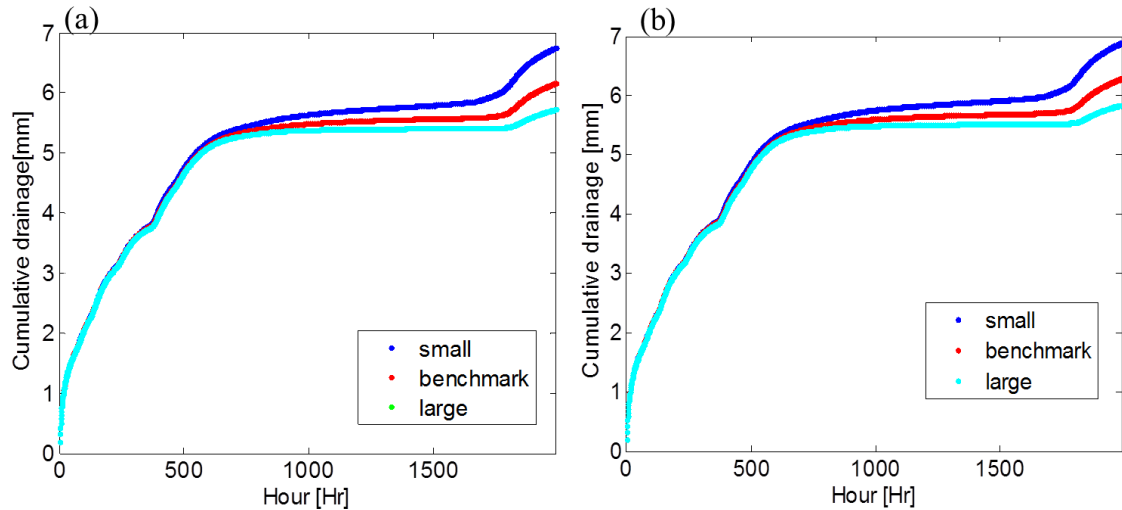
Figure 4.31. The cumulative drainage at the bottom of root zone (80 cm) for (a) 3-D simulation cases and (b) synthetic simulation cases, with scenario of small, benchmark, and large lateral spread.

To better understand how the overlapped root zones influence the dynamics of uptake and the spatial variability of soil moisture, three sets of "standalone" simulations were conducted with a single or two trees in the simulation domain. The first set of "standalone" simulations has a single tree of 25-m DBH in the domain. This tree is referred as "Tree1" hereafter (Figure 4.32). This set of "standalone" simulations contains three cases which correspond to the root system of different lateral spread: small scenario (blue circles), benchmark scenario (red circles), or large scenario (cyan circles). In the second set of "standalone" simulation, an additional tree of 25-m DBH was introduced in the domain and those two trees are located 20-m away from each other (Figure 4.32), this tree is referred as "Tree2" hereafter. This set of simulation also contains three cases corresponding to the lateral spread scenarios of small, benchmark, or large lateral spread. The third set of simulations also has two trees in the domain, but those two trees were located closer with each other, e.g., 10 m, or 5 m (Figure 4.35a, b, and c; and Figure 4.36a, b, and c). This set of simulation contains cases corresponding to the lateral spread scenarios of benchmark and large. All of the simulation cases here have the time series of averaged tree-scale

transpiration demand and the net precipitation as used in the plot-scale simulations.
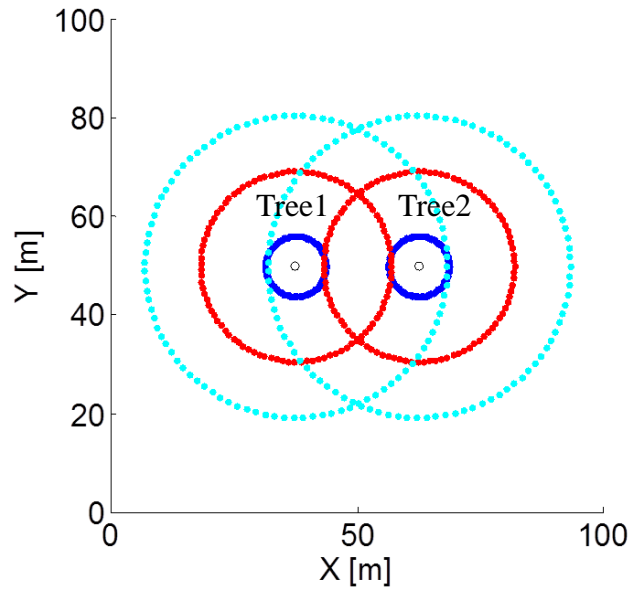
Figure 4.32. A conceptual sketch of two trees (grey dots, "Tree1", and "Tree2") of 25-cm DBH that are located 20-m apart. Their root lateral spreads are 6 m, 19 m, and 30 m in scenarios of small (blue), benchmark (red), and large (cyan), respectively. The trees were assigned with the median values of the K_{comp} inferred from the five root networks. Specifically, the K_{comp} is 5.6 $\times 10^{-8}$, 1.4×10^{-7}, and 1.8×10^{-7} [$m\ s^{-2}$] for the lateral spread scenario of the small, benchmark, and large, respectively.

The first set of simulations with a single tree was compared with the second set of simulations with two trees, to examine how the existence of a neighboring tree influences the spatial pattern of root water uptake. The effect of introducing a neighboring tree Tree2 is found to be sensitive to the scenario of lateral spread. For the small scenario of lateral spread, the spatial pattern of root water uptake of a Tree1 does not change significantly when the neighboring Tree2 is introduced (Figure 4.25a, b). This is consistent, as the root systems in this scenario are small and do not have overlapped root zones. In simulations with the scenarios of benchmark or large lateral spreads, for Tree1 without a neighboring tree, the root water uptake is symmetrical with respect to the stem location. That is, the tree takes up half of its total transpiration from the left and right side of the soil domain. When the neighboring Tree2 is introduced to its right, Tree1 is shown to uptake more water uptake from the soil domain on its left side, as this region has more soil water than the soil domain on its right.

Specifically, the effect of the overlapped root zone on the spatial pattern of root water uptake was quantified by examining the spatial distribution of the compensatory term $UF2_k$ (Figure 4.35 and Figure 4.36). The total $UF2_k$ of Tree1 in the soil domain on its left or right side was calculated and compared among simulation cases in the second and third sets of simulations, which involve different overlapped root zone areas with Tree2. As an example, in the simulation case with two trees located 5-m away (Figure 4.35a), averaged over all simulation hours when there are transpiration demands (Figure 4.35d), the total $UF2_k$ of Tree1 from the soil domain to its left is 0.07 [-] versus -0.07 [-] from the soil domain to its right where the neighboring Tree2 is located. This means Tree1 increases its root water uptake in the relatively wetter soil domain to its left by an amount of 7% of the total transpiration of the two trees (see the definition of $UF2_k$ in Equation (4.8) and Equation (4.9)), compensating the decreased root water uptake in the

relatively drier soil domain to its right. This expresses the adjustment of fractional root water uptake of trees as a result of the competition of water resources with neighboring trees. If the neighboring Tree2 is located further away (e.g., 10-m, or 5-m), as the overlapped root zone area and the associated water competition among trees is decreased, the adjustment of fractional root water uptake by Tree1 tends to be less (as shown in Figure 4.37, moving from the left side to the right side). The spatial pattern of root water uptake Tree1 in the simulation cases with the large scenario of lateral spread (Figure 4.36a, b, c) is less affected by the existence of neighboring Tree2, as compared to that with the benchmark scenario of lateral spread. This is mainly because in the former simulation cases, the transpiration demand is distributed in a relatively larger soil space, thus the difference of soil moisture in the overlapped and non-overlapped zone is less than that in the latter simulation cases.

Tree1 in all the simulation cases demonstrates consistent compensatory effect in the vertical direction, regardless the extent of overlapped root zones with Tree2 (Figure 4.38). For example, when the top 20-cm soil layer is relatively drier as compared to the root-zone average situation, the temporally-averaged total $UF2_k$ from Tree1 within the top 20-cm layer (or deeper layer) is negative (or positive) (Figure 4.35g, h, i; and Figure 4.36g, h, i). This means the root system decreases root water uptake from the dryer shallow layer and increases the uptake from the deeper and more moisture layer. Vice versa, when the deeper soil layer is relatively drier, the root system uptakes more water from the shallower and wetter layer, to compensate the decreased uptake from the deeper and drier layer (Figure 4.35j, k, m; and Figure 4.36j, k, m).
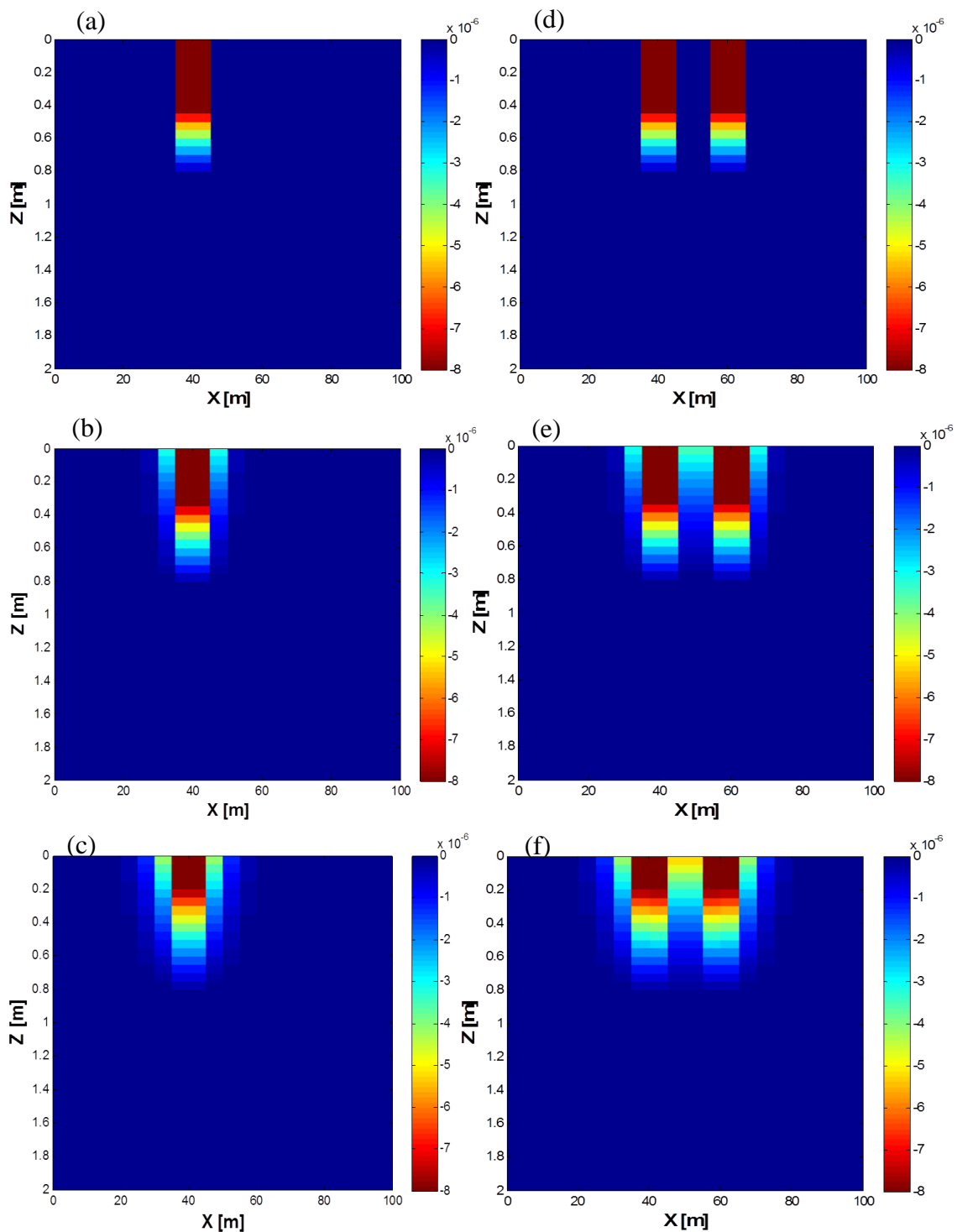
Figure 4.33. The spatial distribution of the hourly averaged root water uptake (in an unit of [*kg s⁻¹*]) at soil grid cells on the vertical plane of y = 50 m, for (a, b, c) the first set of "stand-alone" simulation cases with only one tree, or (d, e, f) the second set of "stand-alone" simulation cases with two trees and overlapped root zone, with scenarios of (a, d) small, (b, e) benchmark, and (c, f) large lateral spread.
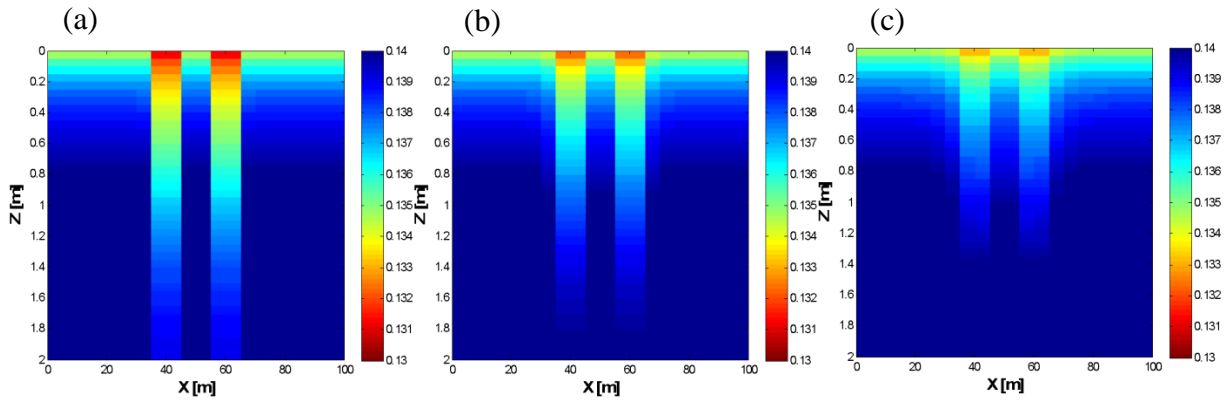
Figure 4.34. The spatial distribution of the hourly averaged soil moisture (in an unit of $[m^3\ m^{-3}]$) at the vertical plan of y = 50 m, for the second set of "standalone" simulation in in which two trees are located 20-m apart, and with scenarios of (a) small, (b) benchmark, or (c) large lateral spread.
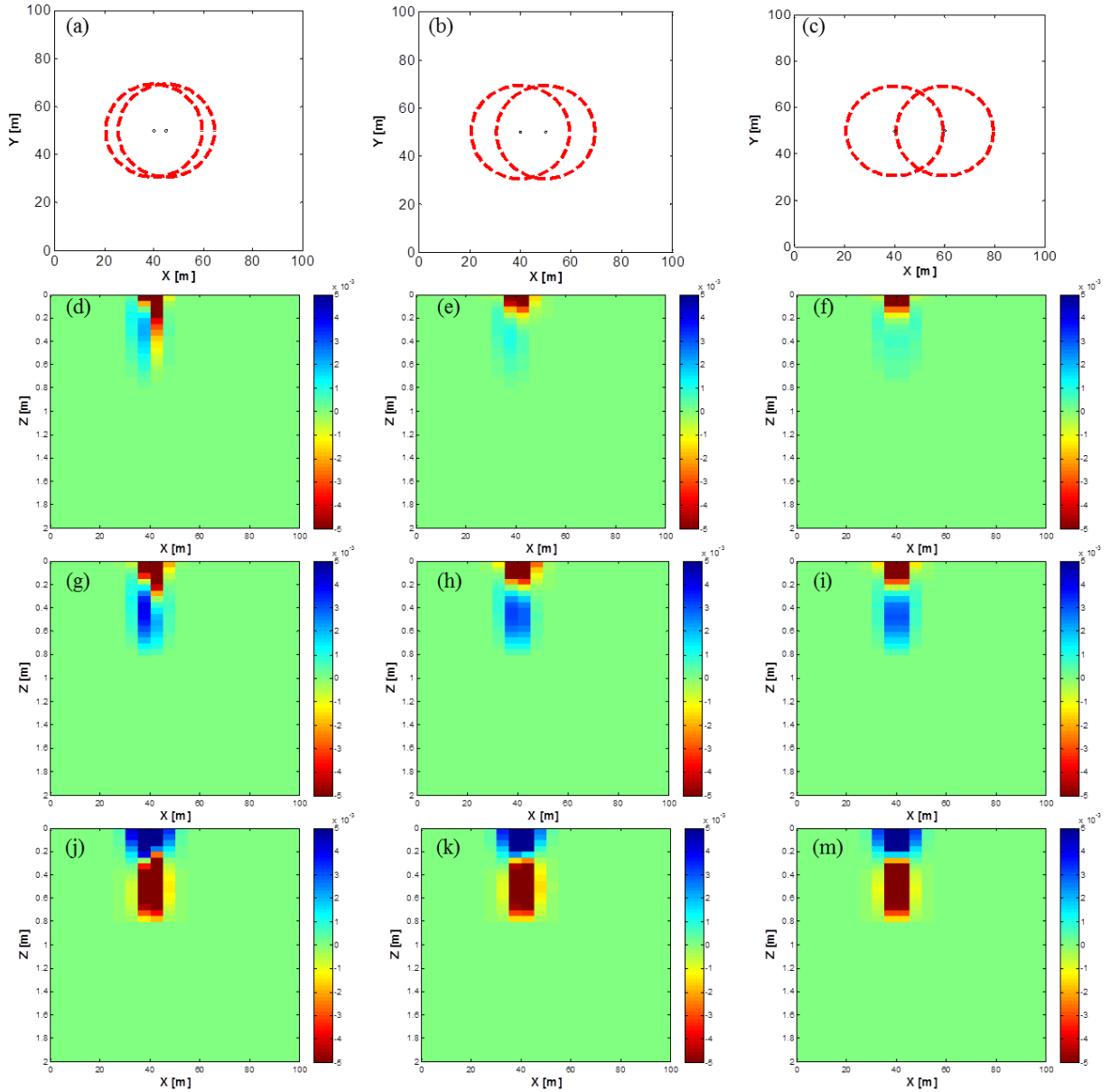
Figure 4.35. The location of Tree1 (black circle on the left) and Tree2 (black circle on the right) in simulation cases where they are located (a) 5-m, (b) 10-m, or (c) 20-m away and with the benchmark scenario of lateral spread (red circles); and the temporally-averaged compensatory term $UF2_k$ (in an unit of [-]) of Tree1 at soil grid cells on the vertical plane of y = 50 m where Tree1 and Tree2 are located (d, g) 5-m, (e, h) 10-m, or (f, i) 20-m away, over all simulation hours with transpirational demand (d, e, f), or over simulation periods when the soil in the top 20-cm depth is (g, h, i) drier or (j, k, m) wetter than the soil in the root zone.
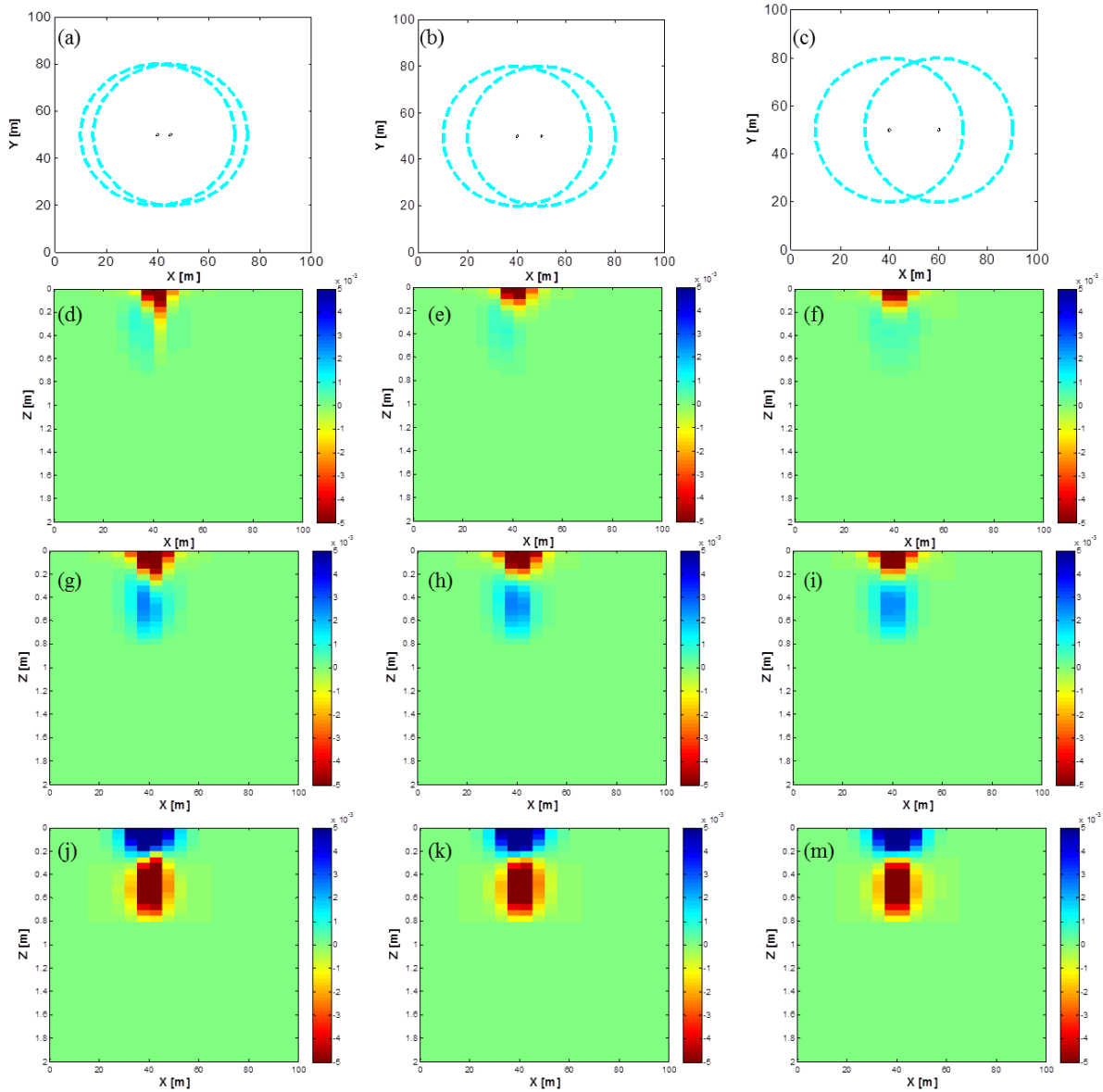
Figure 4.36. The location of Tree1 (black circle on the left) and Tree2 (black circle on the right) in simulation cases where they are located (a) 5-m, (b) 10-m, or (c) 20-m away and with the large scenario of lateral spread (cyan circles); and the temporally-averaged compensatory term $UF2_k$ (in an unit of [-]) of Tree1 at soil grid cells on the vertical plane of y = 50 m where Tree1 and Tree2 are located (d, g) 5-m, (e, h) 10-m, or (f, i) 20-m away, over all simulation hours with transpiration demand (d, e, f), or over simulation periods when the soil in the top 20-cm depth is (g, h, i) drier or (j, k, m) wetter than the soil in the root zone.
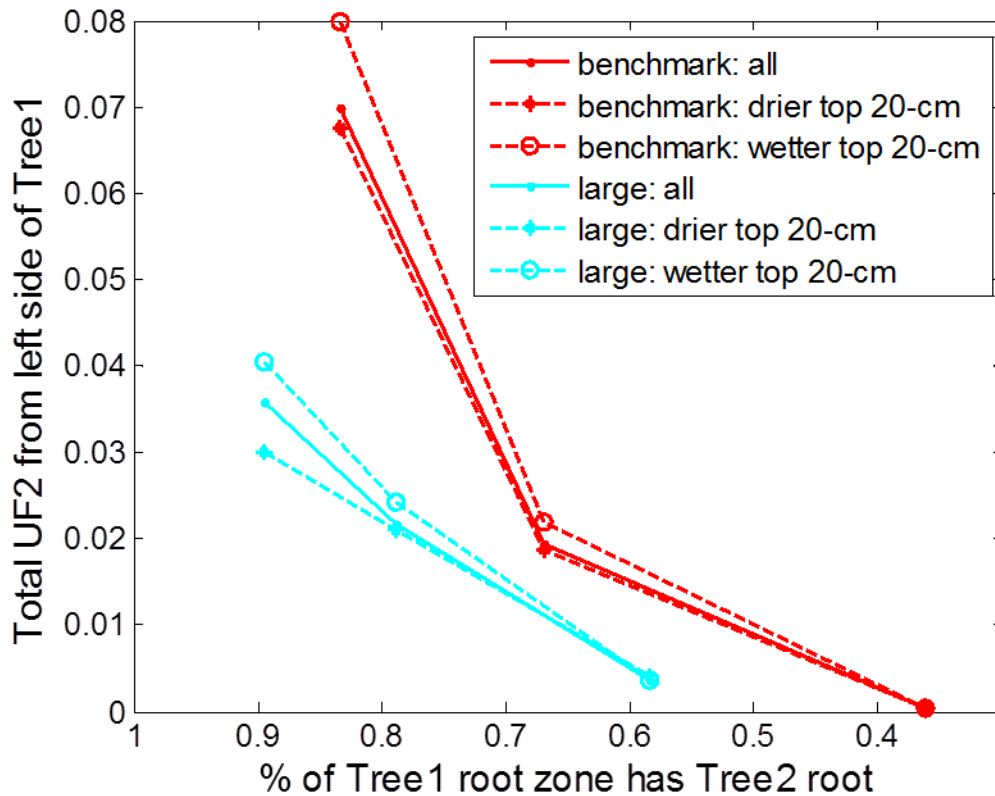
Figure 4.37. The relationship between the percentage of Tree1 root zone that has the overlap with the Tree2 root zone (x-axis) and the temporally-averaged total compensatory term $UF2_k$ (in an unit of [-]) in the soil domain to the left of Tree1 (y-axis) for simulation cases with scenarios of benchmark (red colors) or large lateral spread (cyan colors), during all simulation hours ("benchmark: all", "large: all"), or simulation hours when the top 20-cm layer is drier than the root zone ("benchmark: drier top 20-cm", " large: drier top 20-cm"), or simulation hours when the top 20-cm layer is wetter than the root zone ("benchmark: wetter top 20-cm", "large: wetter top 20-cm"). From the left to the right, the corresponding simulation cases are two trees located 5-m, 10-m, and 20-m away.
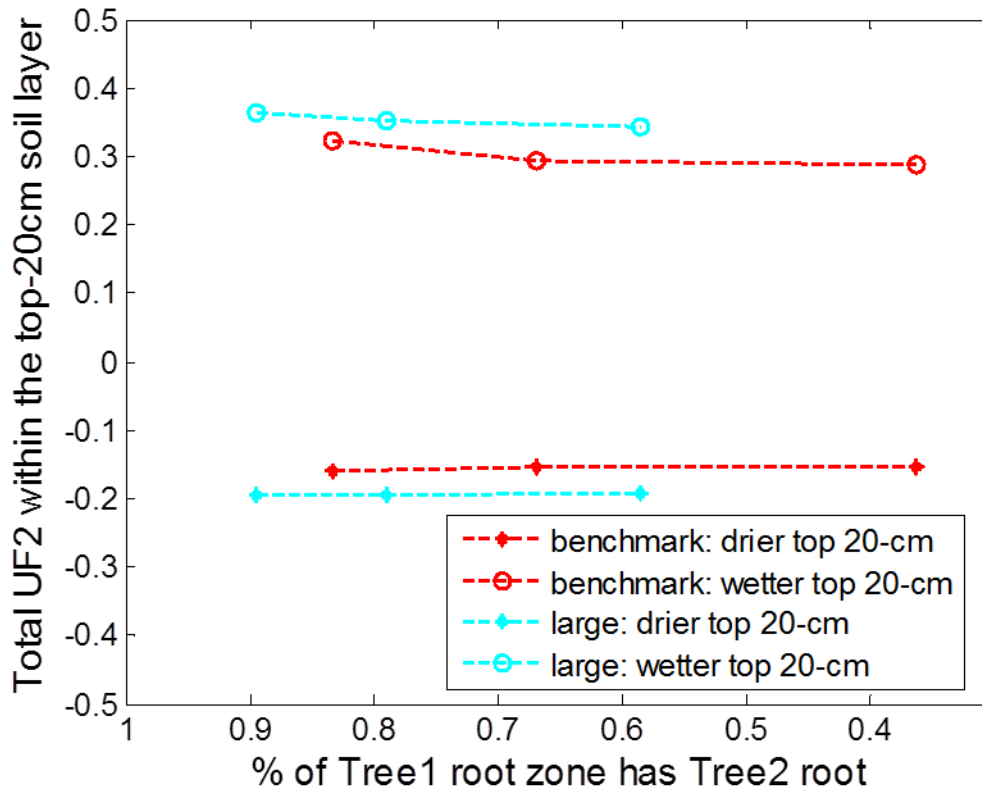
Figure 4.38. The relationship between the percentage of Tree1 root zone that has the overlap with the Tree2 root zone (x-axis) and the temporally-averaged total compensatory term $UF2_k$ (in an unit of [-]) in the top 20-cm layer (y-axis) for simulation cases with scenarios of benchmark (red colors) or large lateral spread (cyan colors), over simulation hours when the top 20-cm layer is drier than the root zone ("benchmark: drier top 20-cm", " large: drier top 20-cm"), or simulation hours when the top 20-cm layer is wetter than the root zone ("benchmark: wetter top 20-cm", "large: wetter top 20-cm"). From the left to the right, the corresponding simulation cases are two trees located 5-m, 10-m, and 20-m away.

Rooting depth

Results from the simulation cases using scenarios of spatially uniform or varying rooting depths are compared. As expected, the simulation case with the spatially varying rooting depth shows more spatially heterogeneous distribution of the root water uptake (Figure 4.39), as some root systems can uptake water from soil layers deeper than 80 cm. The spatial distribution of soil moisture from those two sets of simulation cases showed slightly different spatial distribution of soil moisture (Figure 4.40).
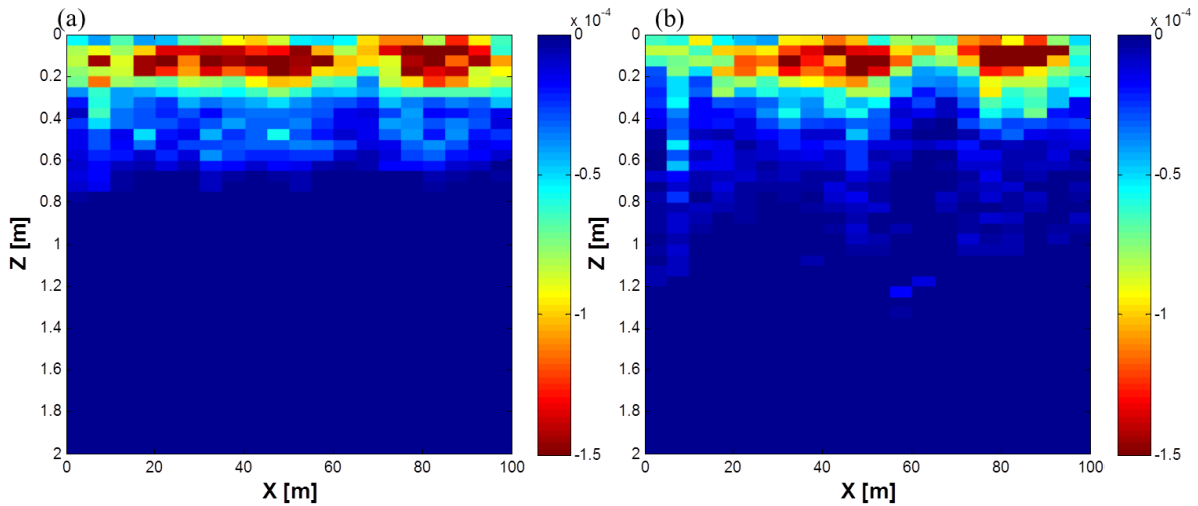
Figure 4.39. The spatial distribution of the hourly averaged root water uptake (in an unit of [$kg\ s^{-1}$]) at soil grid cells on the vertical plane of y = 50 m, for simulation case of (a) spatially uniform rooting depth, and (b) spatially varying rooting depth. The shown figures are from simulation cases with benchmark scenario of lateral spread.

Although those two sets of simulation cases demonstrated different spatial distribution of soil water potential, the plot-scale transpiration from those two sets of simulation cases are almost the same. Specifically, when the small scenario of lateral spread is used, the simulation case with the spatially varying rooting depth also shows water-constrained plot-scale transpiration, the cumulative value of which during the simulation period is smaller than the

potential value by ~13 mm. Although relatively tall trees have access to water resources at deep depth, they could still be water stressed when their K_{comp} are smaller than $\tilde{K}_{comp}$ (Equation (4.24)).
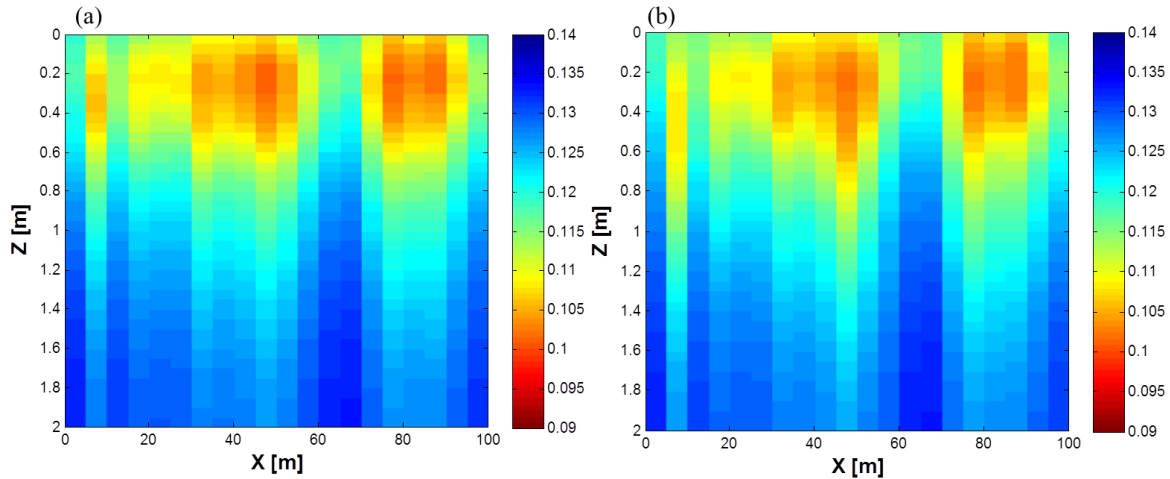
Figure 4.40. The spatial distribution of the hourly averaged volumetric soil moisture (in an unit of $[m^3 \ m^{-3}]$) at soil grid cells on the vertical plane of y = 50 m, for simulation case of (a) spatially uniform rooting depth, and (b) spatially varying rooting depth. The shown figures are from simulation cases with benchmark scenario of lateral spread.

4.7.4 Comparison with the "bucket" model

The "80-cm bucket" simulation case demonstrates a severe water stress of transpiration because of its overly dry soil between hour 1000 and 1600. The "2-m bucket" simulation case demonstrates sustained transpiration throughout the entire simulation period (Figure 4.41). This is because the latter simulation case has a larger soil water storage available for root water uptake, as compared to the simulation case of the 80-cm depth: the average water storage in the domain was 69 mm (in simulation case of 80-cm depth) versus 209 mm (in simulation case of 2-m depth).
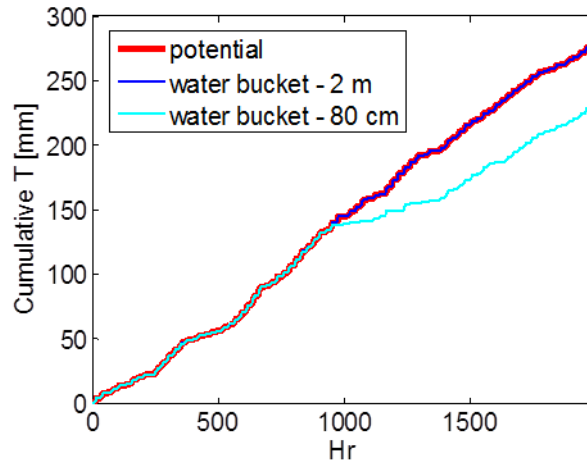
Figure 4.41. A comparison of cumulative transpiration simulated with the soil water bucket model that have different depths: 2 m ("water bucket – 2 m", blue line), or 80 cm ("water bucket – 80 cm", cyan line). The potential transpiration is indicated by the red line.

4.8 Discussion

4.8.1 Significance of representing 3-D root water uptake process

The simulation domain that considers the 3-D root water uptake process is shown to be less water stressed, as compared to that with the 1-D representation of root water uptake (i.e., the 1-D finely resolved simulation case, and the water bucket model with the 80-cm depth). For the studied forest ecosystem, the difference of cumulative transpiration during a vegetation season by the two types of approaches (i.e., 3-D versus 1-D) varies in the range of 8% to 20% (Section 4.7.2, and Section 4.7.4). The discrepancy of those two approaches may differ for other ecosystems, depending on plant characteristics (root architecture and hydraulic strategies), spatial distribution of stem locations, soil properties, and climate characteristics (e.g., precipitation pattern). For example, different precipitation pattern could result in varying available water in the shallow layers, and influencing the onset and magnitude of water stress in both the 1-D approach and 3-D approach (Manoli et al., 2014).

The simulated plot-scale transpiration was not compared with the measured latent heat, as

the measurement might be underestimated by ~20% (Section 3.3.4). Despite the uncertainty of the measured latent heat, analysis of the temporal correlation between soil water content in root zone and measured latent heat indicated that, the actual evapotranspiration was not constrained even when the soil moisture in the top 20-cm or 40-cm layer was near the residual value. This empirical observation is supported by the simulation results of the 3-D root water uptake approach, i.e., that plant roots have the capability to meet potential transpiration by dynamically adjusting root water uptake density according to the distribution of hydraulic gradients in the root zone.

The 1-D water bucket model of larger size (e.g., 2 m) generates non-stressed plot-scale transpiration as in the simulation case with the 3-D root water uptake process. However, the 1-D water bucket model uses coarse spatial resolution and ignores the propagation of infiltration front in the vertical direction. As a result, it neglects the fine-scale spatial heterogeneity of soil moisture, which nonlinearly influences plot-scale drainage and streamflow (Vrugt et al., 2001a) in land surface models. Therefore, the choice of 1-D or 3-D component of root water uptake would depend on study specific purposes.

4.8.2 Sensitivity of plot-scale water stress to root hydraulic architecture and lateral interactions

The plot-scale transpiration or water stress is found to be sensitive to different representations of lateral spread. If a tree has a relatively larger lateral spread, it tends to be less water stressed. This is because the values of compensatory conductivity K_{comp} increase with the lateral spread (Section 4.5.3). This result is consistent with the intuition that, a larger root system may be associated with a stronger capacity to compensate decreased root water uptake in dry regions by adjusting uptake in wetter regions. Simulation results indicate that, an optimal degree of lateral spread may exist for an individual root system, which makes the root system has a

compensatory conductivity K_{comp} that is always larger than the a threshold value ($\tilde{K}_{comp}$) at any time with the minimum root length (thus minimum metabolic cost of expanding the root system). A larger lateral spread beyond the optimal scale won't imply higher "efficiency" in root water uptake, the efficiency here can be defined as the amount of root water uptake per root length. For example, if a tree in the benchmark or large scenarios of lateral spread have the same amount of transpiration (i.e., equals to the potential value), the tree in the former case has a higher "efficiency" as it has a less amount of root length than in the latter case.

The plot-scale transpiration is shown to be barely sensitive to the different representations of rooting depth (i.e., spatially uniform or heterogeneous rooting depth). This is probably because the values of K_{comp} by the "Couvreur" approach are insensitive to the rooting depth of root networks (Figure 4.13), trees with deeper root systems can still be water stressed despite access to more water resources.

4.8.3 Effect of assumptions

This study involves several assumptions and the major effect of them is discussed below.

First of all, all root systems were considered as the oak species that exhibit the primary root system. Other species with different root systems may demonstrate varying root architecture and hydraulic properties (e.g., aspen has a secondary root architecture system), thus influencing the spatial distribution of soil moisture and the sensitivity of plot-scale transpiration to the overall soil water state. However, the implication that the modeling approach with the 3-D root water uptake tends to generate less water-limited transpiration as compared with 1-D approaches should remain unchanged.

Secondly, in this study, the root topologic networks were scaled spatially to have the desired values of lateral spread. There is a concern that for root systems with a large lateral

spread this process may generate artificially sparse root density at certain locations in the simulation domain, thus reducing the fractional root water uptake at that location. This would lead to artificial spatial heterogeneity of soil water content in simulations. A scenario with a synthetic potential fractional root water uptake was generated to evaluate the significance of the scaling process; this scenario was supposed to generate a reasonable spatial distribution of the potential water uptake fractions in soil grid cells. A comparison of the simulation results appears to demonstrate that the scaling process does not introduce significant difference in the spatial distribution of soil moisture or plot-scale transpiration.

Thirdly, certain hydraulic strategies of root water uptake have not yet been incorporated in this study. For example, an oak root system can reach as deep as 5 m (Breda et al., 1995) or a depth of the groundwater. The latter situation may enhance trees' capability to meet the potential transpiration demand regardless of the wetness condition in the unsaturated zone above the water table. This study used a soil domain with a 2-m depth due to the concern of the computational expense; and therefore all simulation cases used rooting depths smaller than 2 m. The simulations approached the observation that small-size trees tend to occupy small soil space and large-size trees might explore more soil water storage in a greater size of soil space.

Last but not the least, there are a few simplifications of the boundary conditions and parameterizations used for the 3-D simulation cases. First, the net precipitation input to the domain was assumed to be spatially uniform. An accurate representation of the spatially varying net precipitation (due to the spatially heterogeneous canopy) would require more advanced fine-scale measurements. Secondly, the soil evaporation was not considered in the domain, which might lead to an even drier simulation soil domain, especially near the top. Thirdly, there exist uncertainties in parameters such as radial and axial conductance, and their variation with root order. More conductive root systems were shown to have a stronger "compensation" effect due to relatively larger value of the compensatory conductivity.

4.9 Summary

In this chapter, a microscopic root water uptake model based on the "Couvreur" approach was coupled with a 3-D Richards' equation solver PFLOTRAN to simulate a plot-scale transpiration. The study was conducted using spatially varying forest setting near the UMBS, where observational evidence suggests little or no control of transpiration by soil moisture. Yet, the commonly used 1-D "Feddes-type" approach implies severe water limitation on transpiration during dry episodes of growing season.

Through an improved spatiotemporal representation of small-scale root water uptake process, the microscopic modeling framework led to a better agreement with the observational data as compared to the 1-D "Feddes-type" approach. During dry periods, relatively high transpiration demands are sustained, as the main root water uptake regions shift from densely to sparsely rooted layers, or from drier to moister soil areas. The plot-scale transpiration or water stress is shown to be sensitive to different representations of lateral spread, but insensitive to different representations of rooting depths. If a tree has a relatively larger lateral spread, it tends to be less water stressed due to its stronger capacity to compensate decreased root water uptake in dry regions by increasing root water uptake in relatively wetter regions. The dynamical compensatory effect of root systems increases with the extent of overlapped root zone with neighboring root systems. The simulation domain with larger root systems and a higher degree of overlapped root zones, tends to have a less spatial heterogeneity of soil moisture and a later onset of plot-scale water stress.

Although the 1-D soil water bucket model with the 2-m depth also generated unconstrained plot-scale root water uptake, it uses coarse spatial resolution and ignores the propagation of infiltration front in the vertical direction. Therefore, it lacks the ability to consider fine-scale

spatial heterogeneity of soil moisture, which nonlinearly influences plot-scale drainage and streamflow in the land surface models.

Chapter 5 : Summary and future directions

5.1 Summary and conclusion

5.1.1 Temporal dynamics of soil moisture after a prescribed intermediate disturbance: impact of crown-scale canopy biomass on soil wetness state and root water uptake profile

An intermediate disturbance was prescribed in in a northern temperate mixed forest near the University of Michigan Biological Station (UMBS). The disturbance was conducted through stem girdling of all canopy-dominant, early successional aspen and birch trees to simulate the anticipated large-scale succession process in the Upper Great Lakes area. Measurement data were collected at the four plots to provide observational evidence of changes in hydrological dynamics that were induced by species-specific crown-scale disturbances of the canopy structure.

Data analysis reveals that soil water storage under the girdled aspen was persistently higher, as compared to the undisturbed plots over the observational period of 2009 through 2011. It was argued that the larger water storage resulted from increased net precipitation and reduced transpiration during growing seasons following the girdling operation. These processes "outcompeted" the presumably enhanced interception and transpiration by understory plants as well as increased soil evaporation. Additionally, surface soil layer at the disturbed plot exhibited highest temporal variability among all monitored plots. The moisture profiles at the four plots were different, with the disturbed plot exhibiting relatively wetter shallow soil layers.

156

Furthermore, water loss at the disturbed plot was concentrated in shallower soil layers, signifying a shift of root water uptake and/or change of dominant processes.

5.1.2 Eco-hydrologic effects of heterogeneous vegetation canopy on temporal and spatial variations of energy fluxes and their coupling with soil moisture

A high-resolution, physically-based ecohydrological model tRIBS + VEGGIE was used as a data integration tool to upscale spatial heterogeneities resolved at a tree-scale to a coarse-scale (several kilometers). Several scenarios of tree-scale leaf area, soil moisture, and radiative forcing spatial variability were designed. A scenario with a spatially uniform canopy, corresponding to the commonly used "big-leaf" scheme in land surface parameterizations was used to infer the effects of coarse-scale averaging.

The results show that heterogeneous canopies adjust spatial soil water state to the scaled inverse of the canopy biomass by transpiring spatially varying amounts of water, regardless of the initial moisture state. The tree-scale effects on light exposure and shading result in smaller spatially aggregated transpiration and lower water stress, as compared to the results of the *lumped* representation. Specifically during dry period, exposed trees experience higher radiation load and deplete soil moisture more rapidly; consequently, their transpiration is limited by availability of soil water. In combination with light-limited transpiration of shaded trees, the domain-scale flux becomes lower than that simulated with the *lumped* case.

Note that the demonstrated water stress in Chapter 3 is based on a heuristic Feddes-type water stress function which might predict unreal water stress, as well as an assumption that root water uptake region of an individual tree is within a single grid cell of $5 \times 5 \times 2$ m^3 dimension. The water stress of larger trees might be exaggerated as all of its uptake is forced to originate within the top 80 cm in a single grid cell and there its subsurface might be modeled

drier than in reality. On the other hand, the water stress of short trees might be underestimated, because the existence of roots from neighboring trees was not accounted for and the subsurface might be modeled wetter than in reality. These constraints were released in Chapter 4 by considering 3-D root system for trees of varying sizes.

5.1.3 The importance of representing 3-D root water uptake in plot-scale simulations

The microscopic root water uptake process of individual trees into was upscaled to a plot scale (10^2 m^2) based on the "Couvreur" approach. Through an improved spatiotemporal representation of small-scale root water uptake process, the microscopic modeling framework leads to a set of simulation results that are in a better agreement with the observational data, showing less water stress as compared to that simulated by the heuristic 1-D approach. During dry periods, relatively high transpiration demands are sustained, as water uptake regions shift from densely to sparsely rooted layers, or from drier to moister soil areas. This microscopic approach can simulate plant's ability to compensate the suppressed root water uptake in water-stressed regions by increasing uptake density in wetter regions. The plot-scale transpiration is shown to be sensitive to different representations of root lateral spread. The dynamical compensatory effect of root systems in the domain increases with the extent of overlapped root zone with neighboring root systems. Simulation domain with larger root systems higher degree of overlapped root zones also tends to have less spatial heterogeneity of soil moisture.

Note that, in Chapter 4, a relatively tall tree with a larger lateral spread tends to be less water stressed because of its stronger capability of adjusting its spatial root water uptake density according to the spatially heterogeneous soil water potential. This result was derived from a numerical scheme that considers the 3-D root systems for trees of different sizes, i.e., tall trees

can uptake water from a soil space much larger than the dimension of $5 \times 5 \times 2$ m^3 used in Chapter 3, and the existence of overlapped root zones is accounted for.

5.2 Critical assumptions of this study

There are several critical assumptions in modeling. Their possible effects are summarized as below.

5.2.1 Tree-scale heterogeneous radiative forcing

In Chapter 3, tree-scale effects on radiative forcing (i.e., "shading" or "exposure" effects) were considered by generating "effective input shortwave radiation" above individual canopies. The "boundary effects" for individual crowns was generated by modifying the two-stream radiative transfer approximation for a semi-infinite homogeneous canopy layer (Dickinson, 1983; Sellers, 1985). Although not exact, the modified approach nonetheless permitted qualitatively correct effects of exposure and shading related to the actual Lidar-derived spatial variation of canopy "topography". Yet, the scheme is not a true physical solution of the 3-D effects of canopy structure on radiative transfer and the role of such characteristics as outer canopy surface, bottom-heaviness of canopy, vertically elongated space, and leaf inclination angle distribution, among others cannot be addressed (Parker et al., 2004; Wang and Jarvis, 1990). These axes of variation can be vital for exploring even finer scales of heterogeneity. For example, in an empirical study carried out at the UMBS forest, Hardiman et al. (2011) showed that a higher degree of canopy heterogeneity (expressed as a 3-D arrangement of both overstory and understory biomass) can lead to an enhanced aboveground biomass production. Such an increase in light-use efficiency can be significant for system scale energy-soil moisture interactions but require a higher level of complexity in a modeling approach that is not currently feasible for the

space-time scales considered in this study.

5.2.2 Species-specific differences

This study did not represent species-specific differences in root architectures, canopy biomass optical properties, and leaf stomatal regulation that might be very important for accurate simulation of the transpiration rate. The impact of ignoring those species-specific variations on the larger scale transpiration is still unclear. A better representation of the forest with those species-specific differences needs further collection of fine-scale data and research on appropriate parameterizations. For this matter, possible directions for future developments were discussed in Section 5.3.

5.2.3 Root architecture of mature trees

The studied forest ecosystem involves large mature tree systems, e.g., the lateral spread is at a scale of tens of meters. Due to the difficulty of the current root architecture models to generate reasonable root architectures for such a large scale, this study used two approaches to approximate the distribution of root nodes in a three-dimensional domain. One approach is by spatially scaling root networks generated by a root architecture model (at a scale of few meters) to root systems with the desired magnitude of lateral spread. The other approach is a heuristic three-dimensional root water uptake function based on the common assumption that the potential root water uptake fraction is proportional to the fractional root biomass and the amount exponentially decreases with the distance to the stem location. To completely solve this issue, more practical models of root architecture are needed.

5.2.4 Boundary conditions for microscopic root water uptake

There are two simplifications of the boundary conditions for the microscopic root water uptake model. One simplification is about the transpiration demand. The potential transpiration demand is first prescribed at the root collar, and when the simulated water potential at the root collar drops below a threshold value (i.e., the root system is water stressed), the boundary condition at the root collar is switched to a fixed water potential value. In reality, a water potential gradient exists from the root systems to stem and to leaves along the soil-vegetation-atmosphere (SVAT) continuum (Jackson et al., 2000b). This continuum is driven by the atmospheric water demand at the leaves and soil control of the flux. The stomata control of the leaves might constrain the transpiration. For this matter, possible directions for future developments were discussed below (Section 5.3).

The other simplification concerns the spatial distribution of precipitation. Net precipitation over the domain was generated by assuming spatially uniform interception of the canopy. An accurate representation of the spatially varying net precipitation (due to the spatially heterogeneous canopy) would require more advanced fine-scale measurements.

5.3 Possible future directions

5.3.1 Root architecture and dynamical root growth

Root systems have been shown to respond to spatially and temporally variable resources supply, e.g., water and nutrients (Dunbabin et al., 2004; Lynch and Brown, 2012). Root growth can be reduced at locations with severe water stress level (Smith and De Smet, 2012).

This research thus can be further improved by considering the dynamic change of root architecture and the associated hydraulic properties in response to the spatiotemporal

heterogeneous soil environment. Although the current generation of models of root architecture has limitations in generating mature systems with large lateral spread (and its dynamical change), the improvement of the root architecture models is promising (Dunbabin et al., 2013). Several mechanisms can be included: root hair morphology, root exudation, cluster root growth, up-regulation of nutrient transport carriers, locally enhanced root proliferation (Dinkelaker et al., 1995; Dunbabin et al., 2013; Lambers et al., 2011; Robinson, 2005; Zhu et al., 2010), root growth in response to objects and barriers in soil (Dunbabin et al., 2011; Leitner et al., 2010), and partitioning of carbon resources for root growth (Bidel et al., 2000; Nielsen et al., 1994). Such a "plastic response" of root systems allows the plant to (1) more efficiently capture mobile nutrients and local dry or wet spots of water resources (e.g., caused by local barriers in soil), and (2) minimize the metabolic cost of soil exploration by matching plant investment in root biomass and root function with resources supply in soil (Dunbabin et al., 2003; Lynch, 2007).

Hopefully, recent developments of new imaging measurement techniques will facilitate more accurate parameterization of root architecture simulations. Some non-destructive methods include computed tomography (Flavel et al., 2012), neutron radiography (Oswald et al., 2008), magnetic resonance imaging (Schulz et al., 2012), and tomography in transparent gels (Clark et al., 2011).

5.3.2 Water transfer from root collar to stem, leaf, and atmosphere

There is another well-known physical process of a plant might mitigate transpiration besides the water transfer process in root system: stomatal control of leaves. In this study, the stomatal control was simplified as being triggered by a low water potential at the root collar. Partial or complete stomatal closure might happen during mid-day periods of high evaporative demands, so that plants can maintain certain water potential above a minimum threshold in the stem to

prevent cavitation. A more complete mechanistic understanding of soil-plant hydraulics on transpiration need to account for water movement within stem and leaves (Bohrer et al., 2005). The timing and magnitude of stomatal control depends on xylem structure of a species (e.g., ring, diffuse, and non-porous) (Thomsen et al., 2013).

If a plant is considered as a one-dimensional vertical hydraulic path length l $[mm]$ (positive upward), the water potential (φ_l $[mm]$) along the path can be obtained from (Brisson et al., 1993):

$$C(\varphi_l)\frac{\partial \varphi_l}{\partial t} = \frac{\partial}{\partial l}\left[K(\varphi_l)\frac{\partial(\varphi_l+l)}{\partial l}\right] - S, \tag{5.1}$$

where $C(\varphi_l)$ $[mm^{-1}]$ is the stem xylem capacity, $K(\varphi_l)$ $[mm\ s^{-1}]$ is the stem xylem conductivity, S $[s^{-1}]$ is the transpiration sinks. The boundary condition is a weighted root water pressure or a surrogate soil water pressure.

Moisture uptake from the soil by a root system provides water for transpiration, while soil water deficit acts to constrain fluxes through a control on stem xylem water potential φ_l. As the root potential (φ_{root}) becomes more negative (Blizzard and Boyer, 1980; Brisson et al., 1993), the stem xylem conductivity is reduced to guard against xylem cavitation (Sperry, 2000). The constrained stem xylem or leaf water potential can exert a control on the stomatal response and limit the actual transpiration rate (Bunce, 2004; Jones and Sutherland, 1991; Tuzet et al., 2003).

Based on the one-dimensional physical representation of the aboveground tree hydrodynamics, Bohrer et al. (2005) represented a three-dimensional tree structure by including a branch angle conversion term to correct for the non-vertical branches. Janott et al. (2011) further extends the approach of Bohrer et al. (2005). They included the subsurface component by incorporating information on three-dimensional root architecture in one-dimensional plant root-xylem water flow model coupled to a one-dimensional water flow model (HYDRUS-1D,

Simunek et al, 2007). Janott's model is an advanced method for computing the one-dimensional transpiration flux.

The modeling framework developed in this research is capable to further include a module to consider the water transfer from the root collar and stem and leaf as continuous soil-vegetation-atmosphere unit, and at the same time solve for the resulting three-dimensional heterogeneity of soil moisture.

5.3.3 Species-specific variations and implications of future climate change

Climate change bringing about warmer temperatures and increased occurrence of seasonal droughts will overlap with forest succession process, altering species composition of forests (Bergen and Dronova, 2007; Hanson and Weltzin, 2000; Kirschbaum, 2000; Lewis et al., 2004; Shugart et al., 2003; Wolter and White, 2002). One projection of future climate is that by the end of the 21st century, Northern Michigan is projected to have a 20%~33% drier soil condition during growing seasons, as compared to 1961-1990, based on analysis of high/mid/low CO_2 emission scenarios (A2/A1B/B1) (Fatichi et al., 2011). Sustainable forest management for the region, such as mitigation and adaptation options and conservation plans, depends on robust understanding of the future species composition and abundance (Janowiak and Webster, 2010; Malmsheimer et al., 2008). Failure to accurately predict how species will respond to climate change may lead to ill-informed conservation plans to maximize species diversity and abundance, impacting billion-dollar forestry-related enterprises (e.g., timber production) as well as recreational opportunities, biodiversity, and life qualities of millions of people living in the region (Galik and Jackson, 2009; Lindenmayer et al., 2000).

The new forest composition will be impacted by advantages of individual species in hydraulic responses to future drought conditions (Coomes and Grubb, 2000; Ewers et al., 2007;

Holmgren et al., 1997; Leuschner et al., 2001; Wullschleger et al., 2002). However, current regional ecohydrological models will not be capable of predicting species-specific hydraulic response to decreased water availability, as these models usually ignore inter-species variations and overly simplify the representations of tree architecture and hydraulics (Feddes et al., 2001; Hinsinger et al., 2009; Medvigy et al., 2008; Oleson et al., 2004a; Pitman, 2003; Rodriguez-Iturbe et al., 2007; Walko and Avissar, 2008). A model scheme can be proposed for future research (Figure 5.1a), that is able to incorporate those species-specific variations, in terms of tree canopy structures, root architectures, and hydraulic strategies (stomatal control, access to groundwater table, and etc.). The proposed future development can target the following question: which species are less likely to be water stressed and thus more successful in drier conditions of the future?
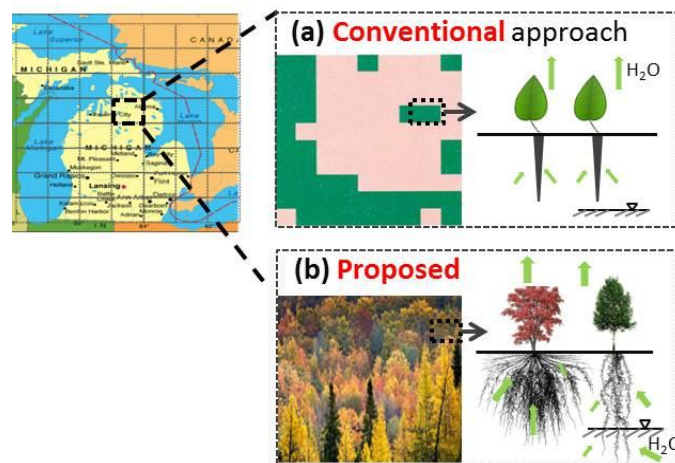
Figure 5.1. A conceptual sketch of representations of inter-species variations in tree architecture and hydraulics by: (a) conventional, coarse-scale "big-leaf" approach in current models; (b) proposed mechanistic approach that considers tree-scale, species-specific root characteristics and biomass distribution differences.

Inferences from this possible future research to incorporate species-specific variations (Figure 5.1b) will significantly contribute to projections of future forest conditions in the Upper Midwest and the Great Lakes region, such as species mortality rate and abundance, carbon storage, wood production, water yields, and etc. The impacts will also extend beyond the implications for sustainable forests to sustainable crop production; the methodologies and modeling tools developed in this study can be easily adapted for agriculture applications (Blum, 2005; Porter and Semenov, 2005). For example, the developed model can be used to assess drought-tolerance of economic crop species and efficiency of irrigation practices to maximize production for future generations in vulnerable regions (Schneider et al., 2010; Zegada-Lizarazu et al., 2012; Zhang and Oweis, 1999).

Tables

Table 1. Values of parameters used in the tRIBS+VEGGE at UMBS**:** soil properties, biomass storage variables, autocorrelation length of LAI and SM, and vegetation properties

	Parameter	Value	Unit	Source
Soil Properties	K_s, Saturated hydraulic conductivity	350	$mm\ s^{-1}$	
	θ_s, Saturated volumetric soil moisture	0.37	$m^3\ m^{-3}$	
	θ_r, Residual volumetric soil moisture	0.04	v/v	Adjusted from the inverse routine results
	α, Shape parameters in Van Genuchten equation	-0.0052	mm^{-1}	
	n, Shape parameters in Van Genuchten equation	1.68	--	
Biomass Storage Variables	$C_{pL\text{-}dry}$, Specific heat capacities of moist green biomass	3.218	$J\ g^{-1}\ K^{-1}$	Gu et al. (2007)
	C_w, Specific heat capacities of water	4.186	$J\ g^{-1}\ K^{-1}$	
	r_L, Leaf water to dry mass ratio	1.5	--	Gu et al. (2007)
	r_n, Nongreen biomass water to dry mass ratio	0.7	--	Gu et al. (2007)
	LMA, Dry leaf mass per area	40	$g\ m^{-2}(leaf)$	UMBS template
	$M_{agb\text{-}dry}$, Aboveground dry biomass	15921	$g\ m^{-2}(ground)$	UMBS template
Autocorrelation Length	Autocorrelation length of LAI	1.16	m	Analyses from a 2-m LAI datasets over a 50 50 m plot near the AmeriFlux tower (He et al., 2012a, in preparation)
	Autocorrelation length of SM	0.94	m	Analyses from a 2-m SM datasets over a 50 m plot near the AmeriFlux tower (He et al., 2012a, in preparation)
Vegetation Variables	Leaf reflectance in VIS band	0.1	--	
	Leaf reflectance in NIR band	0.45	--	
	Stem reflectance in VIS band	0.16	--	
	Stem reflectance in NIR band	0.39	--	
	Leaf transmission in VIS band	0.05	--	Calibrated by using the big leaf case
	Leaf transmission in NIR band	0.25	--	
	Stem transmission in VIS band	0.001	--	
	Stem transmission in NIR band	0.001	--	
	Maximum catalytic capacity of Rubisco at 25 °C	47	$\mu mol\ CO_2\ m^{-2}\ s^{-1}$	
	Soil water potential threshold for stomatal closure	-1	MPa	
	Soil water potential threshold for wilting	-7	MPa	

Table 2. The average daily decrease of root-zone soil water storage ($\overline{-\Delta SWS_{0-80}}$) at the four plots for each of the five interstorm periods. The superscript "*" signifies the lowest value among the four plots for each period.

Periods	Duration [day]	$\overline{-\Delta SWS_{0-80}}$ [mm day^{-1}]			
		AAP	AOP	FAP	FOP
a	19	2.30	2.56	1.95*	2.06
b	18	2.19	2.48	2.01*	2.20
c	28	1.76	1.90	1.60*	1.95
d	9	2.03	2.68	1.41*	1.44
e	10	1.27	3.02	1.20*	1.29

Table 3. Values of root hydraulic properties, scenario 1.

Order (0-coarse; 4-fine)	Radius [mm]	Radial Resistance [s]	Radial Conductance [cm/day/cm]	Axial Resistance [s/m3]	Axial Conductance [cm4/day/cm]
0	150	5.00E+11	1.73E-07	5.00E+06	172800
1	80	1.00E+11	8.64E-07	1.00E+06	86400
2	20	5.00E+10	1.73E-06	5.00E+07	17280
3	5	1.00E+10	8.64E-06	1.00E+07	8640
4	2	2.50E+9	3.46E-05	5.00E+08	1728

Table 4. Values of root hydraulic properties, scenario 2: less conductive root system.

Order (0-coarse; 4-fine)	Radius [mm]	Radial Resistance [s]	Radial Conductance [cm/day/cm]	Axial Resistance [s/m3]	Axial Conductance [cm4/day/cm]
0	150	5.00E+12	1.73E-08	5.00E+07	17280
1	80	1.00E+12	8.64E-08	1.00E+07	8640
2	20	5.00E+11	1.73E-07	5.00E+08	1728
3	5	1.00E+11	8.64E-07	1.00E+08	864
4	2	2.50E+10	3.46E-05	5.00E+09	173

Table 5. Values of root hydraulic properties, scenario 3: more conductive root system.

Order (0-coarse; 4-fine)	Radius [mm]	Radial Resistance [s]	Radial Conductance [cm/day/cm]	Axial Resistance [s/m3]	Axial Conductance [cm4/day/cm]
0	150	5.00E+10	1.73E-06	5.00E+05	1728000
1	80	1.00E+10	8.64E-06	1.00E+05	864000
2	20	5.00E+9	1.73E-05	5.00E+06	172800
3	5	1.00E+9	8.64E-05	1.00E+06	86400
4	2	2.50E+8	3.46E-04	5.00E+07	17300

Appendix

6.1 Calibration of soil moisture sensor (MiniTrase system, Soil Moisture Equipment Corp., Santa Barbara, CA, USA.)

A sensor calibration curve was generated and is shown in **Error! Reference source not found.**.
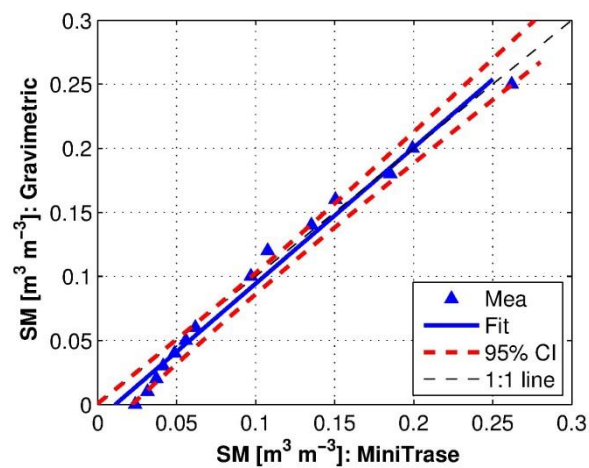
Figure 6.1. A relationship between soil moisture values estimated with the gravimetric method (y-axis) and readings obtained with the MiniTrase soil moisture system (x-axis): the measured data points ("Mea"); a fitted line ("Fit"): $y = 1.06x - 1.19$; and the 95% confidential interval of the fitted line ("95% CI"). The determination coefficient is $R^2 = 0.98$, the root mean square error is 0.0076 [$m^3\ m^{-3}$].

6.2 Calibration of optical precipitation sensor (Model 5.4103.20.041, Thies Clima GmbH., Göttingen, Germany)

To simulate natural rainfall, two nozzle types (460.326.5E.BA and 460.368.17.BA, Venture Technology Groups Inc., U.S.A.) were used. The rainfall rates were simulated over a range of 0.003 to 1.0 [$mm\ min^{-1}$]. The cumulative amounts of sprinkled water recorded by the optical sensor were compared to the actual water volumes collected in a container. A sensor calibration curve was generated (Figure 6.2). The sensor noise was filtered out from the observational data by using a threshold of 0.00105 [$mm\ min^{-1}$], which was determined experimentally.
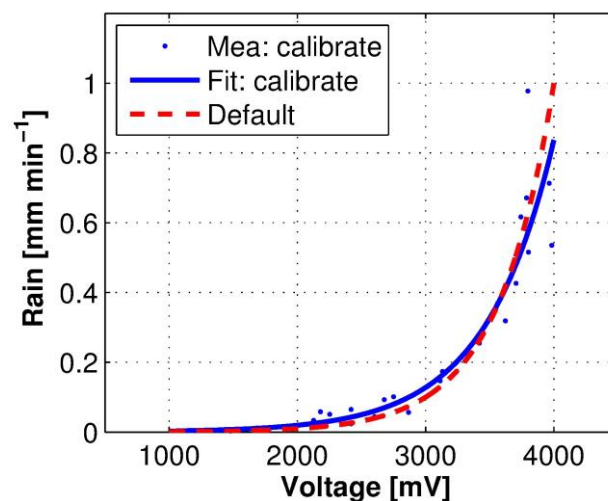
Figure 6.2. A relationship between the output voltage of optical precipitation sensor (x-axis) and water volumes collected in a container (y-axis). Measured data are shown as points ("Mea: calibrate"). A fitted relationship ("Fit: calibrate") converting the output voltage x (in mV) to rain flux rate y (in mm min^{-1}) is $y = 0.000455 \times \exp(0.001880x)$, the determination coefficient of a log-linear fit is $R^2 = 0.92$. The default equation ("Default") was provided as $y = 0.000100 \times \exp(0.002306x)$.

6.3 Analysis of gravitational drainage at the depth of 300 cm

At our sites, soil water contents between 100 cm and 300 cm were observed to be temporally uniform and unaffected by groundwater or changes of the position of capillary fringe. One dimensional dynamics at the depth of 300 cm were therefore assumed and primarily affected by drainage due to gravity. Drainage can be approximated as

$$q = -K(\theta), \tag{6.1}$$

$$K(\theta) = K_s S^{0.5} (1 - (1 - S^{1/m})^m)^2, \tag{6.2}$$

where q [$mm\ hr^{-1}$] is the drainage rage, $K(\theta)$ [$mm\ hr^{-1}$] is the unsaturated hydraulic conductivity, which is derived using the Van Genuchten (van Genuchten, 1980) hydraulic parameterization; K_s [$mm\ hr^{-1}$] is the saturated hydraulic conductivity; S [-] is the relative saturation [$m^3\ m^{-3}$], and can be calculated as $S = (\theta - \theta_r)/(\theta - \theta_s)$, where θ_r [$m^3\ m^{-3}$] and θ_s [$m^3\ m^{-3}$] are residual and saturated soil water contents, respectively; m [-] is the shape parameter. The soil hydraulic properties K_s, θ_r, θ_s, and m were derived from pedo transfer functions using percentages of sand, silt, and clay (Schaap et al., 2001); and equal to 297 [$mm\ hr^{-1}$], 0.04 [$m^3\ m^{-3}$], 0.45 [$m^3\ m^{-3}$], and 0.61 [-] respectively.

As the soil moisture contents at the 300 cm depth during growing seasons were recorded to vary in the range of 0.04-0.08 [$m^3\ m^{-3}$], a range of drainage rates was calculated to be in the range of 10^{-8} to 0.016 [$mm\ hr^{-1}$]. Suppose a rainstorm period lasts for 24 hours (note that all rainstorm periods at UMBS lasted smaller durations), the possible maximum total drainage at the 300 cm depth is smaller than 0.38 mm. As compared to the total water storage in the 0-300 cm soil column, which varied from 100 to 300 mm (Figure 2.7), the

magnitude of such a drainage loss is smaller than 1%, which is negligible.

The estimates of possible maximum total drainage by using other soil hydraulic parameterizations are small as well. For example, for the same range of soil moisture contents (0.04-0.08 [$m^3\ m^{-3}$]), the Brooks-Corey parameters (Brooks and Corey, 1964; Rawls et al., 1982) for sand result in a calculated maximum drainage rate of 0.11 [$mm\ hr^{-1}$]. The 24-hour possible maximum total drainage at the 300 cm depth is smaller than 2.64 mm, which is still negligible compared with the magnitude of 0-300 cm soil water storage.

6.4 Biomass heat storage module

Simulations carried out using the previous version of tRIBS + VEGGIE demonstrated that the peak of the simulated diurnal cycle of sensible heat lagged the observed peak. This issue was addressed by incorporating the biomass heat storage module. For a computational element where vegetation is present (referred to by the superscript "*veg*"), the energy balance equations for the vegetated part (referred to by the subscript "*v*") and the under-canopy soil surface (referred to by the subscript "*g*") are written in the same notation as in Ivanov et al. (2008a):

$$\vec{S}_v^{veg} + \vec{L}_v^{veg} - H_v^{veg} - \lambda E_v^{veg} - B_v^{veg} = 0 \tag{6.3}$$

$$\vec{S}_g^{veg} + \vec{L}_g^{veg} - H_g^{veg} - \lambda E_g^{veg} - G = 0 \tag{6.4}$$

where $\vec{S}_v^{veg}$ and $\vec{S}_g^{veg}$ [$W\ m^{-2}$] are the absorbed shortwave radiation by vegetation and by under-canopy ground, $\vec{L}_v^{veg}$ and $\vec{L}_g^{veg}$ [$W\ m^{-2}$] are net longwave radiation fluxes for vegetation and for understory ground, which equal to the absorbed longwave radiation minus emitted longwave radiation (calculated from *Stefan-Boltzmann law*); H_v^{veg}, H_g^{veg} [$W\ m^{-2}$] and λE_v^{veg}, λE_g^{veg} [$W\ m^{-2}$] are the sensible and latent heat fluxes from vegetation or under-canopy ground; G [$W\ m^{-2}$] is the ground heat flux; and B_v^{veg} [$W\ m^{-2}$] is the heat storage in vegetation biomass (metabolic biochemical energy storage is not considered in the current version of the tRIBS+VEGGIE model). The canopy and ground surface energy budgets (Equation (6.3) and (6.4)) constitute a system of equations that are non-linear functions of vegetation T_v and ground T_g [K] temperatures. The value of B_v^{veg} is computed using the following formulation (Gu et al., 2007):

$$B_v^{veg} = (C_{pL}M_L + C_{pn}M_n + C_{pw}M_w)(dT_v / dt), \tag{6.5}$$

where C_{pL}, C_{pn}, and C_{pw} [$J\ g^{-1}\ K^{-1}$] are the specific heat capacities of moist leaf biomass, moist non-green biomass (e.g., stems and branches), and water, respectively; M_L, M_n, and M_w [$g\ m^{-2}$ (ground)] are the densities of moist leaf biomass, moist non-green biomass, and water mass covering the biomass surface (e.g., dew, and rainfall interception), respectively. The C_{pL}, C_{pn}, M_L, and M_n are computed as (Gu et al., 2007):

$$C_{pL} = (C_{pL-dry} + r_L C_{pw}) / (1 + r_L), \tag{6.6}$$

$$C_{pn} = (C_{pn-dry} + r_n C_{pw}) / (1 + r_n) + 100 r_n (-0.06191 + 0.000236 T_v - 0.0133 r_n), \tag{6.7}$$

$$C_{pn-dry} = 0.1031 + 0.003867 T_v, \tag{6.8}$$

$$M_L = LAI \cdot LMA \cdot (1 + r_L), \tag{6.9}$$

$$M_n = (M_{dry} - LAI \cdot LMA)(1 + r_n), \tag{6.10}$$

where C_{pL-dry} and C_{pn-dry} [$J\ g^{-1}\ K^{-1}$] are the specific heat capacities of dry leaves and dry non-green biomass; r_L and r_n [-] are the ratios of water to dry biomass for leaves and non-green biomass, respectively ; LAI [m^2 (leaf) m^{-2} (ground)] is the leaf area index; LMA [$g\ m^{-2}$ (leaf)] is the dry leaf mass per unit leaf area; M_{dry} [$g\ m^{-2}$ (ground)] is the total dry aboveground leaf and non-green biomass per unit ground area. The values of C_{pL-dry}, C_{pw}, r_L, and r_n (Table 1) were assigned from Gu et al. (2007). The values of LMA and M_{dry} for the UMBS area (Table 1) were obtained from the Carbon Dioxide Information Analysis Center (http://cdiac.ornl.gov).

6.5 Element-scale heterogeneous radiative forcing due to the light shading and exposure effects

The effect of light shading or exposure on a tree was accounted for by considering either "attenuated" or "surplus" components of shortwave irradiance. For shaded trees, an adapted version of Beer-Lambert law (Iqbal, 1983; Monsi and Saeki, 1953) was used to calculate attenuated radiation by neighboring trees that are located in the direction of the Sun's azimuth. For exposed trees, a surplus radiation was estimated by comparing radiation that arrives at the crown surface in a spatially heterogeneous canopy setting or in a uniform canopy cover. By subtracting the attenuated (shaded tree) or adding the surplus (exposed tree) radiative energy to the above-canopy radiation, "effective" input shortwave radiation is computed. Using such adjusted radiation as the boundary condition at the canopy top, the energy transfer processes for each grid cell were further calculated with the tRIBS+VEGGIE model by using the two-stream approximation (Dickinson, 1983; Sellers, 1985).

As the focus of the developed scheme is to parsimoniously approximate the effects of horizontally variable canopy heights on the light regime, for computational efficiency, the individual canopy in a given element was assumed to have a shape of a cuboid. The cuboid is characterized by a height equal to the crown height H, and by a width and a length, both of which were assumed to be equal to the grid size (i.e., 5 m). Other crown shapes (e.g., ellipsoid and cylindrical) could be also considered using alternative parameterizations of crown envelope and computations of shadow area or crown volume. Leaves and shoots and their inclination angles are assumed to be randomly distributed within each canopy envelope. The scheme differentiates the direct and diffuse radiation. The scheme is implemented at the hourly scale and used for each element within the domain.

The computational process to calculate the spatially heterogeneous radiation on individual trees considering the 'shaded' effect or the 'exposure 'effect of direct and diffuse radiation is shown in the Figure 6.3.
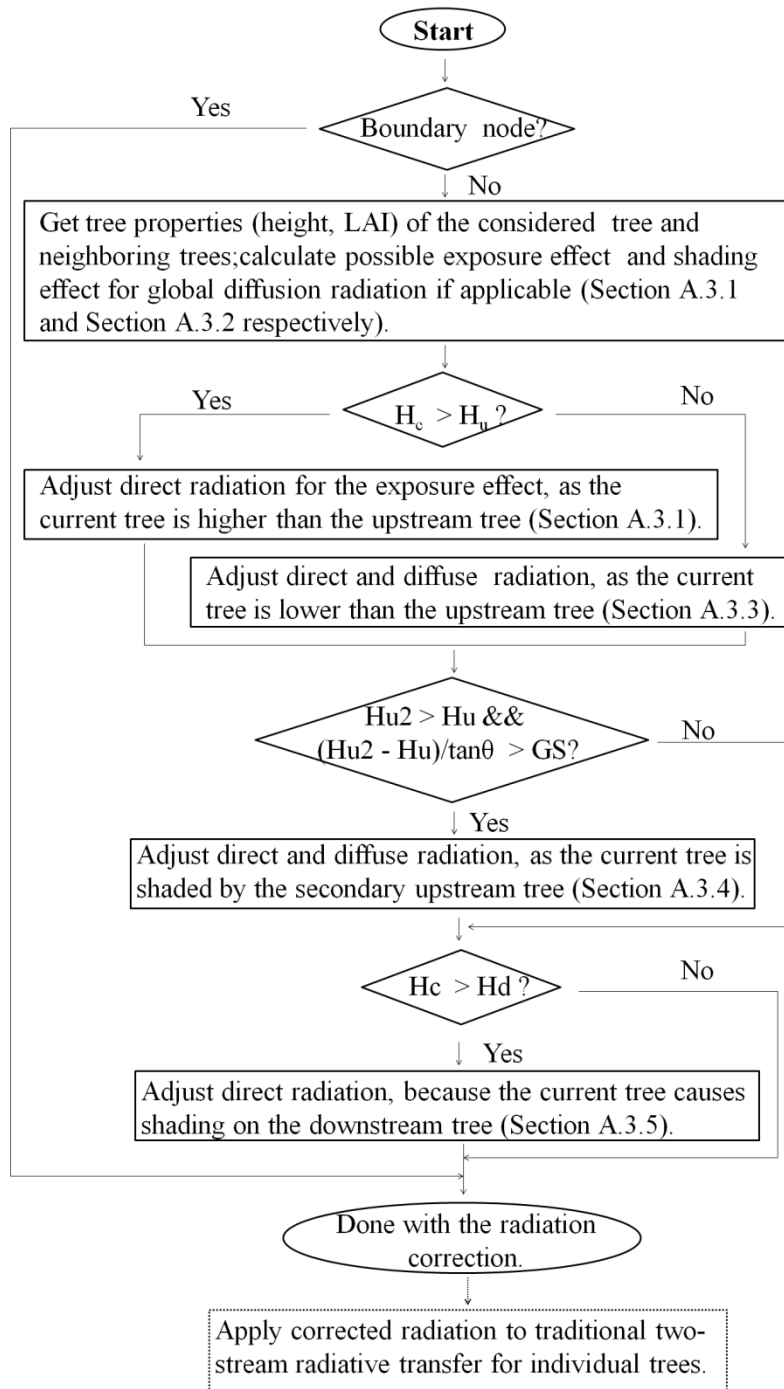
Figure 6.3. A flowchart to calculate the heterogeneous horizontal radiation on individual trees because of the 'shaded' effect or the 'exposure' effect of direct and diffuse radiations. H_c [m] is the current considered tree height; H_u [m] is the upstream tree height; H_{u2} [m] is the secondary upstream tree height; $tan\theta$ [-] is the tangent of sun solar angle; GS [m] is the grid size, equals to 5m in this case.

6.5.1 Direct radiation

<u>Determination of "upstream" trees</u>

According to the square grid configuration, each tree is surrounded by eight immediate neighbor trees. Consequently, eight azimuthal zones were defined (Figure 6.4) indicating a certain range of the azimuthal angle. At any given time, the Sun's azimuthal direction corresponds to one of these azimuthal zones. The trees located in the zone of the Sun's azimuthal direction are defined as the "upstream" trees and the nearest neighbor tree in this zone is the "immediate upstream" tree.
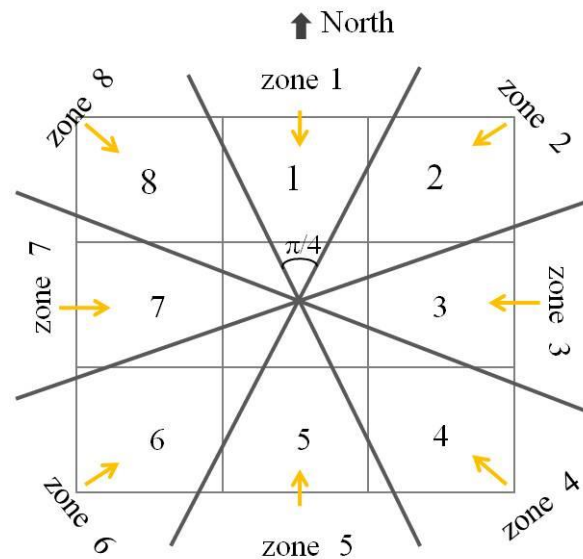
Figure 6.4. A conceptual diagram of spatial relationship between a considered tree (the center grid cell), its immediate neighbor trees (denoted as numbers in grid cells), and eight azimuthal zones. An "immediate upstream" tree is located in the azimuthal zone of the Sun's azimuthal direction. For example, if the Sun's azimuthal direction is in zone 5, neighbor tree No. 5 is the immediate upstream tree.

6.5.2 Shading effect

If a considered tree is relatively short, a part of the horizontal surface at the height of its canopy top (considered to be a 5 m $\times$ 5 m area, hereafter referred to as the "canopy top surface") can be shaded by the biomass of upstream trees. This situation is illustrated in Figure 6.5a. The shaded fraction f [-] of the canopy top surface is approximated as:

$$f = \max(|\Delta H|/(\Delta x \tan \theta),1) \tag{6.11}$$

$$\Delta H = H_c - H_u, \tag{6.12}$$

where ΔH [m] is the difference between the considered tree height H_c [m] and its immediate upstream tree H_u [m]; $\tan \theta$ [-] is the tangent of the Sun's solar angle θ [rad]; and Δx [m] is the crown size of the considered tree, which equals to the grid cell size.

The shaded fraction of the canopy top surface receives direct beam radiation that has passed through neighbor's canopy biomass. This radiation (S_t [$W\ m^{-2}$]) is calculated using the Beer-Lambert law (Monsi and Saeki, 1953):

$$S_t = S_{in} \exp(-k \cdot D \cdot LAD), \tag{6.13}$$

where S_{in} [$W\ m^{-2}$] is the above-canopy incident shortwave radiation (set equal to an observed value); $k = G(\mu)/\mu$ [-] is the extinction coefficient, μ [-] is the sine of the Sun's solar angle, $G(\mu)$ [-] is the relative projected area of leaves in the direction of direct beam; D [m] is the path length of the radiation ray through the tree canopy; and LAD [$m^2\ m^{-3}$] is the leaf area density of trees that attenuate the radiation ray (calculated as LAI [$m^2\ m^{-2}$] of an

upstream tree divided by its tree height in unit in [m]). For computational efficiency, we assumed that upstream trees beyond the immediate upstream tree have the same canopy height and *LAD* as that of the immediate upstream tree. Within the shaded fraction of the canopy top surface (Figure 6.5a), transmitted radiation rays have traveled through different path lengths of biomass of upstream trees, and an average of the transmitted radiation over the shaded area ($\overline{S}_t$ [$W\,m^{-2}$]) is calculated as:

$$
\overline{S}_t = \begin{cases} S_{in}(\displaystyle\int_{0}^{|\Delta H|/\sin\theta} \exp(-k\cdot D\cdot LAD)d(D\cos\theta))/(f\cdot\Delta x), & when\ f<1, \\[2em] S_{in}(\displaystyle\int_{(|\Delta H|-\Delta x\tan\theta)/\sin\theta}^{|\Delta H|/\sin\theta} \exp(-k\cdot D\cdot LAD)d(D\cos\theta))/(f\cdot\Delta x), & when\ f=1, \end{cases}
\tag{6.14}
$$

where the integrals are solved analytically.

The attenuated (either absorbed or scattered) amount of radiation by upstream trees (ΔS [$W\,m^{-2}$]) is:

$$
\Delta S = S_{in} - \overline{S}_t.
\tag{6.15}
$$

The effective input direct radiation $\tilde{S}_{in}$ at the canopy top surface for a shaded tree is calculated as the sum of unobstructed radiation within unshaded fraction and attenuated radiation within the shaded fraction:

$$
\tilde{S}_{in} = (1-f)S_{in} + f\overline{S}_t = S_{in} - f\Delta S.
\tag{6.16}
$$
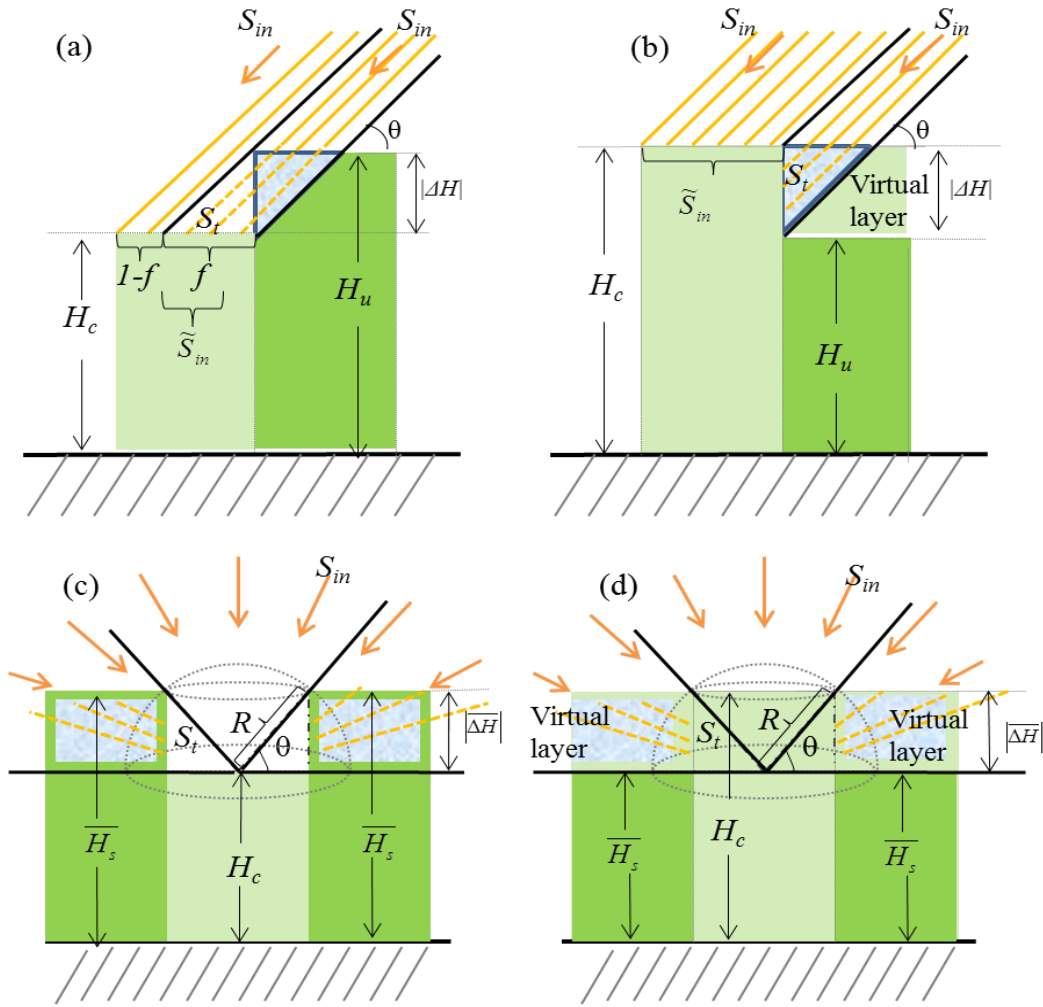
Figure 6.5. A conceptual diagram for calculating effective direct beam and diffuse radiation $\tilde{S}_{in}$ for (a, c) a shaded tree and (b, d) an exposed tree. In the figure, S_{in} is the above-canopy incident (a, b) direct or (c, d) diffuse radiation, H_c is the height of the considered tree, H_u is the height of the immediate upstream tree, $\overline{H_s}$ is the average height of eight immediate surrounding trees, ΔH is the absolute height difference between H_c and H_u, $\overline{\Delta H}$ is the height difference between H_c and $\overline{H_s}$, S_t (shown as yellow dash line) is transmitted radiation that has been attenuated through biomass of immediate trees (the blue area in plot (a) and (c)) or by a virtual homogeneous layer (the blue area in plot (b) and (d)), f is the shaded fraction of the canopy top surface, θ is the horizontal incident angle of transmitted radiation, R is the radius of a defined reference upper hemisphere.

6.5.3 Exposure effect

If a given tree is taller than its immediate upstream tree, a section of a tree edge is exposed to direct beam radiation (Figure 6.5b) and this exposure is neglected in traditional models that assume a uniform canopy cover. As a result of exposure, the exposed tree edge receives higher radiation, as compared to a horizontally uniform canopy that has the same height and biomass density. In the latter situation, the tree edge is immerged in a virtual homogeneous layer (Figure 6.5b), direct radiation received by the tree edge is attenuated by canopy and transmitted radiation $\overline{S_t}$ is calculated using Equation (6.14). The "surplus" radiative energy ΔS is calculated using Equation (6.15).

The effective direct beam radiation of an exposed tree is computed as:

$$\widetilde{S}_{in} = S_{in} + f\Delta S, \qquad (6.17)$$

where f has the same expression as in Equation (6.11) but denotes the fraction of surplus radiation at the tree edge with regard to radiation received by the crown top. As $\widetilde{S}_{in}$ would be further used in the two-stream approximation as boundary condition, the way how $\widetilde{S}_{in}$ is calculated involves a crude assumption that the surplus radiation at the tree edge has the same effect on the within-canopy radiative transfer process as if it is at the canopy top surface.
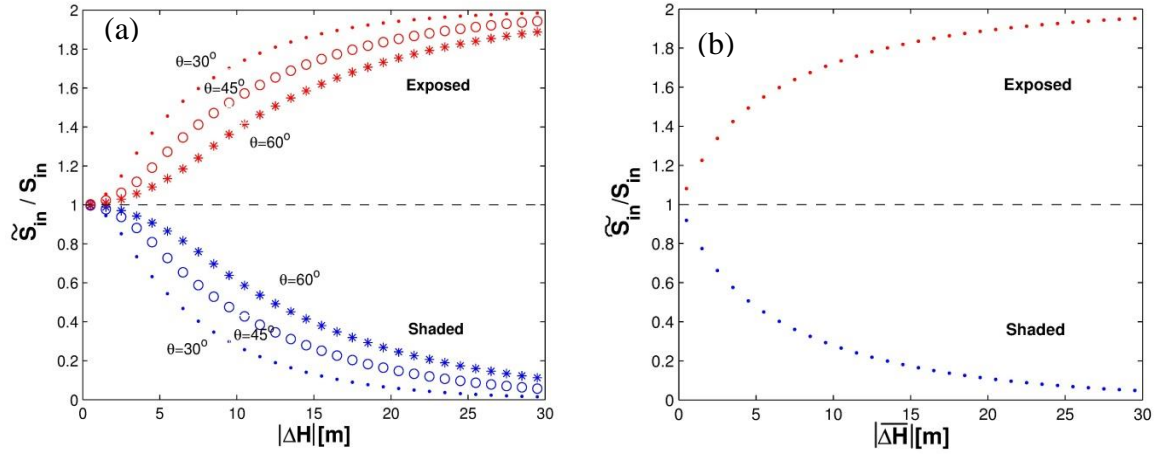
Figure 6.6. The normalized element-scale effective (a) direct or (b) diffuse shortwave radiation ($\tilde{S}_{in}/S_{in}$) as a function of $|\Delta H|$ or $|\overline{\Delta H}|$. In the figure, $|\Delta H|$ is the absolute canopy height difference between a considered tree and its immediate upstream tree, $|\overline{\Delta H}|$ is the absolute average canopy height difference between the considered tree and its eight neighbor trees, θ is the Sun's solar angle. The blue symbols denote shaded trees, and the red symbols denote exposed trees. The plotted results were calculated following Equation (6.11) to Equation (6.17) using shown values of θ, $|\Delta H|$, and $|\overline{\Delta H}|$.
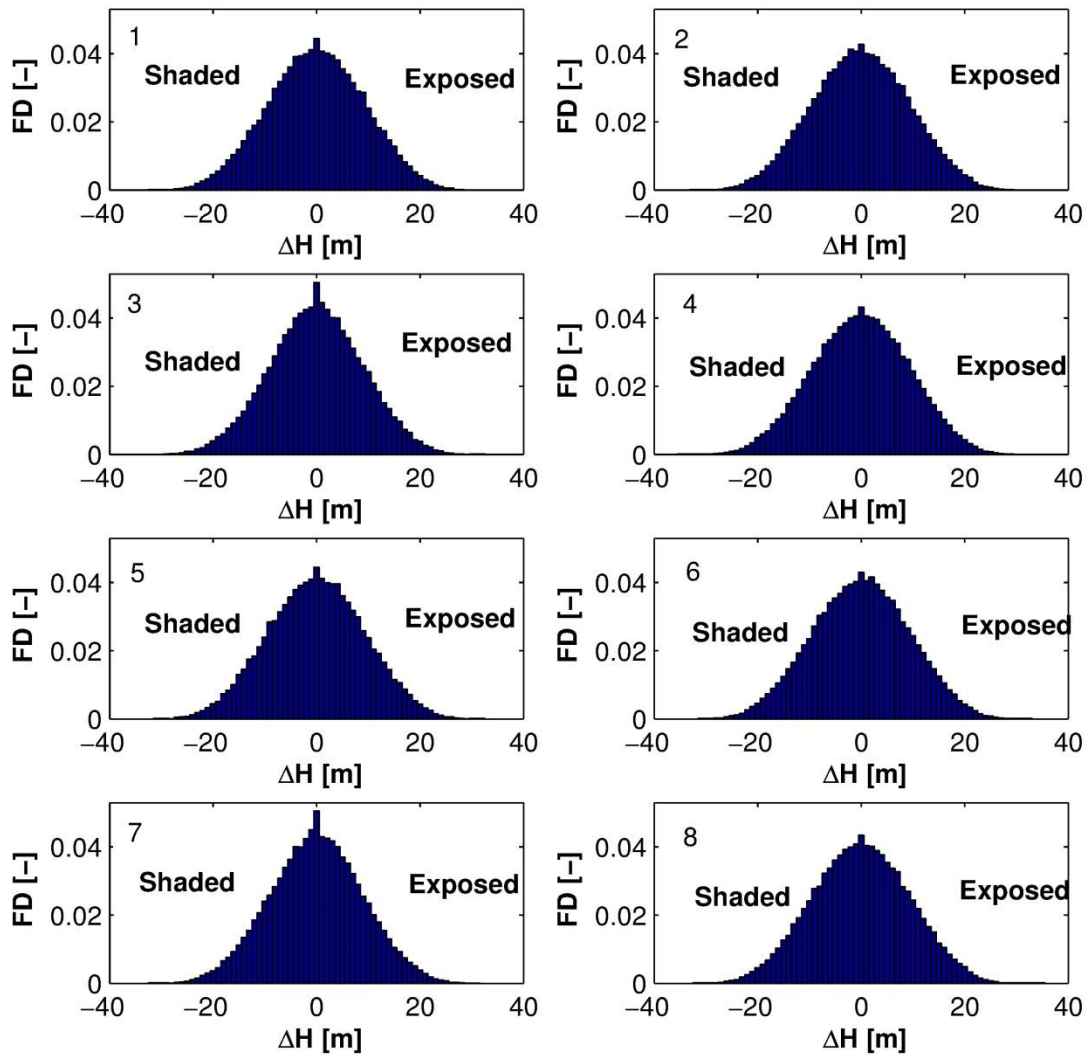
Figure 6.7. The Frequency Distribution (FD) of the element-scale canopy height differences (ΔH, between a considered tree and its immediate upstream tree) for different Sun's azimuthal aspects computed for the study domain. An azimuthal zone is denoted with the number in the upper left corner of each plot. The frequency distribution to the left/right of $\Delta H = 0$ corresponds to shaded/exposed trees.

6.5.4 Diffuse radiation

Because of the hemispherical distribution of diffuse radiation, any immediate neighbor tree that is taller than a given tree would attenuate a certain fraction of diffuse radiation that comes from the upper hemisphere. One can approximate the attenuated fraction of diffuse radiation by the immediate neighbor trees as the total fraction of obstructed sky viewed from the center of a considered element at the height of canopy top. To calculate the attenuated fraction, a referenced upper hemisphere is defined (Figure 6.5c) with a radius R [m]:

$$R = \sqrt{\overline{\Delta H}^2 + \Delta x^2 / 4}, \tag{6.18}$$

$$\overline{\Delta H} = H_c - \overline{H_s}, \tag{6.19}$$

where $\overline{H_s}$ is the average height of eight immediate surrounding trees, $\overline{\Delta H}$ is the height difference between the considered tree and $\overline{H_s}$.

The fraction of the attenuated diffuse radiation with regard to the reference upper hemisphere is approximated as:

$$f = \left|\overline{\Delta H}\right| / R. \tag{6.20}$$

Transmitted diffuse radiation with a horizontal incident angle θ [rad] arriving at the center of the shaded canopy top surface travels an averaged path length of $\left|\overline{\Delta H}\right| / \sin\theta$. Assuming that diffuse irradiation is isotropic over the upper hemisphere, the average of transmitted diffuse radiation (with horizontal incident angles ranging from 0 to $\arctan(2\left|\overline{\Delta H}\right| / R)$) arriving at the center of the canopy top surface is approximated as:

$$\overline{S}_t = S_{in}(\int_0^{\arctan(2|\overline{\Delta H}|/\Delta x)} \exp(-k \cdot LAD \cdot |\overline{\Delta H}| / \sin\theta) d\theta) / \arctan(2|\overline{\Delta H}| / \Delta x) \tag{6.21}$$

where the integral is approximated numerically using intervals of $\pi/90$.

The effective diffuse radiation $\tilde{S}_{in}$ for a shaded tree is calculated with Equation (6.16) but with values of f and $\overline{S}_t$ calculated using Equation (6.20), and Equation (6.21) for diffuse radiation.

If a considered tree is taller than the averaged tree heights of surrounding trees, the exposure effect of diffuse radiation is accounted for by considering a surplus diffuse radiation received by its exposed tree area following the same concept as described in Section B.1.3. The effective input diffuse radiation at the canopy top surface $\tilde{S}_{in}$ for the exposed tree is calculated with Equation (6.17) but with values of f and $\overline{S}_t$ calculated using Equation (6.20) and Equation (6.21). The variables for the situation of exposure are illustrated in Figure 6.5d.

6.5.5 Domain-scale average of direct and diffuse radiation

Following the above procedures, instantaneous, element-scale effective direct beam shortwave radiation corresponding to a given Sun's solar angle θ is a nonlinear function of the canopy height difference between a considered tree and its immediate upstream tree (a). If an exposed and a shaded tree have the same absolute canopy height difference ($|\Delta H|$) with respect to their respective immediate upstream trees, the average of their calculated effective input shortwave radiation equals to the above-canopy radiation (defined in Section 3.1).

At the domain scale, the average of the element-scale effective direct beam shortwave radiation is mathematically equal to the above-canopy radiation if exposed trees have a

190

similar frequency distribution of ΔH as that of shaded trees. For a forested domain such as the one used in this study, such a similarity is indeed observed (Figure 6.7) for any instant hour. As a result, the domain-scale average of adjusted shortwave radiation for the UMBS site nearly equals to the observed radiation for a horizontal plane, with a difference smaller than 1% for each simulated hour.

For diffuse radiation, a nonlinear relationship exists between the effective input diffuse radiation and the average canopy height difference ($\overline{\Delta H}$) between a considered tree and its eight immediate neighboring trees (Figure 6.6b). As the direction of incident diffuse radiation is hemispherically isotropic, the frequency distribution of $\overline{\Delta H}$ for exposed or shaded trees is constant in time. Within the study domain, exposed trees result in a frequency distribution of $\overline{\Delta H}$ similar to that for shaded trees (Figure 6.8). The domain-scale average of the element-scale input diffuse shortwave is very close to the observed radiation for a horizontal plane, with a difference less than 0.2%.
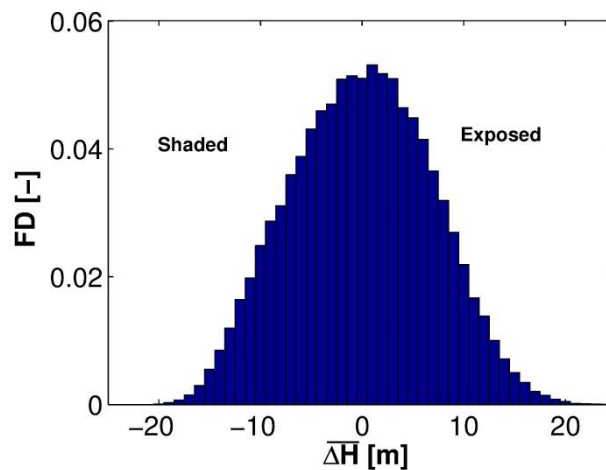
Figure 6.8. The Frequency Distribution (FD) of the element-scale average canopy height difference $\overline{\Delta H}$ computed for the study domain. The frequency distribution to the left/right of the line of $\overline{\Delta H} = 0$ corresponds to shaded/exposed trees.

6.6 Five study root network used in the simulation
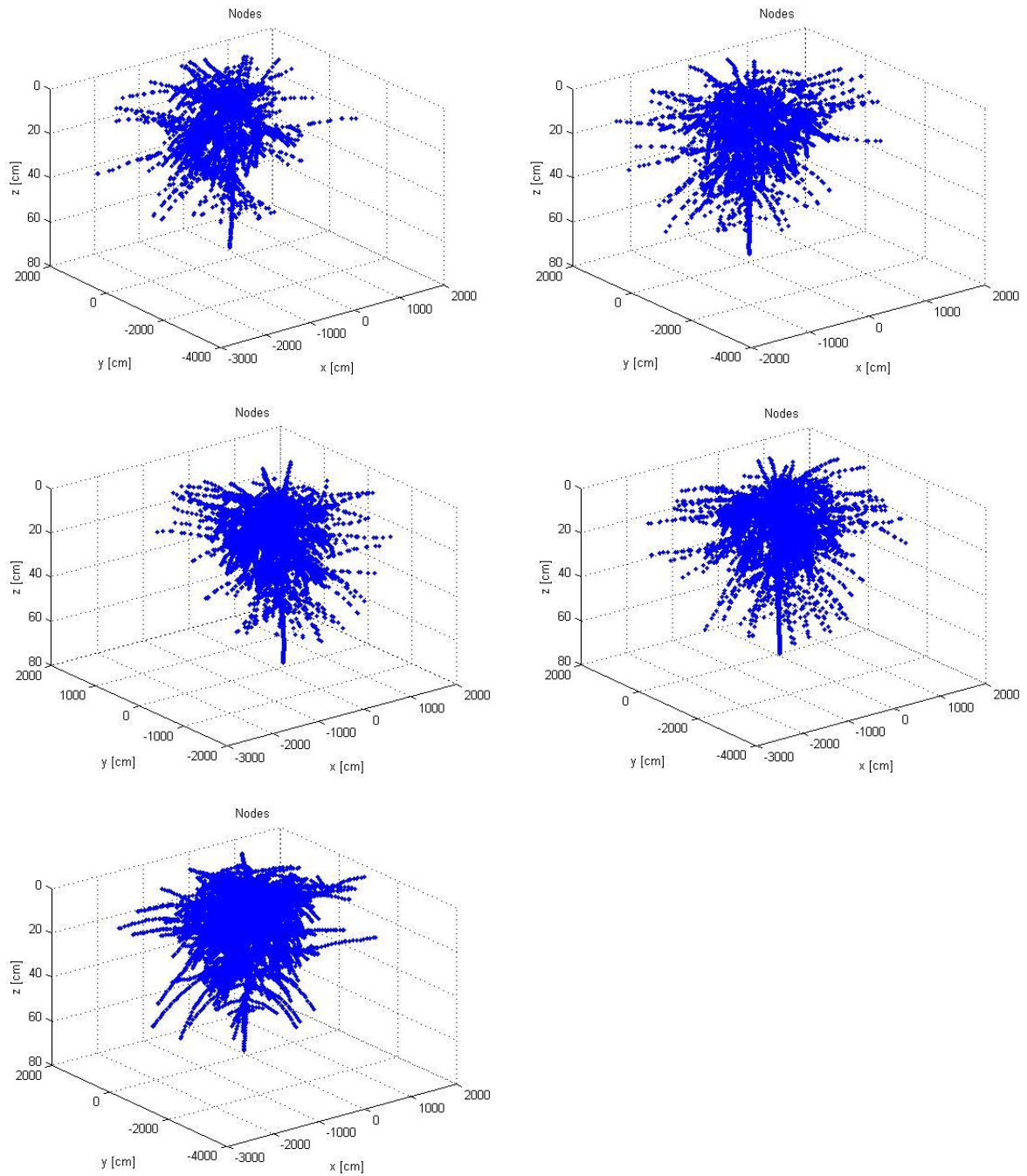
Figure 6.9. The spatial distribution of root nodes (blue dots) in the five root networks used in the simulation. For the purpose of demonstration, all the root networks were shown with a lateral spread of 20 m.

6.7 Sensitivity of K_{comp} to hydraulic properties of the root system

Besides the set of hydraulic properties shown in Table 3, two more scenarios representing less or more conductive root systems were considered (Table 4 and Table 5), and the value of K_{comp} is shown to be positively related to the conductivities of the root system (Figure 6.10 and Figure 6.11).
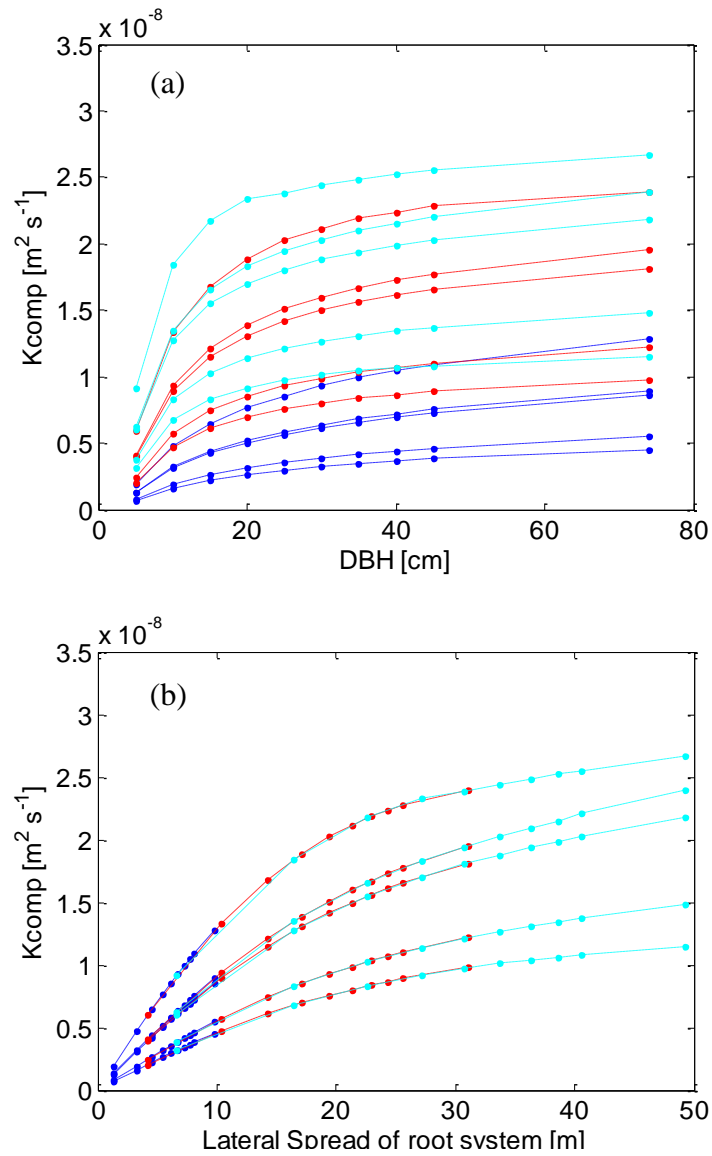
Figure 6.10. The relationship between K_{comp} and (a) lateral spread of the root system or (b)

the DBH of the trees for the five root networks with hydraulic properties in Table 4, which represents less conductive root systems. Different color indicates the scenarios of lateral spread (Section 4.6.1): blue indicates small scenario of lateral spread; red indicates benchmark scenario of lateral spread; and cyan indicates large scenario of lateral spread.
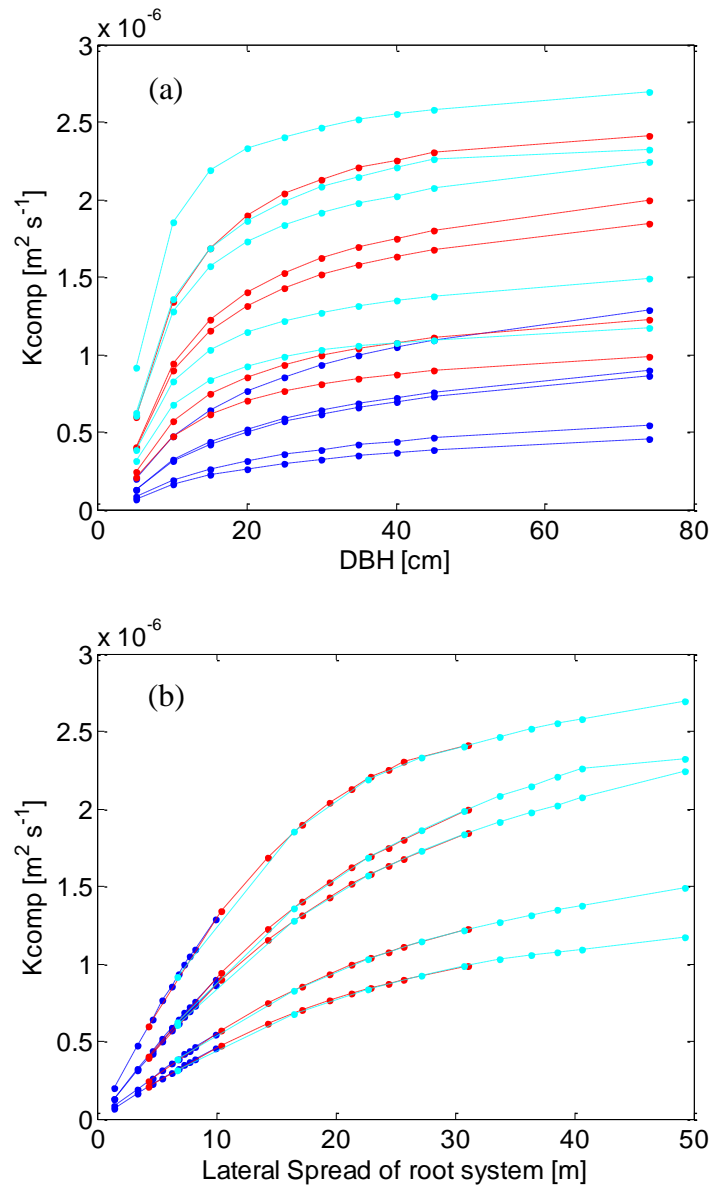
Figure 6.11. The relationship between K_{comp} and (a) lateral spread of the root system or (b)

the DBH of the trees for the five root networks with hydraulic properties in Table 5, which represents more conductive root systems. Different color indicates the scenarios of lateral spread (Section 4.6.1): blue indicates small scenario of lateral spread; red indicates benchmark scenario of lateral spread; and cyan indicates large scenario of lateral spread.

References

Adar, E.M. et al., 1995. Utilization of oxygen-18 and deuterium in seem flow for the identification of transpiration sources: Soil water versus groundwater in sand dune terrain. Application of Tracers in Arid Zone Hydrology(232): 329-338.

Albergel, C. et al., 2008. From near-surface to root-zone soil moisture using an exponential filter: an assessment of the method based on in-situ observations and model simulations. Hydrology and Earth System Sciences, 12(6): 1323-1337.

Ali, G.A., Roy, A.G., Legendre, P., 2010. Spatial relationships between soil moisture patterns and topographic variables at multiple scales in a humid temperate forested catchment. Water Resources Research, 46.

Amenu, G.G., Kumar, P., 2008. A model for hydraulic redistribution incorporating coupled soil-root moisture transport. Hydrology and Earth System Sciences, 12(1): 55-74.

Anderson, M.C., Kustas, W.P., Norman, J.M., 2003. Upscaling and downscaling - A regional view of the soil-plant-atmosphere continuum. Agronomy Journal, 95(6): 1408-1423.

Atchley, A.L., Maxwell, R.M., 2011. Influences of subsurface heterogeneity and vegetation cover on soil moisture, surface temperature and evapotranspiration at hillslope scales. Hydrogeology Journal, 19(2): 289-305.

Avissar, R., Pielke, R.A., 1989. A parameterization of heterogeneous land surfaces for atmospheric numerical models and its impact on regional meteorology. Monthly Weather Review, 117(10): 2113-2136.

Avissar, R., Schmidt, T., 1998. An evaluation of the scale at which ground-surface heat flux patchiness affects the convective boundary layer using large-eddy simulations. Journal of the Atmospheric Sciences, 55(16): 2666-2689.

Bergen, K.M., Dronova, I., 2007. Observing succession on aspen-dominated landscapes using a remote sensing-ecosystem approach. Landscape Ecology, 22(9): 1395-1410.

Bhatti, J.S. et al., 2000. Simulations of pre- and post-harvest soil temperature, soil moisture, and snowpack for jack pine: comparison with field observations. Forest Ecology and Management, 138(1-3): 413-426.

Bidel, L.P.R., Pages, L., Riviere, L.M., Pelloux, G., Lorendeau, J.Y., 2000. MassFlowDyn I: A carbon transport and partitioning model for root system architecture. Annals of Botany, 85(6): 869-886.

Biondini, M., 2001. A three-dimensional spatial model for plant competition in an heterogeneous soil environment. Ecological Modelling, 142(3): 189-225.

Bisselink, B., van Meijgaard, E., Dolman, A.J., de Jeu, R.A.M., 2011. Initializing a regional climate model with satellite-derived soil moisture. Journal of Geophysical Research-Atmospheres, 116: 13.

Blanquies, J., Scharff, M., Hallock, B., 2003. The design and construction of a rainfall simulator, International Erosion Control Association, Las Vegas, Nevada.

Blizzard, W., Boyer, J., 1980. Comparative resistance of the soil and the plant to water transport. Plant Physiol., 154(2): 227-237.

Blum, A., 2005. Drought resistance, water-use efficiency, and yield potential - are they compatible, dissonant, or mutually exclusive? Australian Journal of Agricultural Research, 56(11): 1159-1168.

Bohrer, G., Katul, G.G., Walko, R.L., Avissar, R., 2009. Exploring the Effects of Microscale Structural Heterogeneity of Forest Canopies Using Large-Eddy Simulations. Boundary-Layer Meteorology, 132(3): 351-382.

Bohrer, G. et al., 2005. Finite element tree crown hydrodynamics model (FETCH) using porous media flow within branching elements: A new representation of tree hydrodynamics. Water Resources Research, 41(11).

Bohrer, G., Wolosin, M., Brady, R., Avissar, R., 2007. A virtual canopy generator (V-CaGe) for modelling complex heterogeneous forest canopies at high resolution. Tellus Series B-Chemical and Physical Meteorology, 59(3): 566-576.

Bonan, G.B., 1996. A land surface model (LSM version 1.0) for ecology, hydrological, and atmospheric studies: Technical description and user's guide, Natl. Cent. for Atmos. Res., Boulder, Colorado.

Bonan, G.B. et al., 2002. The land surface climatology of the community land model coupled to the NCAR community climate model. Journal of Climate, 15(22): 3123-3149.

Bovard, B.D., Curtis, P.S., Vogel, C.S., Su, H.B., Schmid, H.P., 2005. Environmental controls on sap flow in a northern hardwood forest. Tree Physiol., 25(1): 31-38.

Breda, N., Granier, A., Barataud, F., Moyne, C., 1995. Soil water dynamics in an oak stand. I. Soil moisture, water potentials and water uptake by roots. Plant and Soil, 172(1): 17-27.

Brisson, N., Olioso, A., Clastre, P., 1993. Daily transpiration of field soybeans as related to hydraulic conductance, root distribution, soil potential and midday leaf potential. Plant and Soil, 154(2): 227-237.

Bruckler, L., Lafolie, F., Doussan, C., Bussieres, F., 2004. Modeling soil-root water transport with non-uniform water supply and heterogeneous root distribution. Plant and Soil, 260(1-2): 205-224.

Bruijnzeel, L.A., 2004. Hydrological functions of tropical forests: not seeing the soil for the trees? Agriculture Ecosystems & Environment, 104(1): 185-228.

Brunner, A., 1998. A light model for spatially explicit forest stand models. Forest Ecology and Management, 107(1-3): 19-46.

Brunsell, N.A., Gillies, R.R., 2003. Scale issues in land-atmosphere interactions: implications for remote sensing of the surface energy balance. Agricultural and Forest Meteorology, 117(3-4): 203-221.

Brunsell, N.A., Mechem, D.B., Anderson, M.C., 2011. Surface heterogeneity impacts on boundary layer dynamics via energy balance partitioning. Atmospheric Chemistry and Physics, 11(7): 3403-3416.

Bunce, J.A., 2004. Carbon dioxide effects on stomatal responses to the environment and water use by crops under field conditions. Oecologia, 140(1): 1-10.

Calvet, J.C., Noilhan, J., 2000. From near-surface to root-zone soil moisture using year-round data. Journal of Hydrometeorology, 1(5): 393-411.

Canham, C.D., 2005. GLI Ray Analyzer Help, pp. http://www.sortie-nd.org/other_downloads/ GLI_Ray_Analyzer_Help/help.html.

Cannon, W.A., 1949. A tentative classification of root systems. Ecology, 30(4): 542-548.

Caple, M., 2012. Impacts of climate change on forests: physiological responses of Acer rubrum, Quercus rubra, and Populus grandidentata to variable air and soil moisture, University of Michigan Biological Station, Ann Arbor, MI.

Casper, B.B., Schenk, H.J., Jackson, R.B., 2003. Defining a plant's belowground zone of influence. Ecology, 84(9): 2313-2321.

Caylor, K.K., D'Odorico, P., Rodriguez-Iturbe, I., 2006. On the ecohydrology of structurally heterogeneous semiarid landscapes. Water Resources Research, 42(7).

Chakraborty, A., Li, B.L., 2009. Plant-to-plant direct competition for belowground resource in an overlapping depletion zone. Journal of Arid Land, 1(1): 9-15.

Chen, F. et al., 2003. Land surface heterogeneity in the cooperative atmosphere surface exchange study (CASES-97). Part I: Comparing modeled surface flux maps with surface-flux tower and aircraft measurements. Journal of Hydrometeorology, 4(2): 196-218.

Chen, J.M., Li, X., Nilson, T., Strahler, A., 2000. Recent advances in geometrical optical modelling and its applications. Remote Sensing Reviews, 18(2-4): 227-262.

Clark, R.T. et al., 2011. Three-Dimensional Root Phenotyping with a Novel Imaging and Software Platform. Plant Physiology, 156(2): 455-465.

Clawges, R., Vierling, L., Calhoon, M., Toomey, M., 2007. Use of a ground-based scanning lidar for estimation of biophysical properties of western larch (Larix occidentalis). International Journal of Remote Sensing, 28(19): 4331-4344.

Cleland, D.T., Leefers, L.A., Dickmann, D.I., Usda, 2001. Ecology and management of aspen: A lake states perspective. Sustaining Aspen in Western Landscapes: Symposium Proceedings(18): 81-99.

Cole, K.L. et al., 2002. Historical landcover changes in the Great Lakes region. USGS.

Collet, C., Lof, M., Pages, L., 2006. Root system development of oak seedlings analysed using an architectural model. Effects of competition with grass. Plant and Soil, 279(1-2): 367-383.

Coomes, D.A., Grubb, P.J., 2000. Impacts of root competition in forests and woodlands: A theoretical framework and review of experiments. Ecological Monographs, 70(2): 171-207.

Couvreur, V., Vanderborght, J., Javaux, M., 2012. A simple three-dimensional macroscopic root water uptake model based on the hydraulic architecture approach. Hydrology and Earth System Sciences, 16(8).

Crow, W.T., Wood, E.F., 2002. Impact of soil moisture aggregation on surface energy flux prediction during SGP'97. Geophysical Research Letters, 29(1).

Curtis, P.S. et al., 2005. Respiratory carbon losses and the carbon-use efficiency of a northern hardwood forest, 1999-2003. New Phytol., 167(2): 437-455.

Danjon, F., Barker, D.H., Drexhage, M., Stokes, A., 2008. Using three-dimensional plant root architecture in models of shallow-slope stability. Annals of Botany, 101(8): 1281-1293.

Danjon, F., Sinoquet, H., Godin, C., Colin, F., Drexhage, M., 1999. Characterisation of structural tree root architecture using 3D digitising and AMAPmod software. Plant and Soil, 211(2): 241-258.

Denslow, J.S., Ellison, A.M., Sanford, R.E., 1998. Treefall gap size effects on above- and below-ground processes in a tropical wet forest. Journal of Ecology, 86(4): 597-609.

Desborough, C.E., 1997. The impact of root weighting on the response of transpiration to moisture stress in land surface schemes. Monthly Weather Review, 125(8): 1920-1930.

Deutschman, D.H., Levin, S.A., Pacala, S.W., 1999. Error propagation in a forest succession model: The role of fine-scale heterogeneity in light. Ecology, 80(6): 1927-1943.

Di Iorio, A., Lasserre, B., Scippa, G.S., Chiantante, D., 2005. Root system architecture of Quercus pubescens trees growing on different sloping conditions. Annals of Botany, 95(2): 351-361.

Dickinson, R.E., 1983. Land surface processes and climate surface albedos and energy balance. Advances in Geophysics, 25: 305-353.

Dickinson, R.E., Henderson-Sellers, A., Kennedy, P.J., 1993. Biosphere-atmosphere transfer scheme (BATS) version 1E as coupled to the NCAR community climate model., National Center for Atmosphere Research, Bounlder, CO.

Dickinson, R.E. et al., 2006. The Community Land Model and its climate statistics as a component of the Community Climate System Model. Journal of Climate, 19(11): 2302-2324.

Diggle, A.J., 1988. Rootmap - a model in 3-dimensional coordinates of the growth and structure of fibrous root system. Plant and Soil, 105(2): 169-178.

Dinkelaker, B., Hengeler, C., Marschner, H., 1995. Distribution and function of proteoid rests and other root clusters. Botanica Acta, 108(3): 183-200.

Doussan, C., Pierret, A., Garrigues, E., Pages, L., 2006. Water uptake by plant roots: II - Modelling of water transfer in the soil root-system with explicit account of flow within the root system - Comparison with experiments. Plant and Soil, 283(1-2): 99-117.

Doussan, C., Vercambre, G., Pages, L., 1999. Water uptake by two contrasting root systems (maize, peach tree): results from a model of hydraulic architecture. Agronomie, 19(3-4): 255-263.

Draye, X., Kim, Y., Lobet, G., Javaux, M., 2010. Model-assisted integration of physiological and environmental constraints affecting the dynamic and spatial patterns of root water uptake from soils. Journal of Experimental Botany, 61(8): 2145-2155.

Drewitt, G.B. et al., 2002. Measuring forest floor CO2 fluxes in a Douglas-fir forest. Agricultural and Forest Meteorology, 110(4): 299-317.

Dunbabin, V., Rengel, Z., Diggle, A., 2003. Root architecture and nutrient capture - the complex riddle of what constitutes optimality of root form and function. Innovative Soil-Plant Systems for Sustainable Agricultural Practices, 2-16 pp.

Dunbabin, V., Rengel, Z., Diggle, A.J., 2004. Simulating form and function of root systems: efficiency of nitrate uptake is dependent on root system architecture and the spatial and temporal variability of nitrate supply. Functional Ecology, 18(2): 204-211.

Dunbabin, V.M. et al., 2011. Simulating the interaction between plant roots, soil water and nutrient flows, and barriers and objects in soil using ROOTMAP. 19th International Congress on Modelling and Simulation (Modsim2011): 975-981.

Dunbabin, V.M. et al., 2013. Modelling root-soil interactions using three-dimensional models of root growth, architecture and function. Plant and Soil, 372(1-2): 93-124.

Dwyer, L.M., Stewart, D.W., Balchin, D., 1988. Rooting characteristics of corn, soybeans and barley as a function of available water and soil physical characteristics. Canadian Journal of Soil Science, 68(1): 121-132.

Edwards, N.T., Rosstodd, B.M., 1979. Effects of stem girdling on biogeochemical cycles within a mixed decidudous forest in eastern tennessee. 1. soil solution chemistry, soil respiration, litterfall and root biomass studies. Oecologia, 40(3): 247-257.

Ek, M.B. et al., 2003. Implementation of Noah land surface model advances in the National Centers for Environmental Prediction operational mesoscale Eta model. Journal of Geophysical Research-Atmospheres, 108(D22).

El Maayar, M., Chen, J.M., 2006. Spatial scaling of evapotranspiration as affected by heterogeneities in vegetation, topography, and soil texture. Remote Sensing of Environment, 102(1-2): 33-51.

Elliott, J.A., Toth, B.M., Granger, R.J., Pomeroy, J.W., 1998. Soil moisture storage in mature and replanted sub-humid boreal forest stands. Canadian Journal of Soil Science, 78(1): 17-27.

Entekhabi, D. et al., 2010. The Soil Moisture Active Passive (SMAP) Mission. Proceedings of the Ieee, 98(5): 704-716.

Ershadi, A., McCabe, M.F., Evans, J.P., Walker, J.P., 2013. Effects of spatial aggregation on the multi-scale estimation of evapotranspiration. Remote Sensing of Environment, 131: 51-62.

Ewers, B.E., Mackay, D.S., Samanta, S., 2007. Interannual consistency in canopy stomatal conductance control of leaf water potential across seven tree species. Tree Physiology, 27(1): 11-24.

Farquhar, G.D., Caemmerer, S.V., Berry, J.A., 1980. A biochemical model of photosynthetic CO2 assimilation in leaves of C-3 species. Planta, 149(1): 78-90.

Fatichi, S., Ivanov, V.Y., Caporali, E., 2011. Simulation of future climate scenarios with a weather generator. Advances in Water Resources, 34(4): 448-467.

Feddes, R.A. et al., 2001. Modeling root water uptake in hydrological and climate models. Bulletin of the American Meteorological Society, 82(12): 2797-2809.

Feddes, R.A., Kowalik, P., Kolinskamalinka, K., Zaradny, H., 1976. Simulation field water-uptake by plants using a soil-water dependent root extraction function. Journal of Hydrology, 31(1-2): 13-26.

Fernandez-Galvez, J., Simmonds, L.P., Barahona, E., 2006. Estimating detailed soil water profile records from point measurements. European Journal of Soil Science, 57(5): 708-718.

Fiscus, E.L., 1972. In-situ measurement of root-water potential. Plant Physiology, 50(1): 191-&.

Flavel, R.J. et al., 2012. Non-destructive quantification of cereal roots in soil using high-resolution X-ray tomography. Journal of Experimental Botany, 63(7): 2503-2511.

Flores, A.N., Ivanov, V.Y., Entekhabi, D., Bras, R.L., 2009. Impact of Hillslope-Scale Organization of Topography, Soil Moisture, Soil Temperature, and Vegetation on

Modeling Surface Microwave Radiation Emission. Ieee Transactions on Geoscience and Remote Sensing, 47(8): 2557-2571.

Foley, J.A. et al., 1996. An integrated biosphere model of land surface processes, terrestrial carbon balance, and vegetation dynamics. Global Biogeochemical Cycles, 10(4): 603-628.

Frelich, L.E., Reich, P.B., 1995. Spatial patterns and succession in a minnesota southern-boreal forest. Ecological Monographs, 65(3): 325-346.

Fuchs, M., Tanner, C.B., 1968. Calibration and field test of soil heat flux plates. Soil Science Society of America Proceedings, 32(3): 326-&.

Galik, C.S., Jackson, R.B., 2009. Risks to forest carbon offset projects in a changing climate. Forest Ecology and Management, 257(11): 2209-2216.

Garre, S., Javaux, M., Vanderborght, J., Pages, L., Vereecken, H., 2011. Three-Dimensional Electrical Resistivity Tomography to Monitor Root Zone Water Dynamics. Vadose Zone Journal, 10(1): 412-424.

Garrigues, E., Doussan, C., Pierret, A., 2006. Water uptake by plant roots: I - Formation and propagation of a water extraction front in mature root systems as evidenced by 2D light transmission imaging. Plant and Soil, 283(1-2): 83-98.

Garrity, S.R., Meyer, K., Maurer, K.D., Hardiman, B., Bohrer, G., 2012a. Estimating plot-level tree structure in a deciduous forest by combining allometric equations, spatial wavelet analysis and airborne LiDAR. Remote Sensing Letters, 3(5): 443-451.

Garrity, S.R., Meyer, K., Maurer, K.D., Hardiman, B.S., Bohrer, G., 2012b. Estimating plot-level tree structure in a deciduous forest by combining allometric equations, spatial wavelet analysis and airborne lidar. *Remote Sensing Letters*, 3: 443-451.

Gerwitz, A., Page, E.R., 1974. Empirical mathematical-model to describe plant root systems. Journal of Applied Ecology, 11(2): 773-781.

Giambelluca, T.W., 2002. Hydrology of altered tropical forest. Hydrological Processes, 16(8): 1665-1669.

Godin, C., Costes, E., Sinoquet, H., 1999. A method for describing plant architecture which integrates topology and geometry. Annals of Botany, 84(3): 343-357.

Godin, C., Guedon, Y., 2001. AMAPmod: Introduction and Reference Manual, Version 1.8.

Gough, C.M., Vogel, C.S., Harrold, K.H., George, K., Curtis, P.S., 2007a. The legacy of harvest and fire on ecosystem carbon storage in a north temperate forest. Global Change Biology, 13(9): 1935-1949.

Gough, C.M. et al., 2007b. Coarse woody debris and the carbon balance of a north temperate forest. For. Ecol. Manage., 244(1-3): 60-67.

Gough, C.M., Vogel, C.S., Schmid, H.P., Su, H.B., Curtis, P.S., 2008. Multi-year convergence of biometric and meteorological estimates of forest carbon storage. Agricultural and Forest Meteorology, 148(2): 158-170.

Govaerts, Y.M., Verstraete, M.M., 1998. Raytran: A Monte Carlo ray-tracing model to compute light scattering in three-dimensional heterogeneous media. Ieee Transactions on Geoscience and Remote Sensing, 36(2): 493-505.

Goward, S.N., Xue, Y.K., Czajkowski, K.P., 2002. Evaluating land surface moisture conditions from the remotely sensed temperature/vegetation index measurements - An

exploration with the simplified simple biosphere model. Remote Sensing of Environment, 79(2-3): 225-242.

Grayson, R.B., Western, A.W., Chiew, F.H.S., Bloschl, G., 1997. Preferred states in spatial soil moisture patterns: Local and nonlocal controls. Water Resources Research, 33(12): 2897-2908.

Greco, S., Baldocchi, D.D., 1996. Seasonal variations of CO_2 and water vapour exchange rates over a temperate deciduous forest. Global Change Biology, 2(3): 183-197.

Green, S.R., Kirkham, M.B., Clothier, B.E., 2006. Root uptake and transpiration: From measurements and models to sustainable irrigation. Agricultural Water Management, 86(1-2): 165-176.

Gu, L.H. et al., 2007. Influences of biomass heat and biochemical energy storages on the land surface fluxes and radiative temperature. Journal of Geophysical Research-Atmospheres, 112(D2).

Guswa, A.J., 2005. Soil-moisture limits on plant uptake: An upscaled relationship for water-limited ecosystems. Advances in Water Resources, 28(6): 543-552.

Hall, B., 1986. Soil moisture as a potential factor preventing revegetation of areas on the Pellston Plain, Univeristy of Michigan Biological Station, Pellston.

Hammond, G., Lichtner, P., Lu, C., 2007. Subsurface multiphase flow and multicomponent reactive transport modeling using high-performance computing, 3rd Annual Scientific Discovery through Advanced Computing Conference (SciDAC 2007), Boston, MA, pp. U214-U223.

Hammond, G.E., Lichtner, P.C., Milis, R.T., Lu, C., 2008. Toward petascale computing in geosciences: application to the Hanford 300 Area - art. no. 012051, 4th Annual Scientific Discovery through Advanced Computing Conference (SciDAC 2008), Seattle, WA, pp. 12051-12051.

Hanson, P.J., Weltzin, J.F., 2000. Drought disturbance from climate change: response of United States forests. Science of the Total Environment, 262(3): 205-220.

Hardiman, B., Bohrer, G., Gough, C., Vogel, C., Curtis, P., 2011. The role of canopy structural complexity in wood net primary production of a maturing northern deciduous forest. Ecological Society of America, 92(9): 1818-1827.

Hardiman, B.S., Bohrer, G., Gough, C.M., Curtis, P.S., 2013. Canopy Structural Changes Following Widespread Mortality of Canopy Dominant Trees. Forests, 4(3): 537-552.

Hardiman, B.S. et al., 2012. Maintaining high rates of carbon storage in old forests: A mechanism linking canopy structure to forest function. Ecological Applications. *In review.* .

He, L. et al., 2011a. Effect of fine-scale canopy heterogeneity on energy and soil water fluxes in a northern temperate deciduous forest. *Proceedings of the AmeriFlux Science Meeting & 3rd NACP All-Investigators Meeting*, New Orleans, LA, USA.

He, L. et al., 2011b. Effect of fine-scale canopy heterogeneity on energy and soil water fluxes in a northern temperate mixed forest. *Proceedings of the AGU Fall Meeting*, San Francisco, CA, USA.

He, L. et al., 2012. Temporal dynamics of soil moisture in a northern temperate mixed successional forest after a prescribed intermediate disturbance. *Submitted to Agriculture and Forest Meteorology*.

He, L.L. et al., 2014. Effects of fine-scale soil moisture and canopy heterogeneity on energy and water fluxes in a northern temperate mixed forest. Agricultural and Forest Meteorology, 184: 243-256.

He, L.L. et al., 2013. Temporal dynamics of soil moisture in a northern temperate mixed successional forest after a prescribed intermediate disturbance. Agricultural and Forest Meteorology, 180: 22-33.

Heinen, M., 2014. Compensation in Root Water Uptake Models Combined with Three-Dimensional Root Length Density Distribution. Vadose Zone Journal, 13(2).

Hinsinger, P., Bengough, A.G., Vetterlein, D., Young, I.M., 2009. Rhizosphere: biophysics, biogeochemistry and ecological relevance. Plant and Soil, 321(1-2): 117-152.

Hirano, T., Kim, H., Tanaka, Y., 2003. Long-term half-hourly measurement of soil CO_2 concentration and soil respiration in a temperate deciduous forest. Journal of Geophysical Research-Atmospheres, 108(D20): 13.

Hodnett, M.G., Bell, J.P., 1986. Soil moisture investigations of groundwater recharge through black cotton soils in Madhya Pradesh, India. Hydrological Sciences Journal-Journal Des Sciences Hydrologiques, 31(3): 361-381.

Holmgren, M., Scheffer, M., Huston, M.A., 1997. The interplay of facilitation and competition in plant communities. Ecology, 78(7): 1966-1975.

Hong, S. et al., 2009. Effects of vegetation and soil moisture on the simulated land surface processes from the coupled WRF/Noah model. Journal of Geophysical Research-Atmospheres, 114.

Hou, Z.S., Rubin, Y., 2005. On minimum relative entropy concepts and prior compatibility issues in vadose zone inverse and forward modeling. Water Resources Research, 41(12).

Hu, Z.L., Islam, S., Jiang, L., 1999. Approaches for aggregating heterogeneous surface parameters and fluxes for mesoscale and climate models. Boundary-Layer Meteorology, 93(2): 313-336.

Iqbal, M., 1983. Introduction to solar radiation. Academic Press, Toronto, 390 pp.

Ivanov, V.Y., Bras, R.L., Vivoni, E.R., 2008a. Vegetation-hydrology dynamics in complex terrain of semiarid areas: 1. A mechanistic approach to modeling dynamic feedbacks. Water Resources Research, 44(3).

Ivanov, V.Y., Bras, R.L., Vivoni, E.R., 2008b. Vegetation-hydrology dynamics in complex terrain of semiarid areas: 2. Energy-water controls of vegetation spatiotemporal dynamics and topographic niches of favorability. Water Resources Research, 44(3).

Ivanov, V.Y. et al., 2010. Hysteresis of soil moisture spatial heterogeneity and the "homogenizing" effect of vegetation. Water Resources Research, 46.

Jackson, R.B. et al., 1996. A global analysis of root distributions for terrestrial biomes. Oecologia, 108(3): 389-411.

Jackson, R.B. et al., 2000a. Belowground consequences of vegetation change and their treatment in models. Ecological Applications, 10(2): 470-483.

Jackson, R.B., Sperry, J.S., Dawson, T.E., 2000b. Root water uptake and transport: using physiological processes in global predictions. Trends in Plant Science, 5(11): 482-488.

James, S.E., Partel, M., Wilson, S.D., Peltzer, D.A., 2003. Temporal heterogeneity of soil moisture in grassland and forest. Journal of Ecology, 91(2): 234-239.

Janott, M. et al., 2011. A one-dimensional model of water flow in soil-plant systems based on plant architecture. Plant and Soil, 341(1-2): 233-256.

Janowiak, M.K., Webster, C.R., 2010. Promoting Ecological Sustainability in Woody Biomass Harvesting. Journal of Forestry, 108(1): 16-23.

Javaux, M., Schroder, T., Vanderborght, J., Vereecken, H., 2008. Use of a three-dimensional detailed modeling approach for predicting root water uptake. Vadose Zone Journal, 7(3): 1079-1088.

Jones, H.G., Sutherland, R.A., 1991. Stomatal control of xylem embolism. Plant Cell and Environment, 14(6): 607-612.

Jourdan, C., Rey, H., 1997. Modelling and simulation of the architecture and development of the oil-palm (Elaeis guineensis Jacq) root system .2. Estimation of root parameters using the RACINES postprocessor. Plant and Soil, 190(2): 235-246.

Khuder, H., Stokes, A., Danjon, F., Gouskou, K., Lagane, F., 2007. Is it possible to manipulate root anchorage in young trees? Plant and Soil, 294(1-2): 87-102.

Kirschbaum, M.U.F., 2000. Forest growth and species distribution in a changing climate. Tree Physiology, 20(5-6): 309-322.

Knyazikhin, Y., Miessen, G., Panfyorov, O., Gravenhorst, G., 1997. Small-scale study of three-dimensional distribution of photosynthetically active radiation in a forest. Agricultural and Forest Meteorology, 88(1-4): 215-239.

Kobayashi, H., Iwabuchi, H., 2008. A coupled 1-D atmosphere and 3-D canopy radiative transfer model for canopy reflectance, light environment, and photosynthesis simulation in a heterogeneous landscape. Remote Sensing of Environment, 112(1): 173-185.

Kolb, T., Maxwell, M., Reynolds, T., Woomer, G., 2002. Distribution of soil types and tree communities as a function of glacial landroms in northern lower Michigan, University of Michigan Biological Station, Ann Arbor, MI.

Koster, R.D., Suarez, M.J., 1992. Modeling the land surface boundary in climate models as a composite of independent vegetation stands Journal of Geophysical Research-Atmospheres, 97(D3): 2697-2715.

Koster, R.D., Suarez, M.J., 2003. Impact of land surface initialization on seasonal precipitation and temperature prediction. Journal of Hydrometeorology, 4(2): 408-423.

Lai, C.T., Katul, G., Ellsworth, D., Oren, R., 2000. Modelling vegetation-atmosphere CO_2 exchange by a coupled Eulerian-Langrangian approach. Boundary-Layer Meteorology, 95(1): 91-122.

Lambers, H. et al., 2011. Phosphorus Nutrition of Proteaceae in Severely Phosphorus-Impoverished Soils: Are There Lessons To Be Learned for Future Crops? Plant Physiology, 156(3): 1058-1066.

Law, B.E., Cescatti, A., Baldocchi, D.D., 2001. Leaf area distribution and radiative transfer in open-canopy forests: implications for mass and energy exchange. Tree Physiology, 21(12-13): 777-787.

Lefsky, M.A., Cohen, W.B., Parker, G.G., Harding, D.J., 2002. Lidar remote sensing for ecosystem studies. Bioscience, 52(1): 19-30.

Leitner, D., Klepsch, S., Bodner, G., Schnepf, A., 2010. A dynamic root system growth model based on L-Systems. Plant and Soil, 332(1-2): 177-192.

Leuning, R., 1995. A critical appraisal of a combined stomatal-photosynthesis model for C-3 plants. Plant Cell and Environment, 18(4): 339-355.

Leuning, R., Condon, A.G., Dunin, F.X., Zegelin, S., Denmead, O.T., 1994. Rainfall interception and evaporation from soil below a wheat canopy. Agricultural and Forest Meteorology, 67(3-4): 221-238.

Leuschner, C. et al., 2001. Drought responses at leaf, stem and fine root levels of competitive Fagus sylvatica L. and Quercus petraea (Matt.) Liebl. trees in dry and wet years. Forest Ecology and Management, 149(1-3): 33-46.

Lewis, S.L., Malhi, Y., Phillips, O.L., 2004. Fingerprinting the impacts of global change on tropical forests. Philosophical Transactions of the Royal Society of London Series B-Biological Sciences, 359(1443): 437-462.

Li, B., Avissar, R., 1994. The impact of spatial variability of land-surface characteristics on land-surface heat fluxes. Journal of Climate, 7(4): 527-537.

Li, K.Y., De Jong, R., Boisvert, J.B., 2001. An exponential root-water-uptake model with water stress compensation. Journal of Hydrology, 252(1-4): 189-204.

Li, Y., Fuchs, M., Cohen, S., Cohen, Y., Wallach, R., 2002. Water uptake profile response of corn to soil moisture depletion. Plant Cell and Environment, 25(4): 491-500.

Lindenma, A., 1968. Mathematical models for cellular interactions in development. 2. simple and branching filaments with 2-sided inputs. Journal of Theoretical Biology, 18(3): 300-&.

Lindenmayer, D.B., Margules, C.R., Botkin, D.B., 2000. Indicators of biodiversity for ecologically sustainable forest management. Conservation Biology, 14(4): 941-950.

Lu, C., Lichtner, P.C., 2007. High resolution numerical investigation on the effect of convective instability on long term CO2 storage in saline aquifers, 3rd Annual Scientific Discovery through Advanced Computing Conference (SciDAC 2007), Boston, MA, pp. U320-U325.

Lynch, J.P., 2007. Roots of the second green revolution. Australian Journal of Botany, 55(5): 493-512.

Lynch, J.P., Brown, K.M., 2012. New roots for agriculture: exploiting the root phenome. Philosophical Transactions of the Royal Society B-Biological Sciences, 367(1595): 1598-1604.

Lynch, J.P., Nielsen, K.L., Davis, R.D., Jablokow, A.G., 1997. SimRoot: Modelling and visualization of root systems. Plant and Soil, 188(1): 139-151.

Mahfouf, J.F. et al., 1996. Analysis of transpiration results from the RICE and PILPS workshop. Global and Planetary Change, 13(1-4): 73-88.

Malmsheimer, R.W. et al., 2008. Forest management solutions for mitigating climate change in the United States. Journal of Forestry, 106(3): 115-117.

Manoli, G. et al., 2014. Tree root systems competing for soil moisture in a 3D soil-plant model. Advances in Water Resources, 66: 32-42.

Martin, J.G., Bolstad, P.V., 2005. Annual soil respiration in broadleaf forests of northern Wisconsin: influence of moisture and site biological, chemical, and physical characteristics. Biogeochemistry, 73(1): 149-182.

Matamala, R., Schlesinger, W.H., 2000. Effects of elevated atmospheric CO2 on fine root production and activity in an intact temperate forest ecosystem. Global Change Biology, 6(8): 967-979.

Maxwell, R.M., Chow, F.K., Kollet, S.J., 2007. The groundwater-land-surface-atmosphere connection: Soil moisture effects on the atmospheric boundary layer in fully-coupled simulations. Advances in Water Resources, 30(12): 2447-2466.

Medvigy, D., Walko, R.L., Avissar, R., 2008. Modeling interannual variability of the Amazon hydroclimate. Geophysical Research Letters, 35(15).

Meissner, M., Kohler, M., Schwendenmann, L., Holscher, D., 2012. Partitioning of soil water among canopy trees during a soil desiccation period in a temperate mixed forest. Biogeosciences, 9(8): 3465-3474.

Mills, R.T., Lu, C., Lichtner, P.C., Hammond, G.E., 2007. Simulating subsurface flow and transport on ultrascale computers using PFLOTRAN, 3rd Annual Scientific Discovery through Advanced Computing Conference (SciDAC 2007), Boston, MA, pp. U387-U393.

Monsi, M., Saeki, T., 1953. Über den Lichtfaktor in den Pflanzengesellschaften und seine Bedeutung für die Stoffproduction. Japanese Journal of Botany, 14: 22-52.

Nave, L.E. et al., 2011. Disturbance and the resilience of coupled carbon and nitrogen cycling in a north temperate forest. Journal of Geophysical Research-Biogeosciences, 116.

Nicoll, B.C. et al., 2006. The architecture of Picea sitchensis structural root systems on horizontal and sloping terrain. Trees-Structure and Function, 20(6): 701-712.

Nielsen, K.L., Lynch, J.P., Jablokow, A.G., Curtis, P.S., 1994. Carbon cost of root systems - an architectural approach. Plant and Soil, 165(1): 161-169.

Oleson, K., Dai, Y., Bonan, G.B., Bosilovichm, M., Dickinson, R., 2004a. Technical description of the Community Land Model (CLM), *Tech. Note NCAR/tn-461+STR.*, National Center for Atmospheric Research, Boulder, Colorado.

Oleson, K.W. et al., 2004b. Technical description of the community land model (CLM), Boulder, Colorado.

Oltchev, A. et al., 2002. Transpiration of a mixed forest stand: field measurements and simulation using SVAT models. Boreal Environment Research, 7(4): 389-397.

Oswald, S.E. et al., 2008. Quantitative imaging of infiltration, root growth, and root water uptake via neutron radiography. Vadose Zone Journal, 7(3): 1035-1047.

Pages, L., Jordan, M.O., Picard, D., 1989. A simulation-model of the 3-dimensional architecture of the maize root-system. Plant and Soil, 119(1): 147-154.

Pages, L. et al., 2004. Root Typ: a generic model to depict and analyse the root system architecture. Plant and Soil, 258(1-2): 103-119.

Parker, G.G. et al., 2004. Three-dimensional structure of an old-growth Pseudotsuga-tsuga canopy and its implications for radiation balance, microclimate, and gas exchange. Ecosystems, 7(5): 440-453.

Pataki, D.E., Oren, R., 2003. Species differences in stomatal control of water loss at the canopy scale in a mature bottomland deciduous forest. Advances in Water Resources, 26(12): 1267-1278.

Person, M. et al., 2010. Assessment of basin-scale hydrologic impacts of CO(2) sequestration, Illinois basin. International Journal of Greenhouse Gas Control, 4(5): 840-854.

Phillips, O.L. et al., 2010. Drought-mortality relationships for tropical forests. New Phytologist, 187(3): 631-646.

Pieruschka, R., Huber, G., Berry, J.A., 2010. Control of transpiration by radiation. Proceedings of the National Academy of Sciences of the United States of America, 107(30): 13372-13377.

Pitman, A.J., 2003. The evolution of, and revolution in, land surface schemes designed for climate models. International Journal of Climatology, 23(5): 479-510.

Plamboeck, A.H., Grip, H., Nygren, U., 1999. A hydrological tracer study of water uptake depth in a Scots pine forest under two different water regimes. Oecologia, 119(3): 452-460.

Porter, J.R., Semenov, M.A., 2005. Crop responses to climatic variation. Philosophical Transactions of the Royal Society B-Biological Sciences, 360(1463): 2021-2035.

Pressley, S. et al., 2005. Long-term isoprene flux measurements above a northern hardwood forest. Journal of Geophysical Research-Atmospheres, 110(D7): 12.

Prusinkiewiez, P., Hanan, J., Mech, R., 2000. An L-system-based plant modeling language. Applications of Graph Transformations with Industrial Relevance, Proceedings, 1779: 395-410.

Raats, P.A.C., 1974. Steady flows of water and salt in uniform soil profiles with plant roots. Soil Science Society of America Journal, 38(5): 717-722.

Ragab, R., 1995. Towards a continuous operational system to estimate the root-zone soil-moisture intermittent remotely-sensed surface moisture Journal of Hydrology, 173(1-4): 1-25.

Raupach, M.R., Finnigan, J.J., 1995. Scale issues in bounary-layer meteorology - surface-energy balances in heterogeneous terrain. Hydrological Processes, 9(5-6): 589-612.

Robinson, D., 2005. Integrated root responses to variations in nutrient supply. Nutrient Acquisition by Plants: Ecological Perspective, 181: 43-61.

Robock, A., Vinnikov, K.Y., Schlosser, C.A., Speranskaya, N.A., Xue, Y.K., 1995. Use of midlatitude soil-mosisture and meterological observations to validate soil-mosisture simulations with biosphere and bucket models. Journal of Climate, 8(1): 15-35.

Rodriguez-Iturbe, I., 2000. Ecohydrology: A hydrologic perspective of climate-soil-vegetation dynamics. Water Resources Research, 36(1): 3-9.

Rodriguez-Iturbe, I., D'Odorico, P., Laio, F., Ridolfi, L., Tamea, S., 2007. Challenges in humid land ecohydrology: Interactions of water table and unsaturated zone with climate, soil, and vegetation. Water Resources Research, 43(9).

Ronda, R.J., van den Hurk, B., Holtslag, A.A.M., 2002. Spatial heterogeneity of the soil moisture content and its impact on surface flux densities and near-surface meteorology. Journal of Hydrometeorology, 3(5): 556-570.

Rowe, C.M., 1993. Incorporating landscape heterogeneity in land surface albedo models. Journal of Geophysical Research-Atmospheres, 98(D3): 5037-5043.

Ryu, D., Famiglietti, J.S., 2006. Multi-scale spatial correlation and scaling behavior of surface soil moisture. Geophysical Research Letters, 33(8).

Sakai, A.K., Roberts, M.R., Jolls, C.L., 1985. Successional changes in a mature aspen forest in northern lower michigan - 1974-1981. American Midland Naturalist, 113(2): 271-282.

Salmun, H., Molod, A., 2006. Progress in modeling the impact of land cover change on the global climate. Progress in Physical Geography, 30(6): 737-749.

Savage, K., Davidson, E.A., Richardson, A.D., Hollinger, D.Y., 2009. Three scales of temporal resolution from automated soil respiration measurements. Agricultural and Forest Meteorology, 149(11): 2012-2021.

Schaap, M.G., Leij, F.J., van Genuchten, M.T., 2001. ROSETTA: a computer program for estimating soil hydraulic parameters with hierarchical pedotransfer functions. Journal of Hydrology, 251(3-4): 163-176.

Schenk, H.J., Jackson, R.B., 2002. Rooting depths, lateral root spreads and below-ground/above-ground allometries of plants in water-limited ecosystems. Journal of Ecology, 90(3): 480-494.

Schier, G.A., Smith, A.D., 1979. Sucker regeneration in a Utah aspen clone after clearcutting, partial cutting, scarification, and girdling, USDA Forest Service Research Note, INT-253.

Schmid, H.P., Grimmond, C.S.B., Cropley, F., Offerle, B., Su, H.B., 2000. Measurements of CO2 and energy fluxes over a mixed hardwood forest in the mid-western United States. Agricultural and Forest Meteorology, 103(4): 357-374.

Schmid, H.P., Su, H.B., Vogel, C.S., Curtis, P.S., 2003. Ecosystem-atmosphere exchange of carbon dioxide over a mixed hardwood forest in northern lower Michigan. Journal of Geophysical Research-Atmospheres, 108(D14).

Schmitt, A., Glaser, B., 2011. Organic matter dynamics in a temperate forest soil following enhanced drying. Soil Biology & Biochemistry, 43(3): 478-489.

Schneider, C.L., Attinger, S., Delfs, J.O., Hildebrandt, A., 2010. Implementing small scale processes at the soil-plant interface - the role of root architectures for calculating root water uptake profiles. Hydrology and Earth System Sciences, 14(2): 279-289.

Schrumpf, M., Axmacher, J.C., Zech, W., Lyaruu, H.V.M., 2011. Net precipitation and soil water dynamics in clearings, old secondary and old-growth forests in the montane rain forest belt of Mount Kilimanjaro, Tanzania. Hydrological Processes, 25(3): 418-428.

Schulz, H., Postma, J., van Dusschoten, D., Scharr, H., Behnke, S., 2012. 3D reconstruction of plant roots from MRI images. Proceedings of the International Conference on Computer Vision Theory and Applications (VISAPP, February 2012), Rome, Italy.

Schymanski, S.J., Sivapalan, M., Roderick, M.L., Beringer, J., Hutley, L.B., 2008. An optimality-based model of the coupled soil moisture and root dynamics. Hydrology and Earth System Sciences, 12(3): 913-932.

Schäfer, K.V.R., Oren, R., Lai, C.T., Katul, G.G., 2002. Hydrologic balance in an intact temperate forest ecosystem under ambient and elevated atmospheric CO_2 concentration. Glob. Change Biol., 8(9): 895-911.

Sellers, P.J., 1985. Canopy reflectance, photosynthesis and transpiration. International Journal of Remote Sensing, 6(8): 1335-1372.

Sellers, P.J., Fennessy, M.J., Dickinson, R.E., 2007. A numerical approach to calculating soil wetness and evapotranspiration over large grid areas. Journal of Geophysical Research-Atmospheres, 112(D18): 16.

Sellers, P.J. et al., 1995. Effects of spatial variability in topography, vegetation cover and soil moisture on area-averaged surface fluxes: A case study using the FIFE 1989 data. Journal of Geophysical Research-Atmospheres, 100(D12): 25607-25629.

Sellers, P.J. et al., 1996. A revised land surface parameterization (SiB2) for atmospheric GCMs .1. Model formulation. Journal of Climate, 9(4): 676-705.

Seneviratne, S.I. et al., 2010. Investigating soil moisture-climate interactions in a changing climate: A review. Earth-Science Reviews, 99(3-4): 125-161.

Seth, A., Giorgi, F., Dickinson, R.E., 1994. Simulating fluxes from heterogeneous land surfaces - explicit subgrid method employing the biosphere-atmosphere transfer scheme (BATS). Journal of Geophysical Research-Atmospheres, 99(D9): 18651-18667.

Shannon, C., Weaver, W., 1964. The Mathematical Theory of Communication. University of Illinois, Urbana.

Sharp, R.E., Davies, W.J., 1985. Root-growth and water-uptake by maize plants in drying soil. Journal of Experimental Botany, 36(170): 1441-1456.

Shugart, H., Sedjo, R., Sohngen, B., 2003. Forests & Global Climate Change: Potential Impacts on US Forest Resources.

Simunek, J., Hopmans, J.W., 2009. Modeling compensated root water and nutrient uptake. Ecological Modelling, 220(4): 505-521.

Simunek, J., van Genuchten, M.T., Sejna, M., 2007. Modeling subsurface water flow and solute transport with HYDRUS and related numerical software packages, International Workshop on Numerical Modelling of Hydrodynamic for Water Resources, Zaragoza, SPAIN, pp. 95-114.

Smith, S., De Smet, I., 2012. Root system architecture: insights from Arabidopsis and cereal crops Introduction. Philosophical Transactions of the Royal Society B-Biological Sciences, 367(1595): 1441-1452.

Snetsinger, S., Ventura, S., 1990. Land cover change in the great lakes region from mid-nineteenth century to present, U.S. Forest Service.

Song, C.H. et al., 2009. Energy, water, and carbon fluxes in a loblolly pine stand: Results from uniform and gappy canopy models with comparisons to eddy flux data. Journal of Geophysical Research-Biogeosciences, 114: 18.

Sperry, J.S., 2000. Hydraulic constraints on plant gas exchange. Agricultural and Forest Meteorology, 104(1): 13-23.

Sridhar, V., Elliott, R.L., Chen, F., 2003. Scaling effects on modeled surface energy-balance components using the NOAH-OSU land surface model. Journal of Hydrology, 280(1-4): 105-123.

Stangl, R., Buchan, G.D., Loiskandl, W., 2009. Field use and calibration of a TDR-based probe for monitoring water content in a high-clay landslide soil in Austria. Geoderma, 150(1-2): 23-31.

Stone, E.L., Kalisz, P.J., 1991. On the maximum extent of tree roots. Forest Ecology and Management, 46(1-2): 59-102.

Tamasi, E. et al., 2005. Influence of wind loading on root system development and architecture in oak (Quercus robur L.) seedlings. Trees-Structure and Function, 19(4): 374-384.

Teuling, A.J., Uijlenhoet, R., Hupet, F., Troch, P.A., 2006. Impact of plant water uptake strategy on soil moisture and evapotranspiration dynamics during drydown. Geophysical Research Letters, 33(3).

Theseira, G.W., Host, G.E., Isebrands, J.G., Whisler, F.D., 2003. SOILPSI: a potential-driven three-dimensional soil water redistribution model-description and comparative evaluation. Environmental Modelling & Software, 18(1): 13-23.

Thomsen, J.E. et al., 2013. Contrasting strategies of hydrodynamic stress management in two deciduous broadleaf tree species in Michigan, *in preparation*. Forest, 4(4): 1106-1120.

Tuzet, A., Perrier, A., Leuning, R., 2003. A coupled model of stomatal conductance, photosynthesis and transpiration. Plant Cell and Environment, 26(7): 1097-1116.

USDA Forest Service, 2001. Forest Inventory Analysis (FIA), Washington, DC.

van Genuchten, M.T., 1980. A close-form equation for predicting the hydrulic conductivity of unsaturated soils. Soil Science Society of America Journal, 44(5): 892-898.

Venkatesh, B., Lakshman, N., Purandara, B.K., Reddy, V.B., 2011. Analysis of observed soil moisture patterns under different land covers in Western Ghats, India. Journal of Hydrology, 397(3-4): 281-294.

Vercambre, G., Pages, L., Doussan, C., Habib, R., 2003. Architectural analysis and synthesis of the plum tree root system in an orchard using a quantitative modelling approach. Plant and Soil, 251(1): 1-11.

Vereecken, H. et al., 2008. On the value of soil moisture measurements in vadose zone hydrology: A review. Water Resources Research, 44: 21.

Vereecken, H., Kollet, S., Simmer, C., 2010. Patterns in Soil-Vegetation-Atmosphere Systems: Monitoring, Modeling, and Data Assimilation. Vadose Zone Journal, 9(4): 821-827.

Vertessy, R.A., Watson, F.G.R., O'Sullivan, S.K., 2001. Factors determining relations between stand age and catchment water balance in mountain ash forests. Forest Ecology and Management, 143(1-3): 13-26.

Vrugt, J.A., van Wijk, M.T., Hopmans, J.W., Simunek, J., 2001a. One-, two-, and three-dimensional root water uptake functions for transient modeling. Water Resources Research, 37(10): 2457-2470.

Vrugt, J.A., van Wijk, M.T., Hopmans, J.W., Simunek, J., 2001b. One-, two-, and three-dimensional root water uptake functions for transient modeling. Water Resources Research, 37(10).

Walko, R.L., Avissar, R., 2008. The Ocean-Land-Atmosphere Model (OLAM). Part II: Formulation and Tests of the Nonhydrostatic Dynamic Core. Monthly Weather Review, 136(11): 4045-4062.

Walko, R.L. et al., 2000. Coupled atmosphere-biophysics-hydrology models for environmental modeling. Journal of Applied Meteorology, 39(6): 931-944.

Wang, Y.P., Jarvis, P.G., 1990. Influence of crown structural properties on PAR absorption, photosynthesis, and transpiration in sitka spruce - application of a model (MAESTRO). Tree Physiology, 7(1-4): 297-316.

Wilderotter, O., 2003. An adaptive numerical method for the Richards equation with root growth. Plant and Soil, 251(2): 255-267.

Wilson, D.J. et al., 2003. Spatial distribution of soil moisture over 6 and 30 cm depth, Mahurangi river catchment, New Zealand. Journal of Hydrology, 276(1-4): 254-274.

Wilson, K.B., Baldocchi, D.D., 2000. Seasonal and interannual variability of energy fluxes over a broadleaved temperate deciduous forest in North America. Agricultural and Forest Meteorology, 100(1): 1-18.

Winter, J.M., Pal, J.S., Eltahir, E.A.B., 2009. Coupling of Integrated Biosphere Simulator to Regional Climate Model Version 3. Journal of Climate, 22(10): 2743-2757.

Wolter, P.T., White, M.A., 2002. Recent forest cover type transitions and landscape structural changes in northeast Minnesota, USA. Landscape Ecology, 17(2): 133-155.

Wood, E.F. et al., 2011. Hyperresolution global land surface modeling: Meeting a grand challenge for monitoring Earth's terrestrial water. Water Resources Research, 47.

Wright, H.E., 1964. Aspects of the Early Postglacial Forest Succession in the Great Lakes Region. Ecology, 45(3): 439-448.

Wullschleger, S.D., Tschaplinski, T.J., Norby, R.J., 2002. Plant water relations at elevated CO_2 - implications for water-limited environments. Plant Cell and Environment, 25(2): 319-331.

Xue, Y., Sellers, P.J., Kinter, J.L., Shukla, J., 1991. A simplified biosphere model for global climate studies. Journal of Climate, 4(3): 345-364.

Yang, R.Q., Friedl, M.A., 2003. Modeling the effects of three-dimensional vegetation structure on surface radiation and energy balance in boreal forests. Journal of Geophysical Research-Atmospheres, 108(D16): 11.

Yates, D.N., Chen, F., Nagai, H., 2003. Land surface heterogeneity in the cooperative atmosphere surface exchange study (CASES-97). Part II: Analysis of spatial heterogeneity and its scaling. Journal of Hydrometeorology, 4(2): 219-234.

Zegada-Lizarazu, W., Zatta, A., Monti, A., 2012. Water uptake efficiency and above- and belowground biomass development of sweet sorghum and maize under different water regimes. Plant and Soil, 351(1-2): 47-60.

Zeng, X.B., Dai, Y.J., Dickinson, R.E., Shaikh, M., 1998. The role of root distribution for climate simulation over land. Geophysical Research Letters, 25(24): 4533-4536.

Zeng, X.B., Shaikh, M., Dai, Y.J., Dickinson, R.E., Myneni, R., 2002. Coupling of the common land model to the NCAR community climate model. Journal of Climate, 15(14): 1832-1854.

Zhang, H.P., Oweis, T., 1999. Water-yield relations and optimal irrigation scheduling of wheat in the Mediterranean region. Agricultural Water Management, 38(3): 195-211.

Zhu, J., Zhang, C., Lynch, J.P., 2010. The utility of phenotypic plasticity of root hair length for phosphorus acquisition. Functional Plant Biology, 37(4): 313-322.

Zwieniecki, M.A., Boersma, L., 1997. A technique to measure root tip hydraulic conductivity and root water potential simultaneously. Journal of Experimental Botany, 48(307): 333-336.